MULTI-SCALE COMPUTATIONAL SIMULATION OF PROGRESSIVE COLLAPSE OF STEEL FRAMES

by

Kapil Khandelwal

A dissertation submitted in partial fulfillment
of the requirements for the degree of
Doctor of Philosophy
(Civil Engineering)
in The University of Michigan
2008

Doctoral Committee:

Professor Sherif El-Tawil, Chair
Professor Subhash C. Goel
Associate Professor Krishnakumar R. Garikipati
Associate Professor Gustavo J. Parra-Montesinos

In memory of my grandmother:

Smt. Oma Devi Khandelwal

To my parents, brother and sister:

Shri. Gopal Das Khandelwal, Smt. Suman Khandelwal
Vikas Khandewal, Saloni Khandelwal

To my wife and sons:
Meenu Garg
Vishrut Khandelwal, Garv Khandelwal

ACKNOWLEDGEMENTS

This doctoral dissertation is the formal presentation of the research that I have completed during my five years as a graduate student in the Department of Civil and Environmental Engineering at the University of Michigan. During my graduate studies at Michigan I received invaluable knowledge, a wealth of advice and generous aid from an incomparable advisor, extraordinary teachers, wonderful friends and a caring family. I would like to take this opportunity to thank all those individuals who have helped me through the completion of this work.

First and foremost I would like to acknowledge, with the most profound gratitude, the guidance, counsel and financial aid that I have received from my thesis advisor Professor Sherif El-Tawil. Professor El-Tawil has taught me the value of a thorough understanding of the fundamentals of my particular area of specialization and he has taken the time to help me develop my proficiency as researcher and educator. For his advice, his help and his guidance, I am eternally indebted. I would also like to thank other members of my thesis committee Professor Subhash C. Goel, Professor Krishnakumar R. Garikipati and Professor Gustavo J. Parra-Montesinos for their helpful suggestions and valuable comments.

I would like to thank my parents, my wife Meenu, and my sons Vishrut and Garv for their patience and uncompromising support. Thanks is also due to my fellow friends and colleagues, including Dr. Vishambhar Nath Pandey, Dr. Ekin Ekiz, Prashant Chaudhary, Kittinun Sirijaroonchai, Supat Suwannakarn and Chung-Chan Hung, for their help at various phases of this study; the technicians of the Structural Engineering laboratory, Robert Spencer, Robert Fisher and Jan Pantolin, for their support in the experimental phase of this study.

TABLE OF CONTENTS

LIST OF TABLES

LIST OF FIGURES

ABSTRACT

Progressive building collapse occurs when failure of a structural component leads to the failure and collapse of surrounding members, possibly promoting additional collapse. Global system collapse will occur if the damaged system is unable to reach a new static equilibrium configuration. The objective of this research is to identify and investigate important issues related to collapse of seismically designed steel building systems using multi-scale computational models.

Coupled multi-scale finite element simulations are first carried out to investigate the collapse response of moment resisting steel frame sub-assemblages. Simulation results suggest that for collapse resistant construction, designers should strive to use a larger number of smaller beam members rather than concentrate resistance in a few larger members and should specify ASTM A-992 steel rather than specifying generic steels. Improved behavior can also be achieved by increasing the shear tab thickness or directly welding the beam web to the column.

Using information gleaned from the sub-assemblage simulations, computationally efficient structural scale models for progressive collapse analysis of seismically designed steel frames systems are developed. The models are calibrated and utilized within the context of the alternate path method to study the collapse resistance of multistory steel moment and braced frame building systems. A new analysis technique termed "pushdown analysis" is proposed and used to investigate collapse modes, failure loads and robustness of seismically designed frames. The collapse and pushdown analyses show that systems designed for high seismic risk are less vulnerable to gravity-induced progressive collapse and more robust than those designed for moderate seismic risk.

Motivated by a number of deficiencies in existing ductile fracture models for steel, a new micro-mechanical constitutive model is proposed. Damage mechanics principles are used and a scalar damage variable is introduced to represent micro-structural evolution related to micro-void nucleation, growth and coalescence during the ductile fracture process in steels. Numerical implementation and parametric studies are presented and discussed. Calibration and validation studies show that the proposed model can successfully represent ductile fracture of steels.

Although the system studies in this dissertation focused primarily on in-plane collapse response, the models and simulation methodologies developed herein can be extended in future work to address the collapse resistance of three-dimensional models.

CHAPTER 1

INTRODUCTION

1.1 General Introduction

During their lifetime, civil engineering structures could be subjected to natural hazards like earthquakes, hurricanes, tornadoes, floods and fires, and manmade hazards such as blast and impact. Structures are usually designed for credible events that can happen during their lifespan, but extreme events for which they were not adequately designed for can result in catastrophic failure. In recent times, events such as the 1994 Northridge earthquake, 1995 Kobe earthquake, 1995 Murrah Federal building bombing and 2001 attack on the World Trade Center have led to structural failures and collapse resulting in related loss of life and staggering economic loss.

After the failure of moment resisting steel frames in the Northridge and Kobe earthquakes, considerable research effort was expended by the engineering community to design and construct steel structures that are more safe and reliable. In particular, extensive research was conducted to make moment resisting connections less susceptible to fracture during earthquakes. As a result of these and other related efforts, earthquake engineering is now moving towards performance based design of structures. Relevant specifications and codes have been developed (FEMA 302 (1997), FEMA 350 (2000), FEMA 356 (2000), AISC Seismic (2005)) to guide designers to achieve performance objectives that are perceived to be appropriate by the structural engineering community and society at large.

In contrast to seismic effects, blast and impact effects on steel structures have not been adequately studied. Most of the studies carried out in the United States to date were commissioned by federal agencies interested in protecting important government buildings, and their results are generally not available to the public. There is a consensus, however, that one of the prime blast protection objectives for any building is to prevent progressive structural collapse. Progressive building collapse occurs when failure of a structural component leads to the failure and collapse of surrounding members, possibly promoting additional collapse. It is a complex, nonlinear dynamic process characterized by multi-scale responses. Global system collapse will occur if the damaged system is unable to reach a new static equilibrium configuration.

Progressive collapse has become an issue of increasing importance because of escalation in terrorist activities worldwide. Therefore, extreme events such as blast and impact which were considered extremely improbable in the past are now considered to be credible events, with a finite probability of occurrence. This increasing interest in progressive collapse issue is highlighted by a special publication on progressive collapse in the *Journal of Performance of Constructed Facilities* (ASCE, 2006): "Mitigating the Potential for Progressive Disproportionate Structural Collapse." Current building codes provide general guidelines to prevent progressive collapse based on redundancy, integrity, continuity, ductility and alternate load paths, but besides these guidelines there is limited understanding of the phenomenon itself.

1.2 Challenges Facing Research on Structural Collapse

Efforts to develop comprehensive progressive collapse resistant specifications have been hindered by a lack of both experimental and analytical information about progressive collapse. On the experimental front, the rate of loading and the scale of the problem, i.e. that it involves a full system, has made testing difficult. On the other hand, numerical simulation is a challenging task because the collapse process involves modeling component and system behavior across several length scales.

In the case of failure of steel structural systems, the length scales of the physical processes involved range from failure at the material atomistic and micro level, progression of failure to the structural member level and then ultimately to the system level (Fig. 1.1). At the atomic scale, the failure process is characterized by dislocation movements and atomic bond breaking/decohesion. At the micro scale, the important physical processes that lead to material disintegration include micro-void initiation, micro-void growth and finally micro-void coalescence resulting in ductile fracture initiation (Fig. 1.1(b)). At the macro scale, the physical processes of interest are crack initiation and propagation, and local buckling of structural members and components (Fig. 1.1(c)). Finally, at the structural scale, important physical processes include global buckling of structural members, failure of structural members and connections, and contact and impact of failed members (Fig. 1.1(d) and 1.1(e)).

Simulation of a collapsing building system requires modeling of the associated physical processes at the corresponding length scales. As will be discussed in Chapter 2, these physical processes can be modeling using quantum mechanics, molecular dynamics and continuum mechanics methods. Quantum mechanics and molecular dynamics methods are suited for atomic and molecular scale studies. A huge computational effort is needed to use these methods for investigating system behavior at the structural scale. Therefore, as described in Chapter 2, direct application of these simulation methods to structural scales is limited. On the other hand, methods based on continuum mechanics frameworks are well suited for studying micro scale to structural scale response. Multi-scale methods are necessary because of the inadequacy of a single method to handle all important physical processes of interests. Such methods are classified as coupled or uncoupled multi-scale methods depending on how the information between the various scales is exchanged. In coupled multi-scale methods, the information available from distinct scales is combined into a single coherent coupled simulation. In uncoupled multi-scale methods, however, the information available from one scale is used to drive model at other scales. The work in this thesis employs such techniques.

1.3 Continuum Multi-scale Methods for Collapse Studies

In the context of structural analysis, continuum multi-scale methods in conjunction with finite element techniques are frequently used to study the behavior of structural systems. In this framework micro-scale behavior is typically modeled using micro-mechanical constitutive models in conjunction with 3-D solid or shell finite elements. Micro-scale behavior of these models is attributed to the constitutive material law which takes into account the evolution of the underlying microstructure of the material. These models are adequate to capture important micro-scale response such as ductile fracture initiation and propagation. On the other hand, macro-scale behavior including local buckling of structural components and global buckling of structural members can also be captured with 3-D solid or shell finite element models. Phenomenological constitutive material models such as classical plasticity theories are adequate for macro-scale applications. Structural scale response, however, is most efficiently modeled using 1-D beam/column and spring finite elements. Constitutive material models for beam/column finite elements are either based on resultant plasticity models (e.g. El-Tawil et al. (1998, 2001)) or fiber models (e.g. Liew et al. (2004)). For problems where contact and impact of failed members is also important, macro-scale models should be used instead of structural scale models. This multi-scale framework based on continuum mechanics is deemed most efficient, in terms of computational effort required, for handling structural engineering problems and is adopted in this work.

As shown in Fig 1.1(b), ductile fracture in steel at the micro-scale is a multistep process resulting from nucleation, growth and coalescence of micro-voids. Micro structure evolution during the void growth phase is highly influenced by the state of stress in the material. Two important modes of void growth include micro-void elongation under deviatoric stress and volumetric void growth under high hydrostatic/triaxial stress. Both of these void growth modes should be accounted for in micro-mechanical models that represent the ductile fracture process. Existing micro-scale models for steel take into account micro structure evolution due to either volumetric growth of micro-voids (Gurson 1977; Gologanu et al (1993, 1994); Leblond et al. (1995), Benzerga et al. (1999,

2001), Lee et al. (1999) and Garajeu et al. (2000)) or due to micro-voids elongation (e.g. Steinmann (1994)). Micro-mechanical constitutive models, which take into account micro structure evolution due to both volumetric and deviatoric components of stress, do not yet exist and are developed in this thesis. Another source of difficulty with existing micro-mechanical models, most which are the extensions of Gurson (1977) model, is that they include a number of non-physically motivated parameters which are difficult to calibrate. This issue is avoided herein by developing a new constitutive model and selecting calibration parameters for it that have physical meaning.

Structural scale models comprised of beam/column and spring finite elements have found numerous applications in structural engineering (cf. Hajjar et al. (1998), Kim et al. (2001), El-Tawil et al. (1998, 2001), Liew et al. (2004), Rassati et al. (2004) and Jin et al. (2005)). However, all of these models were developed primarily for seismic applications. There are, however, a few instances in the literature where structural scale models developed for seismic applications have been applied for progressive collapse investigations, e.g. Gross et al. (1983), Isobe et al. (2003) and Kaewkulchai et al. (2004). The applicability of structural scale models, developed for seismic applications, to collapse modeling is not adequately justified in these studies, however. This is an important issue that is addressed herein and appropriate models which can be used for collapse studies are developed in this work.

1.4 Alternate Path Method

One of the techniques used to design against progressive collapse is known as the alternate path method (APM). This method is advocated by GSA (2003) and UFC (2005), and has become a key tool used by the engineers. APM is a threat independent methodology and is generally applied in the context of a 'missing column' scenario to assess the potential for progressive collapse, i.e. it is used to check if a building can successfully absorb loss of a critical column or columns (Fig. 1.2). When applied in conjunction with nonlinear-dynamic analysis, APM is widely viewed as a comprehensive method for analysis and design of a structural system against progressive collapse.

However, appropriate models that can be used for APM analysis are not widely available. Development of such models and their application to prototype structural systems are two of the key objectives of this work.

Although APM can be used to study progressive collapse behavior, it cannot be used to determine the residual capacity of a structural system which is deemed to be able to survive loss of critical members. Development of a new analysis technique which can be employed to estimate the residual capacity of damaged structure is also one of the objectives of this study.

1.5 Seismic Design versus Progressive Collapse

There is an old perception in the structural engineering community, the earliest reference to which can be found in Ferahian (1972), that seismically designed structural steel frames, such as moment and brace frames, also have better resistance to progressive collapse. In other words, there is an implicit assumption that seismic design and detailing will translate into enhanced progressive collapse resistance. In fact, due to lack of design guidelines for progressive collapse, seismic resistant design is frequently advocated by researchers and practitioners for cases where prevention of progressive collapse is a design objective (Hamburger et al. 2004).

There is no systematic study to date that shows how seismic design and detailing influences structural system behavior in a progressive collapse situation. This is an important issue that has to be addressed because seismic forces impose a very different type of demand on a structure as compared to collapse. For example, for moment frames seismic forces results in high moment demand in the connection region. However, as will be discussed in Chapter 3, collapse is associated with high tensile forces, which may adversely influence the performance of seismically designed connections. This lack of knowledge about structural behavior under collapse conditions is also expressed in Hamburger et al. (2004), where the authors states that “it is not apparent what types of connections of beam to columns possess sufficient robustness to permit the development

of plastic rotations at beam ends together with large tensile forces." Therefore, behavior of seismically designed systems under collapse loads is an open issue that needs thorough investigation before such systems can be recommended for progressive collapse situations. These issues are addressed herein.

1.6 Objectives

The overall goal of this work is to investigate the progressive collapse behavior of seismically designed steel structural systems that have suffered loss of one or more critical members as a result of an extreme loading scenario. Another important goal of this study is to develop design guidelines that ensure that the damage in a structural system is arrested in a local region without compromising the safety and stability of the entire structure. These goals are achieved through multi-scale computational models that can accurately simulate the important physical process in progressively collapsing steel frames. Specific objectives are:

1) Study of seismically designed structural steel sub-assemblages under collapse conditions using micro-scale models.

2) Development of structural scale models, appropriate for collapse simulations, for four types of steel building systems: special moment frames (SMFs), ordinary moment frame (OMFs), special concentric braced frames (SCBFs) and eccentrically braced frames (EBFs). These computationally efficient models will allow practitioners to accurately and economically study the potential for progressive collapse in steel building frames. The developed structural scale models will be used within an APM to study the progressive collapse behavior of prototype frames.

3) Development of new analysis technique termed "pushdown method", which can be used to determine the residual capacity of a damaged system in cases where the structure under consideration is deemed to be able to survive loss of critical members.

4) Development of a new micro-scale model that incorporates microstructure evolution due to both volumetric and deviatoric growth of micro-voids; has physically motivated calibration parameters; and is computationally efficient.

1.7 Structure of the Report

Following is a brief description of the 7 chapters comprising this report.

Chapter 1: Introduction. A general overview of the research program is given. The objectives and scope of the current study are highlighted and an introduction to other chapters is presented.

Chapter 2: Literature Review. Important topics related to progressive collapse are reviewed including: past studies on progressive collapse of structures; building code requirements for prevention of progressive collapse; structural steels and the process that influence ductile fracture in steels; multi-scale issues related to progressive collapse; simulation methods for modeling the collapse of steel structures; and multi-scale simulation methods.

Chapter 3: Collapse Analysis of Steel Moment Frame Sub-assemblages. Formation of catenary action and its stability after formation is investigated. Computational finite element simulations together with micro-mechanical model are used to investigate a number of key design variables that influence formation of catenary action in special moment resisting frame sub-assemblages.

Chapter 4: Structural Scale Models for Progressive Collapse Analysis of Steel Frames. Structural scales models which are suitable for collapse simulations are developed for four types of steel building systems: SMFs, IMFs, SCBFs and EBFs. The developed models are calibrated to the available results in the literature. The developed structural scale models are then used in conjunction with APM to investigate the ability of seismically designed steel frame systems to resist progressive collapse.

Chapter 5: Pushdown Analysis of Steel Frames. A new analysis technique is introduced that can be used to determine the failure load and collapse mechanism of a damaged structure. The presented technique is termed "pushdown analysis". Structural scale models for IMF, SMF, SCBF and EBF building systems are used to investigate the residual capacity for APM analysis cases where the system survive the local loss of load carrying capacity.

Chapter 6: Micro-mechanical Model for Ductile Fracture Simulation. In this chapter a damage mechanics based plasticity model is developed in a finite deformation framework for modeling the micro-mechanical process of ductile fracture in structural steels. Damage mechanics principles of effective stress and strain equivalence are employed to formulate a constitutive model for simulation of material damage due to micro-voids nucleation, growth and coalescence. The numerical implementation of the proposed model is also presented. A parametric study is carried out to study the effect of various parameters on the material response. The proposed model is calibrated to the experimental results obtained for notched steel specimens.

Chapter 7: Summary and Conclusions. This chapter presents a brief summary of the report and key conclusions that can be extracted from the research project. It also includes recommendations for the future research for progressive collapse studies.

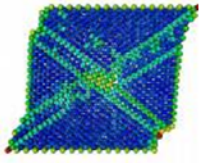

(a) Atomic scales: Dislocation movements

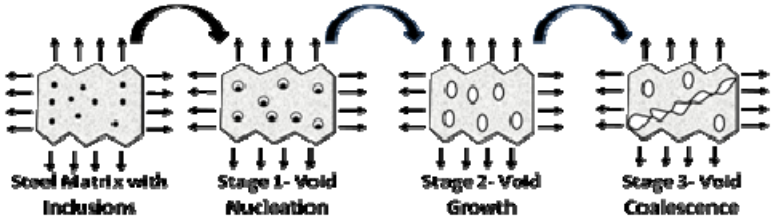

(b) Micro scales: Ductile Fracture Initiation

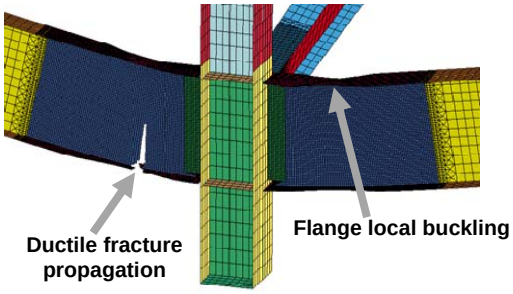

(c) Macro scales: Fracture propagation, Local buckling

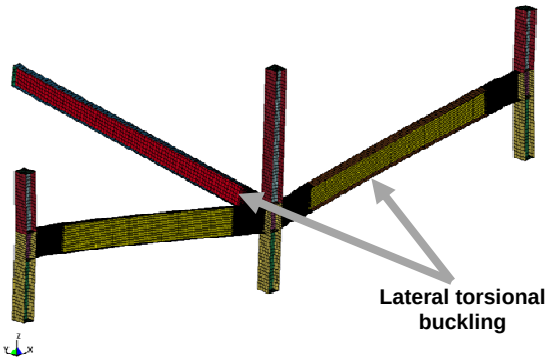

(d) Structural scales: Global Buckling

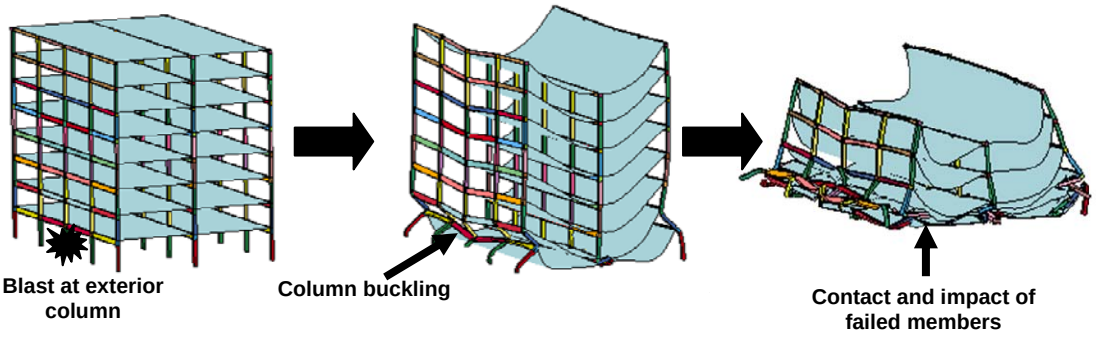

(e) Structural scales: Member/connection failure, load redistribution, impact and contact

Figure 1.1 Multi-scale responses associated with progressive collapse of a steel building system

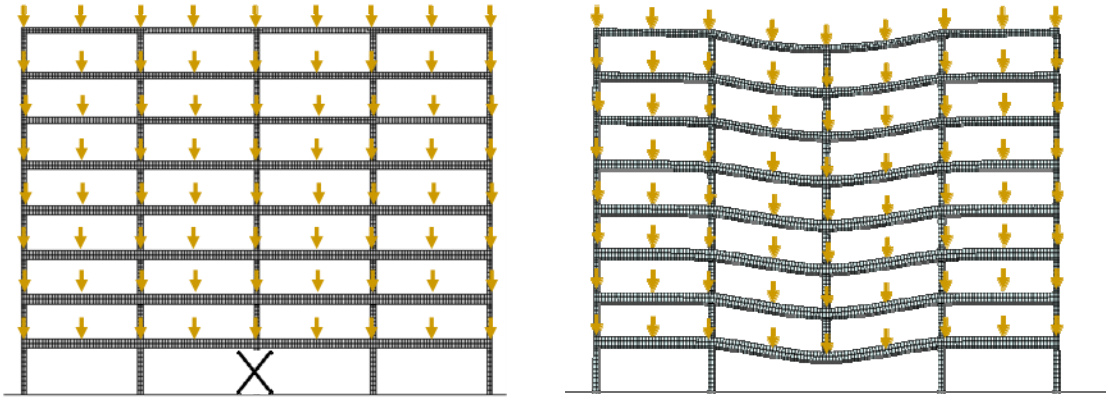

(a) A critical load bearing member is removed after the application of gravity loads

(b) Damage structure is checked to see if it can survive the local loss of load bearing capacity

Figure 1.2 Alternate path method (APM)

CHAPTER 2

LITERATURE REVIEW

2.1 Introduction

Important topics related to progressive collapse are reviewed in this Chapter. Past studies on progressive collapse of structures are surveyed first in Section 2.2. Then, in Section 2.3 building code requirements for prevention of progressive collapse are discussed. Structural steels, the process that influence ductile fracture in steels and multi-scale issues related to progressive collapse are also presented and discussed in Section 2.4. This is followed by a description of the available methods that can be used for modeling the collapse of steel structures in Section 2.5. Specifically, the basic concepts and the application of quantum mechanics (Section 2.5.1), molecular dynamics (Section 2.5.2) and continuum mechanics are discussed (Section 2.5.3). Finally, in Section 2.5.4 a survey of multi-scale simulation methods that can be used for representing the physical phenomena associated with collapse is presented.

2.2 Progressive Collapse Studies

Past research on progressive collapse has proceeded in waves initiated in the aftermath of high profile structural failures. Progressive collapse issues first drew the attention of researchers in 1970's after the partial collapse of a panel type apartment tower at Ronan Point, England (Fig. 2.1). The Ronan Point apartment block was a 22-story building constructed of precast panels of two types – floor and unreinforced bearing wall. On May

16, 1968, a gas explosion occurred near one of the corners of the building on the 18th floor. The explosion blew out the non-load bearing front wall and the load bearing flank wall at the corner thus removing the support for the stories above. Lack of continuity between the structural elements and the absence of an alternate load carrying path lead to the collapse of all the corresponding floors above and below, down to the podium level. This is a classical example of progressive collapse where loss of a single load bearing members led to a cascade of failures.

After the collapse of Ronan Point building, Ferahian (1972) reviewed the changes that were made in the British and Canadian codes to prevent progressive collapse. The author argued that it could be possible for a building designed for earthquakes to resist progressive collapse after a loss of a load carrying component. It was also recommended that ductility and continuity between the structural elements/joints for structural integrity should be provided to enhance the toughness of the structure. In another study, McGuire (1975) concluded that alternate path method and specific local resistance should not be used as the main methods for preventing progressive collapse. The author recommended that codes should provide adequate guidelines to reduce the risk of progressive collapse to within acceptable limits.

Lewicki et al. (1974) discussed recommendations made by CIB working commission W32A on load bearing walls. The authors advocated that although the problem of progressive collapse was more critical for large panel type structures, there was a potential for progressive collapse in other structural systems also. They asserted that although it was possible to design a building to resist progressive collapse after loss of local load carrying capacity, it was not economically practicable to prevent local failure from occurring due to the uncertainties present in the loading environment and the strength of the structure. They also concluded that, with the available knowledge, it was not possible to define the size of a local failure that the building should resist economically. The need for further theoretical and experimental work was stressed for safe and economical structures by limiting the probability of progressive collapse.

Most of the earlier studies on progressive collapse were concerned with panel type pre-cast/prefabricated building systems, flat slab systems and masonry bearing wall structures. These structures, at that time, had inherent weaknesses due to inadequate continuity and ductility at the member joints, presence of punching shear and other failure modes. Little attention was paid to steel structural systems, which were considered to be more ductile and robust than their concrete counterparts and therefore more collapse resistant.

Leyendecker et al. (1977) proposed guidelines for preventing progressive collapse in buildings. The authors outlined three methods to prevent progressive collapse: 1) Event control method – in which abnormal loading on the structure is prevented by indirect measures; 2) Indirect design method – in which the structure is designed to have minimum strength, ductility and redundancy, and then assumed to perform adequately in the presence of local failures; 3) Direct design method – in which structural members are made adequately strong so that they can resist abnormal loading or the structure is designed so that it can tolerate local loss carrying capacity e.g. loss of a critical column. Ellingwood et al. (1978) further examined the design criteria to control progressive collapse and presented a probabilistic framework for their implementation in existing standards at that time. The main objective for such design criteria was to minimize the loss of life and to permit safe evacuation of occupants from the damaged structure.

Arora et al. (1980) proposed a methodology for optimal design of damage tolerant structures based on optimization of cost function, subject to constraints that must hold for the undamaged structure and under projected damage conditions. A structure was called damage tolerant or fail-safe if it continued to perform its basic functions even after sustaining a particular level of local damage. Damage condition was defined as a state of complete or partial removal of selected members or parts of the structure. The fail-safe optimization algorithm was tested for a tail-boom of a helicopter which was modeled as a 3-D space truss-like structure. In particular, the optimization algorithms were developed to minimize the total mass of the structure, with constraints on member stress, nodal displacement, member buckling and natural frequency. Lower bound constraints were

also imposed on the cross sectional area. Static elastic analysis was carried out to determine the response of the structural system after failure of one or more members and only kinematically stable damaged configurations were studied. The reported results show that a structure that was optimized without imposing damage conditions would generally fail catastrophically if any damage occurs to the structure at a later instance, and significant variation in design is required for achieving a damage-tolerant design objective.

The first study involving progressive collapse analysis of steel frames was presented by Gross et al. (1983). In this study, the behavior of 2-D moment resisting steel frames with the loss of one of the columns or increased load on the beams representing fallen debris was examined numerically. The nonlinear analysis program included the modeling of inelastic beam column behavior, beam to column connection behavior, and the effect of shear infill panels. Both material and geometric nonlinear effects were taken into account in an updated Lagrangian formulation. The yield criterion was defined by a two dimensional yield surface which accounted for interaction between axial force and bending moment. A stress resultant plasticity approach, whereby inelasticity was concentrated at the member ends, was utilized. Connection elements to represent the nonlinear behavior of the beam column connection were developed on the basis of a Ramberg-Osgood model. Shear infill panels were modeled as springs with bilinear shear stress – rotational strain relationship. The authors analyzed a four-story, three-bay steel frame representing a low-rise apartment or a small office building, designed according to 1978 AISC specifications. Two cases were considered, one with the second story external column removed and other with the second story interior column removed. For the first case with external column removed the structure was unable to resist more than 69% of the unbalanced load and collapse was predicted. For the second case, the remaining structure was able to resist the full unbalanced loads. The beam with debris load was divided into smaller segments to model the spread of plasticity and results were obtained for different degrees of strain hardening. Catenary action was shown to come into play to carry the loads after the formation of plastic hinges at the support and mid-span of the beam.

The aforementioned studies show that it is possible to get a quasi-static cascade of failures once one member has failed, i.e. the remaining damaged structure cannot sustain the applied loads statically. But this static analysis for load redistribution is not accurate since the actual load redistribution process is dynamic in nature. It is possible that transient analyses may give stresses and strains which are higher than those obtained from static analysis and thus might result in a more critical progressive collapse situation.

Earlier studies accounting for dynamic redistribution of forces in a progressive collapse scenario were carried out by McConnel et al. (1983), Casciati et al. (1984) and Pretlove (1986). McConnel et al. (1983) investigated the progressive collapse failure of warehouse racking, where local failure is initiated by truck collision or static overload. Studies were carried out with pallet racking systems consisting of open section columns, laced in pairs by cross bracings and spanned by pairs of beams front and back. Reduced scale laboratory collapse tests and dynamic numerical analysis methods were used to identify the internal structural mechanisms and rigid body motions of the racks that allow collapse. From the actual collapse studies of half scale laboratory specimens, the pull out strength of the deforming joint emerged as an important parameter which controlled whether the local failure was contained or not. The authors argued that when the joints in the deforming structure are incapable of sustaining the axial tension developed in the beams produced by the catenary action of sagging beam elements, the joints separate. The collapsing part is then no longer connected to the stationary parts of the structure and a confined collapse is likely. If however, the joints have a high 'pull-out' strength, no separation occurs and the members involved in the initial collapse imposes force on the other parts of the rack which may initiate a progressive collapse mechanism. Experimental studies were carried out to quantify the joint pullout strength. Nonlinear dynamic analyses of a 2-D racking system were done to investigate the potential for progressive collapse. It was concluded that for the racking system under consideration, the dynamic effects were significant only in the early stages of collapse. However, the confined collapse can only be ensured if the joint design provides enough rotational stiffness and strength to maximize working load but have low pull out strength to guarantee separation.

Casciati et al. (1984) discussed progressive failure for seismic reliability analysis of 2-D moment resisting reinforced concrete frames. The formulation for beam and column elements was based on lumped plastic hinges at the member ends. A modified Takeda constitutive model was used for the plastic hinges which modeled the cyclic behavior under seismic loading. Two damage parameters were introduced to model damage under cyclic and monotonic effects. A geometric stiffness matrix was used to model P-Δ effects and failure of members was accounted for by removing their contribution from the global stiffness matrix when the damage parameter reached a critical value. Dynamic analysis of a 4-story three bay prototype frame designed according to the US Uniform Building Code (1973 version) was carried out for a suite of earthquake motions. The study concluded that failure of a column initiates a global failure and thus progressive collapse coincides with the failure of the first column.

Pretlove (1986) studied the dynamic effects that occur in the progressive failure of a simple uniaxial tension structure and concluded that a structure that appears to be safe under static load redistribution may actually be unsafe if the transient dynamic effects are taken into account. In another study, Pretlove et al. (1991) carried out experimental and numerical investigations with a tension spoke structure to examine the nature of progressive failure and dynamic effects associated with the loss of one or more spokes. Dynamic and static analysis of the damaged structure is carried out in the framework of Monte Carlo simulations to include statistical variations in the strength of the members. This study also concluded that the transient analysis may predict fracture even though the static analysis predicts safe response.

Malla et al. (1995) examined the effect of member loss in a truss-type space structure to evaluate the potential for progressive collapse. The dynamic effects, associated with the sudden failure of a member due to brittle failure in the elastic region or due to buckling under compressive forces where the member snaps after reaching a critical load, were included. The truss members were modeled as one dimensional truss elements with elastic plastic properties and displacements were considered to be small. Dynamic effects were considered by suddenly applying failed member loads to the structural nodes.

Bombing of the nine story P. Murrah Federal building (Fig. 2.2) in downtown Oklahoma City on April 19, 1995, killed 168 people, injured more than 500 people and damaged more than 300 buildings. An estimated 80% of the causalities were caused by the building collapse rather than the blast itself. The Murrah building had a transfer girder running across the face of the structure at the second floor, which transferred the weight of 10 building columns to five columns down to the ground. The bomb shattered one exterior column at the ground level and damaged a few others in the vicinity of the explosion. The loss of one column meant three above it failed, and the lack of an alternate load path precipitated progressive collapse of the front half of the building. The local damage was not arrested, which resulted in catastrophic failure of the building. After the Oklahoma City bombing, progressive collapse issues were again brought to the forefront and discussed amongst engineering and federal government officials. Most of the subsequent studies were carried out by federal agencies because it was thought that federal buildings were at a greater risk to such types of attacks. Prendergast (1995) stated the views of different people working with federal agencies. The important ones related to progressive collapse were:

1. Efforts should be undertaken to improve the structure's ability to sustain significant local damage without collapse.
2. Structures should be designed and detailed to improve the overall ductile behavior.
3. Sufficient redundancy should be present in the structural elements, beam, columns, girders and slabs to provide alternate load paths in the case of local damage.
4. Progressive collapse should be prevented by providing for mechanisms like catenary and cantilever action to hold the damaged zone in place.
5. Local damage cannot be avoided but damage can be limited by preventing progressive collapse.
6. Providing progressive collapse resistance for existing structures by retrofitting measures is costlier than providing the same measures in a new structure.

Other than these broad guidelines there were no recommendations for improvements in design methodology.

Abedi et al. (1996) examined the behavior of single layer braced domes which are prone to progressive collapse due to propagation of local instability initiated by member or node instability. The process of dynamic snap-through is associated with inertial effects and large localized deformations in the structure, which can propagate and lead to collapse. The snap-through behavior is modeled by providing initial velocity at the nodes in which the snap-through occurs. Elastic perfectly plastic Timoshenko beam elements were used to represent tube-type members and Euler-Bernoulli beam element were used for members with solid cross-section. Static analysis was carried out followed by dynamic analysis and it was concluded from a numerical study of a dome with a span of 1 m and rise of 40 mm that dynamic snap-through can result in progressive collapse. The authors also gave an example of collapse of a pavilion constructed in Bucharest in 1963. The pavilion was a braced dome with a span of 100m and rise of 19m. The dome collapsed as a result of local snap-through due to an unexpected snow load accumulation on a small area. The local buckling propagated rapidly and this propagation of deformation caused the dome to pass from the normal position to a fully reversed position.

Smith (1988) evaluated the progressive collapse potential for space trusses using the alternate path method. Linear and nonlinear static analyses of a hypothetical space truss and of a continuous double-layer offset grid space structure used in the Jacob K. Javits Convention center in New York City was carried out. Analysis indicated that the space truss might be vulnerable to progressive collapse resulting from the redistribution of the loads when a compression member buckles and sheds its load. The process may be exacerbated by post buckling snap-through which causes large redistribution of forces. Likewise, progressive collapse can also result from the loss of a tension member.

There is a renewed interest in progressive collapse after the terrorist attacks on the World Trade Center (WTC) (Fig. 2.3) and Pentagon on September 11, 2001. WTC towers 1 and 2 collapsed after Boeing 767 jetliners hit each of them following this sequence of events: (1) A Boeing 767 jetliner crashed into tower at high speed; (2) the crash caused structural damage at and near the point of impact and also set off an intense fire within the building;

(3) the structure near the impact zone lost its ability to support the load above it as a result of some combination of impact damage and fire damage; (4) the structure collapsed, having lost its support; (5) the weight and impact of the collapsing upper part of the tower caused a progression of failures extending download all the way to the ground. This is a progressive collapse but not a disproportionate collapse as it was caused by a very large impact and fire. And unlike the case with the Murrah Building, simple changes in the structural design that might have greatly reduced the scale of collapse have not yet been identified.

Mlakar et al. (2003) presented the findings from a study of the 2001 Pentagon attack and gave their recommendations for the future design and research needs for collapse prevention. One of the important finding was that despite extensive column damage on the floor where the aircraft struck, immediate collapse of the higher floors was prevented. This was attributed to the following factors: (a) Alternate load path provided by beams and girder framing system; (b) Short spans between columns, and continuity of beam and girder bottom reinforcement throughout the supports; (c) Designing for a higher service loads (designed for 150 psf in excess of the service loads); (d) Significant residual capacity of damaged spirally reinforced columns; (e) Exterior wall performing a dual function, that of a transfer girder. The authors expressed the need for research in the progressive collapse area and related issues, like influence of extreme column deformations on its load carrying capacity and the ability of a structure to withstand extreme impact.

Astaneh-asl et al. (2002) investigated the strength of a typical steel structure and floor system to resist progressive collapse in the event of removal of a column. They tested a specimen of size 60ft by 20ft one story steel structure with steel deck and concrete slab floor and wide flange beams and columns. The connections were either standard shear tab or bolted seat angle under bottom flange and a bolted single angle on one side of the web. It was observed that after removal of the middle perimeter column, the catenary action of the steel deck and girders was able to redistribute the load of removed column to other columns. The floor was able to resist the design dead load and live load without collapse.

Damage to the system was primarily in the form of cracking of floor slab, tension yielding of the steel corrugated deck in the vicinity of collapsed column, bolt failure in the seat connections of the collapsed column and yielding of the web of the girders acting in a catenary configuration.

Astaneh-asl (2003) carried out an experimental investigation of the viability of steel cable based systems to prevent progressive collapse of buildings. The tests were conducted on a full scale specimen of a one story building. One side of the floor of the specimen had steel cables placed within the floor representing new construction and the other side had cables placed on the outside as a measure of retrofit of the existing building. The author claimed that the test results showed that the system could economically and efficiently prevent progressive collapse of the floor in the event of removal of one of the exterior columns.

Kaewkulchai et al. (2004) presented a beam element formulation and solution procedure for dynamic progressive collapse analysis of planar frame structures. Inelastic beam-column elements were formulated using flexibility based lumped plasticity approach with inelasticity concentrated at the element ends. Axial force and bending moment interaction, cyclic behavior, multi-linear force deformation relationship with Morz hardening rule and P-Δ effects using geometric stiffness matrix were considered. A damage index was used to take into account the strain softening behavior under cyclic/monotonic loading as a result of damage. Failure at member ends was assumed to happen when the damage index reaches a value of one and the hinge is assumed to be separated completely from the structure. After failure the stiffness matrix is updated using a condensation process where the degrees of freedom at the failed member ends are released. Rotational inertia was ignored and mass and stiffness proportional Rayleigh damping was assumed. To illustrate the importance of dynamic effects, static and dynamic analyses of two-bay, two-story frame were carried out. The analysis results showed a significant increase in nodal displacements, number of plastic hinges and plastic rotations when inertial effects were included. It was concluded that static analysis might not provide conservative estimates of the collapse potential of frame structures.

In other recent efforts, Grierson et al. (2005) proposed a quasi-static framework to study progressive collapse. Discussions on progressive collapse which are more of a qualitative nature can be found in Baldridge et al. (2003), Magnusson (2004), Hamburger et al. (2004), Nair (2006), Dusenberry et al. (2006), Marjanishvili et al. (2006) and Ellingwood et al. (2006).

2.3 Current Provisions in Codes for Preventing Progressive Collapse in Structures

2.3.1 General Building Codes

The current philosophy of most of the present building codes is to design structures for credible loads that may occur during their lifetime. Structures are not usually designed for abnormal events such as explosion due to ignition of gas, vehicle impact, blast effects, etc, which can cause catastrophic failure. Most of the mainstream codes have only general recommendations for mitigating the effect of progressive collapse in structures that are overloaded beyond their design loads.

ASCE Standard 7, Minimum Design Loads for Buildings and Other Structures, (ASCE 7, 2005): ASCE-7 is the only mainstream standard which addresses the issue of progressive collapse in some detail. It emphasizes the need to protect the structure against extreme events which can result in progressive collapse, and gives two design alternatives to resist progressive collapse: Direct Design Method and Indirect Design Method. In the direct design method, the resistance to progressive collapse is considered directly during the design process through: (a) Alternate Path Method (APM), which seeks to provide alternate load path after a local failure has occurred, so that the local damage is arrested and major collapse is prevented, (b) Specific Local Resistance Method, which seeks to provide sufficient strength to resist failure at critical locations. The indirect design method implicitly considers the resistance to progressive collapse through provisions of minimum levels of strength, continuity and ductility. It also provides guidelines for the provision of general structural integrity and stresses the need to provide ductile

connections between the structural components which can undergo large deformations and absorb large amounts of energy under the effect of abnormal conditions.

Progressive collapse issue are briefly discussed in NEHRP Recommended Provisions for Seismic Regulations for New Buildings and Other Structures (Part 2): Commentary (FEMA 369). It highlights the need to design more redundant structures so that alternate load paths are available in the event of local failure and the structure retains its integrity and continues to resist lateral load. Additional redundancy in framed structures is to be provided by incorporating moment resisting joints in the vertical load carrying system and providing different types of seismic force resisting systems, where a backup system can prevent catastrophic effects if distress occurs in the primary system. The increase in redundancy is considered to be a function of moment resisting frame placement and the total number of such frames. It summarizes by stating that "*it is a good practice to incorporate redundancy into seismic-force-resisting system and not to rely on any system wherein distress in any member may cause progressive or catastrophic collapse*". Beyond these guidelines in the commentary there are no specific criteria to design for progressive collapse.

There are no specific guidelines in the International Building Code (IBC, 2006), Building Construction and Safety Code (NFPA 5000, 2006), Uniform Building Code (UBC, 1997) and Standard Building Code (SBCCI 1999) to design structures for progressive collapse.

2.3.2 US Government Documents

Design guidelines for progressive collapse resistant design can be found in several US Government documents, e.g. General Services Administration (GSA, 2003) - *Progressive Collapse Analysis and Design Guidelines for New Federal Office Buildings and Major Modernization Projects*; Department of Defense (DoD) - *Unified Facilities Criteria - Design of Buildings to Resist Progressive Collapse* (UFC, 2005) and Interagency Security Committee – "*ISC Security Design Criteria for New Federal Office Buildings and Major Modernization Projects*", ISC (2004). The GSA (2003) guidelines provide a

threat independent methodology to mitigate progressive collapse potential in structures based on APM. The GSA criteria are modeled after performance-based seismic design concepts that were first proposed in FEMA-273 (1997) and allow both linear and nonlinear analysis procedures to investigate alternate load path configurations. GSA categorizes building systems into typical and atypical structural systems and proposes a different design methodology for each category. It defines scenarios where one of the building's columns is removed and the "damaged" structure is analyzed to study system response. It also prescribes the loads for which the damaged structure should be analyzed. The Demand Capacity Ratio (DCR) of each primary and secondary member is calculated to determine the potential for progressive collapse. GSA criteria require that in order to prevent progressive collapse, DCR values should not exceed 2.0 and 1.5 for structures with typical and atypical configurations, respectively.

The UFC (2005) methodology is also a performance-based design one, and is partly based on the GSA (2003) provisions. In it, progressive collapse resistance depends on the desired level of protection (i.e. performance), which are very low, low, medium and high levels of protection. Most buildings structures fall in the first two categories and only structures that are mission critical or have unusually high risk fall in the last 2 categories. Two design approaches are specified, namely the Tie Force Method (TFM) and APM. The former is essentially an indirect design approach, wherein a minimum tie force capacity must be made available in the system to transfer loads from a damaged part to the remainder of the structure. In other words, the intent of the tie force method is to quantify minimum ductility, continuity and redundancy requirements. For a very low level of protection, it is sufficient to provide prescribed horizontal tie force capacity, while for low level of protection both horizontal and vertical tie capacity has to be provided. If adequate vertical tie capacity is not present, then APM is required. When the objective is to achieve medium or high levels of protection, structures have to be designed for prescribed horizontal and vertical tie forces, should satisfy minimum ductility requirement and should additionally be checked by APM for specific damage scenarios. In all the cases, APM is permitted only if horizontal tie capacity is present.

The TFM relies implicitly on the formation of catenary action to mitigate collapse. As with any prescriptive criteria, these provisions do not allow designers the choice of a desired structural performance level. For instance, it is not clear how much catenary action will take place in response to a specified event, or alternatively, must be developed to mitigate collapse. Unlike other existing prescriptive provisions, however, these provisions are not based on a wealth of publicly available field experience, extensive data and analytical results. For example, it is not clear how will a steel moment resisting connection behave in the presence of potentially large catenary forces? Therefore, the accuracy of the criteria and their appropriateness for adoption by civilian design documents are both questionable at this time.

In the ISC (2004) document the problem of progressive collapse is handled indirectly through reference to the ASCE 7 standard and GSA (2003), and it recommends engineering guidelines to mitigate the effect of blast on structures.

2.4 Structural Steels

The most commonly used steel in structural engineering applications are carbon steels (ASTM A36), high strength low alloy steels (HSLA) (ASTM A572, A992) and corrosion resistant high strength low alloy steels (ASTM A588). Carbon structural steels have maximum carbon content varying from 0.25 to 0.29 wt % and these are used primarily for angles, channels and plates. HSLA steels are designed to provide better mechanical properties and/or greater resistance to atmospheric corrosion than conventional carbon steels in the normal sense because they are designed to meet specific mechanical properties rather than a chemical composition. The HSLA steels have low carbon contents (0.05 - 0.25 wt %) in order to produce adequate formability and weldability, and they have manganese contents up to 1.5%. Small quantities of chromium, nickel, molybdenum, copper, nitrogen, vanadium, niobium, titanium and zirconium are used in various combinations. Total content of alloying elements other than carbon is less than 5 wt %.

At ambient temperature and pressure the atomic structure of pure iron is body-centered cubic (bcc) and it is also known as α-iron or ferrite. This bcc structure is stable up to about 910^{o}C. However, in HSLA steels (ASTM A572, A992) with carbon and other alloying elements, the two phase's ferrite and pearlite are the principal constituents of the microstructure. For low carbon steels, i.e. below 0.3 wt % such as HSLA, pearlite occupies a substantially smaller volume of microstructure as compared to ferrite. Inclusions including cementite (Fe_3C) and silicates (size $1 - 40\ \mu m$), together with other second phase particles (size < $1\ \mu m$) such as sulphides (e.g. MnS) and other carbides (ZrC, TiC, VC_x, Mo_2C etc) are also present in small amounts at grain boundaries. Cementite or iron carbide has an orthorhombic crystal structure and it is a hard, brittle material, normally classified as a ceramic in its pure form. Pearlite is a two-phased, lamellar structure composed of alternating layers of ferrite (88 wt %) and cementite (12 wt %). Alloying elements in HSLA influences the strength by controlling the ferrite grain size and by other mechanisms involving strengthening by interstitial or substitutional atoms.

2.4.1 Ductile Fracture Process in Steel

Ductile fracture in steel is a multi-scale and multi-step process resulting from microvoid nucleation, growth and coalescence of voids at a microscale level in a plastically deforming material. Microvoids typically nucleate at inclusions either by decohesion/debonding of the inclusion matrix interface or by fracture of the inclusion itself. In a pure material, creation of voids requires a very high stress to break the atomic bonds but the deformation is not heterogeneous enough for large stress concentrations to reach the atomic bond strength. However, inclusions provide areas where void nucleation can easily occur. Hard inclusions are obstacles to dislocations; and pile up can produce large stress concentrations in the inclusion itself and at its boundary, large enough to cleave it or for interface decohesion.

Following void nucleation under the applied deformation field, voids grow and interact until localized plastic flows and necking of the intervoid matrix occurs, which eventually

leads to coalescing of adjacent microvoids. The process of microvoid coalescence is often accelerated by the rapid growth and coalescence of the secondary microvoids which nucleates at the second phase particles (sulphides and carbides) in the localized plastic flow zone between the microvoids. This process describes the ductile fracture of steels for cases in which void nucleation initiates at small strains and void growth occurs over a large strain increment. Under such conditions, fracture properties are controlled by the growth and coalescence of voids; and ductility depends on the growth phase of microvoids and is strongly influenced by state of stress in the material. Figure 2.4 shows the schematic diagram of void nucleation, growth and nucleation in steels. Figure 2.5 shows a scanning electron micrograph of the surface of steel fractured due ductile fracture process.

The third stage of void coalescence mechanism is not predominantly due to dilational plastic void growth. Very large volumetric dilation of voids, needed to bring voids in close proximity, are not observed in metallurgical examination of regions immediately adjacent to ductile fracture surfaces. Scanning electron microscope (SEM) micrographs of the fracture surface of tension specimens show void coalescence by complete internal necking of the intervoid matrix, between the sites of inclusions, which is not the result of dilational plastic void growth. In this stage, failure is due to the plastic limit load instability of the intervoid matrix which leads to the catastrophic process of internal microscopic necking and causes localized plastic failures and separation of intervoid matrix material. This results in the region above and below the ductile fracture surface moving apart by rigid body displacements, under decreasing loads, as the intervoid matrix necks down to virtually 100% reduction in area.

Plastic instability associated with void coalescence stage has not been studied as much as the growth stage. Two important mechanisms of coalescence that are assumed to occur are flat dimple mode and void sheet instability. Flat dimple mode occurs for those cases in which inclusions-initiated voids nucleate at small strains and void growth occurs over a large strain increment. In such cases, at the onset of material failure, there is significant density of voids which is nearly uniformly distributed within the deforming section and

the void volume fraction typically approaches 0.05 - 0.25 (Bandstra et al., 1998) at failure. When growing voids reach a critical size, relative to their spacing, a local plastic instability develops between the voids, resulting in failure. In these cases, the fracture initiation is characterized by a dimple fracture surface roughly oriented normally to the maximum principal stress axis.

In addition to ductile fractures occurring as a result of a global accumulation of damage as described above, a "void sheet" failure has been observed in steel containing large concentrations of second phase particles. Void sheet failure is caused by nucleation, growth and linking of voids but in a manner which leaves the fracture surface with a zig-zag fracture profile comprised of segments roughly 45^{o} to the principal stress axis. Studies by Bandstra et al. (1998) shows that void sheet mechanism involves large elongated 'primary' voids which are subsequently linked on inclined planes by a sheet of microvoids nucleated at a 'secondary' population of particles. Hence void sheet failure is a result of deformation localization between the primary voids. Plastic instability is concentrated along a sheet of voids, and local necking instabilities develop. There is little damage in this case (i.e. void volume fraction much less than 0.10) at the onset of localization and failure. The orientation of the fracture path depends on the stress state.

In case where the inclusions are well bonded to the matrix, void nucleation is often the critical step and fracture occurs soon after the voids are formed. In this case, on the onset of microvoid nucleation, the intervoid matrix immediately undergoes plastic limit load failure across a sheet of microvoids to form ductile fracture surface and the void coalescence process occurs by a mechanism of internal microscopic necking. Under these conditions there is no opportunity for dilational plastic void growth to occur and the microvoid nucleation strain is equal to the ductile fracture strain.

2.5 Modeling of Ductile Fracture and Failure of Steel Members

Ductile fracture in structural steel members is a multi-scale process with several processes occurring at different length scales. The important physical processes with the associated length scales are:

1) Dislocation movements and atomic bond breaking/decohesion ~ $10^{-10}\ m$

2) Microvoid initiation ~ $10^{-6}\ m$

3) Microvoid growth and coalescence ~ $10^{-6} - 10^{-4}\ m$

4) Crack initiation and propagation ~ $10^{-3} - 10^{1}\ m$

5) Structural system collapse ~ $10^{1} - 10^{2}\ m$ or more

Researchers in the past have used various mathematical theories to model these physical phenomenon occurring at various length scales. Some of the important mathematical frameworks in which the above phenomena's are studied include quantum mechanics, molecular dynamics, continuum mechanics and multi-scale methods. Usually a single mathematical theory cannot be used to model all problems at every length scale. An overview of quantum mechanics, molecular dynamics, continuum mechanics and multi-scale approaches and the range of their applicability are presented next. See Fig. 2.6 for an overview of these analysis methods.

2.5.1 Quantum Mechanics (QM)

In quantum mechanics (QM) techniques the motion of electrons is explicitly considered, and thus these techniques can be used to study properties of systems which depend on electronic distribution. Structural, mechanical and thermo-dynamical properties of systems can also be investigated using QM techniques. At the heart of quantum mechanics is the Schrödinger wave equation, which for a single electron system is given by Eq. 2.1:

$$\left\{-\frac{\hbar^2}{2m}\left(\frac{\partial^2}{\partial x^2}+\frac{\partial^2}{\partial y^2}+\frac{\partial^2}{\partial z^2}\right)+V(t)\right\}\Psi(\underline{r},t)=i\hbar\frac{\partial\Psi(\underline{r},t)}{\partial t} \qquad (2.1)$$

Equation 2.1 refers to a single electron of mass m, moving through space (given by position vector $\boldsymbol{r}=x\boldsymbol{i}+y\boldsymbol{j}+z\boldsymbol{k}$) and time t, under the influence of an external potential field $V(t)$. Here, $\hbar$ refers to Plank's constant divided by π and $i=\sqrt{-1}$. The function $\Psi(\boldsymbol{r},t)$ is known as the wave function and it characterizes the motion of the electron under the applied potential field. Various properties of electron can be derived from this wave function. In most of the problems of practical interest, the external potential V is

independent of time. In this case, the wave function can be written as the product of a spatial part and a time part, i.e. $\Psi(\boldsymbol{r}, t) = \psi(\boldsymbol{r})\phi(t)$. The Schrödinger equation can then be written in time-independent form as follows:

$$\left\{-\frac{\hbar^2}{2m}\nabla^2 + V\right\}\psi(\boldsymbol{r}) = E\psi(\boldsymbol{r}) \tag{2.2}$$

where $\nabla^2 = \left(\frac{\partial^2}{\partial x^2} + \frac{\partial^2}{\partial y^2} + \frac{\partial^2}{\partial z^2}\right)$ is the Laplacian operator and E is the energy of the particle. Alternatively Eq. 2.2 can also be written in compact operator form as follows:

$$\mathcal{H}\psi(\boldsymbol{r}) = E\psi(\boldsymbol{r}) \quad and \quad \mathcal{H} \stackrel{\text{def}}{=} -\frac{\hbar^2}{2m}\nabla^2 + V \tag{2.3}$$

where $\mathcal{H}$ is known as Hamiltonian operator. Equation 2.3 represents an eigen-value problem where $\psi(\boldsymbol{r})$ is the eigen-function of operator $\mathcal{H}$ and E is the corresponding eigen-value. Mathematical tools from functional analysis are used to find solution of these eigen-value problems. In particular, the wave functions $\psi(\boldsymbol{r})$ are assumed to exist in Hilbert space, i.e. the space of square-integrable functions. Most of the important classes of solutions of time independent Schrödinger equations are constructed in separable Hilbert spaces with orthonormal bases functions. Moreover, the solutions are either real or occur in complex conjugate pairs. Wave functions are also referred to as orbitals and are characterized by discrete integers referred to as quantum numbers.

Using Born's statistical interpretation of wave functions, the probability of finding an electron in a given volume Ω is given by Eq. 2.4 below:

$$\int_{\Omega} \psi^*(\boldsymbol{r})\psi(\boldsymbol{r})d\Omega = Prob\{electron\ in\ volume\ \Omega\} \tag{2.4}$$

Additionally, the normality condition of the wave functions is assumed, i.e., $\int_{Space} \psi^*(\boldsymbol{r})\psi(\boldsymbol{r})d\Omega = 1$. The concept of operators is important in QM. The expected or mean value of quantity such as energy, position or linear momentum can be can be determined using an appropriate operator. For instance, energy can be calculated using Hamiltonian operator as follows:

$$E = \int_{\Omega} \psi^*(\boldsymbol{r})\mathcal{H}\psi(\boldsymbol{r})d\Omega \tag{2.5}$$

The Schrödinger Eq. 2.3 can be solved exactly for only a few problems, such as the particle in a box, the harmonic oscillator, the particle on a ring, the particle on a sphere and the hydrogen atom. For most of the problems of practical interest numerical methods are used. An introduction to QM can be found in Shankar (1994), Griffiths (2004) and Atkins & Friedman (2005). Some of the important numerical methods and techniques in used in QM are discussed next.

2.5.1.1 Born-Oppenheimer Approximation

Solving Schrödinger equation for polyelectronic and molecular systems is complicated by the fact that exact solution of Schrödinger equation with three or more interacting particles does not have a closed form. Thus solutions for all such systems are only an approximation to the exact solutions. A second complication is that for multi-electron species spin of electron has to be accounted, which introduces another quantum number known as spin quantum number. One of the important assumptions for polyelectronic and molecular systems is the Born-Oppenheimer (BO) approximation. This assumption is based on physical reasoning that dynamics of electrons is much faster than the dynamics of nuclei. Thus electrons can instantaneously respond to the any change in position of nuclei. Hence the electronic wave functions are assumed to be dependent on position of nuclei and not on their momenta. With BO approximation the total wave function of the multi-electron systems is written in the following form:

$$\psi_{total}(nuclei, electrons) \approx \psi_{nu}(nuclei)\psi_{el}(electrons) \qquad (2.6)$$

The total energy is represented as the sum of the nuclear energy (electrostatic repulsion between positively charged nucleuses) and the electronic energy. The electronic energy is comprised of sum of kinetic and potential energy of electron moving in the electrostatic field of nuclei, together with electron-electron repulsion. When the Born-Oppenheimer approximation is used, the electronic motions are of prime importance and the nuclei are considered to be fixed. For each arrangement of the nuclei the Schrödinger equation is solved for the electrons alone in the field of the nuclei. If it is desired to change the nuclear positions then it is necessary to add the nuclear repulsion to the electronic energy in order to calculate the total energy of the configuration.

2.5.1.2 Molecular Orbital Theory

In multi-electronic molecular systems, the electronic distribution for the entire molecule is of prime importance as opposed to electronic distribution of electrons in individual atoms. Molecular orbital calculations give solutions that are "smeared out" throughout the entire molecule, whereas electron orbitals are usually localized in specific regions (e.g. in the bonds between atoms). The rules for obtaining the atomic orbitals for N-electron system are mathematically expressed in terms of Slater determinants. Molecular orbitals are expressed as a linear combination of atomic orbitals as given in Eq. 2.7. below:

$$\psi_{m_i} = \sum_{j=1}^{k} c_{ij}\psi_{a_j} \tag{2.7}$$

Here ψ_{m_i} are the molecular orbitals, ψ_{a_i} are the atomic orbitals and c_{ij} are unknown scalars. Total energy, E_{tot}, of an N-electron system can be expressed as the sum of components as given in Eq. 2.8 below:

$$E_{tot} = E_{core} + E_{ele} + E_{exch} \tag{2.8}$$

where E_{core} is the kinetic and potential energies of the electrons moving in the electrostatic field of the nuclei and E_{ele} associated with the Columbic electron-electron repulsion. The third contribution to the energy, E_{exch}, is the exchange 'interaction'. E_{exch} is due to quantum nature of electrons (since electrons are "fermions" they cannot be distinguished when exchanged) and has got no classical counterpart.

Once the expression for the total energy is obtained, the unknown coefficients, c_{ij}, can be obtained using variational principle. The variational principle states that the energy of any generalized wave function is the upper bound of the ground state energy. So by minimizing the energy of the generalized wave function of a system one can obtain the approximated ground state wave function. An integro-differential system of equations known as Hartree-Fock equations is obtained by imposing minimization condition on the expression for the energy, subject to the constraint that the molecular orbitals remain orthonormal. Hartree-Fock equations can be reformulated in standard matrix form and this matrix form is known as Roothaan-Hall equations. Further details on the solution of

such systems can be found in Leach (2001), Lewars (2003) and Cook (2005) and in the references therein.

2.5.1.3 Ab initio and Semi-empirical methods

Ab initio strictly means “from the beginning” or “from first principles”, which implies that a calculation using such an approach requires as input only physical constants such as the speed of light, Planck’s constant, the masses of elementary particles, and so on. Ab initio usually refers to a calculation which uses the full Hartree-Fock / Roothaan-Hall equations, without ignoring or approximating any of the integrals or any of the terms in the Hamiltonian. By contrast, semi-empirical methods simplify the calculations, using parameters for some of the integrals and/or ignoring some of the terms in the Hamiltonian. Further details on semi-empirical methods can be found in Leach (2001), Lewars (2003) and Cook (2005).

2.5.1.4 Tight-Binding, Density Functional Theory and Other Methods

Various approximations are used in QM to obtain results of physical interest. The success of these approximate methods depends on how closely they can model the phenomena of interest. The tight-binding approximation treats a solid as an extended molecule, and takes as its starting point orbitals that are confined to individual atoms (hence the name of the approach). The molecular orbitals are then formed that spread throughout the solid. The tight-binding model is typically used for calculations of electronic band structure and energy gaps in solids in the static regime. Density functional theory (DFT) begins with the concept of the electron probability density and it takes into account electron correlation while being less computationally demanding than Ab initio methods. Furthermore, for systems involving d-block metals, DFT yields results that very frequently agree more closely with experiment than Ab initio methods calculations do. The basic idea behind DFT is that the energy of an electronic system can be written in terms of the electron probability density, $\rho(\boldsymbol{r})$. For a system of n electrons, $\rho(\boldsymbol{r})$ denotes the total electron density at a particular point $\boldsymbol{r}$ in space. The electronic energy E is said to be a functional of the electron density and is denoted E[$\rho(\boldsymbol{r})$], in the sense that for a

given function $\rho(\boldsymbol{r})$, there is a single corresponding energy E[$\rho(\boldsymbol{r})$]. Details on implementation and application of these methods can be found in Leach (2001) and Lewars (2003).

Discussion on other advanced QM methods such as those for open shell systems, valance bond theory, hybrid Hartree-Fock/DFT methods, gradient enhanced DFT methods, linearized augmented plane wave (LAPW) method for DFT calculations, band theory for metals and other advanced QM methods can be found in Szabo & Ostlund (1996), Leach (2001) and Singh & Nordstrom (2005).

In an application to steels, Hao et al. (2004) used DFT to compute binding energy relations for the interfacial debonding between the matrix and the primary & secondary inclusion particles in high strength steels. In iron matrix, normal adhesion and sliding were also considered. The primary aim of these first principles computation was to design binding and barrier potentials, which can be used in molecular dynamics simulations.

2.5.2 Molecular Dynamics (MD) and Related Methods

In MD, the classical Newtonian dynamics is used to study the motion of a large number of atoms by numerically integrating the equations-of-motion governed by prescribed inter-atomic forces. Normally, one has to rely on classical MD to simulate system sizes above 50,000 atoms and time-scales on the order of nanoseconds; such system sizes and time scales are still beyond the capabilities of quantum mechanics-based methods. One of the fundamental differences between MD and QM is that in MD the dynamics of electrons is ignored. Thus MD methods cannot provide properties that depend upon the electronic distributions. Hence, the total energy (E) of the system in MD is only the sum of potential energy (U) and kinetic energy ($\mathcal{K}$) of the nuclei. Theoretical foundations of molecular dynamics are based on Hamiltonian formulation of classical Newtonian mechanics (Goldstein et al., 2002). For a system with N-atoms, the Hamiltonian (H) of the system is the total energy (E) of the system, i.e.,

$$H = KE + U = E \tag{2.9}$$

$$\mathcal{K} = \sum_{i=1}^{N} \frac{p_i^2}{2m_i} \qquad U = U(\boldsymbol{r}_1, \boldsymbol{r}_2, \ldots, \boldsymbol{r}_N) \tag{2.10}$$

where m_i, p_i and $\boldsymbol{r}_i$ are the mass, momentum and position vector of the i[th] atom respectively. The equations of motion are then expressed in terms of Hamiltonian as follows:

$$\dot{p}_i = -\frac{\partial H}{\partial r_i} \; and \; \dot{r}_i = -\frac{\partial H}{\partial p_i} \tag{2.11}$$

The current state of the system by a 6N dimensional vector made up of the positions and momenta of all the particles. This vector defines a point in "phase space". When the Hamiltonian is not an explicit function of time, the Hamiltonian, and consequently the energy, is conserved. Conservation of the Hamiltonian implies that in the 6N dimensional phase space our system is confined to exist on a 6N-1 dimensional manifold. Further, taking into account conservation of momentum, the system has only 6N-5 degrees of freedom.

The equations of motions (Eq. 2.11) are integrated numerically to study the evolution of system as time progresses. Most commonly used integration algorithm in MD simulation is Verlet (Leapfrog) algorithm, however, higher order integration schemes are sometimes also considered. For stable time integration, typical time steps used in MD simulations are in the range of 1-10 femtoseconds ($10^{-15} - 10^{-14}$ sec). Global energy minimization techniques such as conjugate gradient methods are also commonly used in MD simulations to study the energy landscape of such systems.

Forces at the atomic level are conservative, and hence, a corresponding potential energy, $U = U(\boldsymbol{r}_1, \boldsymbol{r}_2, \ldots, \boldsymbol{r}_N)$, associated with force fields can be defined. Such inter-atomic potentials are the core of any MD simulation. Success of MD simulations depends on how efficiently and accurately inter-atomic potential can describe structural, mechanical, energetic, and other important properties of complex systems. During the last two decades, a number of inter-atomic potentials have been proposed with each potential having its own strengths and weaknesses. Some of the important commonly used empirical force field functions include bonded interactions (bond stretching, angle

bending, bond rotation/torsion) and non-bonded interactions (electrostatic, van der Waals). Other potential functions that are used range from quantum mechanics based methodologies, for e.g. tight-binding potentials, to multi-body and bond order potentials.

Results from equilibrium MD simulations are usually analyzed in a framework of statistical mechanics and statistical thermodynamics. These statistical methods are typically concerned with statistical properties, known as ensemble averages, of a large number of interacting particles. At large length and time scales, the motion of individual atoms is not of interest. The important quantities at this scale are macroscopic properties such as temperature, pressure, diffusion coefficients, stresses etc. Thermodynamic variables such as temperature (T), pressure (P), entropy (S), Hemholtz free energy, Gibbs free energy and chemical potentials (μ) are introduced by statistical methods. In addition, ensemble averages provides a consistent method for calculating such macroscopic quantities and thermodynamic variables from MD simulations. For example, the instantaneously value of the property $\mathcal{A}$ can be written as $\mathcal{A}(t) = \mathcal{A}(\boldsymbol{r}^N(t), \boldsymbol{p}^N(t))$, where $\boldsymbol{r}^N \equiv \boldsymbol{r}_1, \boldsymbol{r}_2, \ldots, \boldsymbol{r}_N$ and $\boldsymbol{p}^N \equiv \boldsymbol{p}_1, \boldsymbol{p}_2, \ldots, \boldsymbol{p}_N$ are the position vectors and momentum of all the particles in the system. The value that is measured experimentally is an average of $\mathcal{A}$ over the time of the measurement and is therefore known as a time average. As the time over which the measurement is made increases to infinity, so the value of the following integral approaches the "true" average value ($\mathcal{A}_{avg}$) of the property defined in Eq. 2.12:

$$\mathcal{A}_{avg} = \lim_{t\to\infty} \frac{1}{\tau} \int_{\tau} \mathcal{A}\big(\boldsymbol{r}^N(t), \boldsymbol{p}^N(t)\big) d\tau \qquad (2.12)$$

Statistical mechanics gives a useful tool for estimating $\mathcal{A}_{avg}$, by replacing time average by ensemble average, i.e. by using the "ergodic" hypothesis, which is the fundamental axiom of statistical mechanics, i.e.:

$$\mathcal{A}_{avg} = \langle \mathcal{A} \rangle = \int \mathcal{A}(\boldsymbol{r}^N, \boldsymbol{p}^N)\, P(\boldsymbol{r}^N, \boldsymbol{p}^N)\, d\boldsymbol{r}^N d\boldsymbol{p}^N \qquad (2.13)$$

where the integral in Eq. 2.13 is taken over the entire phase space and $P(\boldsymbol{r}^N, \boldsymbol{p}^N)$ is the probability density of the ensemble. For constant number of particles, volume and temperature, the probability density is given by Boltzmann distribution:

$$P(\boldsymbol{r}^N, \boldsymbol{p}^N) = \exp\left(-\frac{E(\boldsymbol{r}^N, \boldsymbol{p}^N)}{k_b T}\right)/Q \tag{2.14}$$

where E is the energy, k_b is the Boltzmann constant, T is the temperature and Q is the partition function. In practice, thermodynamics averages are obtained from MD simulations as time averages using numerical integration of Eq. 2.11.

$$\langle \mathcal{A} \rangle = \frac{1}{M}\sum_{i=1}^{M} \mathcal{A}(\boldsymbol{r}^N, \boldsymbol{p}^N) \tag{2.15}$$

where M is the number of time steps. For example, temperature (T), internal energy (U), heat capacity (C_v) and pressure (P) of a system with N-particles can be estimated from MD as follows:

$$T = 2\mathcal{K}/k_b(3N - N_c) \tag{2.16}$$

$$U = \langle E \rangle = \frac{1}{M}\sum_{i=1}^{M} E_i \tag{2.17}$$

$$C_v = \langle (E - \langle E \rangle)^2 \rangle / k_b T^2 \tag{2.18}$$

$$P = \frac{1}{V}\left[N k_b T - \frac{1}{3}\sum_{i=1}^{N}\sum_{j=i+1}^{N} r_{ij} f_{ij}\right] \tag{2.19}$$

where N_c are the number of constraints on the system; and r_{ij} and f_{ij} is the distance and force acting between the particles i and j respectively. A comprehensive discussion of classical statistical mechanics and thermodynamics concepts can be found in Attard (2002) and in the references therein.

One of the most popular statistical techniques for estimating equilibrium properties of a large system of particles is the Monte Carlo method (MCM). Traditional MCM samples from canonical ensemble, i.e. it estimates statistical properties of a system with constant number of particles (N), constant temperature (T) and constant pressure (P). MD simulations, on the other hand are typically performed under the conditions of constant N, constant volume (V), and constant E (microcanonical ensemble). However, MD can be modified to simulate from other ensembles such as canonical ensemble, grand canonical ensemble (fixed N, T, P) or isothermal-isobaric ensemble (fixed μ, V, T) by appropriately modifying the Hamiltonian. But in modified MD simulations, individual

trajectories of particles no longer represent the solution of Newton's equations. Similarly, MCM can also be modified to sample from other ensembles.

In the canonical, microcanonical and isothermal-isobaric ensembles the number of particles is constant but in a grand canonical simulation the composition can change i.e. the number of particles in simulation can increase or decrease. The equilibrium states of each of these ensembles are characterized as follows: canonical ensemble - minimum Helmholtz free energy, microcanonical ensemble - maximum entropy, isothermal-isobaric ensemble - minimum Gibbs free energy, and grand canonical ensemble - maximum pressure × volume. One of the important benefits of MD simulation is that it can be used for non-equilibrium simulations (e.g. surface diffusion and bond failure), as opposed to MCM which are only used to estimate equilibrium properties. In some cases, however, modified MCM such as Kinetic Monte Carlo method and other related techniques can be used for estimation of non-equilibrium properties. Detailed information MD methods and related statistical techniques can be found in Haile (1997), Leach (2001), Frenkel & Smit (2001) and Rapaport (2004).

An example of application of MD simulations to metals is the study by Horstemeyer et al. (2001). In this work authors carried out simple shear molecular dynamics simulations of single crystals using EAM potentials. The important variables that were investigated in this work were: crystal orientation (single slip, double slip, quadruple slip, octal slip), temperature (300 and 500 K), applied strain rate ($10^6 - 10^{12}\ 1/sec$), specimen size (100 atoms to 100 million atoms (2 μm)), specimen aspect ratio size (1:8 – 8:1), deformation path (compression, tension, simple shear, torsion), and material (nickel, aluminum and copper). The largest of these simulations took 13 CPU hours on the 3000 processors Sandia/Intel Teraflop machine. The important conclusions drawn from this study were: 1) The yield stress is a function of size scale parameter and as the size scale decreases the yield strength increases. 2) Although the thermodynamic force (stress) varied at different size scales, the kinematics of deformation appeared to be very similar based on atomistic simulations, finite element simulations and physical experiments.

2.5.3 Continuum Mechanics (CM)

In continuum mechanics (CM) a physical object is modeled in a continuum sense as opposed to discrete particle models in QM or MD. In CM, physical behavior of continuum bodies is described using kinematic, kinetic and balance principles together with appropriate constitutive model for the material under consideration. The CM theories are phenomenological in a sense that they strive to represent the immediate phenomena of experience without looking into detail as of what is happening at atomistic or quantum scales. In a statistical sense, field variables in CM represent statistical averages of microscopic quantities over continuum length scales. For example, in crystal plasticity theories where the deformation of single crystals is considered, the continuum length scales is of the order of 10^{-6} m. Field variables in crystal plasticity such as dislocation density tensors represents the ensemble average of the tensor product of the dislocation line and Burgers vectors over the continuum length. Thus the discrete dislocation substructure is not explicitly considered. In other CM theories material response is usually studied at length scales that are several order of magnitudes greater than the inter-atomic distances (usually greater then 10^{-4} m). For structural engineering applications, the continuum models that are of interest include 1-D objects (for example beams, columns and springs), 2-D objects (e.g. shells and plates) and 3-D objects (e.g. 3-D solids). Finally, numerical techniques such as the finite element method is used to solve problems of practical interests as closed formed solution of the problems posed by CM can be obtained only for a few cases.

Comprehensive treatment of CM for 3-D solids can be found in the classical treatise of Truesdell & Toupin (1960) and Truesdell & Noll (2004). Other standard references on this subject include Malvern, L.E., (1969), Gurtin, M.E., (1981), Marsden & Hughes (1994), Ogden, R. W., (1997) and Holzapfel, G.A. (2000). In Marsden & Hughes (1994) mathematical framework of differential geometry on manifolds is used to develop the theory, and thus it provides a rich geometrical structure to the CM theory. The geometrical structure is particularly useful in understanding fundamental tensors operations such as pull back and push forward, and in understanding objective stress rates

in nonlinear constitutive theories. A more comprehensive geometric treatment of the theory can be found in Van der G.E. et al. (Part I and II, 1996). In this work, the concept of dual variables is used, and inner products and scalar products are distinguished. Thus a consistent distinction in between self-duality and symmetry of tensors, and in between transpose and dual of tensors can be made in this framework. Theories for 1-D and 2-D continuum bodies can be found in Antman (1995), Crisfield (1996, 1997), Belytschko et al. (2000), Wempner & Talaslidis (2002), and Bathe & Chapelle (2003).

2.5.3.1 Constitutive Models

Constitutive theories play an important role in CM as they represent intrinsic properties of material. Kinematic, kinetic and balance principles hold for any continuum body for all times and they do not distinguish one material from another. For deformable bodies these principles are not sufficient enough to determine the material response. Thus additional constitutive laws which are furnished to specify ideal material in question have to be established. Such constitutive laws approximate the observed physical behavior of the real materials under specific conditions of interests.

Constitutive theory of materials usually deals with continuum bodies which in a local neighborhood of a material point can be considered as homogeneous, i.e., kinematical and kinetical properties are homogeneous within a small neighborhood of a material point. The global material response can be heterogeneous, however. As a prerequisite, the continuum itself must be locally homogeneous in the sense of Hill (1956). Real materials are heterogeneous locally, as well as possibly globally. Thus the success of CM approach depends on the two basic relative length scales: (1) Greatest dimension of the micro-constituents of the material (e.g. atomic bonds, dislocations, micro-voids, micro-cracks, etc) relative to the smallest dimension of the elementary continuum material neighborhood (continuum length scale); and (2) the greatest dimension of the elementary continuum material neighborhood relative to the smallest dimension of the overall continuum. For example, in a polycrystalline solid (e.g. steels) consisting of crystals of tens of microns, each crystal can be viewed as a micro-constituent. The elementary

continuum material neighborhood must then be, at smallest, of the order of fractions of a millimeter, and the overall solid, i.e., the structural component, may have dimensions of the order of centimeters or greater. To this end, the concept of a representative volume element (RVE) is introduced. In this approach, the actual dimensions of an RVE are of no concern. It is only its dimension relative to the dimension of its essential microstructure that is of importance. If the smallest dimension of the RVE is D and the greatest dimension of its micro-constituent is d, Hill (1956) suggested that an effective continuum can be produced for $d/D < 10^{-3}$.

A comprehensive discussion on nonlinear constitutive theories can be found in Truesdell & Noll (2004). Other references on this subject include Malvern, L.E., (1969) and Simo & Hughes (1998), and Holzapfel, G.A. (2000). Broadly, the constitutive theories can be formulated in two mathematical frameworks. In one framework constitutive models are formulated without any associated thermodynamic considerations, while in the other framework constitutive models are formulated using thermodynamic postulates. Most often, thermodynamics postulates of Coleman and co-workers, Coleman & Noll (1963) and Coleman & Gurtin (1967), are used. Furthermore, constitutive models can also be classified on the basis of length scale at which they are formulated, as follows:

(a) Micro-mechanical Models

In this class of models the underlying micro-structure of RVE is also modeled using CM theories. The final overall properties of RVE are then obtained using averaging techniques. A comprehensive introduction to such averaging techniques can be found in Nemat-Nasser & Hori (1998) and Nemat-Nasser, S. (1999). As an example, Castaneda et al. (1994) proposed a constitutive model for the effective behavior of porous nonlinear materials using variational principles. The proposed model was capable of approximately accounting for the evolution of microstructures under large quasi-static deformations. Variational principles were used to estimate the bounds and the effective behavior of porous nonlinear materials from the exact results obtained for the linear material with the same microstructure.

Continuum damage mechanics based models can also be classified as micro-mechanical models. In these models, the evolution RVE micro-structure is modeled by internal damage variables which can be either scalars or tensors. A damage mechanics based model was first introduced in the pioneering work of Kachanov (1958, 1986) in the context of isotropic damage models. Example of other damage mechanics based models can be found in Lemaitre (1985), Ortiz (1985), Simo and Ju (1987a, b), Ju (1989), Hansen & Schreyer (1994), Govindjee et al. (1995) and Armero & Oller (Part I and II, 2000), among others.

(b) Phenomenological models

In this class of models the constitutive theory is postulated for RVE. No direct consideration is made to the underlying structure of RVE. Internal field variables may be introduced, however, to take into account the effect of evolving micro-structure. Standard models such as elasticity, plasticity, viscoplasticity, viscoelasticity etc, fall in this category. More information on this class of models can be found in Hill (1998), Lubarda (2001), Nemat-Nasser, S., (2004), Ottosen & Ristinmaa (2005) and Lubliner (2008).

2.5.3.2 Finite Element Method

Finite element method (FEM) is a numerical technique for solving a boundary/initial value problems formulated in CM framework. Mathematically, FEM is based on weak form of the governing equations of CM and seeks solution of the resulting equations in finite dimensional functional spaces known as Sobolev spaces. Weighted residual methods such as Bobnov-Galerkin method are usually used to construct solutions of the governing equations. Mathematical theory of FEM can be found be Oden & Reddy (1976) and Strang & Fix (1973). Other monographs on FEM which are geared towards numerical implementations and application are Hughes (1987), Crisfield (1991, 1997), Bathe (1996), Simo & Hughes (1998), Belytschko et al. (2000), Zienkiewicz et al. (2005), Oden (2006), and Bonet & Wood (2008).

In case of building system failure, impact and contact between the failing members can be modeled efficiently in the framework of FEM. Such contact algorithms are formulated

within the framework of either the kinematic constrained method or the penalty method. A comprehensive discussion of the theory and implementation aspects of these algorithms can be found in Wriggers (2006) and in the references therein.

2.5.3.3 Micro-Mechanical Models for Ductile Fracture in Steels

Various micro-mechanical models have been proposed in the literature to model the three stages of ductile fracture in steels i.e. void nucleation, void growth and fracture initiation by void coalescence. In micro-mechanical models, the physical length scale of these processes is in the range 10^{-6} to 10^{-4} m. The proposed models for ductile fracture of steels fall in two categories. In the first category, discrete voids are considered, while in the second category micro-structure evolution is considered in a damage mechanics framework. In this section the important micro-mechanical models proposed in the literature are reviewed.

A) Models based on Discrete Voids

i) Void Nucleation

The proposed models for void nucleation are based on either continuum theory (Argon et al., 1975) or dislocation particle interactions (Goods et al., 1979). Both these models assume that the void nucleates due to decohesion between inclusion and matrix interface. The Argon model (Eq. 2.20) applies to inclusions with radius r > 1μm and it is independent of the size of the inclusion. This model predicts lower nucleation strain at high hydrostatic (tensile) stresses.

Argon Model $$\sigma_c = \sigma_h + k\sigma_{eq} \tag{2.20}$$

where σ_c, is the critical stress at failure, σ_h is the hydrostatic stress and σ_{eq} is the von Mises equivalent stress. The parameter *k* is a function of particle shape. The Goods model applies to inclusions with radius r < 1μm and it shows that the local stress concentration increases with decreasing particle size. In this case, the critical strain, ϵ_c, for cavity nucleation is given by Eq 2.21:

Goods Model $$\epsilon_c = Kr(\sigma_c - \sigma_h)^2 \tag{2.21}$$

where σ_c is the interface strength, r is the radius of particle and K is a material constant.

Experimental results often vary from the results of these models as nucleation tends to occur more readily at large particles. This discrepancy is due to the fact these models fail to consider the cracking of the inclusions itself or the pre-cracked and debonded inclusions during the fabrication phase. Large particles are more likely to crack under plastic deformation as they are more likely to contain defects which can act as Griffith-like small cracks (Roy et al. (1981), Anderson (2004)). Studies by Beremin (1981) on fracture of A508 steel, shows that the mode of cavity formation with MnS inclusions depends on the orientation of inclusion with respect to applied loading. In longitudinal direction most of the inclusions breaks, while in the short transverse direction, cavity formation is usually due to decohesion of particle matrix interface. Using Eshelby's theory for inclusions extended to include plastic deformation, the author shows that internal stress in the inclusion is given by $k(\sigma_h + \sigma_{eq})$, where k depends on the inclusion shape and loading direction.

ii) Void Growth

Once the void forms, further plastic strain and hydrostatic stress causes them to grow. McClintock (1968) considered growth of a single cylindrical hole, either in a perfectly plastic or viscous material. Rice & Tracey (1969) considered growth of isolated spherical and cylindrical voids in a non hardening material for the case of a remotely applied strain field with superimposed hydrostatic stresses. In the case spherical cavity and von Mises material, the rate of increase of radius of cavity was expressed as follows:

$$\frac{\dot{R}}{R} = 0.283\dot{\epsilon}^p_{eq} \exp\left(\frac{3\sigma_h}{2\sigma_y}\right) \tag{2.22}$$

where R is the radius of cavity, ϵ^p_{eq} is the equivalent plastic strain, and σ_h and σ_y are hydrostatic and yield stress respectively. Equation 2.22 shows that the void growth rate is proportional to the increment of equivalent plastic strain and an exponential function of triaxial stress state. Stress triaxiality is defined as a ratio of hydrostatic stress to Mises stress. Huang (1991) made some improvements in the velocity fields assumed by Rice & Tracey to derive Eq. 2.23. Huang (1991) suggested that for high triaxiality ($\sigma_h/\sigma_y >$

1.0), the factor 0.283 in Eq. 2.22 should be replace by 1.28, while for low triaxiality ($\sigma_h/\sigma_y < 1.0$), the void growth equation is expressed as follows:

$$\frac{\dot{R}}{R} = 1.28\dot{\epsilon}^p_{eq}\left(\frac{\sigma_h}{\sigma_y}\right)^{0.25}\exp\left(\frac{3\sigma_h}{2\sigma_y}\right) \tag{2.23}$$

The first micromechanical constitutive model for porous plastic materials was proposed by Gurson (1977). Using the upper bound theorem of plasticity, approximate yield criterion for dilatant materials was derived by considering unit cell simulations with a single spherical or circular cylindrical void in a rigid-plastic cell matrix. The yield criterion, thus obtained exhibits weak pressure dependence as opposed to classical J_2-flow theory which is pressure independent. This model was modified by Tvergaard (1981) who carried out numerical studies of materials containing periodically distributed circular cylindrical or spherical voids and showed that the Gurson model gives better agreement with numerical studies when two more parameters are introduced in the model. Tvergaard and Needleman (1984) further modified the Gurson model by introducing an effective porosity parameter which accounts for increasing cavitation after the voids start to coalesce to more closely match experimental observations. Recent application of Gurson model can be found in Dos Santos & Ruggieri (2003) and Rakin et al. (2004). Gologanu et al. (1993, 1994) proposed a variation of the Gurson model in which voids are modeled as ellipsoids and their orientation and shape evolve during the deformation process. The drawback of the Gologanu model is that it has numerous parameters that are difficult to calibrate.

The above models describe void growth under monotonic loading conditions. Ristinmaa (1997) proposed a void growth model for cyclic loaded porous plastic solids for study of low cyclic fatigue. An axisymmetric cell model containing spherical voids was used to simulate a porous material and the matrix material was modeled using von Mises yield criterion characterized by perfect plasticity and isotopic or kinematic hardening. Kanvinde (2004) also proposed a void growth model for materials subjected to very low cycle fatigue as in the case of seismic loading. He modified the Rice and Tracey void

growth model to take into account the shrinking of voids during the cycles of negative hydrostatic tension.

iii) Void Coalescence and Fracture Initiation

Fracture initiation criteria are usually based on the assumption that for the fracture of the material to take place, the voids coalesce to reach some critical value of void growth ratio or porosity. McClintock (1968) proposed the first fracture criterion according to which fracture occurs when two neighboring voids come into contact. The criterion was presented in terms of critical strain and stress, and it is assumed that fracture occurs when the strain and stress history over a region of the order of the void whole spacing attains a critical value. Thus a length scale parameter of the order of void spacing was introduced. However, this criterion greatly overestimates ductility because the actual fracture occurs by flow localization between the void and not by the impingement of voids.

Hancock et al. (1976) suggested that failure initiation may take place at a critical volume fraction of large voids. This is equivalent to a critical hole-spacing averaged over all orientations, and corresponds to the observation that void coalescence does not occur on a single well defined plane. They proposed an expression for failure strain in steel (Eq. 2.24), which was a function of stress triaxiality and a material constant.

$$e_f = e_n + \alpha \exp\left(-\frac{3\sigma_h}{2\sigma_m}\right) \tag{2.24}$$

where e_f is the failure strain, e_n is the void nucleation strain, α is a material constant and σ_h and σ_m are hydrostatic and Mises stresses respectively. For materials in which appreciable plastic flow occurs before the voids nucleate, the nucleation strain is also added to get the failure strain. The authors also recognized the importance of length scale and asserted that it is not sufficient for the failure criterion to be reached at a single point but the failure criterion must involve a certain minimum amount of material which is a characteristic of the scale of physical events leading to local failure. Further, it was observed that large voids often do not coalesce completely but are linked by microvoids which are the result of the second generation of small scale void growth based on carbides and other precipitates between the large holes. In order to produce necessary

small scale void growth, high strain and/or high triaxiality are required. These conditions may be provided by plastic instability, resulting in flow localization between the large holes. The authors concluded that the failure initiation can be taken as a critical volume ratio of large voids, which is equivalent to critical void spacing averaged over all orientations at the instance of fracture initiation. This fracture initiation criterion is known as the stress modified critical strain criterion (SMCS model).

Mackenzie et al. (1977) used the SMCS criterion to study fracture initiation in circumferentially notched tension specimens. Bridgman's (1952) analysis was used to obtain the plastic strain and distribution of stresses across the cross section. According to Bridgman model the maximum triaxiality occurs at the center of the cross-section and the fracture was assumed to initiate at this point. The strain at which the average stress drops was defined as the failure initiation strain. It was observed that strain at fracture initiation decreases with the increase in triaxiality. The authors concluded that both triaxiality and plastic strain were overestimated by Bridgman's results and the more severe the notch, the greater the errors. It was also indicated that error in the plastic strains at the center may be large, which overestimated the failure strains at fracture initiation.

Ritchie et al. (1979) used a SMCS criterion for their fracture initiation studies and used a small multiple of ferrite grain diameters as the characteristic length. Bandstra et al. (1998) carried out the experiments with notched bars of different notch geometry to vary the constraint and also used a similar relationship to model the fracture initiation strain. Failure was taken as a point during the test at which the specimen loses significant load carrying capacity. They identified two regions where the relationship between triaxiality and fracture strain was different. For the first region where triaxiality was small (< 1.05), fracture strain decreased rapidly with increase in triaxiality, but in the second region where the triaxiality was high (> 1.05), fracture strains were small and decreased slowly with increasing triaxiality.

Norris et al. (1978) proposed a fracture criterion based on mean stress and effective plastic strain and fracture was assumed to occur when the criterion was satisfied over the

characteristic length, r_c, of material which they assumed to be about 25μm. Fracture was assumed to occur when accumulated damage variable, D, in Eq. 2.25 reaches a critical value D_c over a characteristic length r_c.

$$D = \int f(\sigma_h) d\bar{\epsilon}^p \tag{2.25}$$

where σ_h is the hydrostatic stress and $d\bar{\epsilon}^p$ is the increment in the equivalent plastic strain. The function $f(\sigma_h)$ used in this study is given by Eq. 2.26:

$$f(\sigma_h) = \frac{1}{[1 - c\sigma_h]} \tag{2.26}$$

where c is assumed to be a material parameter such that $c\sigma_h < 1.0$. Clearly, as the hydrostatic stress increases, the rate of damage accumulation also increases. A critical value of damage accumulation, $D_c = 1.16$, was used in this study.

Rousselier (1987) proposed a fracture criterion based on Rice and Tracey void growth model (VGM). The functional form of the criterion was expressed as follows:

$$D_c = \int F\left(\frac{\sigma_h}{\sigma_m}, \epsilon_{eq}^p\right) d\epsilon_{eq}^p \tag{2.27}$$

The fracture was assumed to occur when D_c in Eq. 2.27 is exceeded over the characteristic length, r_c, of the material, which was assumed to be a function of the number of inclusions per unit volume. In particular, the functional form that was used is given by Eq. 2.28, where A and B are constants.

$$D_c = \left[\ln\left(\frac{R}{R_o}\right)\right]_c = A\epsilon_{eq}^p (B\frac{\sigma_h}{\sigma_m}) \tag{2.28}$$

Panontin et al. (1995) used the criterion based on the Rice and Tracey void growth model and the SMCS model to predict the fracture initiation strain. The critical characteristic distance was calculated using the physical material characteristics and from the phenomenological approach by correcting the values by trial and error procedure until experimental fracture initiation data was predicted. In another related study, Kanvinde (2004) proposed a fracture initiation model for very low cycle fatigue. A damage parameter was included in this model to account for the accumulated damage in the cyclic loading process. Fracture initiation was assumed to occur when the critical growth ratio is reached over a characteristic length which was determined from SEM studies of

the fracture surface. The calibrated the model for monotonic and cyclic loading case was used to predict fracture initiation under large scale plasticity.

Thomason P.F. (1985) developed a void coalescence criterion based on limit load analysis of the intervoid matrix. This criterion states that coalescence occurs when the net section stress between the voids reaches a critical value. However, this criterion does not taken into account the formation and growth of micro-voids in the ligaments separating the main void, and thus may lead to overestimation of critical stress and ductility.

Benzerga et al. (1999) studied the effects of void shape and inter particle spacing on void coalescence using localization based and plastic limit-load based models. They studied the anisotropic ductile fracture of rolled plates containing elongated inclusion. It was shown that the decrease in ductility with increasing triaxiality was more rapid when the macroscopic loading was perpendicular to the common axis of the voids. Initial void spacing was shown to be important when triaxiality was high whereas the initial volume fraction of inclusions was not important. It was also shown that void shape was important for low to intermediate stress triaxiality.

The Gurson model also contains a failure criterion; and failure is assumed to occur as a result of a plastic instability that produces a band of localized deformation. Such instability occurs more readily in Gurson material because of the strain softening term introduced by hydrostatic stress. Although the Gurson model may adequately characterize plastic flow in the early stages of the ductile fracture process, it does not provide a good description of the events that lead to final failure. Ductile failure results from local instabilities; however, because the model does not consider discrete voids, it is unable to predict the necking instability between voids. Because of this deficiency the Gurson model gives very high values of fracture strains in real materials. This deficiency was removed in Gurson-Tvergaard-Needleman (GTN) model (Tvergaard (1981), Tvergaard & Needleman (1984)), which has a failure criterion that introduces an abrupt failure point when the critical porosity is reached. Xia et al. (1995) used the GTN model in their ductile crack growth study using computational cells. Computational cells are the

standard solid finite elements with size equal to some characteristic length of the material, i.e. RVE, under consideration. Dos Santos and Ruggieri (2003) used the GTN model in a computational cell framework to model the ductile fracture behavior in tensile specimens. Size of computational cell was assumed to be 100 μm in this study. In another related study, Rakin et al. (2004) used specimens without initial crack to calibrate the GTN model and then used the calibrated model to predict failure initiation in pre-cracked specimens.

In applications to structural engineering, El-Tawil et al. (1999) proposed a rupture index based on plastic equivalent strain and failure strain proposed by Hancock (1976). The rupture index was used as a performance indicator to study the potential for ductile fracture initiation and used it to develop in moment resistant connections with different access hole geometries so as to minimize the potential for ductile fracture initiation. Ricles et al. (2000) also used the rupture index proposed by El-Tawil et al. (1999) to develop access hole geometries in moment resisting connections. The rupture index proposed in El-Tawil et al. (1999) was modified by Shih-Ho et al. (2006), to obtain a better correlation with the experimental results on notched steel specimens. The modified rupture index was used to evaluate potential for fracture in shear links with different geometries.

B) Models Based on Damage Mechanics

For application to steels, Lemaitre (1985) proposed a model of isotropic ductile plastic damage, where the damage was linear with the equivalent strain and showed a large influence of triaxiality by means of a damage equivalent stress. Rousselier (1987), Tia (1990), Dhar et al. (1996) and Reusch et al. (2003) also presented damage models based on continuum thermodynamics.

Steinmann et al (1993) proposed a damage model in the context of large deformation plasticity, with multiplicative decomposition of the deformation gradient. A scalar damage parameter was introduced to model the deviatoric damage leading to a degradation of the deviatoric elastic properties of the material. They also formulated the

Gurson model in the framework of multiplicative plasticity. Mahnken (1999) discussed some of the important aspects of implementation of Gurson model in large deformation multiplicative plasticity framework. Other damage models in a large deformation, multiplicative plasticity framework for ductile fracture of metals can be found in Mahnken (2002, 2005). In another related study, Menzel et al. (2001, 2003) proposed a framework for modeling of anisotropic damage in continuum bodies, in the context of large deformations.

2.5.4 Multi-Scale Methods

It is not possible to simulate all problems of practical interests using Ab initio methods. In fact, even with the availability of high performance parallel computing environment it is not possible to solve a problem with more than about 50,000 atoms using QM. In QM the motion of electron is explicitly considered, so that even if some of the electrons are ignored (as in semi-empirical methods) a large number of particles must still be considered. Therefore, many of the problems that are to be tackled in practice are unfortunately too large to be considered by QM.

In MD, on the other hand, electronic motions are ignored and the energy of a system is as a function of the nuclear positions only. MD therefore, can be used to perform calculations on systems containing significant numbers of particles. Moreover, in some cases efficiently designed and calibrated empirical force fields can provide answers that are as accurate as even the highest-level quantum mechanical calculations, in a fraction of the computational time. However, MD cannot provide properties that depend upon the electronic distributions. With current computational resources, largest size of the simulation models that can be handled MD is of order of tens of nanometers (less than 1 million atoms).

CM methods ignore the particle structure of the matter altogether, and model the physical object as a continuum body. Typical problems that can be handled by CM methods have length scale larger than about 10^{-4} m. However, in some cases micro-structure behavior at

length scales of 10^{-6} m can be modeled using micro-mechanical methods. Although, CM models can be used to simulate a wide range of material response, they cannot to simulate physical processes at atomic length scales such as atomic bond breaking.

The above limitation of the various methods has led to new development of new methods commonly referred to as multi-scale methods. Multi-scale methods have become necessary and popular due to the following reasons. First is the recent discovery of new nano-scale materials and the corresponding interest in nanotechnology research. Second is that experiments have conclusively shown the connection between micro-scale physics and macro-scale response. Finally, the concept of linking disparate length and time scales has become feasible recently due to the ongoing increase in computational power. Multi-scale methods can be classified as coupled multi-scale methods and uncoupled multi-scale methods, and are discussed next.

2.5.4.1 Coupled Multi-Scale Methods

Coupled multi-scale methods (Fig. 2.7) are those in which the information available from distinct length and time scales is combined into a single coherent, coupled simulation. Coupled multi-scale analysis is a very active area of research and robust techniques for such analysis still do not exist.

Abraham et al. (1998) presented a framework for concurrent multi-scale method. In this work tight binding (TB), molecular dynamics (MD) and finite elements (FE) were linked concurrently together in a unified approach called MAAD (macroscopic, atomistic, ab initio dynamics). Concurrent linking implies that all three simulations run at the same time, and dynamically transmit necessary information to and receive information from the other simulations. In this approach, the FE mesh is graded down until the mesh size is on the order of the atomic spacing, at which point the atomic dynamics are governed via MD. Finally, at the physically most interesting point, i.e. at a crack tip, TB is used to simulate the atomic bond breaking processes. The interactions between the three distinct simulation domains are governed by conserving energy in the system. The overlapping regions (FE/MD and MD/TB) are termed ‘‘handshake’’ regions, and it is in these regions

where the information between the computational sub-domains is exchanged. The three equations of motion (TB/MD/FEM) are all integrated forward using the same time-step. This method was applied to the simulation of brittle fracture by Abraham et al. (1998). In a related approach, Rudd & Broughton (1998) used only MD and FEM sub-domains. Again, the FE mesh is graded down to the atomistic scale and statistical mechanics principles are used to estimate the energy of MD system to approximately account for loss of electronic degrees of freedom. The success of these approaches depends on modeling of "handshake" regions, where the information between two scales is exchanged. Common problems associated with this technique were: (1) spurious reflection of waves from MD-FE interface, which results in higher temperature in MD domain (2) use of a very small FE mesh and a very small time-step even for the FE domain i.e. it means that both macro and micro variables are allowed to evolve at the same rate, which is not a natural time scale for macroscopic variables. Furthermore, use of FE constitutive laws, which are typically determined for RVE, is questionable at atomistic length scales in the regions with refined mesh.

Some of these issues were addressed by the bridging scale method proposed by Wagner & Liu (2003). In this method, the coarse scale exists everywhere and is not meshed down to the atomic spacing allows for a staggered time integration algorithm, which allows the atomistic and continuum simulations to evolve on their natural time scales. The boundary coupling between the simulations is achieved by use of the Langevin equation, which eliminates fine scale reflection at the interface. Further improvements and extensions of this method based on multi-scale variational approach can be found in Liu et al. (2006).

In continuum mechanics, variational multi-scale method proposed by Hughes et al. (1998) is also used as a basis of coupled multi-scale methods. In variational multi-scale method, the displacement field is decomposed into coarse and fine scale components, i.e., $\boldsymbol{u}(\boldsymbol{x}) = \boldsymbol{u}_c(\boldsymbol{x}) + \boldsymbol{u}_f(\boldsymbol{x})$. The coarse scale, $\boldsymbol{u}_c(\boldsymbol{x})$, is that part of the solution which can be represented by a set of standard FE basis functions. The fine scale $\boldsymbol{u}_c(\boldsymbol{x})$ is defined as the part of the total solution whose projection onto the coarse scale is zero. The fine scale component was used to resolve a local field of interest using an element level enrichment.

Mote (1971) proposed a 'global-local' formulation to enrich the FE solution. The underlying philosophy of this method is to combine the approximate global shape functions known a priori to enhance the 'local' finite element field. The author combined the assumed global Rayleigh-Ritz field with a local finite element field in the solution of beam and plate problems. Dong (1983) generalized the concept of combining Rayleigh-Ritz approximations with the conventional finite element method and surveyed the application of this technique. Although these formulations might give better results in some applications, their efficacy depends on the a priori knowledge of the global fields.

Belytschhko et al. (1990) proposed a methodology based on spectral overlay method to uncouple the FE mesh topography and field orientations effects. In this method, spectral approximation was superimposed on the sub-domain of the finite element mesh rather than on the individual element domains. In the spectral domain, the displacement field consisted of the spectral displacement field and finite element field. The boundaries of the spectral patch need not be coincident with the boundary of elements, and hence high gradients inclined at an angle to the mesh can be taken into account. The constructions of spectral fields require a priori knowledge of the form of the solution. A drawback of this method was that it could not resolve the structure of the field tangential to the boundaries of the domain because of the homogeneous boundary conditions on the entire spectral field. Its efficiency is also reduced if the high gradient fields follow complicated shapes and boundaries or if singularities exist within the spectral domain.

Mathematical theory of asymptotic homogenization has been used for analyzing heterogeneous medium at different length scales. This theory was developed from the studies of partial differential equations with rapidly varying coefficients and is based on two important assumptions: 1) fields vary on multiple scales due to the existence of a microstructure but are uniform within the same scales; and 2) microstructure is spatially periodic. The homogenization theory decomposes the boundary value problem of a heterogeneous medium into problems at different length scales and may result in coupled or uncoupled models at different length scales and provides a consistent basis for

transferring information between different length scales. Theory, limitations and applications of this methods, and improvements to take into account the local variation of fields and non-periodicity can be found in Hollister et al (1992), Ghosh et al. (1995, 1996), Fish et al. (1993, 1994, 1997) and Takano et al. (2003).

2.5.4.2 Uncoupled multi-scale methods (UMM)

Uncoupled multi-scale methods (Fig. 2.8) are those in which information available from a lower length and/or time scale is used to derive the models at larger length and time scales or vice versa. Thus, various scales are decoupled in this method. UMM are routinely used in various fields, for example, Ab initio calculations are used to calibrate empirical force fields in MD. In CM, response of polycrystalline materials (length scale > 10^{-4} m) are derived from response of individual crystal grains (length scale ~10^{-6} m). Micro-mechanical model in CM also represents a class of UMM models, where macro-scale behavior is estimated from micro-structural properties. Some of other important uncoupled multi-scale methods, particularly in FEM, are discussed next.

In FE, sub-modeling technique (Fig. 2.9) can also be to improve the FE solution in the region of high gradients. In this method a global model with a relatively coarse FE mesh is used to obtain boundary conditions for some local region or sub-model where a much more refined FE mesh is used. In a displacement based finite element formulation, the displacements converge faster than the stress and strains. Thus, in regions of high stress/strain gradients a more refined FE mesh is needed than that required for displacements to get the similar level of accuracy for stresses and strains. The submodel technique has been used in the past by various researchers (e.g. Shih-Ho et al. (2006)) obtain more accurate local solutions and has been implemented in popular finite element programs like ABAQUS®. In the analysis of the sub-model, different material properties or different constitutive relationship for the material can also be used.

Uncoupled finite element models for structural analysis can be classified into three categories: micro scale models, macro scale models and structural scale models. In micro scale models, 3-D solid or shell finite elements are used to model the structural

components. Micro-scale behavior of these models is attributed to the constitutive material law which is derived from micro-mechanical study of the underlying micro-structure. In macro scale models, 3-D solid or shell finite elements are also used to model the structural components. However, material properties for these models are obtained from phenomenological models as opposed to micro-mechanical models as in case of micro-scale models. Structural scale models, on the other hand, utilize a combination of beam-column and discrete spring finite elements to simulate the overall response of the structure. The success of structural scale models stems from their ability to adequately mimic, in a phenomenological manner, the local and global responses of importance to the physical processes being modeled. These types of models are used separately or in combination to economically capture the behavior of a structure at different length scales. Fig 2.10 shows various modeling techniques for structural analysis and how they span the various length scales.

As an example of application to steel, Hao et al. (2004) proposed a UMM approach for calculating the fracture toughness and strength of high strength steels. QM calculations using density functional theory were carried out to calibrate empirical potentials. These potentials were then used in a quasi particle dynamics approach to scale the model up to micron size. Finally, properties of effective continuum were also obtained using averaging techniques.

2.6 Summary

This chapter summarized the various issues related to progressive collapse of structural systems. Current design requirements for prevention of progressive collapse in structures, both in public domain and government documents, were discussed. The mechanisms of ductile fracture processes in steels together with the available methods for simulation of these processes were also presented. In particular, models based on quantum mechanics, molecular dynamics, continuum mechanics and multi-scale methods were reviewed.

Figure 2.1 Ronan Point building after 16th May 1968 collapse (Nair 2004)

Figure 2.2 Murrah Federal building after April 19, 1995 attack

Figure 2.3 World Trade Center 1 and 2 on 11th September 2001

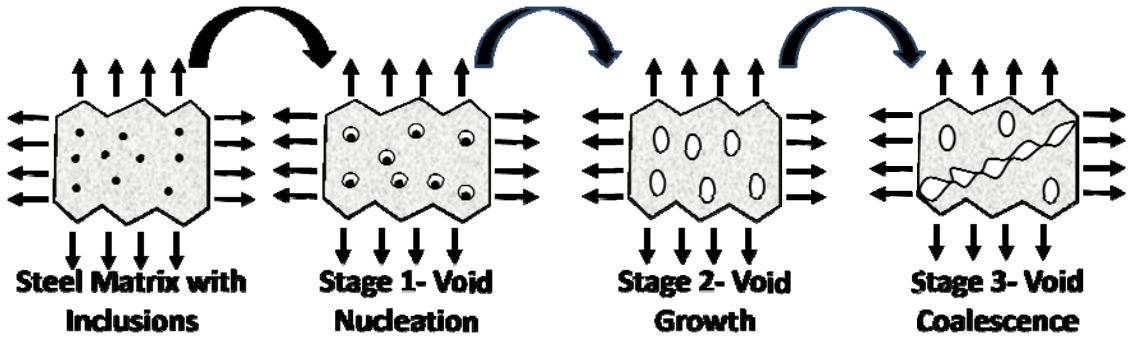

Figure 2.4 Ductile fracture processes in steel

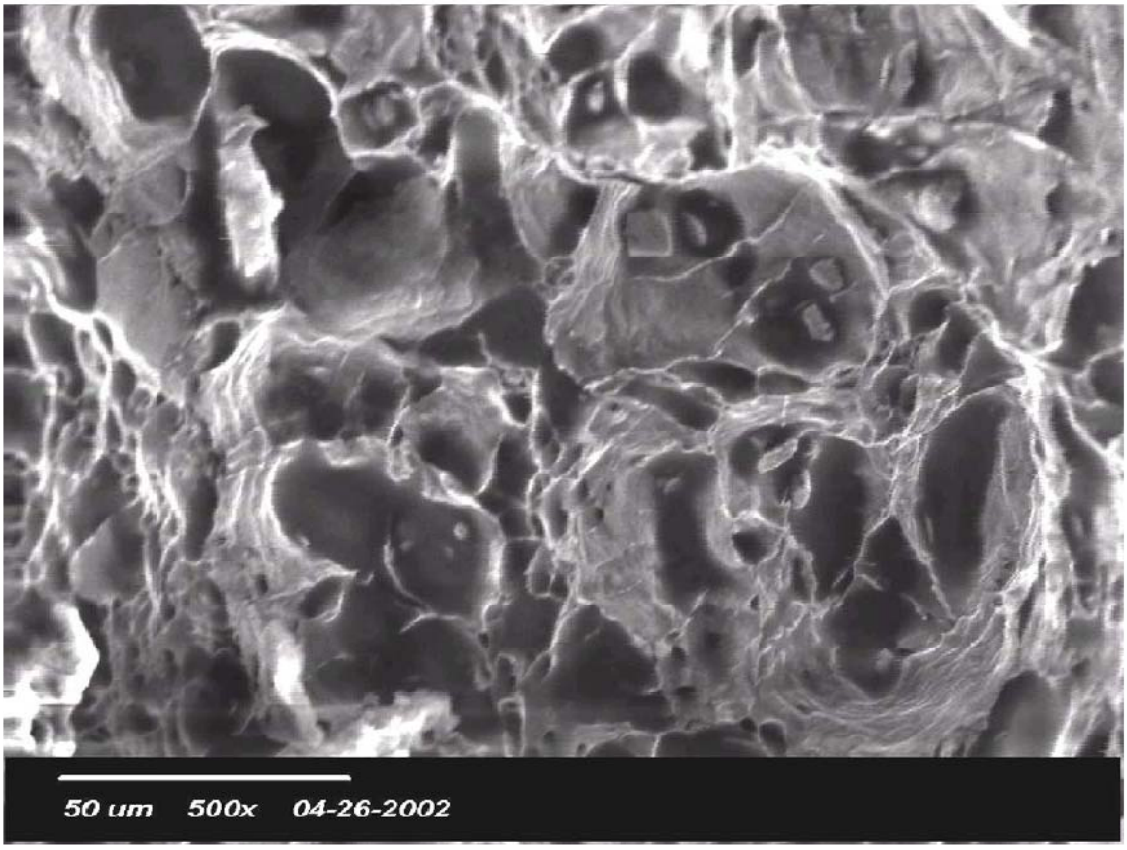

Figure 2.5 Scanning electron micrograph of the surface of steel fractured due ductile fracture process (Kanvinde, 2004)

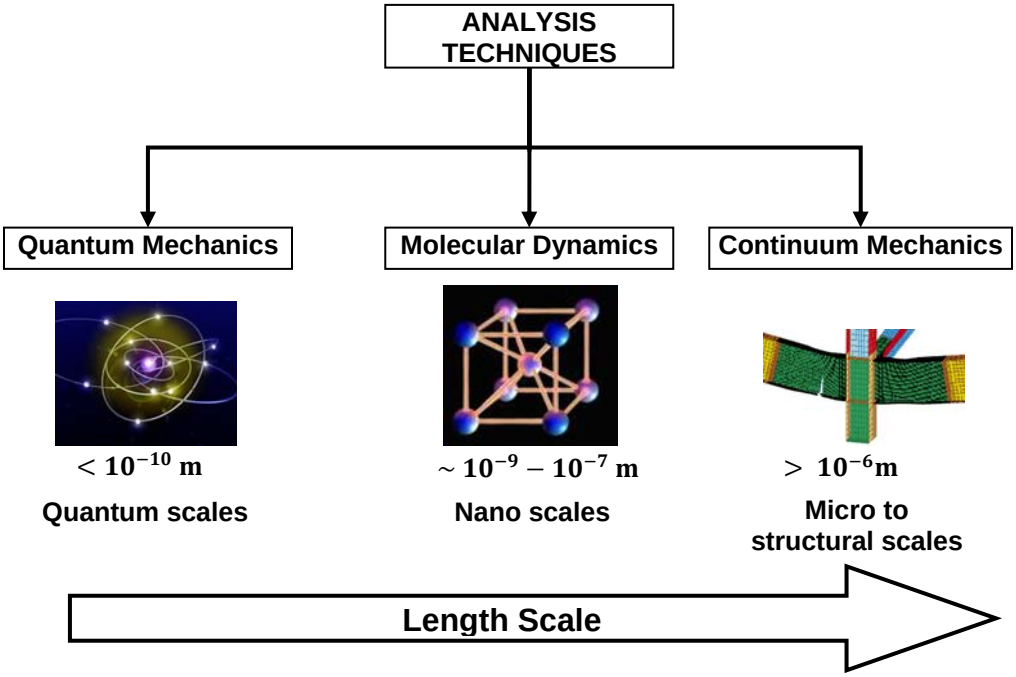

Figure 2.6 Overview of analysis methods

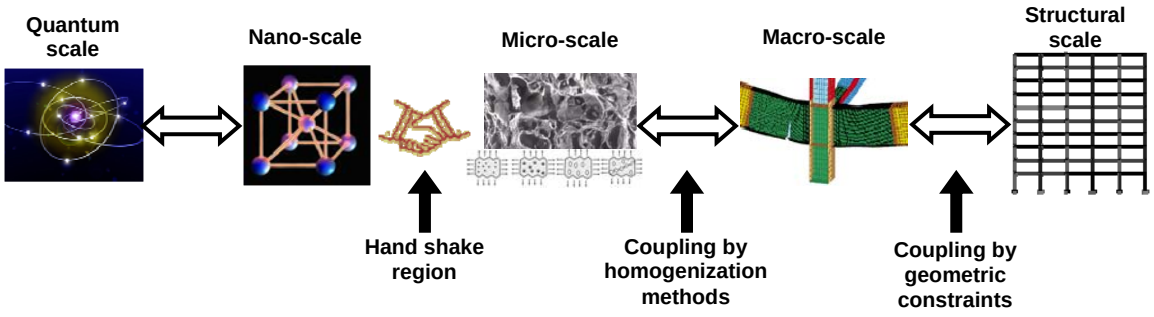

Figure 2.7 Coupled multi-scale methods

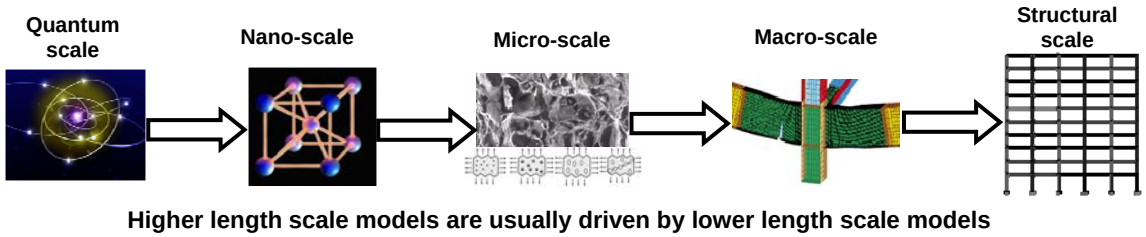

Figure 2.8 Uncoupled multi-scale methods

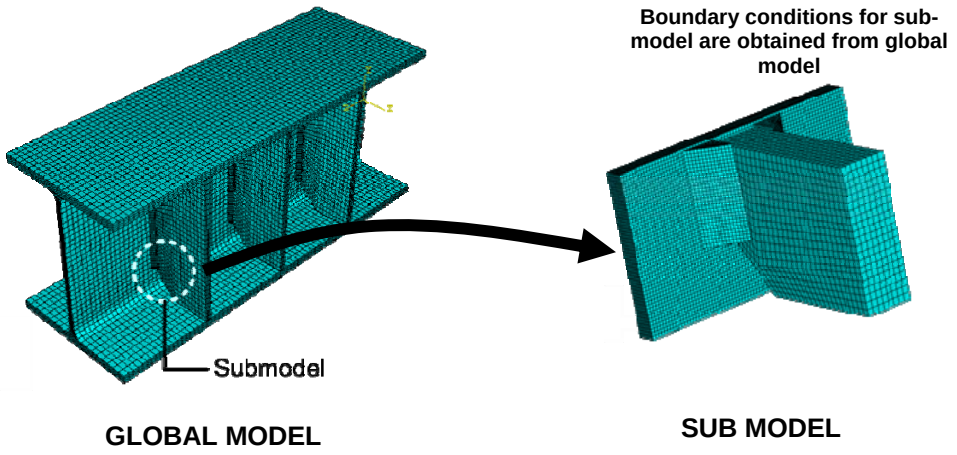

Figure 2.9 Sub-modeling technique: Lower length scale model is driven by higher length scale model

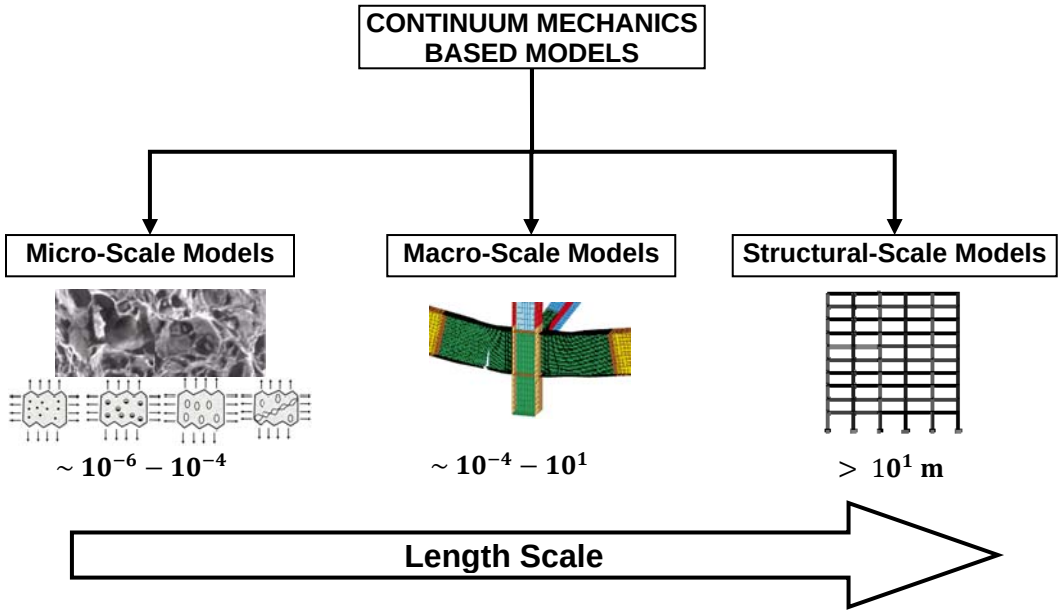

Figure 2.10 Overview of continuum mechanics based models

CHAPTER 3

COLLAPSE ANALYSIS OF STEEL MOMENT FRAME SUB-ASSEMBLAGES

3.1 Introduction

There are various mechanisms that could contribute to the capacity of a typical steel moment frame system to resist collapse. These includes: a) Catenary action of beams and slabs allowing loads to span adjacent elements; b) frame action from the structural frame members around a damaged region; and c) support provided by nonstructural elements such as partitions and infills. Of the three mechanisms listed above, catenary action represents the last line of defense against collapse because it is activated only after large deformations have occurred. It is furthermore regarded by many practitioners, researchers and code developers as a mechanism that will inevitably develop during collapse.

As shown in Fig. 3.1, the term catenary action refers to the ability of beams to resist vertical loads through formation of a catenary-like mechanism. At low vertical displacements catenary forces developed in the slab may be important; however, at large deformations the effect of the slab is relatively insignificant due to damage in the slab itself and loss of composite action. Thus, catenary action here implies the development of large enough deformations such that gravity and associated debris impact loads are mainly resisted by the vertical components of axial forces that develop in the beams, i.e. catenary forces. Under such conditions, the beams are unable to resist the applied loads through flexural action alone and seek supplemental resistance through formation of the

catenary configuration. The structural system must be ductile enough to allow the new configuration to be achieved while maintaining sufficient integrity to support the developing catenary forces. For example, the connection should not fail prematurely by either bolt failure or steel fracture and should have sufficient rotation capacity to reach the desired catenary mode of deformation.

The formation of catenary action and its stability after formation have not yet been adequately studied and the goal of this chapter is to investigate this critical issue. For this purpose, computational finite element simulation is used to investigate a number of key design variables that influence formation of catenary action in special moment resisting frame sub-assemblages. As previously indicated in Chapter 1, steel moment resisting frames are chosen because the inherent toughness of earthquake resistant construction has led to the widespread perception that earthquake resistant design and detailing will also enhance collapse resistance. However, the effect of potentially large catenary forces on connection performance has not yet been adequately investigated.

The micro-mechanical constitutive model for porous plastic materials proposed by Gurson (1977) is used for simulation of micro through structural-scale behavior of the sub-assemblages. This is a coupled multi-scale simulation, in which micro-structural changes during ductile fracture process such as micro-void nucleation, growth and coalescence are taken into account via the micro-mechanical constitutive model. In particular, a history-like variable known as void volume fraction is introduced in the constitutive model which takes into account the disintegration of material at the micro-scale due to nucleation, growth and coalescence of voids.

In Section 3.2 a constitutive material model for modeling ductile fracture initiation and propagation is presented. In Section 3.3, finite element models of special steel moment frame sub-assemblages are presented and important modeling assumptions are discussed. Finally, results from the finite element simulations are discussed in Section 3.4 and important conclusions are presented in Section 3.5.

3.2 Micro-mechanical Constitutive Model for Steel

A constitutive model is required to model the behavior of steel sub-assemblages up to failure. To this end, the constitutive the Gurson model for porous plasticity as modified by Tavergaard (1981) and Tavergaard et al. (1984) is used for modeling ductile fracture mechanism in structural steel. One of main benefits of using the Gurson model over regular J_2-plasticity based models is that in the Gurson model, softening and failure occurs only in the tension regime, while in the compression regime, only plastic flow occurs, which is in agreement with the experimental results. The yield function for the Gurson model is given by Eq. 3.1.

$$\phi = \frac{\sigma_M^2}{\sigma_y^2} + 2q_1 f^* \cosh\left(\frac{3q_2\sigma_H}{2\sigma_y}\right) - 1 - (q_1 f^*)^2 = 0 \tag{3.1}$$

where

$\sigma_M = \sqrt{\frac{3}{2} s_{ij} s_{ij}}$: Mises Stress

$\sigma_H = \frac{\sigma_{ii}}{3}$: Hydrostatic Stress

$s_{ij} = \sigma_{ij} - \sigma_H$: Deviatoric stress tensor

q_1, q_2: Fitting parameters

σ_y: Yield strength of material

f^* is the effective void volume fraction and is given by Eq. 3.2

$$f^*(f) = \begin{cases} f & f \le f_c \\ f_c + \dfrac{\frac{1}{q_1} + f_c}{f_F - f_c}(f - f_c) & f > f_c \end{cases} \tag{3.2}$$

Where

f: Void volume fraction

f_c: Critical void volume fraction

f_F: Failure void volume fraction

The evolution equations for these internal variables are given by Eq. 3.3, 3.4, and 3.5.

$$\dot{f} = \dot{f}_G + \dot{f}_N \tag{3.3}$$

$$\dot{f}_G = (1 - f)\dot{\varepsilon}_{kk}^p \tag{3.4}$$

$$\dot{f}_N = A\dot{\varepsilon}_{kk}^p \tag{3.5}$$

$$A = \frac{f_N}{S_N\sqrt{2\pi}} \exp\left(-\frac{1}{2}\left(\frac{\varepsilon^p - \varepsilon_N}{S_N}\right)^2\right)$$

where

ε^p: Effective plastic strain

ε_N: Mean nucleation strain

S_N: Standard distribution of the normal distribution of plastic strain

Failure in the Gurson model is assumed to occur when the void volume fraction reaches a failure void volume fraction. It is important to observe that failure of steel is inherently a softening process which manifests itself as a dropping load displacement curve in the tension test. The Gurson model exhibits softening behavior as the voids grow and new voids nucleate. It is a well established fact that the use of softening material in finite element gives results which have first order mesh dependency i.e. solution of finite element analysis does not converge no matter how small the mesh size is used. This is because of the loss of hyperbolicity (in the dynamic case) or ellipticity (in the static case) of the underlying partial differential equations. This pathological effect can be removed by introducing a length parameter in the constitutive model thus removing the first order mesh dependency. Some of the techniques which regularize this behavior include non-local formulations, gradient based enhancements and visco-plastic formulations. A recent non-local formulation of the Gurson model was proposed by Reusch et al. (2003). Another way to solve the problem of mesh dependency is to utilize a material model that depends on the size of element. In the present study, the length scale parameter is introduced by making the material model mesh size dependent i.e. the mean nucleation strain, ε_N , is taken a function of element size and thus the problem of mesh dependency is thereby alleviated.

The original Gurson model was applicable for 3-D situations, but in this study a 2-D variation of this model is used in conjunction with shell elements. This is material number 120 in LS-DYNA. Since triaxial stress states are not adequately represented by shell elements, the model parameters are not representative parameters obtained by material testing using notched and un-notched circular bars. Here, these parameters are

only used as fitting parameters which give the best match to experimental results and are determined by trial and error.

3.2.1 Model Calibration

Realistic simulation of the ductile fracture process using the Gurson model requires calibration of model parameters $q_1, q_2, f_F, f_c, \varepsilon_N, S_N, \sigma_y$ and the plastic hardening curve to experimental results. The value of parameters q_1, q_2 and S_N are taken as 1.5, 1 and 0.1 respectively, which are same as those used by Tavergaard et al. (1984). The rest of the parameters are obtained for A572 Grade 50 steel by calibration to experimental results in Kanvinde (2004). The yield strength, σ_y, of the steel used by Kanvinde (2004) is 58 Ksi. The engineering stress strain curve is shown in Fig. 3.2. The hardening curve is shown in Fig. 3.3 and is obtained from the engineering stress-strain data by subtracting elastic strains from total strains to get plastic strains. The yield stress to ultimate stress (YUSR) ratio of this steel is 0.67.

Kanvinde (2004) tested two different plate specimens to fracture under monotonic tensile loading. Figure 3.4 shows schematic views of the specimens. Here these specimens are designated as specimen-1 and specimen-2 (Fig. 3.4(a) and 3.4(b)). Finite element models of these specimens consist of 4-node quadrilateral shell elements with a four-point-through-thickness Lobatto integration scheme, which ensures that two integration points are on the surface of the shell elements. The shell element used is a fully integrated shell based on an assumed strain formulation to avoid locking and to enhance in-plane bending behavior. Additionally, it uses a local coordinate system which rotates with the material to account for rigid body motions and automatically satisfies frame invariance of the constitutive relations. Ductile fracture is modeled by removing elements from the analysis when the effective void volume fraction, f^*, exceeds the failure void volume fraction, f_F, at any integration point. From the calibration, studies parameters f_c and f_F are determined as 0.09 and 0.1 respectively, while the mean nucleation strain, ε_N, is taken as element size dependent.

Using a mean finite element size of 0.125 inch, the mean nucleation strain ε_N is determined to be 0.58 for specimen-1. Figure 3.5 shows the comparison between finite element and experimental results for this case. It can be observed that the finite element model closely simulates yielding, hardening and fracture of the plate. To validate the model, a finite element model of specimen-2 which consists of 3 × 0.375 inches plate with two holes of diameter 0.5 inches was created and analyzed. Figure 3.6 shows the comparison between finite element and experimental results for specimen-2. It can be again observed from Fig. 3.6 that the finite element model results are closely correlated to the experimental results.

Since the analysis time step for explicit finite element analysis is element size dependent and decreases with element size, the smallest element size is taken as 0.5 inches in the simulations of the structural sub-assemblages to reduce the computational load to a manageable level. The nucleation strain for element size 0.5 inch is computed using calibrated results obtained for elements of size 0.125 inch. For this purpose, a rectangular plate of size 3 × 2 inches and thickness 0.375 inches is discretized using element of size 0.125 inch. The coupon is then pulled in tension until it fails by fracture at a displacement of 0.65 inches. The same plate is again discretized using element of size 0.5 inch, and the value of nucleation strain is adjusted such that it again fails at a displacement of 0.65 inches. Figure 3.7 shows results for the two cases. This analysis gives nucleation strain $\varepsilon_N = 0.40$ for element of size 0.5 inches. Calibrated values of material parameters for the Gurson model are summarized in Table 3.1.

3.3 Finite Element Model (FEM) Development

Detailed finite element analyses are carried out for the 1st, 5th and 7th story beam-column sub-assemblages of an eight story special moment resisting perimeter frame building system. Such systems are commonly used on the US West Coast. Figure 3.8 shows the design details of the 8 story prototype building used in the study. As shown in Fig 3.9, the system was designed with radius cut reduced beam sections (RBS) by Jin et al. (2005) according to provisions in FEMA 302 (1997), AISC-Seismic (1997), and FEMA-350

(2000). Building frames were designed for loads on standard office buildings located in a region near Los Angeles such that short period response acceleration parameter, S_s = 2.48 g, and response acceleration parameter at one second period, S_1 = 1.02 g, and site class = C.

The sub-assemblage considered for analysis spans two interior bays of a typical perimeter moment frame. An inflection point is assumed at mid-story height and thus only half the length of the columns is modeled, with pin conditions assumed at their ends. The middle column is assumed to run the full story height, with its top end restrained against all motion except vertical displacement, which is prescribed. To account for the out-of-plane pulling effect that a transverse gravity beam might impose, the transverse beam is modeled and it is assumed pinned at its far end (Fig. 3.10). This beam represents a typical gravity system beam and is connected to the moment frame by a shear connection. Transverse beams in the gravity system are W21×55 and are the same for all the stories considered here. To further investigate the influence of out-of-plane action, other configurations in which the transverse beam is not modeled are also considered. In these models, the column member is shortened to a stub that protrudes just above the beams and the top of the column stub is only allowed to move downwards (Fig. 3.11).

Jin and El-Tawil (2005) had used reduction in the reduced beam section region that ranged from 40% to 50% in their connections. In this study, however, the reduction is taken as 40 percent for the 3 sub-assemblages in order to minimize variables and promote clearer trends in the results. To study the influence of the reduced beam section on behavior, identical sub-assemblages are considered in which the connection regions are not radius cut, but have the full beam section instead. Although these non-RBS sub-assemblages do not strictly satisfy seismic design criteria (e.g. they do not satisfy strong-column-weak-beam criteria), they are intended to shed light – in a qualitative manner – on how the RBS detail influences connection response in comparison with a non-RBS detail.

Square cut shear tabs for these connections are designed per FEMA 350 requirements and are connected to the column flanges by complete joint penetration welds and to the beams through fillet welds. The shear tab welds as well as the complete joint penetration welds joining the beam and column flanges are modeled using rigid point to surface constraints. Since the heat affected zone (HAZ) near the welds can significantly alter local material properties resulting in a local reduction in ductility, the HAZ effect is considered by locally reducing the nucleation strain in the HAZ region for some of the analyses as described later on.

Finite element models of the sub-assemblages consist of fully integrated shell elements. Two different material models are used as shown in Figure 3.12. Connection regions where fracture is likely to occur are assumed to follow the Gurson model. Other regions are modeled with a computationally less expensive piecewise linear J_2 plasticity model. The hardening curve used for this model is the same as that used for the Gurson model. Failure in finite elements characterized by the Gurson model is assumed to occur when failure void volume fraction f_F is achieved. Finite elements that achieve this ratio are removed from the analysis thus allowing fracture initiation and propagation to be modeled. Prescribed displacements are imposed on the top of the center column such that it undergoes a vertical displacement of 100 inches in 2 sec.

The developed finite element models are used to investigate the influence of the following parameters on connection catenary response: (1) out-of-plane pulling action imposed by the transverse beam; (2) reduced beam section versus no reduction in beam flange; (3) yield stress to ultimate stress (YUSR) ratio; (4) beam web connection detail; and (5) and reduction of ductility in the HAZ region. To facilitate referral to various configurations, beam-column models are designated as S-X-RBS-T. In this notation, X is the story number (1, 5 or 7), RBS indicates that the sub-assemblage has a reduced beam section (RBS), while T indicates that the transverse beam is present. For example, S-1-RBS-T represents a 1st story sub-assemblage with reduced beam section and in which the transverse beam is modeled, while S-1 represents 1st story sub-assemblage without reduced beam section and without a transverse beam.

3.4 Model Limitations

The simulation model, as described above, has a number of limitations. First, the model is deterministic, i.e. variability of material and geometric properties are not accounted for. Second, welds are modeled using rigid point to surface constraints, i.e. yielding and subsequent fracture is assumed to occur outside of the weld region. This assumption is deemed reasonable given the current stringent requirements on weld quality control. Third and perhaps most importantly, the Gurson model is used in conjunction with shell elements, which cannot capture triaxial effects. The Gurson model is utilized nevertheless because it represents steel material behavior in a convenient and logical manner, i.e. the model hardens in compression, represents the associated hardening and softening that occurs in tension and captures ductile fracture. Moreover, the influence of triaxiality on connection response is felt to be small because regions outside of the welds where failure will probably initiate (e.g. root of access hole, RBS flange, and shear tab) do not typically have high triaxial constraint. Another important simulation assumption is that the fracture process is ductile fracture propagation and there is no transition from ductile to inter-granular fracture or ductile to cleavage fracture.

3.5 Discussion of simulation results

Explicit dynamic analyses of the above-described finite element models were conducted to investigate catenary action. Copious results were generated and the important results describing the overall global response of the sub-assemblages are shown in Fig 3.17. to Fig. 3.28 and are also discussed next. The behavior of the sub-assemblages is characterized by the following global performance indicators: failure load, P_{Fail}; failure displacement, Δ_{Fail}, where P_{Fail} is the peak load on the top-load vs displacement curve and Δ_{Fail} is the corresponding displacement; total connection rotation, θ, computed from Δ_{Fail} divided by the column center-to-center distance, i.e. 30 ft. The total column rotation, θ_c, and beam end rotations, θ_{b1} and θ_{b2}, are measured at the beam plastic hinge locations as shown in Figure 3.13. The plastic components of θ_c, θ_{b1} and θ_{b1}, i.e. θ_{cp}, θ_{bp1}, and θ_{bp2}, respectively, which are important performance indicators are also

computed. Panel zone distortions at peak loads are small and are not computed. Table 3.2 summarizes the pertinent parameters calculated from the simulation results.

3.5.1 Inelastic Behavior and Failure Characteristics

All of the sub-assemblages deformed in a ductile manner and developed substantial catenary forces prior to failure. The spread of inelasticity in the beams was concentrated in the plastic hinge regions, although the plastic moment capacity was not reached in some cases because of premature instability. Instability in RBS subassemblies was manifested through local buckling of the beam compression flanges and web in the RBS region. The magnitude of local bucking was smallest in the 1st floor beams and was most severe for 7th story beams. The local buckling was accompanied by lateral torsional buckling, which was small in the 1st story, moderate in the 5th story and severe in the 7th story subassemblies. These instabilities developed early in the loading regime when loads were transferred by flexure in the beams. The growth of local and global instabilities was arrested shortly after catenary action started to pick up.

Local buckling in the beams was also observed in non-RBS sub-assemblages. However, unlike RBS subassemblies, there was insignificant lateral torsional buckling in these configurations. In all subassemblies, plastic hinges formed in the columns just above the panel zone region whereas little inelastic action was observed in the panel zones.

Table 3.2 lists the force and deformation characteristics of all the sub-assemblages. Failure initiated in one of the middle connections in all specimens except the sub-assemblages indicated in the table, where failure initiated in one of the exterior connections. In RBS sub-assemblages, ductile fracture first initiated at the shear tab interface with the column flange. Additional fracture occurred in the vicinity of the access hole then propagated through the web into the RBS flange, severing it at its narrowest point (Fig. 3.14). As in RBS connections, initial fracture in non-RBS sub-assemblages first occurred at the shear tab interface with the column flange. Unlike RBS sub-assemblages, however, final failure occurred as a result of fracture in the beam flange

in near the column face and then propagating through the beam flange, completely severing it (Fig. 3.15). No fractures were observed in the transverse beam in all cases.

3.5.2 Deformation Capacity and Catenary Action

It is clear from Table 3.2 and Figures 3.17(a) to 3.28(a) that deeper beams are substantially less ductile than shallower beams. For example, $\theta_{b2} = 0.076$-rad for S-1-RBS, 0.122-rad for S-5-RBS and 0.171-rad for S-7-RBS. Another observation is that RBS subassemblages show somewhat more ductile response with inelasticity spreading in larger regions as compared to subassemblies without RBS where most of the inelastic action is confined in small regions near the beam ends. In addition, RBS subassemblies have higher load capacity. For example, S-1-RBS-T has a failure displacement and load capacity that is 30% and 10% greater than those for S-1-T, respectively.

RBS subassemblies achieved plastic rotations that are much larger than the permitted plastic rotation of 0.035-rad in GSA (2003). The same can be said of the non-RBS connections, which achieved plastic rotations ranging from 0.053-rad to 0.144-rad compared to 0.020-rad permitted in GSA (2003). However, this apparently high ductility is quite sensitive to the yield-to-ultimate stress ratio and web connection detail as discussed later on.

Figures 3.17(b) to 3.28(b) shows how the catenary forces developed versus displacement in sub-assemblages. Peak catenary forces are quite large, reaching 750 Kips, 584 Kips and 424 Kips for S-1-RBS-T, S-5-RBS-T and S-7-RBS-T configurations, respectively. The catenary forces developed are significantly larger than the peripheral tie force capacity required according to the UFC (2005) provisions, which is only 197 Kips for this case.

3.5.3 Effect of Transverse Beam

As shown in Table 3.2, the majority of sub-assemblages with a transverse beam did not have substantially different strength or ductility compared to corresponding

subassemblies without it. The greatest effect is observed when comparing S-7-RBS with S-7-RBS-T. In this case, the failure displacement and load capacity are increased by 8% and 14% respectively when the transverse beam is modeled. The presence of a transverse beam pulling the configuration out of plane promoted some additional lateral torsional buckling in the 7th story configuration compared to cases with no transverse beam. However, S-7-RBS-T was able to carry a higher load in spite of the increased buckling because of the participation of the transverse beam, which has increased influence in this case.

3.5.4 Effect of YUSR, HAZ and Web Connection Detail

The effect of the YUSR ratio was studied by modifying the hardening curves for the Gurson and linear piecewise plasticity models. The three different YUSR used in this study are 0.67, 0.85 and 0.97. The 0.67 ratio represents regular A572-Gr50 steel. The 0.85 ratio corresponds to the maximum limit imposed on ASTM A992 steel, which is required for special moment resisting frames (AISC Seismic 2005). The 0.97 ratio corresponds to a reasonable maximum limit on dual certified Gr. 50 steel (Frank 1997). The assumed hardening curves are shown in Figure 3.29, where the yield strength is fixed, while the ultimate strength is varied to achieve the target YUSR.

Figure 3.30 quantifies the effect of YUSR on the performance of S-1-RBS-T. It is clear from the figure that a high YUSR adversely influences both failure displacement and load capacity of the sub-assemblage and that the effect is substantial. For example, when YUSR = 0.85, the failure displacement and load capacity were 30% and 29% lower, respectively, than the corresponding values for the case where YUSR = 0.67.

The influence of the HAZ in the beam flanges is studied in sub-assemblage S-1-RBS-T and S-1-T by reducing the ductility of the constitutive model in the HAZ. The inherent brittleness in the HAZ is represented by reducing the nucleation strain from 0.4 to 0.2 in a single row of finite elements in the beam flanges near the column face. This results in approximately a 50% reduction in the ductile fracture strain. Simulation results showed that the failure displacement and load capacity remain virtually unaltered for these cases,

and thus the local reduction in ductility within the HAZ does not appear to influence the global response of the sub-assemblages studied.

The web connection detail seems to play an important role because fracture first initiates at the shear tab edge prior to propagating to the rest of the connection. Therefore, it was surmised that improving the web connection could likely improve the response of the sub-assemblage. To investigate this premise, two variations of configuration S-1-RBS-T were considered. In the first, the shear tab thickness was increased from 0.375 inches to 1.0 inches, whereas in the second, the beam web was assumed to be connected to the column through full penetration groove welds. The results of both simulations are shown in Fig. 3.31 and Fig. 3.32 along with the response of the original configuration. In both cases, the stronger web connection shifted fracture initiation to the RBS region, resulting in a substantially stronger and more ductile connection.

3.6 Practical Implications

A number of conclusions with practical implications can be drawn from the simulation studies conducted. Analysis of the data shows that the out-of-plane pulling action imposed by a transverse beam does not significantly influence sub-assemblage structural behavior. The results suggest that it is conservative to conduct simulations and tests that do not model the out-of-plane pulling effect, which considerably simplifies testing and analysis.

Another observation is that system ductility is adversely influenced by an increase in beam depth and an increase in the yield to ultimate strength ratio. This implies that designers should strive to use a larger number of smaller beam members rather than concentrate resistance in a few larger members, which is common practice in earthquake-resistant construction. In addition, designers should specify ASTM A-992 steel (which has a specified maximum YUSR of 0.85) for collapse resistant construction rather than specifying generic steels which could have a detrimentally high YUSR. The simulation results further suggest that improving the beam web connection by either increasing the

shear tab thickness or directly welding the beam web to the column can better protect the beam-column interface by shifting ductile fracture initiation to the reduced flange region thereby making the connection stronger and more ductile.

Together, the latter two conclusions could be construed to imply that the combined effect of a relatively high YUSR and a relatively weak shear tab could be detrimental to the ability of moment resisting connections to adequately develop catenary action. In particular, connections with bolted shear tabs and steels with YUSR > 0.85 could be vulnerable. Bolted shear tabs are substantially weaker than corresponding welded shear tabs because they are susceptible to bolt failure or net section fracture through the bolt holes.

3.7 Summary and Conclusions

In this chapter, computational simulation is used to investigate catenary action in moment resisting steel subassemblages. The numerical simulations employed a calibrated micromechanical constitutive model for steel that accounts for hardening, softening and ductile fracture behavior of steel. After mesh sensitivity studies and a validation exercise, the simulation model was used to investigate the catenary behavior of a number of steel subassemblies taken from a seismically designed special moment frame. Important parameters that influence behavior were identified and studied.

The simulation results demonstrate the ductility of seismically designed special moment frame assemblies and their ability to deform in catenary mode. Simulation results also established that the out-of-plane pulling action induced by transverse beams has no adverse effect on system behavior, but that ductility and strength were adversely influenced by an increase in beam depth and an increase in the yield to ultimate strength ratio. It was also seen that subassemblies with reduced beam sections are somewhat stronger and more ductile than corresponding assemblies without RBS. Furthermore, the heat affected zone in beam flanges did not have a significant deleterious influence on system behavior while an increase in shear tab strength shifted the location of ductile

fracture resulting in better overall system behavior. The above conclusions were drawn from a limited number of simulations and therefore testing and additional detailed studies are needed to confirm and extrapolate them.

The study presented in this chapter is focused on the capacity side of progressive collapse issue. A complete study of collapse issues requires an investigation of the demand side as well. The demand side of the progressive collapse issue is investigated in the next chapter, with an emphasis on the development of reliable and computationally tractable structural scale models that can be used by practicing engineers for collapse-resistant performance-based design.

q_1	1.5	S_N	0.1
q_2	1	f_F	0.1
f_c	0.09	σ_y	58 Ksi
ε_N	Element Size(in)		ε_N
	0.125		0.58
	0.5		0.40

Table 3.1 Gurson model parameters

Model Configuration	P_{Fail} **(Kips)**	Δ_{Fail} **(in)**	θ **(Radians)**	θ_{cp} **(Radians)**	θ_{bp1} **(Radians)**	θ_{bp2} **(Radians)**
S-1-RBS-T	370	27.6	0.08	0.006	0.072	0.078
S-5-RBS-T	356	47.6	0.13	0.039	0.083	0.121
S-7-RBS-T	305	74.0	0.21	0.114	0.064	0.178
S-1-RBS	366	29.5	0.08	0.006	0.070*	0.076
S-5-RBS	340	46.9	0.13	0.036	0.085	0.122
S-7-RBS	266	68.5	0.19	0.095	0.076	0.171
S-1-T	335	22.8	0.06	0.007	0.049*	0.055
S-5-T	319	40.2	0.11	0.033	0.064	0.097
S-7-T	249	59.1	0.16	0.078	0.063	0.141
S-1	327	22.4	0.06	0.006	0.047*	0.053
S-5	307	39.4	0.11	0.034	0.062	0.096
S-7	244	59.4	0.17	0.080	0.064	0.144

*Failure occurred in exterior connection

Table 3.2 Global connection performance parameters

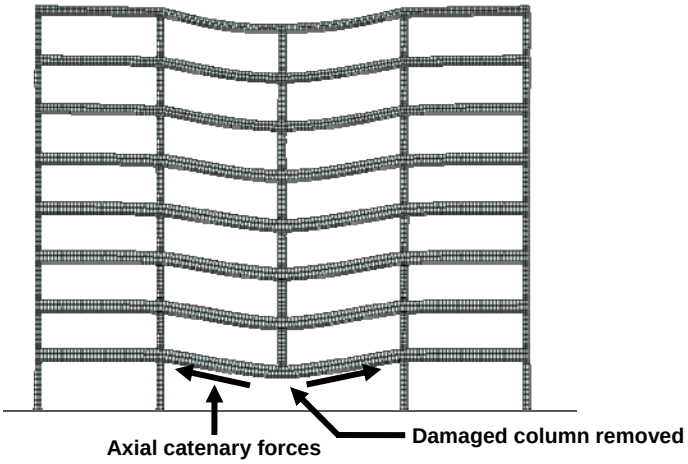

Figure 3.1 Frame system responding to loss of interior column

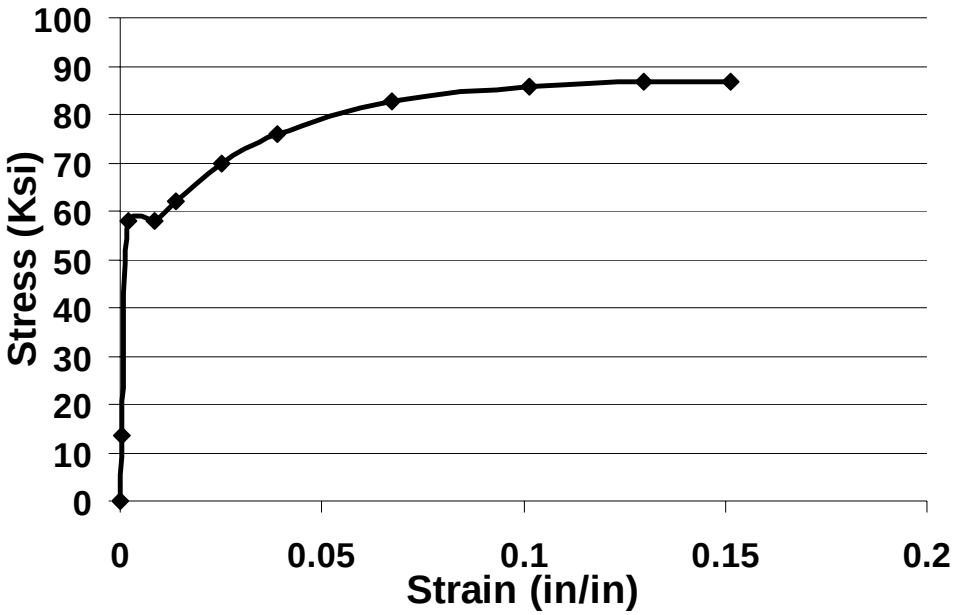

Figure 3.2 Engineering stress vs strain curve for A572 Grade 50 Steel
Kanvinde (2004)

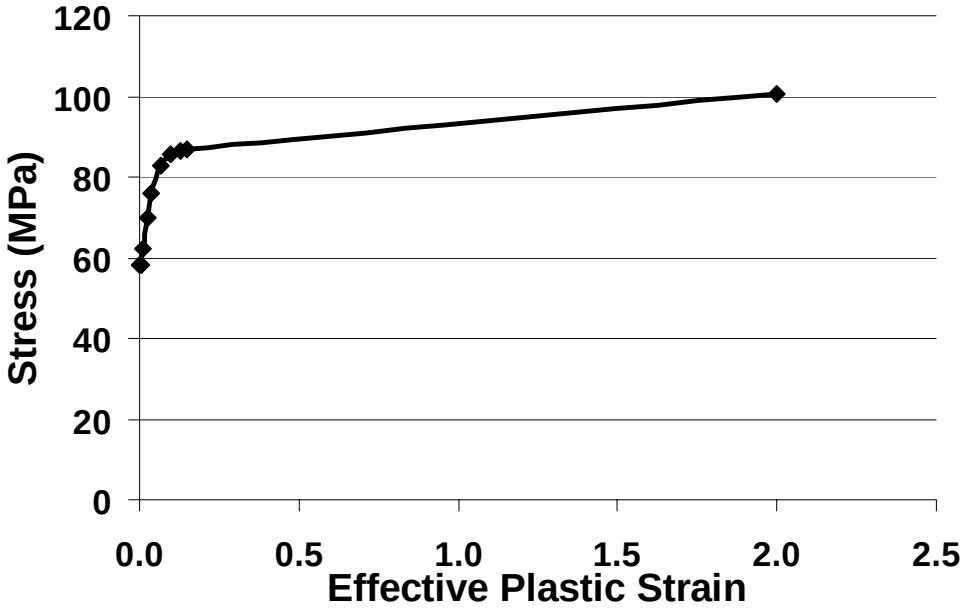

Figure 3.3 Hardening curve for A572 Grade 50 Steel

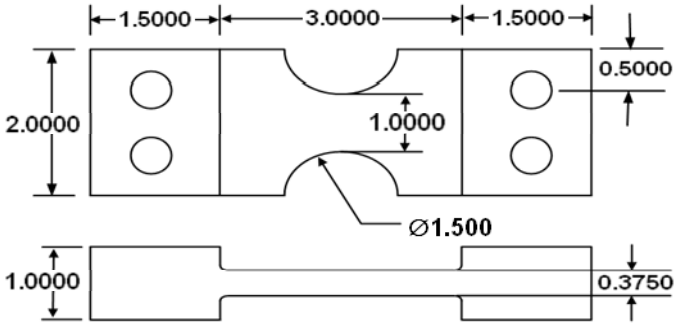

(a) Specimen -1

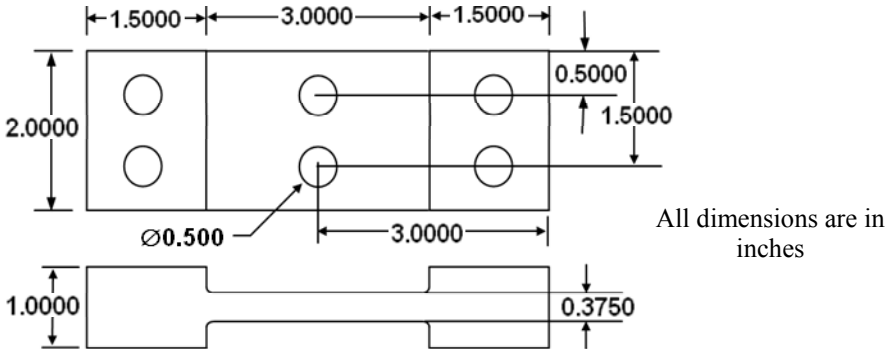

(b) Specimen -2

Figure 3.4 Geometry of steel plates tested by Kanvinde (2004)

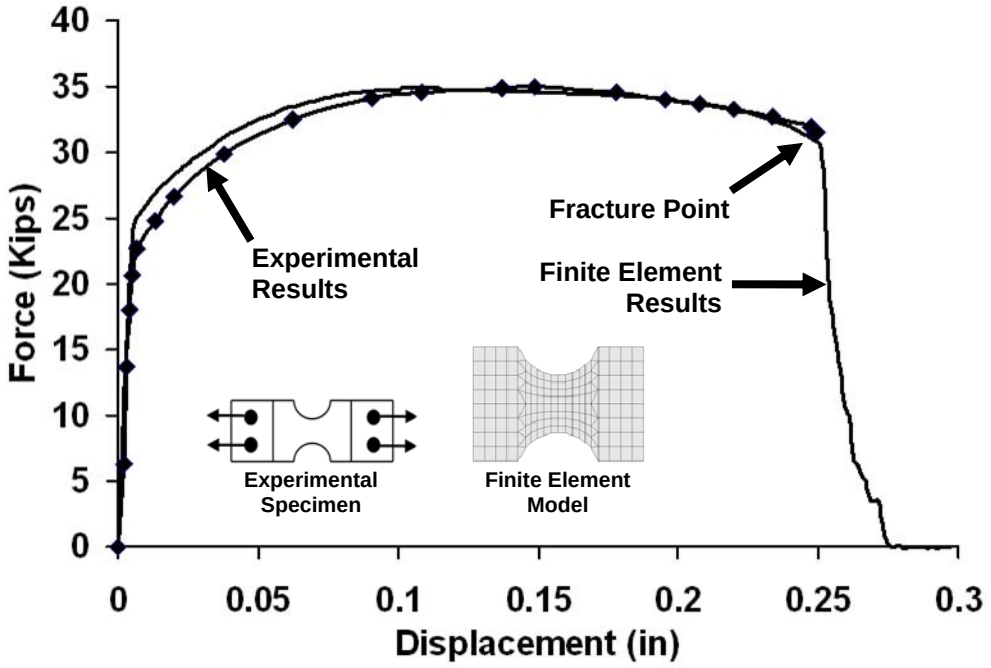

Figure 3.5 Comparison between FEM and experimental results for specimen-1

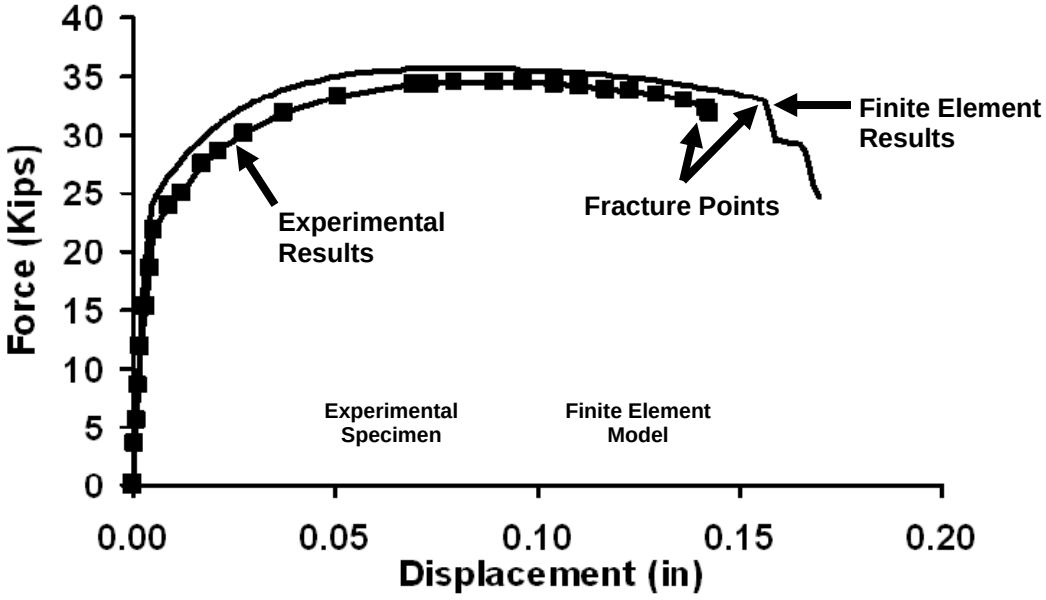

Figure 3.6 Comparison between FEM and experimental results for specimen-2

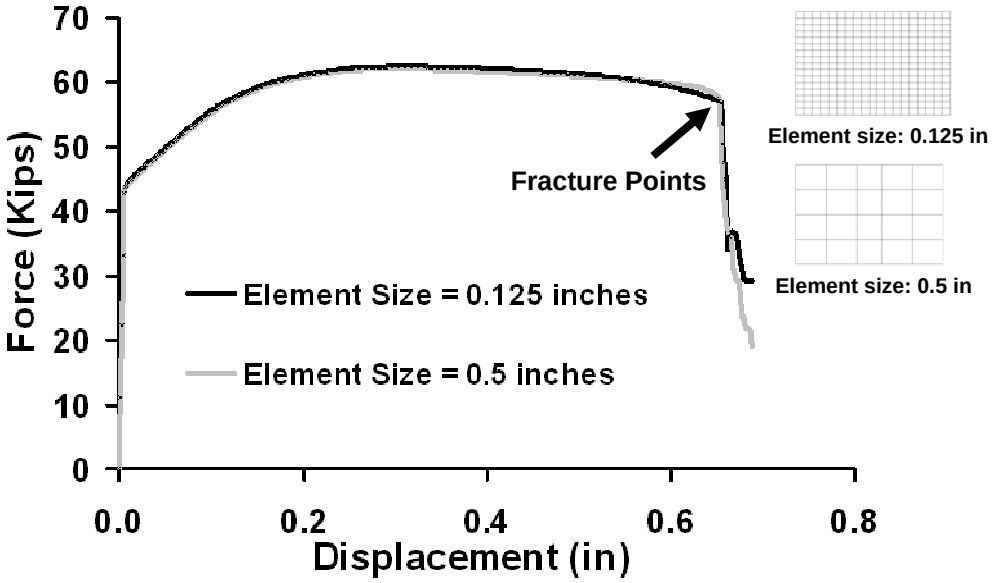

Figure 3.7 Comparison between FEM results for models with different mesh sizes

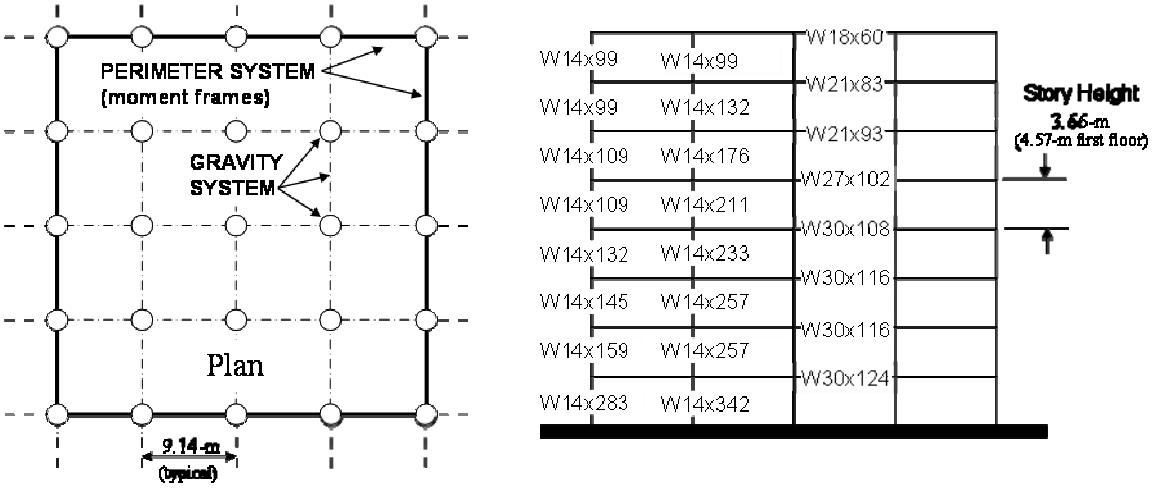

Figure 3.8 Design details of eight stories perimeter moment resisting frames (Jin and El-Tawil 2005)

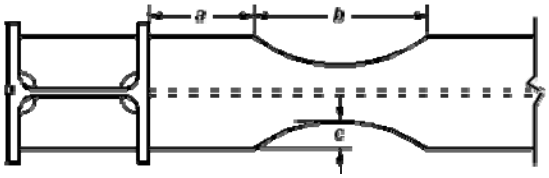

Figure 3.9 Radius cut reduced beam section

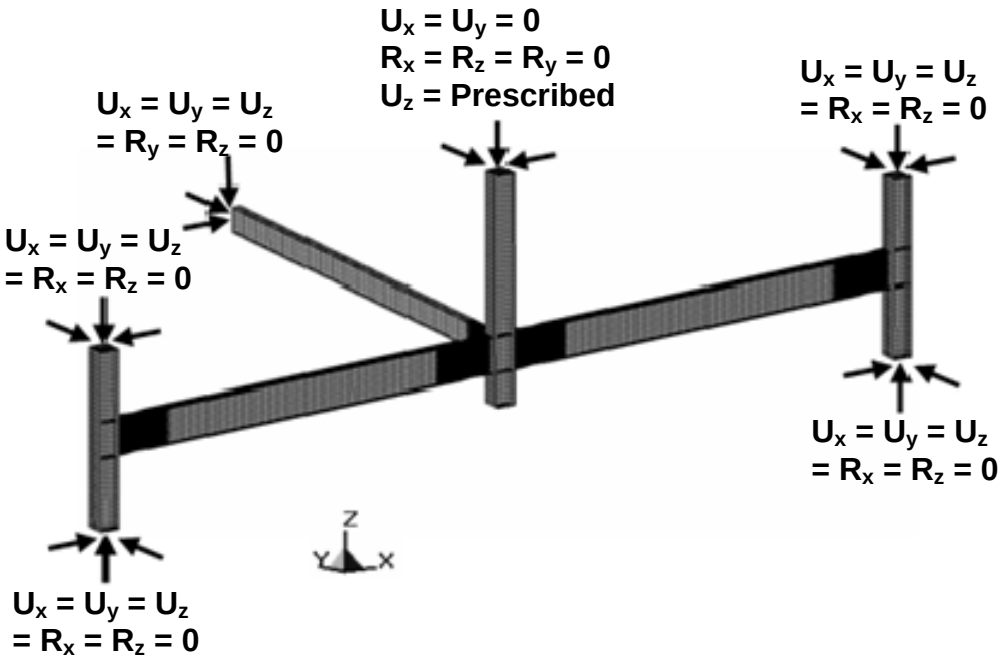

Figure 3.10 Sub-assemblage boundary conditions: Model with transverse beam. U: Displacements, R: Rotations

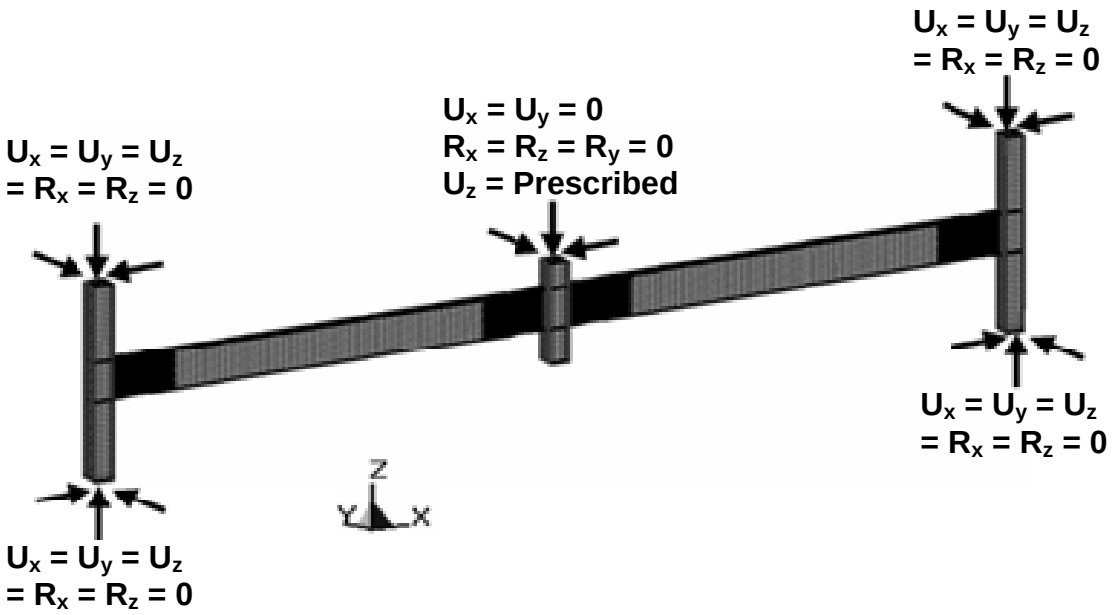

Figure 3.11 Sub-assemblage boundary conditions: Model without transverse beam. U: Displacements, R: Rotations

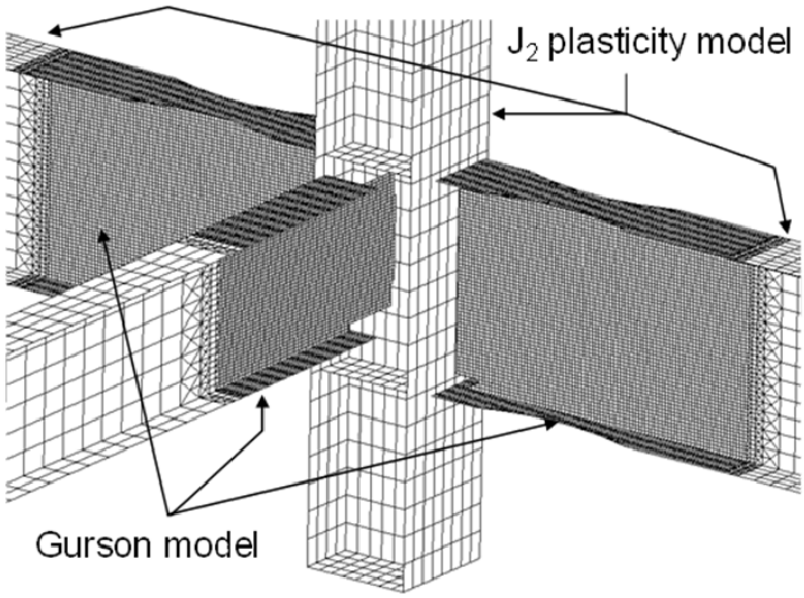

Figure 3.12 Details of finite element mesh and material models in connection region

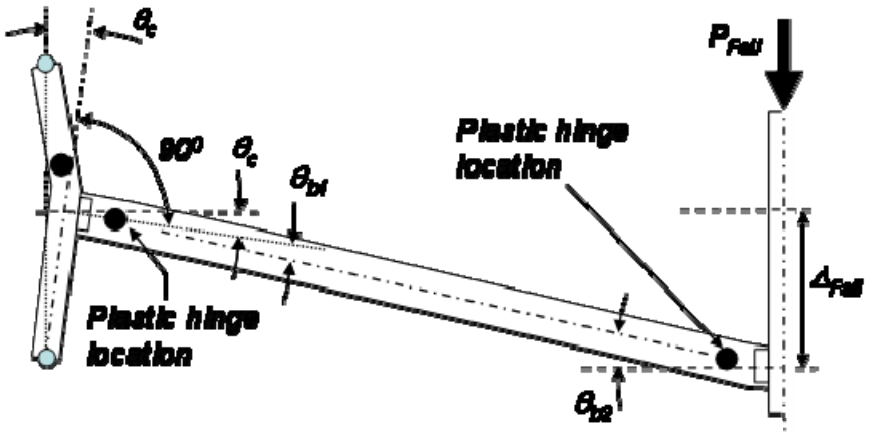

Figure 3.13 Global connection performance parameters (half of symmetric sub-assemblage shown)

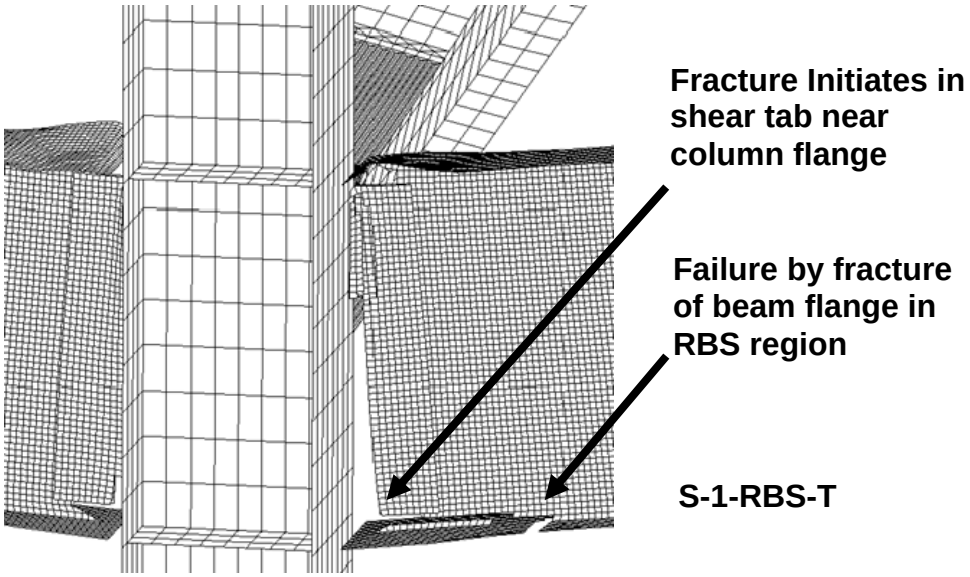

Figure 3.14 Typical failure mode in RBS configurations

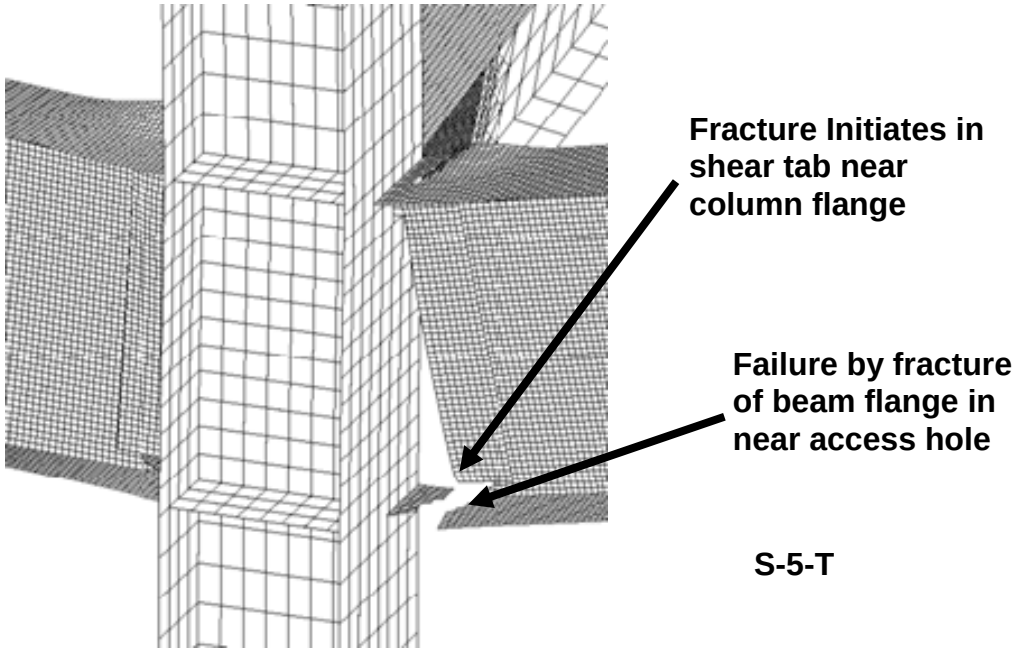

Figure 3.15 Typical failure mode in non-RBS configurations

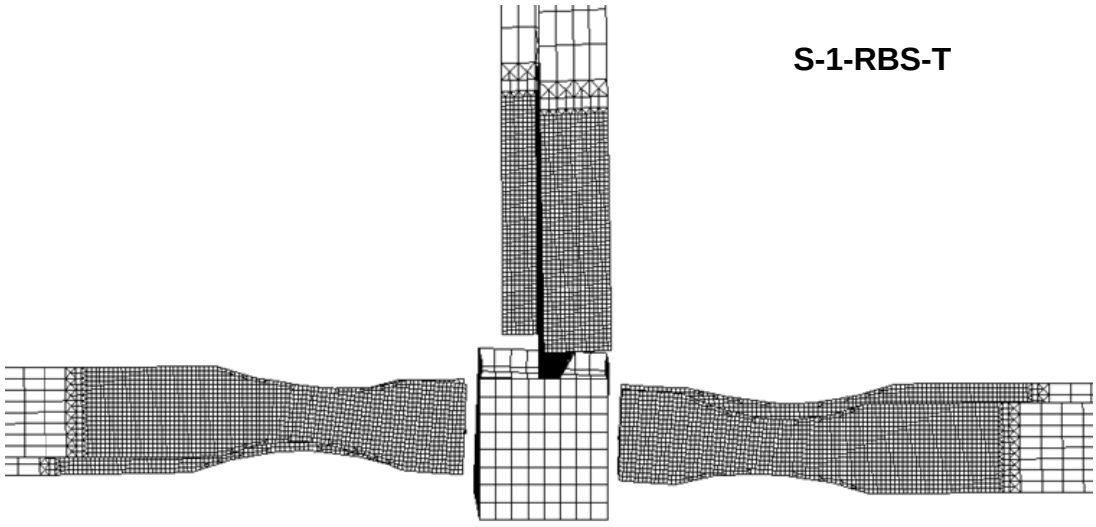

Figure 3.16 Top View: Lateral torsional buckling in beams

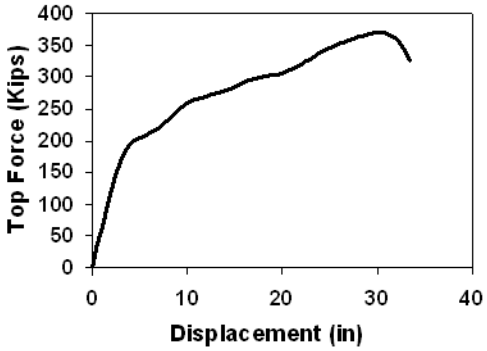

(a) Top Force

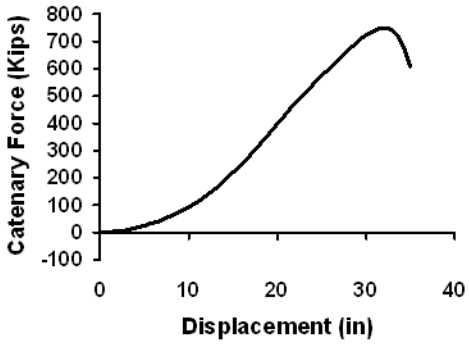

(b) Catenary Force

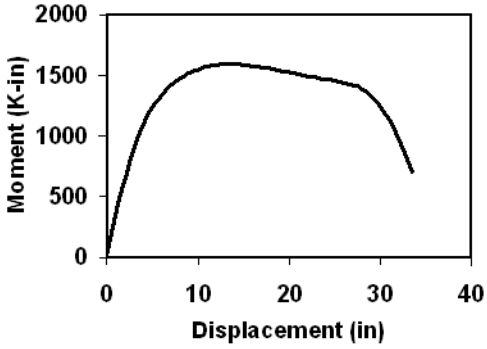

(c) Moment at RBS, interior connection

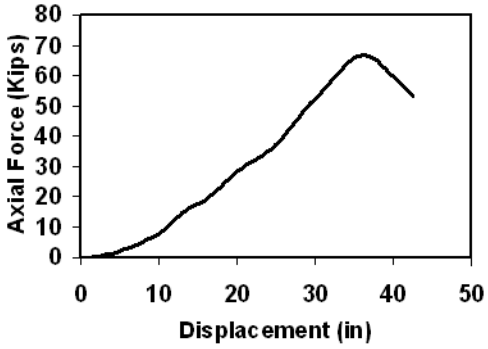

(d) Axial Force: Transverse Beam

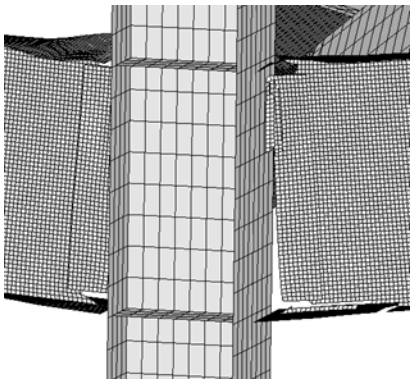

(e) Failure by fracture at interior connection

Figure 3.17 Global response quantities: S-1-RBS-T

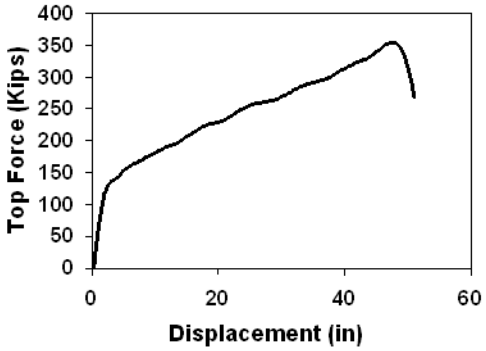

(a) Top Force

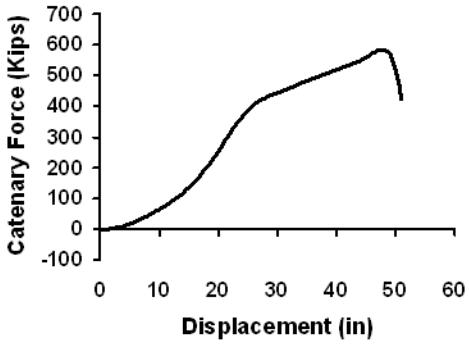

(b) Catenary Force

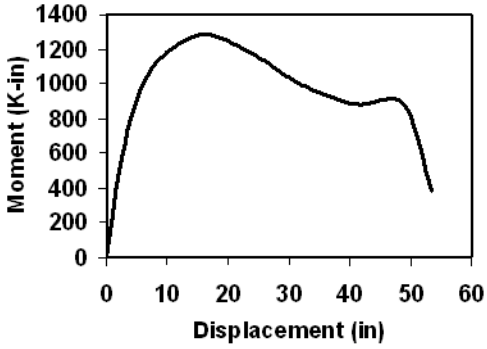

(c) Moment at RBS, interior connection

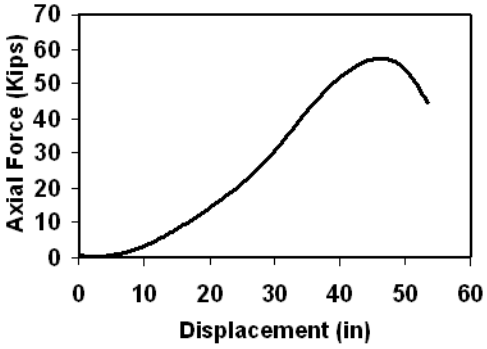

(d) Axial Force: Transverse Beam

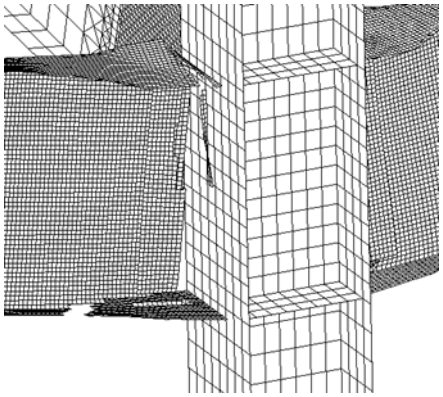

(e) Failure by fracture at interior connection

Figure 3.18 Global response quantities: S-5-RBS-T

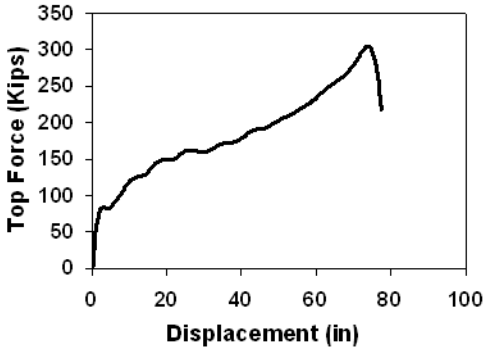

(a) Top Force

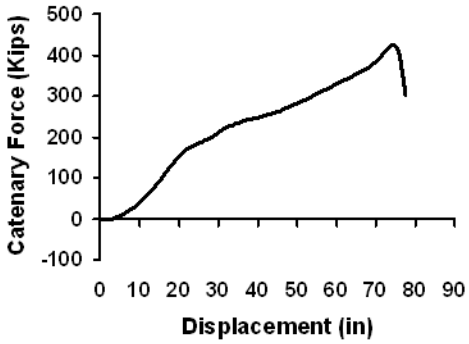

(b) Catenary Force

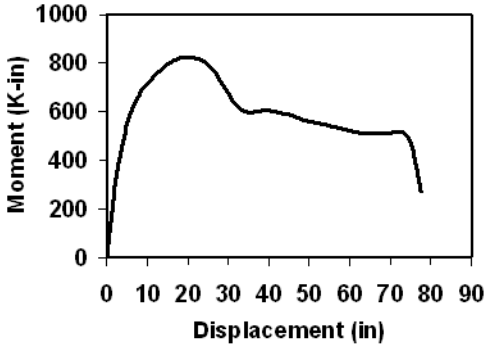

(c) Moment at RBS, interior connection

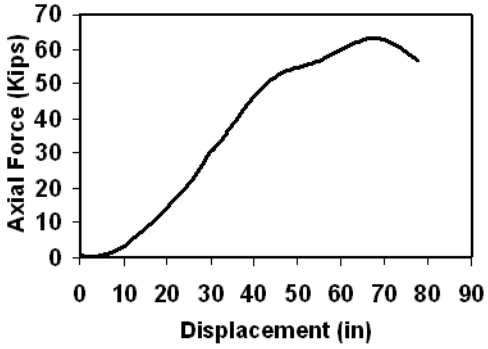

(d) Axial Force: Transverse Beam

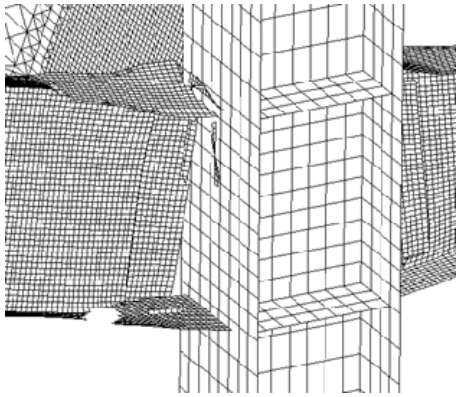

(e) Failure by fracture at interior connection

Figure 3.19 Global response quantities: S-7-RBS-T

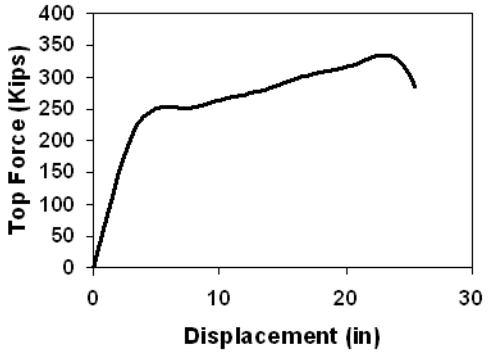

(a) Top Force

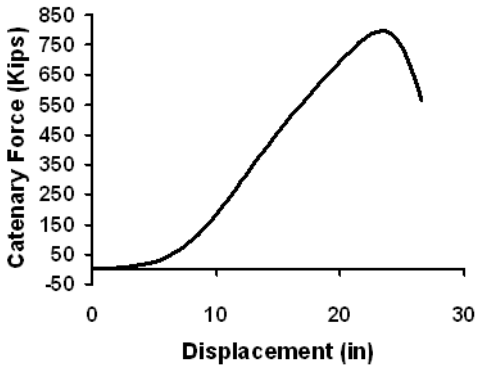

(b) Catenary Force

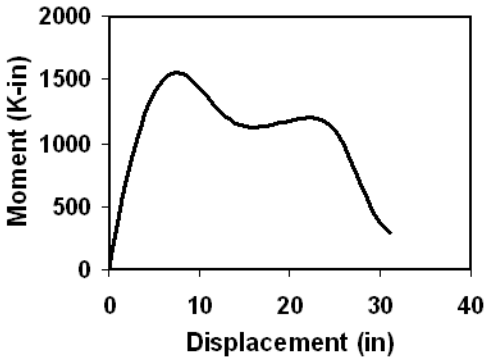

(c) Moment at a distance of $\frac{d}{2}$ (d: depth of beam) from column face, interior connection

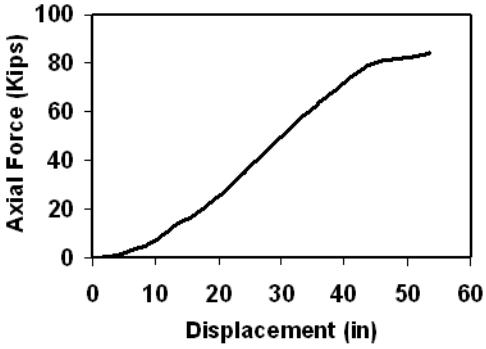

(d) Axial Force: Transverse Beam

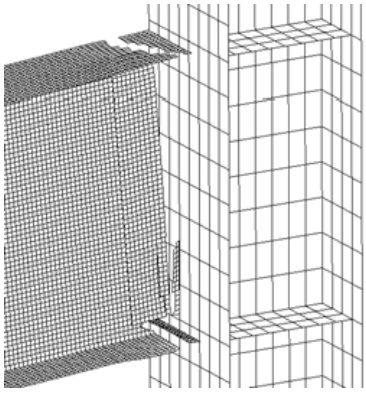

(e) Fracture by failure at exterior connection

Figure 3.20 Global response quantities: S-1-T

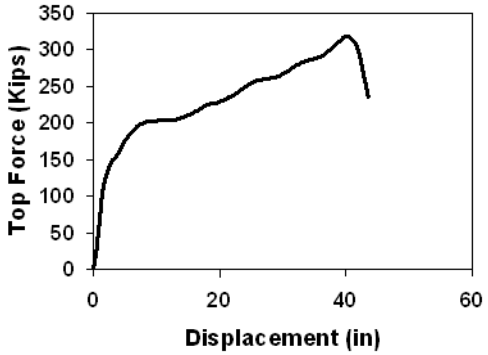

(a) Top Force

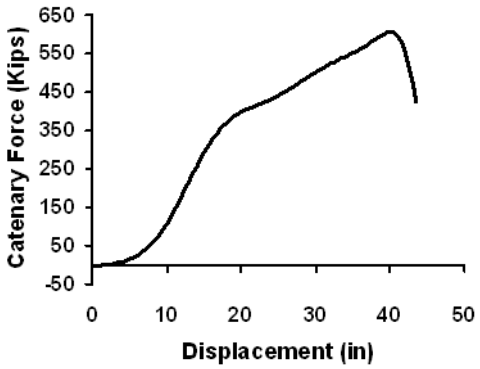

(b) Catenary Force

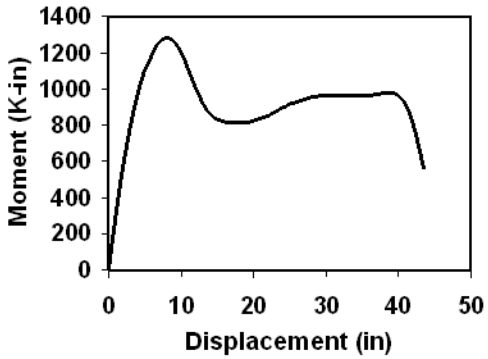

(c) Moment at a distance of $\frac{d}{2}$ (d: depth of beam) from column face, interior connection

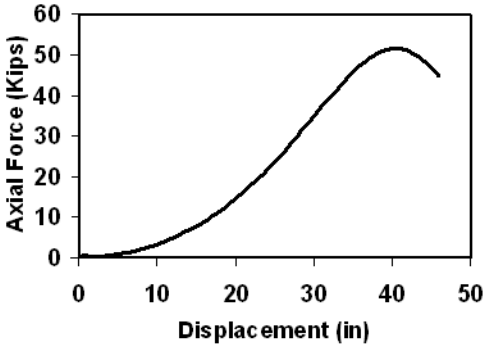

(d) Axial Force: Transverse Beam

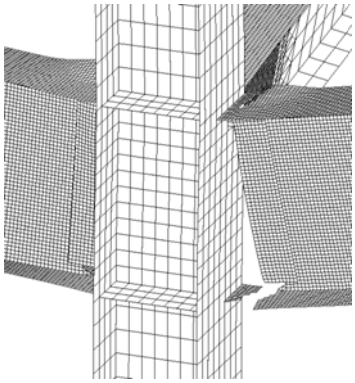

(e) Fracture by failure at interior connection

Figure 3.21 Global response quantities: S-5-T

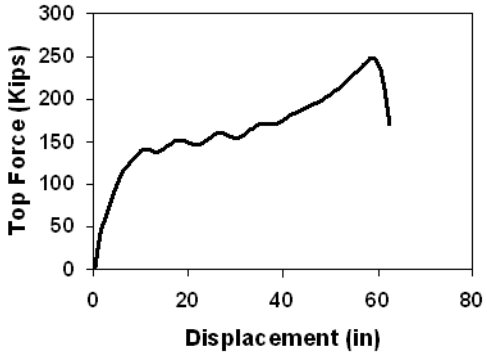

(a) Top Force

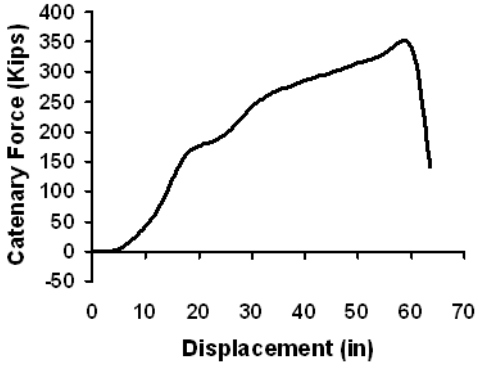

(b) Catenary Force

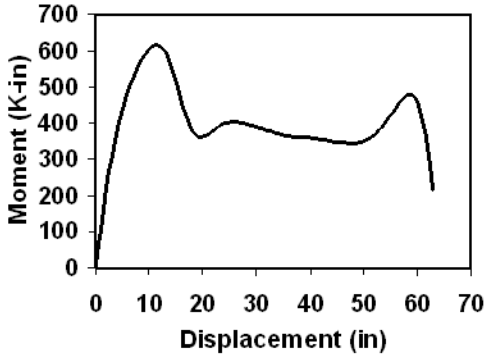

(c) Moment at a distance of $\frac{d}{2}$ (d: depth of beam) from column face, interior connection

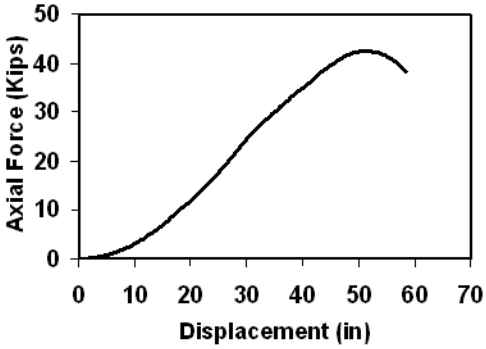

(d) Axial Force: Transverse Beam

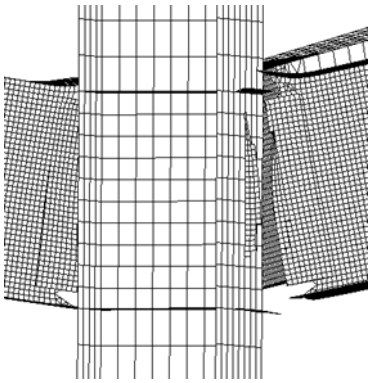

(e) Fracture by failure at interior connection

Figure 3.22 Global response quantities: S-7-T

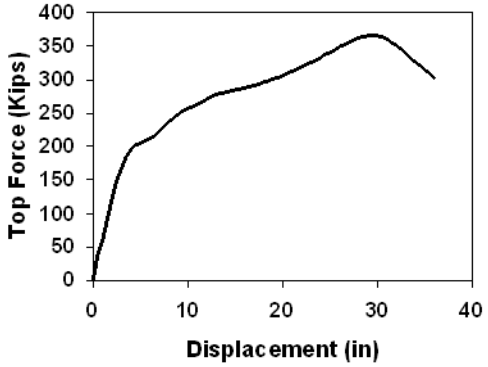

(a) Top Force

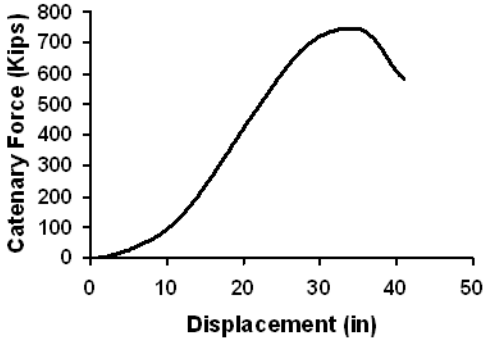

(b) Catenary Force

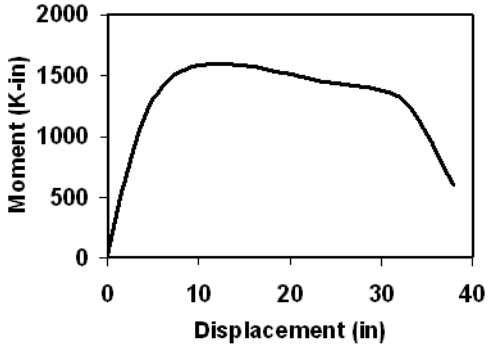

(c) Moment at RBS, interior connection

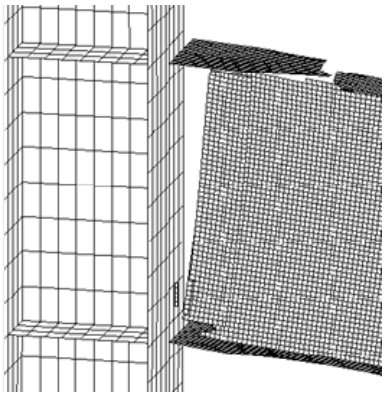

(d) Fracture by failure at exterior connection

Figure 3.23 Global response quantities: S-1-RBS

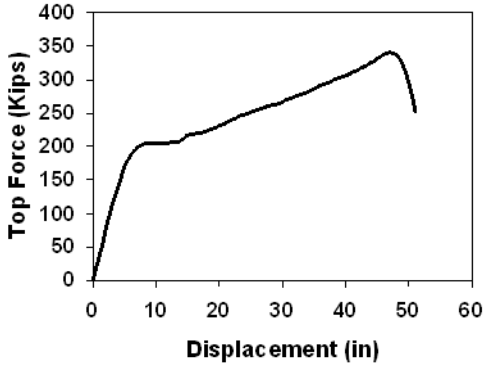

(a) Top Force

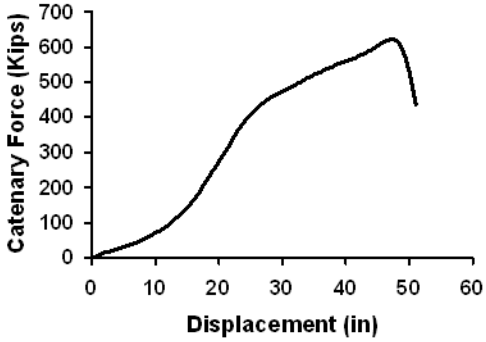

(b) Catenary Force

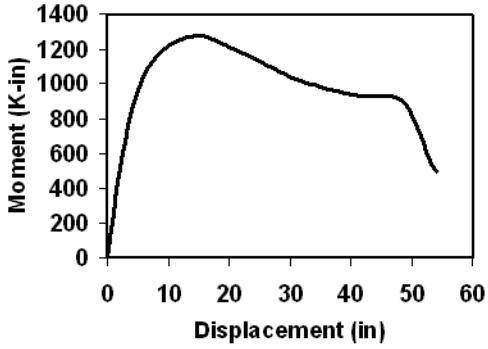

(c) Moment at RBS, interior connection

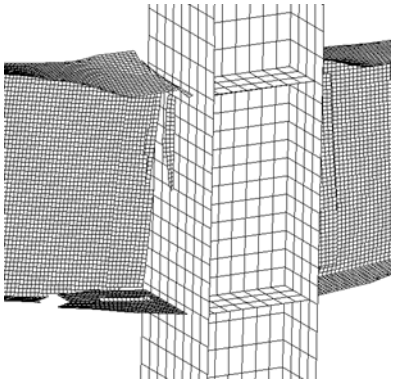

(d) Fracture by failure at interior connection

Figure 3.24 Global response quantities: S-5-RBS

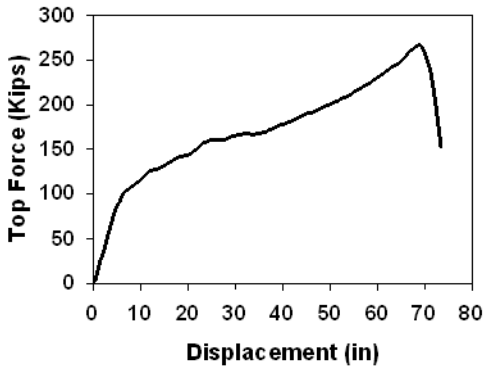

(a) Top Force

(b) Catenary Force

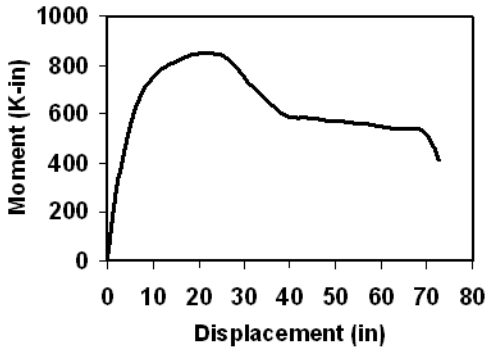

(c) Moment at RBS, interior connection

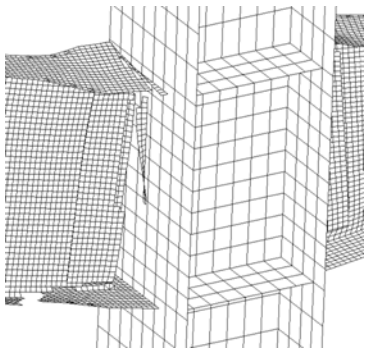

(d) Fracture by failure at interior connection

Figure 3.25 Global response quantities: S-7-RBS

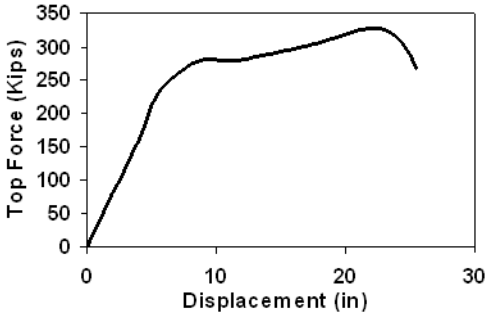

(a) Top Force

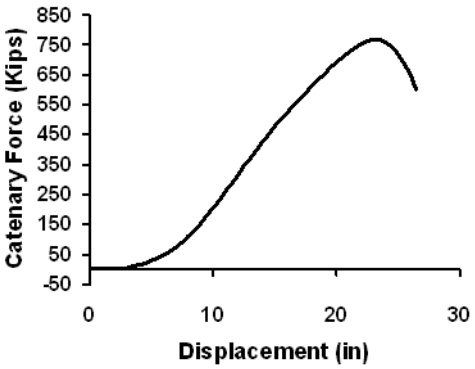

(b) Catenary Force

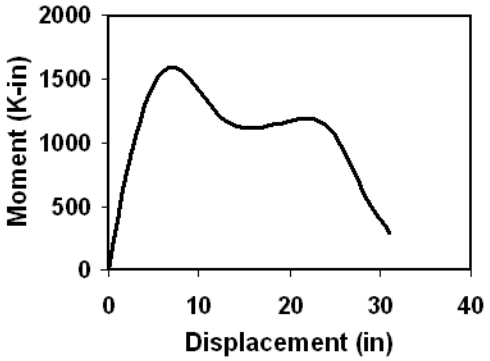

(c) Moment at a distance of $\frac{d}{2}$ (d: depth of beam) from column face, interior connection

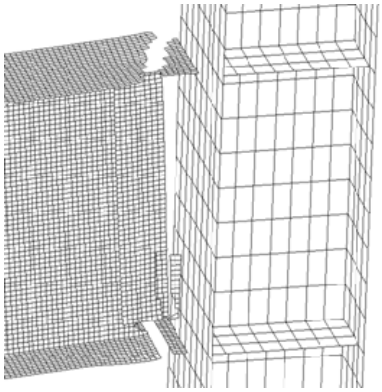

(d) Fracture by failure at exterior connection

Figure 3.26 Global response quantities: S-1

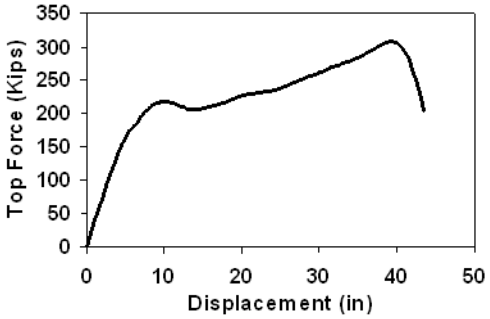

(a) Top Force

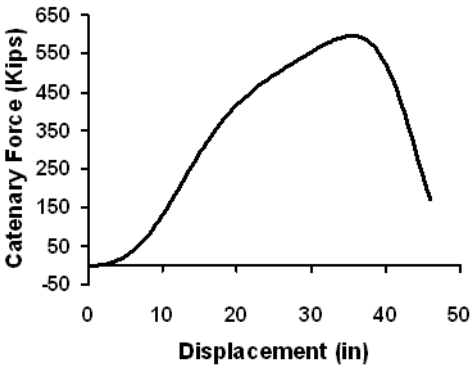

(b) Catenary Force

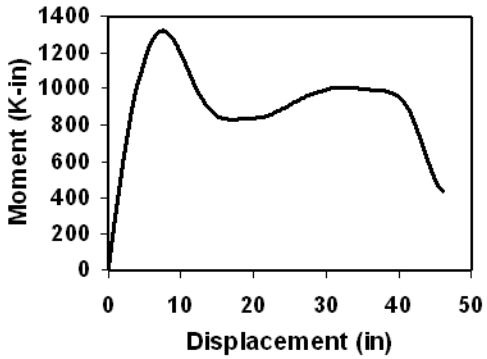

(c) Moment at a distance of $\frac{d}{2}$ (d: depth of beam) from column face, interior connection

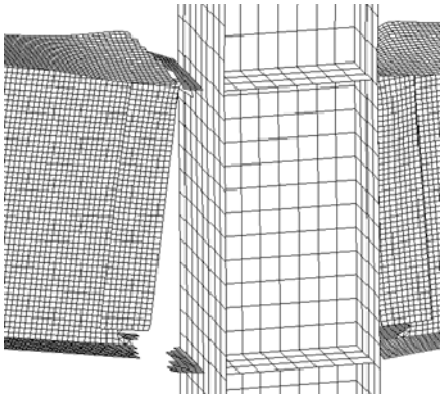

(d) Fracture by failure at interior connection

Figure 3.27 Global response quantities: S-5

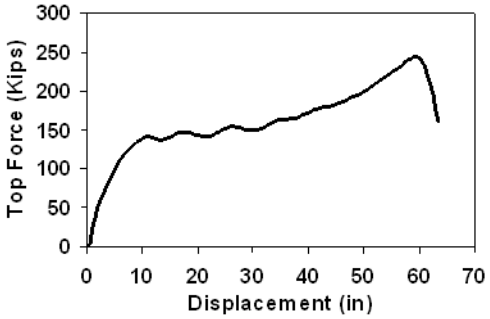

(a) Top Force

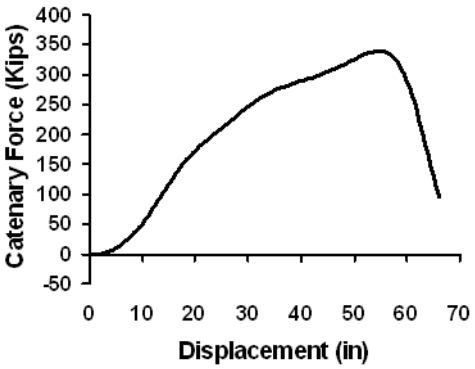

(b) Catenary Force

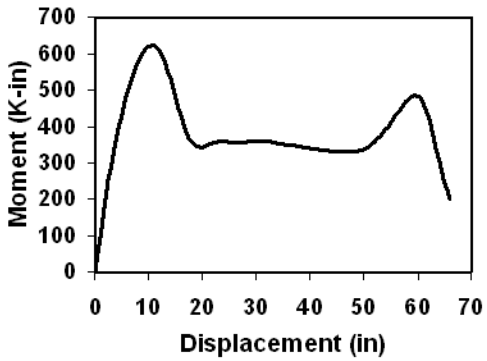

(c) Moment at a distance of $\frac{d}{2}$ (d: depth of beam) from column face, interior connection

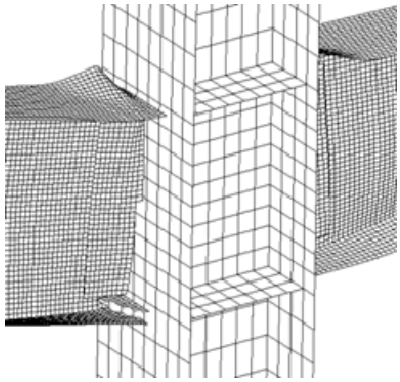

(d) Fracture by failure at interior connection

Figure 3.28 Global response quantities: S-7

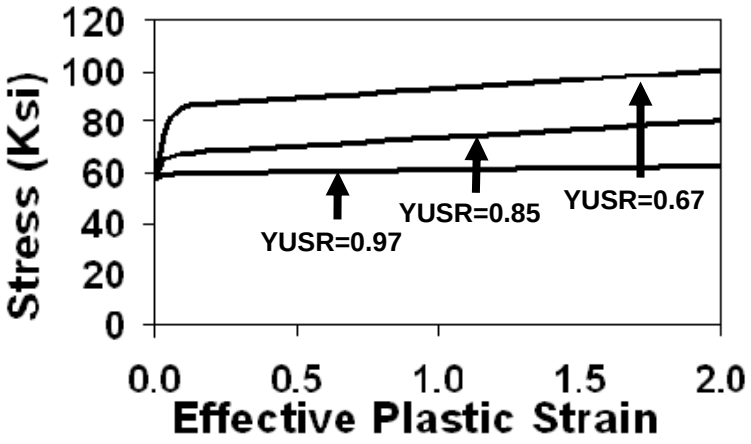

Figure 3.29 Strain hardening curves for steels with different YUSR ratios

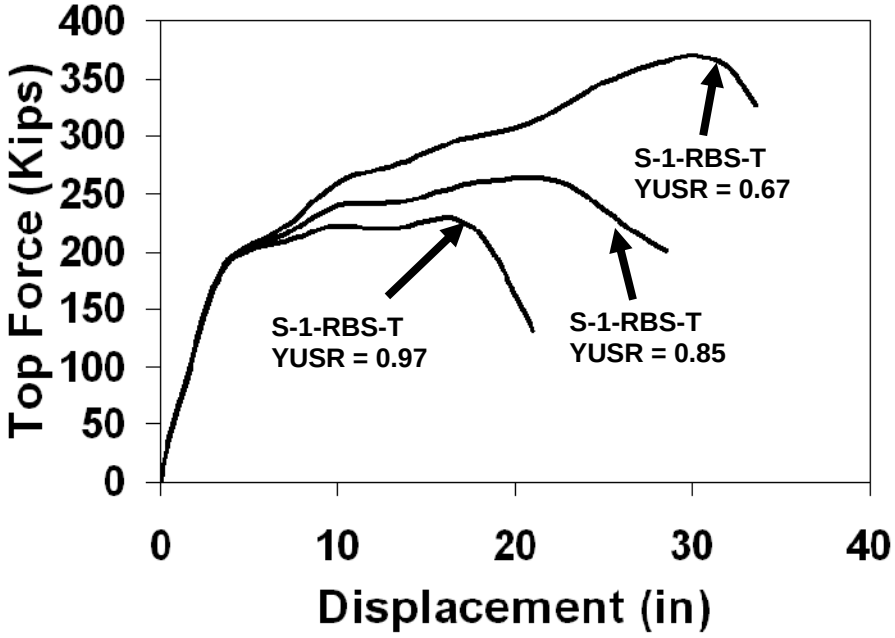

Figure 3.30 Effect of YUSR ratio on the performance of sub-assemblage

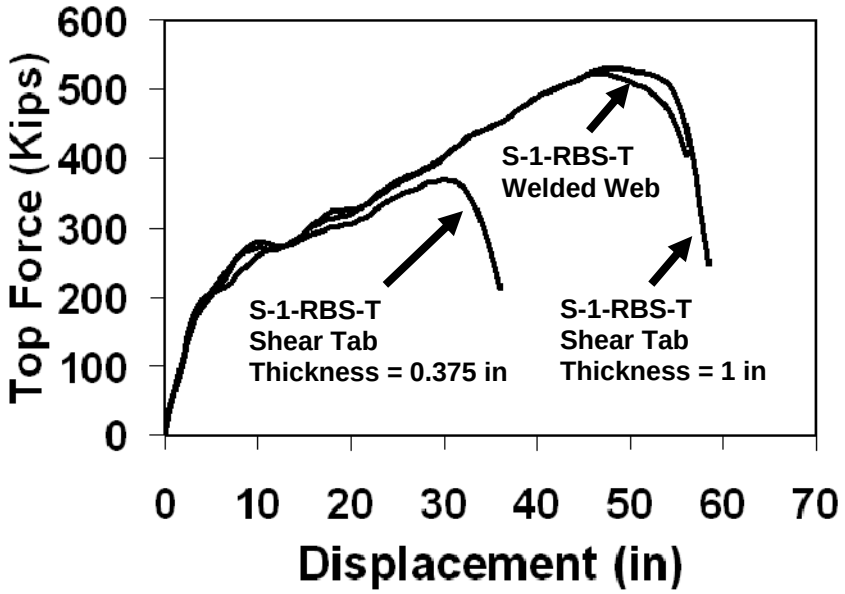

Figure 3.31 Effect of connection detailing on the performance of sub-assemblage

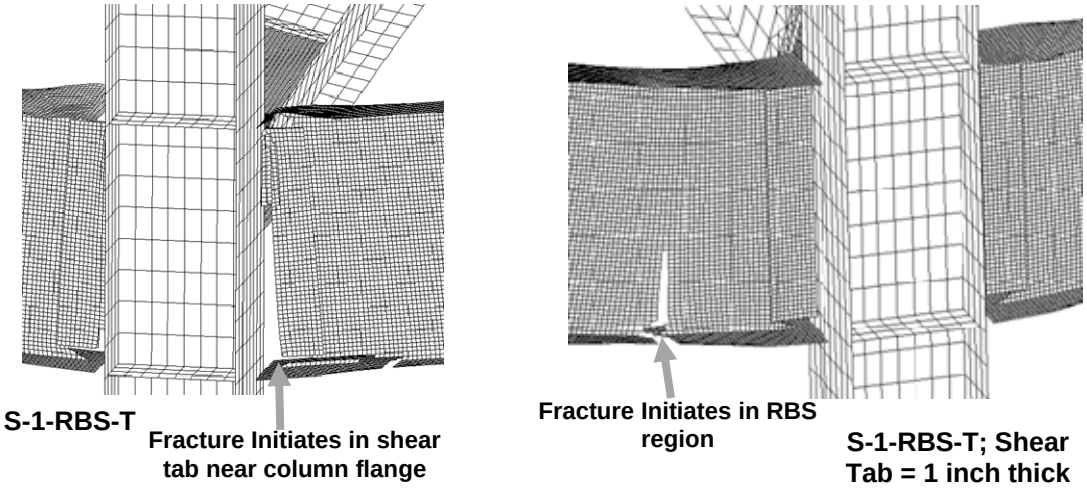

Figure 3.32 Effect of connection detailing on the performance of sub-assemblage: Fracture modes

CHAPTER 4

STRUCTURAL SCALE MODELS FOR PROGRESSIVE COLLAPSE ANALYSIS OF STEEL FRAMES

4.1 Introduction

The alternate path method (APM) advocated by GSA (2003) and UFC (2005) is frequently used to ensure that structural systems have adequate resistance to progressive collapse. When applied in conjunction with nonlinear-dynamic analysis, APM is widely viewed as a comprehensive method for analysis and design of a structural system against progressive collapse. Success of APM, however, depends on the ability of the underlying structural model to represent physical phenomena of interest with high fidelity. This chapter is concerned with the development of structural scale models which enable nonlinear progressive collapse analysis of steel structural systems in a computationally efficient manner. The developed structural scale models are then used in conjunction with the APM to investigate the ability of seismically designed steel frame systems to resist progressive collapse.

The models developed in this study use a combination of beam-column finite elements and nonlinear spring elements to represent important physical processes, such as dynamic load redistribution and global buckling, at the structural scale. Micro-scale behavior such as fracture and local buckling, however, are accounted for by using the appropriate constitutive material properties that are calibrated to the micro-scale studies presented in

Chapter 3 and to available experimental results. Thus, the models developed herein fall in the category of uncoupled multi-scale models, wherein the structural scale models are calibrated to represents important physical processes at lower scales.

Section 4.2 gives an overview of the various structural systems considered in this research work. The design details of prototype structural systems chosen for use in this work are presented in Section 4.3. Section 4.4 and 4.5 describes the proposed structural scale models employed for modeling the prototype structural systems. Section 4.6 gives a brief overview of continuum based beam/column finite element and details of the plasticity model used in this research. Calibration studies of the developed structural-scale models are presented in Section 4.8. The simulation setup, and assumptions and limitations of the simulation model are discussed in Sections 4.9 and 4.10, respectively. Finally, the results from the finite element simulations are discussed in Section 4.11 and 4.12, and important conclusions are presented in Section 4.13.

4.2 Structural Systems and Modeling for collapse

Intermediate moment frames (IMFs) and special moment resisting (SMFs) are commonly used structural steel systems for resisting seismic forces. These systems derive their lateral force resisting capacity from the beam to column joints which are designed as moment connections. IMFs are designed to withstand limited inelastic deformations when subjected to forces resulting from design earthquake motions. However, SMFs are designed to withstand significant inelastic deformations. Inelastic deformations under lateral seismic forces take place in specially designated regions known as “protected zones” or “plastic hinge zones”.

Steel braced frames are also popular structural systems that are commonly used in regions of moderate to high seismic risk. Two important categories of braced systems include: concentrically braced frames (CBF) and eccentrically braced frames (EBF). In CBFs, the steel braces provide lateral strength and stiffness to the structural system and contribute to seismic energy dissipation by yielding in tension and buckling inelastically

in compression. In EBFs, the braces are designed to remain elastic during lateral loading, so that energy dissipation is achieved by inelastic deformations in designated regions termed shear links.

The seismic behavior of IMFs, SMFs, CBFs and EBFs is fairly well understood as a result of extensive research conducted during the past three decades. However, their progressive collapse behavior, when critical members are lost, has not been previously investigated. In this chapter structural scale models are developed for modeling progressive collapse of these steel frames.

Appropriate structural models must be used when the nonlinear version of APM is employed. In particular, the structural models must be able to adequately account for the formation of catenary action and the resulting interaction that occurs between axial tensile loads and moments in beam-column members as shown in Chapter 3. Moreover, models for steel moment frames must also be capable of representing the responses that influence beam-column and connection responses, such as local buckling at the beam-column interface, global buckling and lateral torsional buckling, inelastic panel zone behavior, local flange yielding in reduced beam connections, and connection fracture. Additionally, for braced systems, the structural models must be able to adequately account for buckling and post buckling behavior of braces in EBF and SCBF, and inelastic behavior of shear links in EBF.

The structural scale models presented in this chapter utilize a combination of beam-column and discrete spring finite elements to simulate the overall response of the structure. The success of structural scale models stems from their ability to adequately mimic, in a phenomenological manner, the local and global responses of importance to the physical processes being modeled. Structural scale models are fairly simple to build and run, and are therefore well suited for use in a design office environment. As such, they have been successfully used in the past by many researchers to investigate system response to seismic loading, e.g. Jin et al. (2005) and Rassati et al. (2004). However,

there are only a few instances in the literature where they have been applied to collapse analysis, e.g. Gross et al. (1983), Isobe et al. (2003) and Kaewkulchai et al. (2004).

4.3 PROTOTYPE STRUCTURES

4.3.1 Moment resisting frames

The National Institute of Standards and Technology (NIST) designed prototype steel framed buildings for the purpose of studying their response to an event which may cause progressive collapse (Liang et al., 2006). The buildings are 10-story office buildings with plan dimensions of 150 x 100 ft and utilize moment-resisting frames as the lateral load resisting system. The buildings are designed for: (1) Seismic Design Category C (Atlanta, Georgia), which results in IMFs as defined is the AISC Seismic Provisions (2002), and (2) Seismic Design Category D (Seattle, Washington), which results in SMFs. The two seismic design categories address moderate and high seismic risk, and are considered to study the effectiveness of seismic design and detailing in resisting progressive collapse.

The design loads on the buildings are determined based on the International Building Code (IBC) 2003. The design standards used in the design of members and their connections are those referenced in ASCE 7-02, including the AISC Load and Resistance Factor Design Specifications for Structural Steel Buildings (1999) and the AISC Seismic Provisions for Structural Steel Buildings (2002). For typical floors, the dead load consists of the self-weight of the slab of 46 psf and a super-imposed dead load of 30 psf; while the design live load is assumed to be 100 psf. For the roof, the self-weight of the slab is 46 psf, the super-imposed dead load is 10 psf; and the design live load is 20 psf. The reduction in live loads is based on IBC 1607.9.1.

The building structural system is comprised of moment frames and a gravity system. The design of gravity system is the same for the IMF and SMF buildings. Beams and columns in the gravity system are connected through shear (S) connections, which are comprised of single plate, shear-tab connections that are fillet welded to the column and bolted using

⅞ inch A325 high strength bolts to ⅜ in A36 shear tabs. The IMF building employs welded unreinforced flange – bolted web (WUF-B) moment resisting connections, while the SMF building employs reduced beam section (RBS) connections with bolted webs. To facilitate the modeling exercise, all moment resisting connections are assumed to be welded instead of bolted. A992 structural steel (F_y = 50 ksi) is used for all beams and columns. Furthermore, a 50 percent reduction is assumed in all RBS connections. Plan views of the buildings are shown in Fig. 4.1 and 4.2, while the elevation of the East-West frames considered in this research are shown in Fig. 4.3 and 4.4. The East-West frames are chosen over the North-South perimeter frames based on the results of Liang et al. (2006) that showed that the former are more vulnerable to collapse as a result of their longer spans.

4.3.2 Braced frames

The National Institute of Standards and Technology (NIST) also designed prototype braced steel framed buildings for the purpose of studying their response to an event which may cause progressive collapse (Ghosh, 2006). The buildings are 10-story office buildings with plan dimensions of 150 × 150 ft and utilize braced frames as the lateral load resisting system. The buildings are designed for: (1) Seismic Design Category C (Atlanta, Georgia), which results in SCBFs as defined is the American Institute of Steel Construction (AISC) Seismic Provisions (2005), and (2) Seismic Design Category D (Seattle, Washington), which results in EBFs. The two seismic design categories address moderate and high seismic risk and are considered to study whether more stringent seismic detailing improves braced frame resistance to progressive collapse. The plan views of the buildings are shown in Fig. 4.5 and 4.6, while the East-West (E-W) frames, which are selected for the collapse study, are shown in Fig. 4.7 and 4.8.

The design loads on the buildings are determined based on the American Society of Civil Engineers (ASCE) 7-05 Minimum Design Loads for Buildings and other Structures. The material and design standards used in the design of members and their connections are those referenced in International Building Code (IBC) 2006, Steel Construction Manual

(13th Edition), ANSI/AISC 360-05 Specifications for Structural Steel Buildings (2005) and ANSI/AISC 341-05 Seismic Provisions for Structural Steel Buildings (2005). For typical floors, the dead load consists of the self-weight of the slab of 46 psf and a super-imposed dead load of 30 psf; while the design live load is assumed to be 100 psf. For the roof, the self-weight of the slab is 46 psf, the super-imposed dead load is 10 psf; and the design live load is 20 psf. The reduction in live loads is based on ASCE 7-05 Sec. 4.8.1.

The building structural system is comprised of braced frames and a gravity system. The design of the gravity system in the E-W frames is the same for both the SCBF and EBF buildings. Beams and columns in the gravity system are connected through shear (S) connections, which are comprised of single plate, shear-tab connections that are fillet welded to the column and bolted to the beam web using ⅞ inch A325-N high strength bolts to ⅜ in A36 shear tabs.

The braces in both buildings are square, seismically compact, Hollow Steel Sections (HSS). ASTM A500 Grade B steel (F_y = 46 ksi) is used for the braces, while A992 structural steel (F_y = 50 ksi) is used for all beams and columns. The shear links in the EBFs are proportioned according to AISC seismic provisions (ANSI/AISC 341-05) such that the inelastic response is dominated by shear yielding, whereas, beams, columns and braces are proportioned to behave elastically. Beam-to-column connections away from the links are fully restrained welded moment connections.

The original design in Ghosh (2006) specifies single gusset plates for the brace-to-beam/column connections. Connection of this sort will likely cause the braces to buckle out of plane, rather than in plane, forming three plastic hinges, one in the center of the brace member and one at each of the two end gusset plates. According to the AISC seismic provisions (ANSI/AISC 341-05), the use of cross gusset plates, which are essentially gusset plates reinforced by transverse plates, forces the plastic hinges to form in the braces and not in the gusset plates, thereby improving behavior and energy absorption capacity. Furthermore, since cross plates remain elastic during loading, there is no benefit in explicitly modeling their behavior, which facilitates the simulation

exercise. Therefore, cross gusset plates are assumed to replace the original single gusset plates for the purposes of this research.

4.4 Modeling of steel frame components (IMFs and SMFs)

4.4.1 Moment and shear connection models

The models shown in Fig. 4.9 and 4.10 represent the most important components contributing to inelastic connection behavior in both shear (S-connection) and moment resisting steel connections, respectively. In particular, the models represent transfer of forces at the beam-column interface as well as panel zone behavior.

The S-connection represents the commonly used single plate shear tab connection for joining gravity floor beams and girders. In the proposed S-connection model (Fig. 4.11), connection resistance is modeled by spring A, beam B, and spring C, which represent the binding effect, bolt/shear tab interaction, and concrete slab behavior, respectively. Binding occurs when the top or bottom of the beam bears against the column flange. Therefore Spring A is essentially a contact condition that prevents the beam from penetrating the column flange. Spring C has no resistance in tension and can crush in compression when the slab reaches a given strain. Connection element B is a beam element with integration points that correspond to individual bolts. The element formulation recognizes the interaction between shear and flexural effects through a J_2 plasticity model that was implemented in LS-DYNA (Hallquist, 2006) as a user defined model described in Section 4.7. Each integration point is characterized by a relationship that represents nonlinear bolt behavior up to failure. The size of the force transfer region, l_t, is taken as the distance between the column flange and bolt line, typically 2.5 inches.

The panel zone in both shear and moment connections are modeled using a representation that enforces pure shear deformation (Fig. 4.11(a)). This is consistent with past test results of steel sub-assemblages, where it was observed that the shear stress within the panel is uniformly distributed throughout the column web and that the panel zone region

deforms predominantly in pure shear. As shown in Fig. 4.11(a), the panel zone model is comprised of 4 rigid bars pinned together at their ends to permit the desired deformation to occur. The stiffness and strength of the panel zone is provided by a diagonal spring joining opposite corners of the panel zone. Stiffness of the panel zone spring (K_{pz}) is given by Eq. 4.1, while spring strength (F_{pz}) is derived from the AISC - Steel Construction Manual (2006) recommendations and is given by Eq. (4.2).

$$K_{PZ} = \frac{G\left(d_c - t_{cf}\right)t_{pz}}{\left(d_b - t_{bf}\right)\cos^2\theta} \tag{4.1}$$

$$F_{PZ} = \frac{0.6F_y d_c t_{pz}}{\cos\theta}\left(1 + \frac{3b_{cf}t_{cf}^2}{d_b b_c t_{pz}}\right) \tag{4.2}$$

Where: G: Shear modulus of steel (11150 ksi), F_y: Yield strength of steel (50 ksi), t_{pz}: Thickness of panel zone, d_b: Depth of beam, d_c: Depth of column, t_{bf}: Thickness of beam flange, and t_{cf}: Thickness of column flange.

4.4.2 Beam/Column model

Beams and column members outside the transfer area are represented using a Hughes-Liu beam-column element formulation (Hallquist, 2006). This fiber formulation samples inelastic behavior at one point along the axis of the element and at multiple points across the cross-section. The location of integration points in a typical cross section is shown in Fig. 4.13. This formulation is chosen because it is incrementally objective i.e. rigid body rotations do not generate strains, and thus allows for the treatment of finite strains. The radius cut reduced beam sections in SMF connections are modeled with a beam element of length equal to that of the RBS region but with cross section properties corresponding to that of the minimum cross section in the reduced section.

The proposed model is capable of representing local behavior such as local buckling and fracture by carefully tailoring the stress-strain response at each integration point, as will be described later on in the chapter. The proposed model is also capable of capturing the interaction between moments and axial catenary loads that commonly occur during progressive collapse analysis. Models of the type described above have been successfully utilized in the past by many researchers, although most of their application has been for

flexure coupled with axial compressive load, rather than flexure coupled with tensile load.

4.5 Modeling of steel frame components (EBFs and SCBFs)

The braced frames considered herein are comprised of a variety of components, which are modeled separately. Following is a description of how each component is modeled.

***Fully-restrained beam-to-column connections*:** are modeled by rigidly attaching beams and columns to the connection region.

***Brace-to-beam connections*:** are not explicitly modeled. As previously discussed, their response is expected to be elastic if they are assumed to be of the cross gusset plate type.

***Panel zones*:** are not explicitly modeled. Finite element analyses of sub-assemblages with moment connections in Chapter 3 and APM studies of IMFs and SMFs shows that the panel zone region behaves elastically under collapse conditions. Thus, to facilitate the modeling effort the finite size of the panel zone is also not taken into account for these frames.

***Single plate beam-to-column shear connections*:** are modeled in a similar fashion as for IMF and SMF frames.

***Shear links*:** are represented as shown in Fig. 4.12(a). The model employs a nonlinear spring AC in Fig. 4.12(b), and 4 bars pinned together at their ends to permit the desired shear-flexural deformation to occur. Two of the bars are rigid (AB and CD in Fig. 4.12(b)) and the other two are elastic (AD and CB in Fig. 4.12(b)). The shear stiffness and strength of the link is provided by spring AC. The flexural and axial stiffness of the sub-assemblage is controlled by the two elastic bars, AD and BC, which are assumed to have the stiffness properties of the beam flange. It is expected that the flanges will remain axially elastic even when the shear link behaves in an inelastic manner, since inelastic

behavior is dominated by shear yielding in the web. The elastic stiffness of spring AC in Fig. 4.12(b) is computed by further exploiting the assumption that the panel deforms in pure shear, which is a reasonable assumption that has been commonly observed in shear link tests. By using analogy to steel panel zones, which also deform in pure shear, the elastic stiffness, K_{SL}, and strength, F_{SL}, of the shear link spring AC are therefore given by Eq. 4.3 and 4.4, which are based on the AISC - Steel Construction Manual (2006) recommendations for panel zones. The post-yield stiffness is assumed to be 1.5 % of the initial elastic stiffness and the failure rotation of the shear link spring is assumed to be 0.15 rad as recommended in the Federal Emergency Management Agency (FEMA) 356 (2000).

$$K_{SL} = \frac{G(d_b - t_f)t_w}{Lcos^2\theta} \tag{4.3}$$

$$F_{SL} = \frac{0.6F_y(d_b - t_f)t_w}{\cos\theta}\left(1 + \frac{3b_f t_f^2}{L(d_b - t_f)t_w}\right) \tag{4.4}$$

Where: G: Shear modulus of steel (11150 ksi), F_y: Yield strength of steel (50 ksi), L: Length of shear link, d_b: Depth of beam, t_w: Thickness of beam web, t_f: Thickness of beam flange, b_f: Width of beam flange and θ: Angle between the spring AC and member AB as shown in Fig. 4.12(b).

Beams, columns and brace members: are represented by beam-columns finite elements as in case of IMFs and SMFs. The location of integration points in a typical element is shown in Fig. 4.13. To capture buckling and post buckling response, braces are modeled with an initial imperfection as shown in Fig. 4.14. Parametric studies showed that the magnitude of the imperfection controls the brace buckling strength but that the post buckling response is not dependent upon the imperfection. The imperfection size is assumed to be $L_b/250$ in this research, where L_b is the length of the member. This value is deemed representative of typical imperfections present in a member due to production and erection processes.

4.6 Kinematics of Continuum Based Beam Element

The Hughes-Liu beam finite element used in this work is derived from a continuum solid element by imposing appropriate kinematic and kinetic constraint as discussed next.

4.6.1 Geometry

The initial geometry of a typical beam element (Fig. 4.15) is defined by the following relations:

$$\boldsymbol{x}(\xi,\eta,\zeta) = \overline{\boldsymbol{x}}(\xi,\eta,\zeta) + \boldsymbol{X}(\xi,\eta,\zeta) \tag{4.5}$$

$$\boldsymbol{X}(\xi,\eta,\zeta) = \boldsymbol{X}_{\eta}(\xi,\eta) + \boldsymbol{X}_{\zeta}(\xi,\zeta) \tag{4.6}$$

$$\overline{\boldsymbol{x}}(\xi,\eta,\zeta) = \sum_{a=1}^{n_{en}} N_a(\xi)\overline{\boldsymbol{x}}_a \tag{4.7}$$

$$\boldsymbol{X}_{\eta} = \sum_{a=1}^{n_{en}} N_a(\xi)\boldsymbol{X}_{\eta a}(\eta) \tag{4.8}$$

$$\boldsymbol{X}_{\zeta} = \sum_{a=1}^{n_{en}} N_a(\xi)\boldsymbol{X}_{\zeta a}(\zeta) \tag{4.9}$$

$$\boldsymbol{X}_{\eta a} = \frac{\left\|\boldsymbol{x}_{\eta a}^{+} - \boldsymbol{x}_{\eta a}^{-}\right\|}{2}\eta\widehat{\boldsymbol{X}}_{\eta a} \quad \text{(no sum)} \tag{4.10}$$

$$\boldsymbol{X}_{\zeta a} = \frac{\left\|\boldsymbol{x}_{\zeta a}^{+} - \boldsymbol{x}_{\zeta a}^{-}\right\|}{2}\zeta\widehat{\boldsymbol{X}}_{\zeta a}(\text{no sum}) \tag{4.11}$$

In Eq. 4.5 to 4.11, $\boldsymbol{x}$ denotes the position vector of a generic point on the beam; $\overline{\boldsymbol{x}}$ is the position of a vector point on the reference line; $\boldsymbol{X}$ is a position vector based at a point in the reference surface which defines the "fiber direction" through the point; $\overline{\boldsymbol{x}}_{\boldsymbol{a}}$ is the position vector of the nodal point a; N_a denotes a one dimensional shape function associated with node a; n_{en} is the number of element nodes (two in this case); $\widehat{\boldsymbol{X}}_{\eta a}$ and $\widehat{\boldsymbol{X}}_{\zeta a}$ are the unit vectors emanating from node a in two fiber directions defined by lines for $\zeta = 0$ and $\eta = 0$ respectively. These equations represent a smooth mapping of a bi-unit cube into the physical beam domain. The lines of constant ξ are called fibers and the unit vectors along fibers are called directors. Thus $\widehat{\boldsymbol{X}}_{\eta a}$ and $\widehat{\boldsymbol{X}}_{\zeta a}$ are directors. The lines of constant ζ or constant η are called laminae. In the above mapping the reference line is defined by $\zeta = \eta = 0$.

In describing beam the geometry, ξ determines the location along the axis of the beam and the coordinate pair (η, ζ) defines a point on the cross-section of the beam. The 8-node brick geometry (Fig. 4.15) is degenerated into 2-node beam geometry by using the Eq. 4.5 to 4.11. Orthogonal inextensible fibers (Fig. 4.16) are defined at each node for treating the rotational degrees of freedom.

4.6.2 Kinematics

The kinematics of the beam element is defined by invoking the isoparametric hypotheses, i.e., the same expressions are used for kinematics as well as for the geometry, with displacement variables in place of coordinate variables. The isoparametric assumption leads to the following relations:

$$\boldsymbol{u}(\xi, \eta, \zeta) = \overline{\boldsymbol{u}}(\xi, \eta, \zeta) + \boldsymbol{U}(\xi, \eta, \zeta) \tag{4.12}$$

$$\boldsymbol{U}(\xi, \eta, \zeta) = \boldsymbol{U}_{\eta}(\xi, \eta) + \boldsymbol{U}_{\zeta}(\xi, \zeta) \tag{4.13}$$

$$\overline{\boldsymbol{u}}(\xi, \eta, \zeta) = \sum_{a=1}^{n_{en}} N_a(\xi) \overline{\boldsymbol{u}}_a \tag{4.14}$$

$$\boldsymbol{U}_{\eta}(\xi, \eta) = \sum_{a=1}^{n_{en}} N_a(\xi) \boldsymbol{U}_{\eta a}(\eta) \tag{4.15}$$

$$\boldsymbol{U}_{\zeta}(\xi, \zeta) = \sum_{a=1}^{n_{en}} N_a(\xi) \boldsymbol{U}_{\zeta a}(\zeta) \tag{4.16}$$

where $\boldsymbol{u}$ is the displacement of the generic point; $\overline{\boldsymbol{u}}$ is the displacement of the point on the reference line; and $\boldsymbol{U}$ is the fiber displacement. The fibers are assumed to be inextensible and therefore they can rotate but cannot stretch or contract. To describe the current deformed configuration with respect to undeformed reference configuration, the following representation is introduced:

$$\boldsymbol{y} = \overline{\boldsymbol{y}} + \boldsymbol{Y} \tag{4.17}$$

$$\boldsymbol{Y} = \boldsymbol{Y}_{\eta a} + \boldsymbol{Y}_{\zeta a} \tag{4.18}$$

$$\overline{\boldsymbol{y}} = \overline{\boldsymbol{x}} + \overline{\boldsymbol{u}} \tag{4.19}$$

$$\overline{\boldsymbol{y}}_a = \overline{\boldsymbol{x}}_a + \overline{\boldsymbol{u}}_a \tag{4.20}$$

$$\boldsymbol{Y} = \boldsymbol{X} + \boldsymbol{U} \tag{4.21}$$

$$\boldsymbol{Y}_a = \boldsymbol{X}_a + \boldsymbol{U}_a \tag{4.22}$$

$$\boldsymbol{Y}_{\eta a} = \boldsymbol{X}_{\eta a} + \boldsymbol{U}_{\eta a} \quad \text{and } \widehat{\boldsymbol{Y}}_{\eta a} = \widehat{\boldsymbol{X}}_{\eta a} + \widehat{\boldsymbol{U}}_{\eta a} \tag{4.23}$$

$$\boldsymbol{Y}_{\zeta a} = \boldsymbol{X}_{\zeta a} + \boldsymbol{U}_{\zeta a} \quad \text{and } \widehat{\boldsymbol{Y}}_{\zeta a} = \widehat{\boldsymbol{X}}_{\zeta a} + \widehat{\boldsymbol{U}}_{\zeta a} \tag{4.24}$$

where $\boldsymbol{y}$ is denotes the position vector of a generic point on the beam on the current deformed configuration; $\overline{\boldsymbol{y}}$ is the position of a vector point on the reference line in the deformed configuration; $\boldsymbol{Y}$ is a position vector based at a point in the reference surface which defines the "fiber direction" through the point in the deformed configuration; $\overline{\boldsymbol{y}}_{\boldsymbol{a}}$ is the position vector of the nodal point a in the deformed configuration; $\widehat{\boldsymbol{Y}}_{\eta a}$ and $\widehat{\boldsymbol{Y}}_{\zeta a}$ are the unit vectors emanating from node a in two fiber directions defined by lines for $\zeta = 0$ and $\eta = 0$ respectively in the deformed configuration.

For beam elements, the known quantities are the displacement degrees of freedom $\left(\boldsymbol{u}_a \equiv (u_{xa}, u_{ya}, u_{za})\right)$ at nodal points on the reference surface obtained from the translational equation of motion and rotational quantities ($\theta \equiv (\theta_1, \theta_2, \theta_3)$) at each node obtained from the rotational equation of motion. The kinematic relationships are completed by specifying the relationship between nodal rotation $\boldsymbol{\theta}$ and fiber displacement $\boldsymbol{U}$. In incremental form, the linearized relationships between the incremental components $\Delta\widehat{U}_{\eta a_i}$ and $\Delta\widehat{U}_{\zeta a_i}$ the incremental rotations are given by:

$$\begin{bmatrix} \Delta\widehat{U}_{\eta a_1} \\ \Delta\widehat{U}_{\eta a_2} \\ \Delta\widehat{U}_{\eta a_3} \end{bmatrix} = \begin{bmatrix} 0 & \hat{Y}_{\eta a_3} & -\hat{Y}_{\eta a_2} \\ -\hat{Y}_{\eta a_3} & 0 & \hat{Y}_{\eta a_1} \\ \hat{Y}_{\eta a_2} & -\hat{Y}_{\eta a_1} & 0 \end{bmatrix} \begin{bmatrix} \Delta\theta_1 \\ \Delta\theta_2 \\ \Delta\theta_3 \end{bmatrix} \tag{4.25}$$

$$\begin{bmatrix} \Delta\widehat{U}_{\zeta a_1} \\ \Delta\widehat{U}_{\zeta a_2} \\ \Delta\widehat{U}_{\zeta a_3} \end{bmatrix} = \begin{bmatrix} 0 & \hat{Y}_{\zeta a_3} & -\hat{Y}_{\zeta a_2} \\ -\hat{Y}_{\zeta a_3} & 0 & \hat{Y}_{\zeta a_1} \\ \hat{Y}_{\zeta a_2} & -\hat{Y}_{\zeta a_1} & 0 \end{bmatrix} \begin{bmatrix} \Delta\theta_1 \\ \Delta\theta_2 \\ \Delta\theta_3 \end{bmatrix} \tag{4.26}$$

Equations 4.25 and 4.26 are used to transforms the incremental fiber tip displacements to rotational increments in the equation of motions. Finally, the directors are updated using finite rotations expression as follows:

$$\widehat{\boldsymbol{Y}}^{n+1} = \boldsymbol{R}(\Delta\boldsymbol{\theta})\widehat{\boldsymbol{Y}}^{n} \tag{4.27}$$

$$\boldsymbol{R}(\Delta\boldsymbol{\theta}) = \exp\left(\boldsymbol{\Omega}(\Delta\boldsymbol{\theta})\right) \stackrel{\text{def}}{=} \sum_{n=1}^{\infty} \frac{\boldsymbol{\Omega}(\Delta\boldsymbol{\theta})}{n!} \tag{4.28}$$

$$\boldsymbol{\Omega}(\Delta\boldsymbol{\theta}) = skew(\Delta\boldsymbol{\theta}) = \begin{bmatrix} 0 & -\Delta\theta_3 & \Delta\theta_2 \\ \Delta\theta_3 & 0 & -\Delta\theta_1 \\ -\Delta\theta_2 & \Delta\theta_1 & 0 \end{bmatrix} \tag{4.29}$$

Second order update is used by including quadratic terms of Eq. 4.28, which results in the following relations (Belytschko 2000):

$$\boldsymbol{R}(\Delta\boldsymbol{\theta}) = \boldsymbol{I} + \frac{4}{4 + \|\Delta\boldsymbol{\theta}\|^2}(\boldsymbol{\Omega}(\Delta\boldsymbol{\theta}) + \boldsymbol{\Omega}^2(\Delta\boldsymbol{\theta})) \tag{4.30}$$

$$\|\Delta\boldsymbol{\theta}\| = \sqrt{\Delta\theta_1^2 + \Delta\theta_2^2 + \Delta\theta_3^2} \tag{4.31}$$

4.6.3 Lamina Coordinate System (LCS)

For enforcing the zero stress normal stress conditions transverse to the axis of the beam, a Cartesian reference frame known as lamina system is constructed. This lamina basis deforms rigidly with the element as the element deforms. Zero normal stress conditions are enforced in the lamina system, i.e., $\sigma_{22}^l = \sigma_{33}^l = 0$. The lamina basis vectors are defined as follows:

$$\boldsymbol{e}_1^l = \frac{\overline{\boldsymbol{y}}_2 - \overline{\boldsymbol{y}}_1}{\|\overline{\boldsymbol{y}}_2 - \overline{\boldsymbol{y}}_1\|} \tag{4.32}$$

$$\boldsymbol{e'}_2^l = \frac{\widehat{\boldsymbol{Y}}_{,\eta 1} + \widehat{\boldsymbol{Y}}_{,\eta 2}}{\|\widehat{\boldsymbol{Y}}_{,\eta 1} + \widehat{\boldsymbol{Y}}_{,\eta 2}\|} \tag{4.33}$$

$$\boldsymbol{e}_3^l = \boldsymbol{e}_1^l \times \boldsymbol{e'}_2^l \tag{4.34}$$

$$\boldsymbol{e}_2^l = \boldsymbol{e}_3^l \times \boldsymbol{e}_1^l \tag{4.35}$$

The transformation matrix $\boldsymbol{q} = [q_{ij}]$ from global basis $\{\boldsymbol{e}_1, \boldsymbol{e}_2, \boldsymbol{e}_3\}$ to lamina basis system is given by: $q_{ij} = \boldsymbol{e}_i^l . \boldsymbol{e}_j$

4.7 User defined material model for beam elements

A J_2 plasticity model is implemented for beam elements in LS-DYNA to model the inelastic response and failure of beam elements. Important steps that are used to compute the stresses in beam elements are presented in this section. In a typical time step, the configuration of the beam at step $n + 1$ is written as the function of the configuration at step n and the step length Δt, i.e.

$$\boldsymbol{y}^{n+1} = \boldsymbol{y}^{n+1}(\boldsymbol{y}^n, \Delta t) \tag{4.36}$$

The displacement increment over the time step is given by:

$$\Delta \boldsymbol{u} = \boldsymbol{y}^{n+1} - \boldsymbol{y}^{n} \tag{4.37}$$

The strain and spin increments are calculated from the incremental displacement gradient as follows:

$$\boldsymbol{G} = \frac{\partial \Delta \boldsymbol{u}}{\partial \boldsymbol{y}^{n+1}} \tag{4.38}$$

where $\boldsymbol{y}^{n+1}$ is the current configuration. Now the incremental strain ($\Delta\boldsymbol{\varepsilon}$) and spin ($\Delta\boldsymbol{\omega}$) tensors are obtained as follows:

$$\Delta \boldsymbol{\varepsilon} = \frac{1}{2}(\boldsymbol{G} + \boldsymbol{G}^{T}) \tag{4.39}$$

$$\Delta \boldsymbol{\omega} = \frac{1}{2}(\boldsymbol{G} - \boldsymbol{G}^{T}) \tag{4.40}$$

With the assumption of hypoelastic–plastic material, an update based on the Jaumann stress rate is used and the stress update in the global system is given by:

$$\boldsymbol{\sigma}^{n+1} = \boldsymbol{Q}.\boldsymbol{\sigma}^{n}.\boldsymbol{Q}^{T} + \Delta t \Delta \boldsymbol{\sigma}^{J} \tag{4.41}$$

where $\boldsymbol{Q} = \boldsymbol{I} + (\boldsymbol{I} - \Delta\boldsymbol{\omega})^{-1}\Delta\boldsymbol{\omega}$. Since for explicit analysis time increments are small, the following approximation is made in the formulation of Eq. 4.41:

$$\boldsymbol{Q} = \boldsymbol{I} + (\boldsymbol{I} + \Delta\boldsymbol{\omega} + \Delta\boldsymbol{\omega}^{\boldsymbol{2}} + \cdots)\Delta\boldsymbol{\omega} \approx \boldsymbol{I} + \Delta\boldsymbol{\omega} \tag{4.42}$$

$$\boldsymbol{\sigma}^{n+1} \approx \boldsymbol{\sigma}^{n}.\Delta\boldsymbol{\omega} + \Delta\boldsymbol{\omega}.\boldsymbol{\sigma}^{n} + \Delta t \Delta \boldsymbol{\sigma}^{J} \tag{4.43}$$

$$\boldsymbol{\sigma}^{n+1} = \boldsymbol{\sigma}^{Jn} + \Delta t \Delta \boldsymbol{\sigma}^{J} \tag{4.44}$$

where $\boldsymbol{\sigma}^{Jn} = \boldsymbol{\sigma}^{n}.\Delta\boldsymbol{\omega} + \Delta\boldsymbol{\omega}.\boldsymbol{\sigma}^{n}$. The constitutive relationships are written in the lamina coordinate system. Thus, the stress and strains are transformed to the lamina coordinate system using transformation matrix $\boldsymbol{q}$. The constitutive relationship in the lamina coordinate system is given as follows:

$$\Delta t \Delta \boldsymbol{\sigma}^{lJ} = \boldsymbol{C} : \Delta \boldsymbol{\varepsilon}^{le} \tag{4.45}$$

where $\boldsymbol{C}$ is the elasticity tensor for homogeneous, isotropic material; $\Delta\boldsymbol{\varepsilon}^{le}$ is the elastic component of $\Delta\boldsymbol{\varepsilon}^{l}$, and $\Delta\boldsymbol{\varepsilon}^{lp}$ is the plastic component of $\Delta\boldsymbol{\varepsilon}^{l}$, such that:

$$\Delta \boldsymbol{\varepsilon}^{l} = \Delta \boldsymbol{\varepsilon}^{le} + \Delta \boldsymbol{\varepsilon}^{lp} \tag{4.46}$$

In a user defined material, the objective is to determine the updated stress $\boldsymbol{\sigma}^{l(n+1)}$ in the lamina coordinate systems, given the stress, strains and history variable at step "n" in the lamina system. The local to global transformations and Jaumann stress update is handled internally in LS-DYNA.

4.7.1 J_2 plasticity for beam elements

In this section the formulation of the J_2 plasticity model for beam elements is presented. Typically, the constitutive update is carried out in LCS and thus all the stress and strain quantities are in the local LCS. The yield function in the J_2 plasticity model is given by Eq. 4.47:

$$\phi(\boldsymbol{\sigma}, \zeta^p) = J_2 - \frac{1}{3}\zeta^p(\alpha^p) \tag{4.47}$$

where $J_2 = \frac{1}{2}\boldsymbol{s}:\boldsymbol{s}$ and $\boldsymbol{s} = \boldsymbol{P}_{dev}:\boldsymbol{\sigma}$ is the deviatoric component of the Cauchy stress tensor, $\zeta^p \equiv \zeta^p(\alpha^p)$ is the hardening variable and α^p is the internal variable. Assuming associated flow conditions, the rate equations for plastic strain, $\dot{\boldsymbol{\varepsilon}}^p$, and internal variable, $\dot{\alpha}^p$, are given by Eq. 4.48 and 4.49.

$$\dot{\boldsymbol{\varepsilon}}^p = \gamma \frac{\partial \phi(\boldsymbol{\sigma}, \zeta^p)}{\partial \boldsymbol{\sigma}} = \gamma \boldsymbol{s} \tag{4.48}$$

$$\dot{\alpha}^p = -\gamma \frac{\partial \phi(\boldsymbol{\sigma}, \zeta^p)}{\partial \zeta^p} = \frac{1}{3}\gamma \tag{4.49}$$

where γ is the consistency parameter. The plasticity model is completed by specifying the Kuhn-Tucker complementarity conditions (Eq. 4.50) and consistency condition (Eq. 4.51) as follows:

$$\gamma \geq 0, \phi(\boldsymbol{\sigma}, \zeta^p) \leq 0, \gamma\phi(\boldsymbol{\sigma}, \zeta^p) = 0 \tag{4.50}$$

$$\gamma\dot{\phi}(\boldsymbol{\sigma}, \zeta^p) = 0 \tag{4.51}$$

For beam elements, plane stress conditions are imposed in the LCS which results in:

$$\sigma_{13} = \sigma_{22} = \sigma_{23} = \sigma_{31} = \sigma_{32} = \sigma_{33} = 0 \tag{4.52}$$

With this assumption the stress tensor can be expressed as follows:

$$\boldsymbol{\sigma} = \begin{bmatrix} \sigma_{11} & \sigma_{12} & \sigma_{13} \\ \sigma_{21} & \sigma_{22} & \sigma_{23} \\ \sigma_{31} & \sigma_{32} & \sigma_{33} \end{bmatrix} = \begin{bmatrix} \sigma_{11} & \sigma_{12} & 0 \\ \sigma_{21} & 0 & 0 \\ 0 & 0 & 0 \end{bmatrix} \tag{4.53}$$

The deviatoric component of stress tensor is given by:

$$\boldsymbol{s} = \boldsymbol{\sigma} - p\boldsymbol{I} = \begin{bmatrix} s_{11} & s_{12} & s_{13} \\ s_{21} & s_{22} & s_{23} \\ s_{31} & s_{32} & s_{33} \end{bmatrix} = \begin{bmatrix} \frac{2}{3}\sigma_{11} & \sigma_{12} & 0 \\ \sigma_{21} & -\frac{1}{3}\sigma_{11} & 0 \\ 0 & 0 & -\frac{1}{3}\sigma_{11} \end{bmatrix} \tag{4.54}$$

where $p = \sigma_{11}/3$. Let $\boldsymbol{P_{vol}} = \frac{1}{3}\mathbf{1}\otimes\mathbf{1}$ and $\boldsymbol{P_{vol}} = \boldsymbol{I_4} - \frac{1}{3}\mathbf{1}\otimes\mathbf{1}$ be the 4th order volumetric and deviatoric projection tensors respectively, where $\boldsymbol{I_4}$ is the 4th order identity tensor and $\mathbf{1}$ is the unit vector. The following relationships then hold:

$$\boldsymbol{P}_{vol}:\dot{\boldsymbol{\varepsilon}}^p = \mathbf{0} \Longrightarrow \dot{\varepsilon}^p_{11} + \dot{\varepsilon}^p_{22} + \dot{\varepsilon}^p_{33} = 0 \tag{4.55}$$

$$\begin{aligned}\dot{\boldsymbol{\varepsilon}}^p &= \begin{bmatrix} \dot{\varepsilon}^p_{11} & \dot{\varepsilon}^p_{12} & \dot{\varepsilon}^p_{13} \\ \dot{\varepsilon}^p_{21} & \dot{\varepsilon}^p_{22} & \dot{\varepsilon}^p_{23} \\ \dot{\varepsilon}^p_{31} & \dot{\varepsilon}^p_{32} & \dot{\varepsilon}^p_{33} \end{bmatrix} = \begin{bmatrix} \dot{\varepsilon}^p_{11} & \dot{\varepsilon}^p_{12} & 0 \\ \dot{\varepsilon}^p_{21} & -\dot{\varepsilon}^p_{11}/2 & 0 \\ 0 & 0 & -\dot{\varepsilon}^p_{11}/2 \end{bmatrix} \\ &= \gamma \begin{bmatrix} 2\sigma_{11}/3 & \sigma_{12} & 0 \\ \sigma_{21} & -\sigma_{11}/3 & 0 \\ 0 & 0 & -\sigma_{11}/3 \end{bmatrix}\end{aligned} \tag{4.56}$$

$$\boldsymbol{\varepsilon}^p = \begin{bmatrix} \varepsilon^p_{11} & \varepsilon^p_{12} & \varepsilon^p_{13} \\ \varepsilon^p_{21} & \varepsilon^p_{22} & \varepsilon^p_{23} \\ \varepsilon^p_{31} & \varepsilon^p_{32} & \varepsilon^p_{33} \end{bmatrix} = \begin{bmatrix} \varepsilon^p_{11} & \varepsilon^p_{12} & 0 \\ \varepsilon^p_{21} & -\varepsilon^p_{11}/2 & 0 \\ 0 & 0 & -\varepsilon^p_{11}/2 \end{bmatrix} \tag{4.57}$$

The isotropic material the stress components are given by Eq. 4.58:

$$\begin{Bmatrix} \sigma_{11} \\ \sigma_{22} \\ \sigma_{33} \\ \sigma_{12} \\ \sigma_{23} \\ \sigma_{31} \end{Bmatrix} = \begin{bmatrix} \lambda+2\mu & \lambda & \lambda & 0 & 0 & 0 \\ \lambda & \lambda+2\mu & \lambda & 0 & 0 & 0 \\ \lambda & \lambda & \lambda+2\mu & 0 & 0 & 0 \\ 0 & 0 & 0 & 2\mu & 0 & 0 \\ 0 & 0 & 0 & 0 & 2\mu & 0 \\ 0 & 0 & 0 & 0 & 0 & 2\mu \end{bmatrix} \begin{Bmatrix} \varepsilon^e_{11} \\ \varepsilon^e_{22} \\ \varepsilon^e_{33} \\ \varepsilon^e_{12} \\ \varepsilon^e_{23} \\ \varepsilon^e_{31} \end{Bmatrix} = \begin{Bmatrix} \sigma_{11} \\ 0 \\ 0 \\ \sigma_{12} \\ 0 \\ 0 \end{Bmatrix} \tag{4.58}$$

where λ and μ are the Lamé elastic constants. It is important to note that inextensibility of nodal directors only applies to the motion. Inextensibility contradicts the plane stress assumption and this contradiction is reconciled by not using the motion to compute the nonzero normal strain components ε_{22} and ε_{33}. Instead, these components are obtained from the constitutive requirement that $\sigma_{22} = \sigma_{33} = 0$. Equations 4.57 and 4.58 give:

$$\begin{aligned} \varepsilon^e_{22} = \varepsilon^e_{33} &= -\frac{\lambda}{2(\lambda+\mu)}\varepsilon^e_{11} \\ \varepsilon_{22} = \varepsilon_{33} &= -\frac{\lambda}{2(\lambda+\mu)}\varepsilon^e_{11} - \frac{1}{2}\varepsilon^p_{11} \\ \varepsilon_{23} &= \varepsilon_{23} = 0 \end{aligned} \tag{4.59}$$

Using Eq. 4.58 and 4.59 the constitutive relations can be written as:

$$[\tilde{\boldsymbol{\sigma}}] = [\boldsymbol{C_b}][\tilde{\varepsilon}^e] \tag{4.60}$$

$$[\tilde{\boldsymbol{\sigma}}] = \begin{Bmatrix}\sigma_{11}\\ \sigma_{12}\end{Bmatrix};\ [\boldsymbol{C_b}] = \frac{E}{1+\upsilon}\begin{bmatrix}1+\upsilon & 0\\ 0 & 1\end{bmatrix};\ [\tilde{\boldsymbol{\varepsilon}}^e] = \begin{Bmatrix}\varepsilon_{11}^e\\ \varepsilon_{12}^e\end{Bmatrix} \tag{4.61}$$

where $E = \frac{\mu(3\lambda+2\mu)}{\lambda+\mu}$ is the modulus of elasticity and $\upsilon = \frac{\lambda}{2(\lambda+\mu)}$ is the Poisson ratio of the material. Now, the second invariant of deviatoric stress component, J_2, can be expressed as follows:

$$J_2 = \frac{1}{2}\boldsymbol{s}:\boldsymbol{s} = [\tilde{\boldsymbol{\sigma}}]^T[\boldsymbol{P}_1][\tilde{\boldsymbol{\sigma}}] \text{ where } [\boldsymbol{P}_1] = \begin{bmatrix}1/3 & 0\\ 0 & 1\end{bmatrix} \tag{4.62}$$

Following additional notation is employed to simplify the model formulation for numerical integration:

$$[\tilde{\boldsymbol{\varepsilon}}^p] = \begin{Bmatrix}\varepsilon_{11}^p\\ \varepsilon_{12}^p\end{Bmatrix};\ [\tilde{\boldsymbol{s}}] = \begin{Bmatrix}s_{11}\\ s_{12}\end{Bmatrix} \tag{4.63}$$

$$[\tilde{\boldsymbol{s}}] = [\boldsymbol{P}_2][\tilde{\boldsymbol{\sigma}}] \text{ where } [\boldsymbol{P}_2] = \begin{bmatrix}2/3 & 0\\ 0 & 1\end{bmatrix} \tag{4.64}$$

To advance the solution within an incremental solution scheme in a finite element (FE) framework, the flow rule (Eq. 4.48) and the evolution equations for the internal variables (Eq. 4.48) have to be integrated over a finite time step $\Delta t = t_{n+1} - t_n$. Such a computation is typically carried out at an integration point. The known values at time t_{n+1} includes stress tensor $(\boldsymbol{\sigma}_n)$**,** internal variables (α_n^p) and strains $\boldsymbol{\varepsilon}_n,\ \boldsymbol{\varepsilon}_n^p,\ \boldsymbol{\varepsilon}_{n+1}$. The objective of the integration scheme is to compute the stress tensor $(\boldsymbol{\sigma}_{n+1})$ and internal variable (α_{n+1}^p) at time t_{n+1}. The main difference between implicit and explicit FE formulations is that for an implicit scheme a consistent algorithmic tangent is required to assemble the global tangent stiffness matrix, however for an explicit FE formulation such an algorithmic tangent is not required. The proposed elasto-plastic model is implemented in the commercial explicit finite element code LS-DYNA. Euler backward method is used for integration of flow rule and plastic internal variable.

The integration of plasticity models is usually carried out in two steps (Simo and Hughes, 1998). In the first step known as "elastic" or "trial" step all inelasticity is freezed. If the yielding condition is not exceeded then the trial step gives the correct state. However, if the yielding condition is exceeded the algorithm proceeds to "plastic" step where further computations are carried out assuming that plastic flow occurs and that the consistency

condition is enforced in this step. A two step algorithm based on the above concept is described next.

Step -1: Trial Step (Freeze Plastic Flow)

No plastic flow implies:

$$\gamma_{n+1} = 0;\ \left[\tilde{\boldsymbol{\varepsilon}}_{n+1}^{p^{Tr}}\right] = \left[\tilde{\boldsymbol{\varepsilon}}_{n}^{p}\right];\ \ \alpha_{n+1}^{p^{Tr}} = \ \alpha_{n}^{p} \tag{4.65}$$

$$[\tilde{\boldsymbol{\sigma}}_{n+1}^{Tr}] = [\boldsymbol{C}_b]\left([\tilde{\boldsymbol{\varepsilon}}_{n+1}] - \left[\tilde{\boldsymbol{\varepsilon}}_{n+1}^{p^{Tr}}\right]\right) \tag{4.66}$$

$$\phi_{n+1}^{Tr} = [\tilde{\sigma}]^T[P_1][\tilde{\sigma}] - \frac{1}{3}\zeta^p\left(\alpha_{n+1}^{p^{Tr}}\right) \tag{4.67}$$

The functional form of hardening function is taken as follows:

$$\zeta^p(\alpha^p) = \left[\sigma_y + H(\alpha^p)\right]^2 \tag{4.68}$$

where $H(\alpha^p)$ represents hardening curve which is assumed to be a piecewise linear curve.

If $\phi_{n+1}^{Tr} \leq 0$, this implies that the trial step is admissible and the following updates are carried out.

ELASTIC UPDATES

$$\alpha_{n+1}^{p} = \alpha_{n+1}^{p^{TR}};\ \left[\tilde{\boldsymbol{\varepsilon}}_{n+1}^{p}\right] = \left[\tilde{\boldsymbol{\varepsilon}}_{n+1}^{p^{Tr}}\right] \tag{4.69}$$

$$[\tilde{\boldsymbol{\sigma}}_{n+1}\ ] = [\tilde{\boldsymbol{\sigma}}_{n+1}^{Tr}] \tag{4.70}$$

If $\phi_{n+1}^{Tr} > 0$, this implies that the trial step is not admissible and the algorithm proceed to the second step, i.e. the plastic step.

Step -2: Plastic Step

In this step, the integration of flow rules is carried out and the consistency condition is enforced as described next. The flow rule and evolution equations of internal variable are integrated using the Euler Backward method as follows:

$$\left[\tilde{\boldsymbol{\varepsilon}}_{n+1}^{p}\right] = \left[\tilde{\boldsymbol{\varepsilon}}_{n}^{p}\right] + \Delta\gamma_{n+1}[\tilde{\boldsymbol{s}}_{n+1}\ ] \tag{4.71}$$

$$\alpha_{n+1}^{p} = \alpha_{n}^{p} + \frac{1}{3}\Delta\gamma_{n+1} \tag{4.72}$$

where $\Delta\gamma_{n+1} \equiv \Delta t\gamma_{n+1}$.

Enforcing the consistency condition at time $t = t_{n+1}$ gives:

$$\phi_{n+1}^{p} = [\tilde{\boldsymbol{\sigma}}]^T[\boldsymbol{P}_1][\tilde{\boldsymbol{\sigma}}] - \frac{1}{3}\zeta^p\left(\alpha_{n+1}^{p}\right) = 0 \tag{4.73}$$

Using Eq. 4.72, the consistency condition can be written as follows:

$$\phi_{n+1}^{p} = [\tilde{\boldsymbol{\sigma}}]^{T}[\boldsymbol{P}_1][\tilde{\boldsymbol{\sigma}}] - \frac{1}{3}\left[\sigma_y + H\left(\alpha_{n+1}^{p}\right)\right]^2 = 0 \tag{4.74}$$

Also,

$$[\tilde{\boldsymbol{\sigma}}_{n+1}\,] = [\boldsymbol{C}_b]\left([\tilde{\boldsymbol{\varepsilon}}_{n+1}] - \left[\tilde{\boldsymbol{\varepsilon}}_{n+1}^{p}\right]\right) \tag{4.75}$$

Combining Eq. 4.71 and 4.75 gives:

$$[\tilde{\boldsymbol{\sigma}}_{n+1}\,] = [\boldsymbol{C}_b]\left([\tilde{\boldsymbol{\varepsilon}}_{n+1}] - \left[\tilde{\boldsymbol{\varepsilon}}_{n}^{p}\right] - \Delta\gamma_{n+1}[\tilde{\boldsymbol{s}}_{n+1}\,]\right)$$

$$\Longrightarrow [\tilde{\boldsymbol{\sigma}}_{n+1}\,] = [\tilde{\boldsymbol{\sigma}}_{n+1}^{Tr}] - \Delta\gamma_{n+1}[\boldsymbol{C}_b][\boldsymbol{P}_2][\tilde{\boldsymbol{\sigma}}_{n+1}\,]$$

$$\Longrightarrow [\tilde{\boldsymbol{\sigma}}_{n+1}\,] = \left[\boldsymbol{I}_2 + \Delta\gamma_{n+1}[\boldsymbol{C}_b][\boldsymbol{P}_2]\right]^{-1}[\tilde{\boldsymbol{\sigma}}_{n+1}^{Tr}] \tag{4.76}$$

$$[\boldsymbol{P}_3] = \left[\boldsymbol{I}_2 + \Delta\gamma_{n+1}[\boldsymbol{C}_b][\boldsymbol{P}_2]\right]^{-1} = \begin{bmatrix} \dfrac{3}{2\Delta\gamma_{n+1}E + 3} & 0 \\ 0 & \dfrac{1}{2\mu\Delta\gamma_{n+1} + 1} \end{bmatrix}$$

Equation 4.76 gives:

$$[\tilde{\boldsymbol{\sigma}}]^{T}[\boldsymbol{P}_1][\tilde{\boldsymbol{\sigma}}] = [\tilde{\boldsymbol{\sigma}}_{n+1}^{Tr}]^{T}[\boldsymbol{P}_3]^{T}[\boldsymbol{P}_1][\boldsymbol{P}_3][\tilde{\boldsymbol{\sigma}}_{n+1}^{Tr}]$$

$$\Longrightarrow [\tilde{\boldsymbol{\sigma}}]^{T}[\boldsymbol{P}_1][\tilde{\boldsymbol{\sigma}}] = \frac{3\sigma_{11_{n+1}}^{Tr^2}}{\left[2E\Delta\gamma_{n+1} + 3\right]^2} + \frac{\sigma_{12_{n+1}}^{Tr^2}}{\left[2\mu\Delta\gamma_{n+1} + 1\right]^2} \tag{4.77}$$

Combining Eq. 4.77, 4.72 and 4.74 gives:

$$\phi_{n+1}^{p} = \frac{3\sigma_{11_{n+1}}^{Tr^2}}{\left[2E\Delta\gamma_{n+1} + 3\right]^2} + \frac{\sigma_{12_{n+1}}^{Tr^2}}{\left[2\mu\Delta\gamma_{n+1} + 1\right]^2} - \frac{1}{3}\left[\sigma_y + H\left(\alpha_n^{p} + \frac{1}{3}\Delta\gamma_{n+1}\right)\right]^2 = 0 \tag{4.78}$$

Equation 4.78 is a nonlinear equation in independent variable $\Delta\gamma_{n+1}$, which is solved by standard Newton Raphson method. Starting with the initial values of $\Delta\gamma_{n+1}^{(0)} = 0$, the following iterations are carried out to obtain the solution:

$$\delta(\Delta\gamma_{n+1}^{(k+1)}) = \frac{1}{\left.\dfrac{\partial\phi_{n+1}^{p}}{\partial\Delta\gamma_{n+1}}\right|_{\Delta\gamma_{n+1}^{(k)}}}\phi_{n+1}^{p}(\Delta\gamma_{n+1}^{(k)})$$

$$\Delta\gamma_{n+1}^{(k+1)} = \Delta\gamma_{n+1}^{(k)} + \delta(\Delta\gamma_{n+1}^{(k+1)}) \tag{4.79}$$

The derivative $\frac{\partial\phi_{n+1}^{p}}{\partial\Delta\gamma_{n+1}}$ is given by:

$$\frac{\partial \phi_{n+1}^{p}}{\partial \Delta\gamma_{n+1}} = -\frac{12E\sigma_{11_{n+1}}^{Tr^2}}{\left[2E\Delta\gamma_{n+1}+3\right]^3} - \frac{4\mu\sigma_{12_{n+1}}^{Tr^2}}{\left[2\mu\Delta\gamma_{n+1}+1\right]^3} - \frac{2}{3}\left[\sigma_y + H\left(\alpha_n^p + \frac{1}{3}\Delta\gamma_{n+1}\right)\right]\frac{\partial H}{\partial \Delta\gamma_{n+1}} \tag{4.80}$$

After solving Eq. 4.78, the relevant updates are obtained using Eq. 4.71, 4.72 and 4.75. Two different hardening curves are used to model response in tension and compression. Hardening curve followed at integration point is determined by σ_{11}^{Tr}, i.e. if $\sigma_{11}^{Tr} > 0$ then hardening curve for tension is followed, else hardening curve for compression is followed. Fracture is assumed to occur at an integration point when the tension hardening variable reaches a critical value.

4.7.2 Nodal forces

Nodal forces are obtained by numerical quadrature. Two avoid shear locking in the 2-node finite element described above, a single stack of quadrature points at $\xi = 0$ is used. This quadrature scheme is also called selectively reduced integration. It integrates the axial forces exactly (for rectangular section) but underintegrates the transverse shear stresses. The number of integration points in the η-direction depends on the constitutive law and the degree of accuracy desired. For integration in the η-direction, the trapezoidal rule is used, since Guass quadrature implicitly assumes the smoothness of data and is not optimal for elastic-plastic models having discontinuous derivatives.

4.8 Model Calibration

4.8.1 Moment connection calibration

Beam-column constitutive properties are calibrated to data obtained from the micro-mechanical simulations of sub-assemblages reported in Chapter 3. To ensure that the structural scale model captures the main modes of behavior exhibited by the sub-assemblages results, different stress strain curves for both tension and compression are employed; the tensile response accounts for strain hardening and fracture, while the compressive response accounts for the effects of local and global buckling. Figure 4.18 shows a structural scale model of the sub-assemblages that were considered in Chapter 3.

Using information from the sub-assemblages response, the stress-strain responses in Fig. 17 were found to be sufficiently versatile to account for the main modes of behavior. Table 4.1 lists the calibration parameters obtained for SMF and IMF, which are determined by trial and error. Fig. 4.19, 4.20 and 4.21 shows that the structural scale model results matches well with the data from the detailed study of beam-column sub-assemblages. As shown in Fig. 4.22, linear relationships between fracture strain (e_f) and beam depth (d_b) is obtained from this data and are expressed as follows:

$$\begin{aligned} \text{RBS: } e_f &= -0.0036 d_b + 0.176 \\ \text{No RBS: } e_f &= -0.0011 d_b + 0.064 \end{aligned} \tag{4.81}$$

4.8.2 Shear (S) Connection Calibration

Since S-connection behavior under the type of loading expected during progressive collapse has not been adequately investigated in the past, experimental data for seismic response is used instead to calibrate the model properties. The calibration process entails identification of key attributes of the stress-strain relationships for various connection components.

Bolts are representing by a beam having integration points at the bolt location as shown in Fig. 4.11(b). The J_2 plasticity model described in Section 4.7.1 is used for representing constitutive behavior at integration points. An elastic perfectly plastic model is assumed for each bolt. The area associated with each integration point is determined from the bolt design strength. Bolt strength is taken as the minimum of shear and bearing strength and is given by AISC Construction Manual (2005):

$$\text{Bolt Strength } F_{bolt} = \min\{F_s, F_b\} \tag{4.82}$$

$$\text{Shear Strenght: } F_s = F_{nv} A_b \tag{4.83}$$

$$Bearing\ Strength: F_b = 1.5 L_c t F_u \leq 3 d t F_u \tag{4.84}$$

where F_{nv} is the nominal shear stress in bearing type connections; A_b is the cross sectional area of bolt; d is the bolt diameter; t is the thickness of the connection part; L_c is the clear distance in the direction parallel to the applied load; F_u is the ultimate tensile stress of the connected part. The area at each integration point, A_{int}, is then given by:

$A_{int} = F_{bolt}/F_{nv}$. The fracture plastic strains value is determined from available experimental results from SAC research on the available plastic rotational capacity of simple bolted shear type connections, designed using methods of AISC LRFD specifications. When adequate clearance between the beam flange and column flange is present so that bearing is avoided, the plastic rotational capacity of the connection is then given by:

$$\theta_{p,max} = 0.15 - 0.0036 d_{bg} \tag{4.85}$$

where d_{bg} is the depth of bolt group. An additional elastic rotational capacity of these connections is estimated as 0.02 radians. This gives a total estimated rotational capacity of such connections:

$$\theta_{t,max} = 0.17 - 0.0036 d_{bg} \tag{4.86}$$

When a beam is installed close to the column, the top and bottom edges of the beam have the potential of bearing against the column. FEMA-355D (2000) suggests that the connection flexural strength rises substantially when this happens. Testing reported in FEMA-355D (2000) has shown that the connection has essentially exhausted its ductility when binding occurs. Therefore the maximum rotation is limited by:

$$\theta_{t,max} = \frac{g}{d_{max}} \tag{4.87}$$

where g is the gap and d_{max} is the larger of d_1 and d_2 in Fig. 4.23. Using the smaller of $\theta_{t,max}$ from Eq. 4.86 and 4.87, the deformation limit for the bolt is given by:

$$\Delta_{b,max} = s_{max}\, \theta_{t,max} \tag{4.88}$$

where s_{max} is the distance of the center of the bolt group to the most distance bolt. The fracture strain is for bolt integration point is then given by:

$$e_{f,bolt} = \frac{\Delta_{b,max}}{l_t} \tag{4.89}$$

where l_t is the size of force transfer region.

The concrete spring acts in the plane of the concrete slab. However for modeling convenience it is assumed to act at the top flange of the beam. A bilinear force-displacement relationship is assumed for the compression behavior of the spring as

shown in Fig. 4.24. The strength of the concrete spring is calculated from the following equation (FEMA-355D, 2000):

$$F_c = 0.85 f_c' b_{fc} t_s \tag{4.90}$$

where b_{fc} is the flange width of the column, t_s is the concrete slab thickness and f_c' is the concrete strength in compression. The extra strength provided by the composite action is lost when the plastic rotation reaches a critical value (FEMA-355D, 2000):

$$\theta_{c,max} = 0.029 - 0.0002 d_{bg} \tag{4.91}$$

Therefore the deformation limit for the concrete spring is:

$$\delta_f = \theta_{c,max} d_t \tag{4.92}$$

where d_t is the distance between the center of the bolt group and the center line of the slab. At this level, the compression capacity of the slab is assumed to drop to zero. The tensile capacity of the concrete spring is assumed to be negligible. The stiffness of the concrete spring, K_c, is estimated as:

$$K_c = \frac{E_c b_{fc} t_s}{l_t} \tag{4.93}$$

where E_c is the stiffness modulus for concrete.

To show that the proposed model for S-connection yields reasonable results, the model response is compared to previously published experimental results. Liu and Astaneh (2004) tested a number of shear tab connections under reversed cyclic loading. Figure 4.25 shows an envelope of their normalized experimental data for the 9 specimens they tested. Also plotted in the figure is the result of the model shown in Fig. 4.9 and 4.11. A 0.5 inch gap is assumed to exist between the beam flange and the column flange in the model. As shown in Fig. 4.25, individual bolt failures are manifested as a sudden drop in the moment capacity of the connection, with the connection losing all moment strength when all bolts fail (3 in this particular case). The figure also shows that the effect of binding on negative bending strength is significant; it not only markedly increases strength, but also leads to a reduction in ductility.

A close examination of the figure shows that the model underestimates negative moment capacity at low plastic rotations ranging from 0 to -0.05 radians. This is attributed to the

fact that the steel, metals deck and tension stiffening in the concrete slab are not represented in the model. These effects, however, disappear at larger rotations and the model approaches the experimental data when binding does not occur. At larger negative plastic rotations and for all positive plastic rotations, the model captures overall behavior rather well, including the effect of binding. Since binding is a variable that depends on construction tolerances which are inherently unpredictable, it is not considered further in this work.

4.8.3 Shear Link Calibration

Test data in Arce (2002) is used to evaluate the accuracy of the proposed shear link model. As shown in Fig. 4.26, Arce (2002) tested shear links made from ASTM A992 steel (F_y = 50 ksi) to investigate the adequacy of current requirements for EBF links with higher nominal strength. Figure 4.27 shows a comparison between model results and the envelope of the cyclic experimental results for Link 4A. Good comparison is achieved in the initial stiffness, yield strength and post-yield stiffness. The macro model, however, predicts a much larger failure displacement than observed experimentally, partly because the test employed a severe loading regimen that resulted in premature failure and also because of non standard test details that promoted early web fracture. In spite of this discrepancy, the proposed model should be capable of accurately representing shear links that conform to the AISC Seismic (2005) specifications.

4.8.4 Brace Calibration

Brace member properties are tailored to simulate its overall behavior, including buckling and post bucking response, as observed in experimental results. Test data from experimental studies done by Popov et al. (1979) and Lee et al. (1987) are used to calibrate the brace properties. Important properties that are calibrated include constitutive behavior at the integration points and initial imperfection. To ensure that the macro model captures the main modes of behavior exhibited by the braces, different stress strain curves for both tension and compression are used; the tensile response accounts for strain

hardening, while the compressive response accounts for the effects of local buckling. Using information from the available test data, the general shapes of stress-strain responses in Fig. 4.17(a) and (b) were found to be adequate for accounting for the main modes of behavior. A hardening modulus of 2% and is assumed for both compression and tension, while 5% softening is considered in compression. Fracture of braces is not considered since buckling is assumed to be the dominant failure mode.

To validate the brace model experimental results from Popov et al. (1979) are compared to those obtained from the numerical model. Popov et al. (1979) studied the cyclic inelastic buckling of tubular braces in a Southern California offshore platform. Test result of one of the tested struts (Strut-1) is presented here. The diameter of strut was 4 inches and the wall thickness was 0.083 inches. Imperfection in form of measured initial camber is applied at as shown in Fig 4.14. Yield strength of steel is 32 ksi and constitutive properties in Fig. 4.17 are used. The analytical versus test results for axial force–displacement response are plotted in Fig. 4.28. This result shows that the structural scale model reasonably reproduces the inelastic buckling and post buckling behavior of the strut.

In another validation study, brace model results are compared to test data in Lee and Goel (1987). Lee and Goel (1987) tested 13 brace specimens with hollow and concrete filled HSS sections under reversed cyclic loading. The test results for one of the tested hollow braces with HSS 4×4×1/4 cross-section is used for validation. This particular brace was selected because it had the same compactness as the braces in the prototype building and also the same type of end connections, i.e. a cross gusset plate connection. Although the HSS 4×4×1/4 member has a compact section, it experienced both global and local buckling effects, particularly at larger deformations. The yield strength of steel is 74 ksi. Figure 4.29 shows a comparison between model results and the envelope of cyclic test results obtained by Lee and Goel (1987). Good comparison is achieved; in particular, the model accurately represents the buckling strength and post buckling response of the tested specimen.

4.9 Simulation setup

Two-dimensional models of the two moment frames (Fig. 4.3 and Fig. 4.4) and two braced frames (Fig. 4.7 and Fig. 4.8) are represented using the developed structural scale models. Tables 4.4 to 4.10 gives the important properties of members and elements used in the simulation models. Frame loads are computed from the design specifications in Liang et al. (2006) and Ghosh (2006), and account for the dead loads plus 25 % of the live loads. The gravity loads are slowly ramped up during a 5 sec period then they are held constant for an additional 2.5 sec to avoid exciting dynamic effects. Once the gravity loads have been fully applied at 7.5 sec, a 1st floor column and its associated brace members (if it exists) are forcibly removed by instantaneously deleting them (as shown in Fig. 4.30), and the subsequent response of each braced frame is then investigated. The simulations are conducted with 5 percent mass proportional damping.

Table 4.2 and Table 4.3 show the list of APM analysis cases considered in this study together with the members that are forcibly removed in each case. To facilitate the following discussion, the columns, beams and braces are designated as follows: e.g. column C-1 represents a first story column in column line C (Fig. 4.3); similarly, beam CD-2 represents a second story beam in bay CD (Fig. 4.3); while brace members in the first story are represented by letters A, B, C or D as shown in Fig. 4.7 and 4.8. Important response quantities of interest obtained from the above APM cases are presented in Fig. 4.31 to 4.45.

4.10 Assumptions and limitations of the simulation model

The developed models have a number of assumptions and limitations that should be taken into consideration when evaluating the results of this research. It is assumed that the fixed foundations are able to withstand the redistribution of forces that occurs when individual columns are removed. Debris impact loads due to separating pieces are not considered in the simulations. Fracture is permitted to occur only in the connection regions, i.e. beam, column and brace members cannot fracture and separate into two or more pieces. They

can however, respond in an inelastic manner if required. Subsequent analysis of simulation results show that strains in the beams and columns do not approach the high strain levels observed in the connection regions, i.e. it is unlikely that any beams or columns will undergo fracture for the simulation period of interest. Furthermore, strain rates during the period of interest are observed to be in the seismic loading range, i.e. rather low, which justifies not accounting for strain rate effects in the analysis model. Another primary assumption is that the responses of the 2-D models are representative of the response of the 3-D buildings when a column is lost. The calibration model does take into account some critical 3-D effects such as local and global buckling. However, the beneficial effects of structural components outside of the plane of the frames including the slab are not considered in the analysis. The compressive strength of the slab and its contribution to the moment capacity of the S-connection is, however, accounted for.

4.11 Moment system response to sudden member loss

4.11.1 IMF building system

When column F-1 is suddenly removed (APM case 1 in Table 4.2), the node corresponding to the top of the column vibrates substantially reaching a peak vertical displacement of 5 inches (Fig. 4.31(e)). The response eventually damps out coming to rest at 2.9 inch. The final axial force in column E-1 increases from 322 kips to 550 kips. Frame action in the remaining intact system creates a peak compressive force of 66 kips in the first floor beam EF-1 and a peak tensile force of 19 kips in the top floor beam EF-10. No significant catenary effects develop in this case.

Removal of columns E-1 and D-1 (APM case 2 and 3) result in almost identical responses. The peak vertical displacements corresponding to top column nodes are 3.2 inches and 3.3 inches, respectively, and the final equilibrium displacements are 1.7 inches and 1.73 inches, respectively. Low tensile forces occurred in the affected first floor beams in both cases, but the deformations are not large enough to activate catenary action in the beams.

Removal of column C-1 led to a relatively large deformation at the node corresponding to the top of the column. The peak vertical displacement in this case is 9.4 inches and the damped response is 7.7 inches (Fig. 4.34(f)). The relatively large displacements led to the development of a peak catenary force of 22 kips in the gravity beam BC-1. However, the demands on this beam are not large enough to precipitate failure in the shear connections. Inelastic behavior occurs in the frame in plastic hinge regions in bay CD and in shear connections in bay BC as shown in Fig. 4.34(a). The black circles in Fig. 4.34(a) show the locations where beam cross-sections are partially plastified. Very large force redistribution is observed. For example, as shown in Fig. 4.34(b), the axial force in first-floor column D-1 triples from 319 kips to a peak load of 994 kips before settling down at 822 kips. Even though the simulation predicts 'no-collapse', the large axial force that develops in first-floor column D-1 is concerning. This force is only about 10% below the 1124 kips axial design capacity of the column (with $\phi = 1.0$) and, together with the peak moment that develops, exceed the design axial/flexural interaction capacity of the column by 18%. These peak demands develop during a short duration (0.24 seconds) and quickly retreat to below the design capacity of the column, where the final design interaction demand is 0.86. However, given the non-ductile nature of compressive column failure, it appears that the frame is vulnerable to collapse.

Removal of column B-1 created catenary forces that initially overloaded the shear connections in the lower levels of the corresponding bays (Fig. 4.35(a)). The shear connection failures traveled up the frame as the affected bays progressively collapsed and the simulation therefore shows that both bays AB and BC could suffer collapse. It is possible that the bay adjacent to the collapsing bays, i.e. bay CD (for column loss B-1) could suffer damage by potential debris impact.

Column A-1 in the IMF is not truly a 'gravity' column, since it belongs to a moment frame in the transverse direction (Fig 4.1). Given the results associated with loss of column F-1, it is unlikely that loss of column A-1 will lead to collapse.

4.11.2 SMF building system

Three APM analyses (cases 6, 7, and 8) are conducted due to symmetry, i.e. removal of first story columns D-1, E-1 and F-1. The resulting damaged systems are able to successfully absorb unbalanced forces in all 3 cases, i.e. the simulations predict that the system will not collapse for these scenarios. Elastic system behavior occurs when columns E-1 and F-1 are removed, but some inelastic behavior occurs when column D-1 column is removed. The panel zones behaved in an elastic manner in all three cases.

With the loss of column D-1, the peak vertical displacement of the node corresponding to the top of the column D-1 is 6.5 inches. The response eventually damps out coming to rest at 5.23 inches. This scenario leads to the development of a peak tensile force of 45 kips in gravity beam CD-1. The demands on the shear connections, however, are not large enough to precipitate failure. This scenario also leads to a substantial redistribution of forces where the axial force in column E-1 increase from 329 kips to a peak value of 945 kips. Unlike the C-1 scenario in the IMF frame, the peak demands remains well below the column design capacity (Fig. 4.36(b)). As shown in Figure 4.36(a), the RBS regions of beams in bay DE and shear connections in bay CD undergo some inelastic behavior.

4.11.3 Discussion of results for moment frames

The simulation results suggest that the SMF building designed for high seismic risk is generally less vulnerable to progressive collapse than the IMF building designed for moderate seismic risk. There are two reasons for this. First, the structural layout for the SMF building is somewhat better than that for the IMF building in that it includes fewer gravity columns on the perimeter. Gravity bays with one or more gravity columns are vulnerable to the increased force and deformation demands imposed by the system when it loses a first floor gravity column. The SMF building has only one such column on each NS frames and none on the EW frames. The IMF building, on the other hand, has a total of 4 gravity columns, one in each of the 4 exterior faces of the building. Second,

members of the moment bays in the SMF building are stronger and stiffer than corresponding members of the IMF building, which facilitates force redistribution when critical members are lost.

The deformations associated with column loss in the moment bays are rather small, which prevents catenary action from developing fully. The inelastic deformation demands are not large and are well within the capacity of the seismic detailing employed, which implies that the frames do not benefit from the ductility of seismic detailing for the scenarios investigated. Column loss is resisted primarily through frame action that mobilizes members throughout the entire frame.

In contrast, catenary action does develop in gravity bays and plays a critical role in providing resistance against collapse. Since catenary action only develops after large deformations occur, gravity connections must therefore be ductile enough to permit catenary action to occur and must also be strong enough to resist the large tensile catenary forces that develop. Based on the limited simulation exercises presented, it appears that the shear tab connections considered herein have the necessary ductility, but not the strength to resist progressive collapse. As previously mentioned, the resistance of gravity bays to collapse must take into consideration the effect of catenary action in the slab. However, without a full 3-D analysis, it is difficult to determine the beneficial effect of this source of resistance and whether catenary action in the slabs combined with catenary action in the beams is sufficient to mitigate collapse.

The APM analyses presented show that substantial redistribution of forces occurs for cases where the building frame survives a column loss. However, the APM analyses do not provide information about the reserve capacity of the frame. For example, the simulation results predict that the loss of column C-1 in the IMF will not lead to progressive collapse, whereas engineering judgment, based on the design capacity of the adjacent column, suggests that this is likely a critical situation.

4.12 Braced system response to sudden member loss

4.12.1 SCBF building system

When the corner column A-1 is suddenly removed (APM Case I in Table 4.3), the shear connections in the lower floors in bay AB are initially overloaded and start deforming inelastically. The shear connection at the right end of beam AB-1 fails first at a vertical displacement of 35 inches. Shear connection failures propagate up the frame as the affected bay AB progressively collapses as shown in Fig. 4.39(a). It is possible that the bay adjacent to the collapsing bays, i.e. bay BC could suffer damage by potential debris impact from the collapsing bay.

APM Case II involves sudden removal of column B-1 and brace A. The simulation results show that the system is able to successfully absorb the loss of the two members. The node corresponding to the top of the removed column vibrates substantially reaching a peak vertical displacement of 1.3 inches. The response eventually damps out coming to rest at 0.94 inches as shown in Fig. 4.40(f). A large redistribution of forces is observed to take place as shown in Fig. 4.40(b). For example, the force in column C-1 doubles from 445 kips to a peak of 901 kips before settling down at a steady value of 759 kips. The peak compression force is accompanied by a peak moment of 123 k-ft. Concurrently, the force in brace B spikes from 36 kips to a peak value of 283 kips before settling down at a steady value of 248 kips. Other frame members and connections remain in the elastic regime.

By assuming a strength reduction factor of 1.0 and an effective length factor, K=1.0, the axial capacity of column C-1 (a W14×233) is 2827 kips. This is substantially more than the peak load computed in that column, which when combined with the relatively small moment generated on the column, implies that the column will not be overloaded. More seriously, however, is brace B, which is a HSS7×7×½. Assuming a strength reduction factor of 1.0 and an effective length factor, K = 0.85, the capacity of this brace is 312 kips. This is only 10 % more than the peak load of 283 kips to which the brace is subjected.

Even though the simulation predicts “no collapse”, the large axial force that develops in brace B is of concern given the non-ductile and softening post buckling behavior of braces. Another simulation (Case III), where brace B is removed simultaneously with column B-1 and brace A, is conducted to investigate whether failure of brace B will initiate progressive collapse. The results of this simulation (Fig. 4.41) show that the system still does not collapse and that the gravity loads tributary to the BC bays are channeled into column C-1. The column, which is designed to support the seismically induced overturning forces, is so massive that is still able to successfully carry all the gravity loads. Bays AB and BC derive their stability from the intact bay DE and they therefore do not collapse. Transmission of loads between the damaged and intact bays takes place through the gravity beams in bay CD. These beams are under significant tension forces, but the members and their gravity connections are able to successfully transmit these loads. The magnified deformed shapes for both cases are shown in Fig. 4.40(a) and 4.41(a).

The sudden simultaneous loss of column C-1 and brace B is considered in APM Case IV. The results of this simulation (Fig. 4.42) are very similar to APM Case II and will therefore not be discussed further.

4.12.2 EBF building system

Three APM analyses are conducted for the EBF frame as outlined in Table 4.3. Loss of corner column A-1 is not considered because it is part of the transverse EBF system. It is deemed not vulnerable based on the previously discussed simulation results for the SCBF where simultaneous loss of column B-1 and braces A and B did not lead to collapse. The simulations results (Fig. 4.43-4.45) shows that the EBF system is capable of successfully absorbing the loss of the various elements considered, i.e. the simulations predict that the system will not collapse for these scenarios. The force levels in the remaining beams, column and braces are small enough that they essentially respond in an elastic manner. The shear links and shear connections also behave in an elastic manner in all 3 cases.

The peak vertical displacements of the nodes corresponding to the top of the removed columns are 1.8 inches, 0.63 inches and 1.93 inches for analyses Cases V, VI and VII, respectively. The corresponding damped out responses are 1.3 inches, 0.47 inches and 1.4 inches respectively. In Case V, the axial force in column C-1 triples from 415 kips to a peak value of 1288 kips. However, this force, combined with the peak moment developed on the column, is well below the capacity of the column. Figure 4.43(b) shows the column force redistribution that occurs in this case. The peak axial force in brace B (HSS 8×8×½) is 51 kips, which is significantly below it nominal axial capacity of 429 kips. The demands are comparably low for Cases VI and VII, signifying that the EBF configuration has much resistance to progressive collapse.

4.12.3 Discussion of results for braced frames

The results of the simulations suggest that the EBF building, which is designed for high seismic risk, is less vulnerable to progressive collapse than the SCBF building, which is designed for moderate seismic risk. An examination of the simulation results shows that the main reasons for the improved response is that the structural layout for the EBF building is better than that for the SCBF building in that it includes no gravity columns on the perimeter (Fig. 4.5 and Fig. 4.6). Gravity bays with one or more gravity columns are vulnerable to the increased force and deformation demands imposed by the system when it loses a first floor gravity column. The EBF building has no such column on its perimeter. The SCBF building, on the other hand, has four gravity columns on the perimeter, one in each of the corner of the building.

An important observation is that none of the seismically designed bays collapsed when one or more critical members were removed. For example, in Case III, column C-1 successfully supported all the gravity loads previously carried by adjacent column B-1 and the two adjacent braces. This is directly a result of seismic design, albeit not ductile detailing, in which the need for lateral seismic resistance fortuitously resulted in sufficient vertical resistance to resist progressive collapse. Clearly, this will occur in perimeter systems, where seismic resistance is concentrated on the exterior of building.

While this is a common practice in the U.S. West Coast, it is also common to place seismic frames within the building, leaving the outside columns as gravity columns, which are vulnerable to first floor column loss, as demonstrated in Case I.

4.13 Summary and Conclusions

The study in this chapter was concerned with the development of computationally efficient structural scale models which can be used for progressive collapse analysis of steel building moment and braced frames using nonlinear dynamic APM. Specifically, structural scale models for three popular connections types: reduced beam sections for SMF, welded unreinforced flange – welded web moment resisting connections for IMF and shear connections, were developed in this work. In addition, models for braces and shear links were proposed for SCBF and EBF. The structural scale models were calibrated and validated through sub-assemblages results obtained in Chapter 3 and through available experimental results. Developed models were then utilized within the context of APM to study the progressive collapse resistance of 2-dimensional, 10-story SMF, IMF, SCBF and EBF buildings designed according to contemporary seismic design specifications and practices. Based on the simulation studies conducted and within the assumptions and limitations described in the chapter, the following conclusions can be drawn. These conclusions are valid only for the particular framing schemes chosen and generalization requires a broader study involving many buildings of different configurations.

1. The SMF designed for high seismic risk is less vulnerable to gravity-induced progressive collapse than the IMF designed for moderate seismic risk. The relative success of SMF versus IMF stems from a somewhat improved layout that consists of more as well as generally stronger moment bays.

2. The simulation results suggest that while SCBF and EBF systems benefited from locating the seismic systems on the perimeter of the buildings, the EBF designed for high seismic risk is less vulnerable to gravity-induced progressive collapse than the

SCBF designed for moderate seismic risk. The relative success of EBF versus SCBF stems essentially from an improved system layout rather than activation of ductile detailing.

3. Ductility demands associated with column loss in the moment bays of all types of buildings are rather small and therefore the advantage of using ductile seismic detailing for mitigating progressive collapse is not evident. The ductility demands are likely small because the moment bays, which are primarily proportioned for lateral seismic loading, carry light gravity loads. This is, nevertheless, a common situation because designers tend to concentrate seismic resistance in a few moment bays arranged mostly around the building perimeter to reduce the number of expensive-to-construct moment resisting connections.

4. Shear tab connections, which are used in gravity bays, have the necessary ductility to develop catenary action. For the system designs considered herein, they do not have the strength to resist progressive collapse once a gravity column is lost. This conclusion is reached without taking into consideration the beneficial effect of catenary action in the slab. However, even if the combined resistance of catenary action in the slab and beams is enough to prevent collapse of adjacent gravity bays, it is likely that large deformations and severe damage will occur in the affected bays. It is therefore recommended that gravity columns not be placed on the perimeter of a seismically designed building when gravity induced progressive collapse due to an external threat, e.g. blast, is a design consideration. If such columns are necessary, structural designers should carefully evaluate collapse resistance of perimeter gravity bays through refined analysis models or detailed simulations methods of the sort proposed here.

5. A nonlinear APM analysis is useful for judging the ability of a system to absorb the loss of a critical member. Compared to an elastic APM analysis, inelastic APM simulation provides more resolution, shows failure progression and provides information on the likelihood of complete versus partial collapse. It does not,

however, provide information about the reserve capacity of the system and so its results should be carefully evaluated.

	Beam depth = 30.2 in		Beam depth = 27.1 in		Beam depth = 21.4 in	
	WUF-W	RBS	WUF-W	RBS	WUF-W	RBS
E_h	2%	2%	2%	2%	2%	2%
E_s	5%	3%	5%	3%	5%	3%
e_o	-	2.55E-02*	-	2.63E-02*	-	2.57E-02*
e_f	0.03	0.06	0.035	0.09	0.04	0.095

*Corresponding to 0.04 radian rotation

Table 4.1 Moment connection calibration parameters

APM Case	Building Frame	Members removed
1	IMF	Column F-1
2	IMF	Column E-1
3	IMF	Column D-1
4	IMF	Column C-1
5	IMF	Column B-1
6	SMF	Column D-1
7	SMF	Column E-1
8	SMF	Column F-1

Table 4.2 Alternate path method (APM) analysis cases for moment frames

APM Case	Building Frame	Members removed
I	SCBF	Column A-1
II	SCBF	Column B-1, Brace A
III	SCBF	Column B-1, Brace A, Brace B
IV	SCBF	Column C-1, Brace B
V	EBF	Column B-1, Brace A
VI	EBF	Column C-1, Brace B, Brace C
VII	EBF	Column B-1, Brace A, Brace B

Table 4.3 Alternate path method (APM) analysis cases for braced frames

Story	Column	Axial Capacity P_u (kips)	Beam	Plastic Moment Capacity M_p (k-ft)
10	W18×55	397	W21×50	458
9	W18×55	397	W21×50	458
8	W18×55	397	W21×50	458
7	W18×97	1073	W24×62	642
6	W18×97	1073	W24×62	642
5	W18×97	1073	W24×76	833
4	W18×97	1073	W24×76	833
3	W18×119	1333	W24×76	833
2	W18×119	1333	W24×76	833
1	W18×119	1124	W24×76	833

Table 4.4 Member properties for IMF (SDC-C)

Story	Column	Axial Capacity P_u (kips)	Beam	Plastic Moment Capacity M_p (k-ft)
10	W24×84	732	W16×26	184
9	W24×117	1366	W21×50	458
8	W24×117	1366	W21×50	458
7	W24×131	1536	W27×94	1158
6	W24×131	1536	W27×94	1158
5	W24×131	1536	W27×94	1158
4	W24×146	1726	W27×94	1158
3	W24×146	1726	W27×94	1158
2	W24×146	1726	W27×94	1158
1	W24×146	1506	W27×94	1158

Table 4.5 Member properties for SMF (SDC-D)

Story	Column	Axial Capacity P_u (kips)	Beam	Plastic Moment Capacity M_p (k-ft)	Brace	Axial Capacity P_n (kips)
10	W14×43	361	W21×50	458	HSS4½×4½×3/8	70
9	W14×43	361	W21×50	458	HSS4½×4½×3/8	70
8	W14×74	789	W21×50	458	HSS5½×5½×3/8	152
7	W14×82	868	W21×50	458	HSS5½×5½×3/8	152
6	W14×120	1531	W21×50	458	HSS6×6×1/2	251
5	W14×132	1685	W21×50	458	HSS6×6×1/2	251
4	W14×176	2290	W21×50	458	HSS6×6×1/2	251
3	W14×193	2515	W21×50	458	HSS6×6×1/2	251
2	W14×193	2515	W21×50	458	HSS7×7×1/2	352
1	W14×233	2827	W24×76	833	HSS7×7×1/2	312

Columns: Effective Length Factor (K) = 1.0, Braces: Effective Length Factor (K) = 0.85

Table 4.6 Member properties for SCBF (SDC-C)

Story	Column	Axial Capacity P_n (kips)	Beam	Plastic Moment Capacity M_p (k-ft)	Brace	Axial Capacity P_n (kips)
10	W14×48	409	W10×39	195	HSS7×7×1/2	367
9	W14×48	409	W10×39	195	HSS7×7×1/2	367
8	W14×61	642	W10×39	195	HSS7×7×1/2	367
7	W14×82	868	W10×39	195	HSS7×7×1/2	367
6	W14×109	1387	W12×45	268	HSS8×8×1/2	469
5	W14×109	1387	W12×45	268	HSS8×8×1/2	469
4	W14×109	1387	W12×45	268	HSS8×8×1/2	469
3	W14×132	1685	W12×45	268	HSS8×8×1/2	469
2	W14×145	1883	W12×45	268	HSS8×8×1/2	469
1	W14×176	2122	W14×48	327	HSS8×8×1/2	429

Columns: Effective Length Factor (K) = 1.0, Braces: Effective Length Factor (K) = 0.85

Table 4.7 Member properties for EBF (SDC-D)

Story	Stiffness (kip/in)	Strength (kips)
1, 2, 3	15100	689
4, 5	12371	544
6, 7	12356	543
8, 9, 10	8796	344

Table 4.8 Panel zone spring properties IMF (SDC-C)

Story	Stiffness (kip/in)	Strength (kips)
1, 2, 3, 4	25788	1348
5, 6, 7,	24787	1274
8, 9	12400	583
10	11415	444

Table 4.9 Panel zone spring properties SMF (SDC-D)

Story	Stiffness (kip/in)	Strength (kips)
1	11730	412
2, 3, 4, 5, 6	14387	402
7, 8, 9, 10	12868	374

Table 4.10 Shear link spring properties EBF (SDC-D)

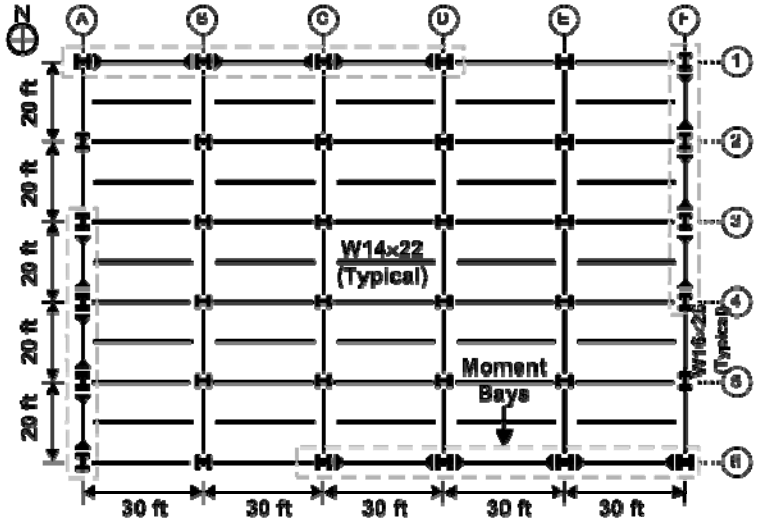

Figure 4.1 Plan layout for IMF building system

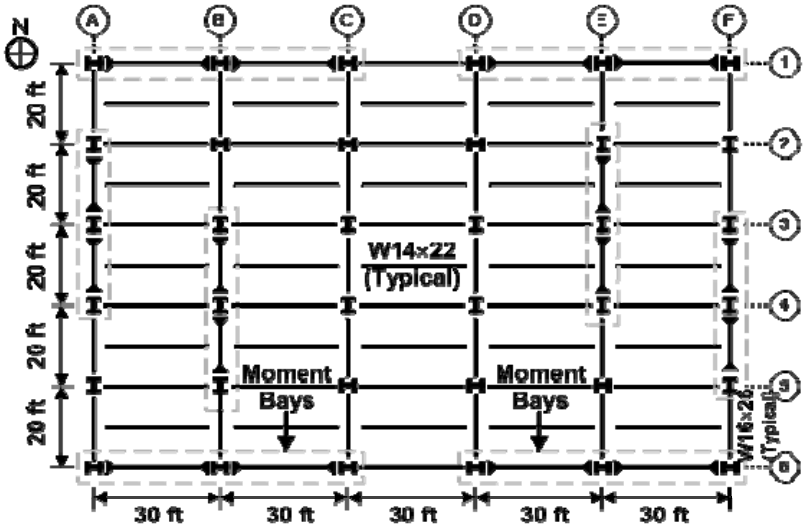

Figure 4.2 Plan layout for SMF building system

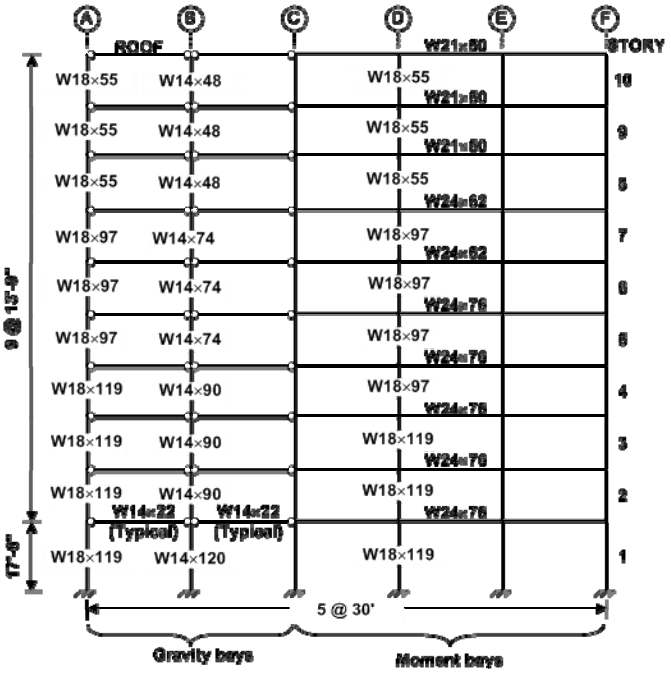

Figure 4.3 IMF Building Frame (SDC-C): E-W Elevation (Line 6)

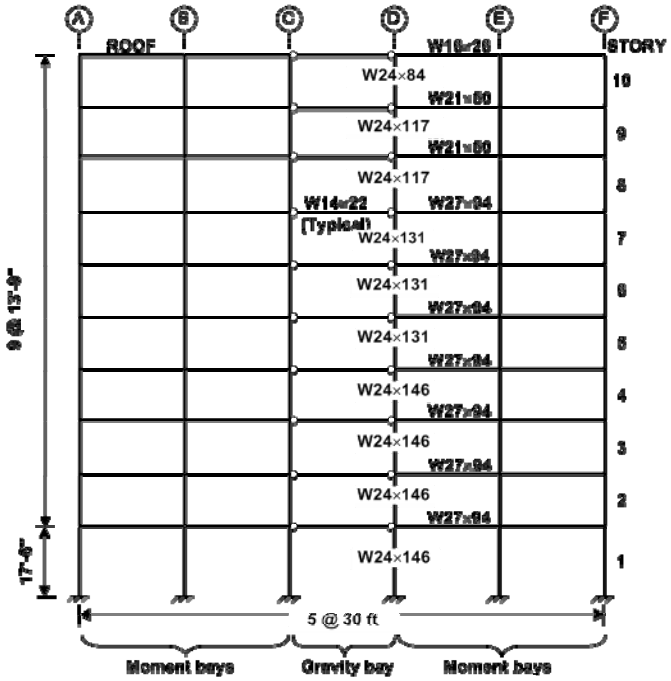

Figure 4.4 SMF Building Frame (SDC-D): E-W Elevation (Line 6)

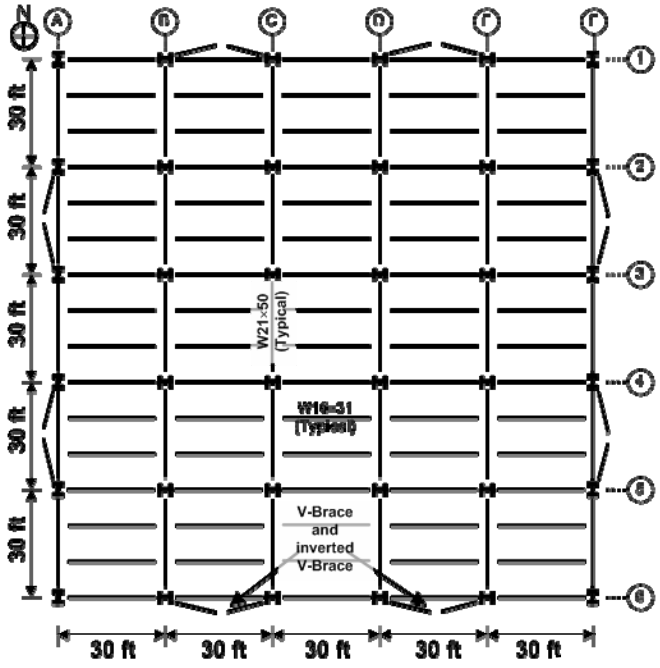

Figure 4.5 Plan layout for SCBF building system

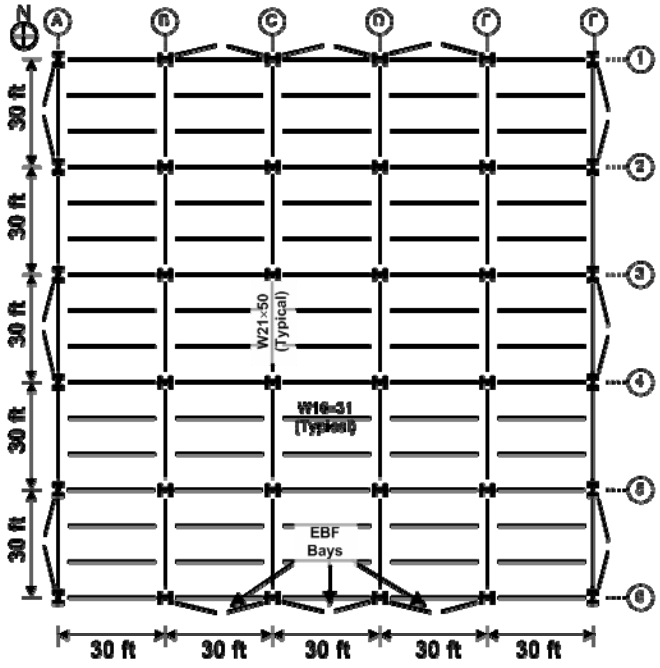

Figure 4.6 Plan layout for EBF building system

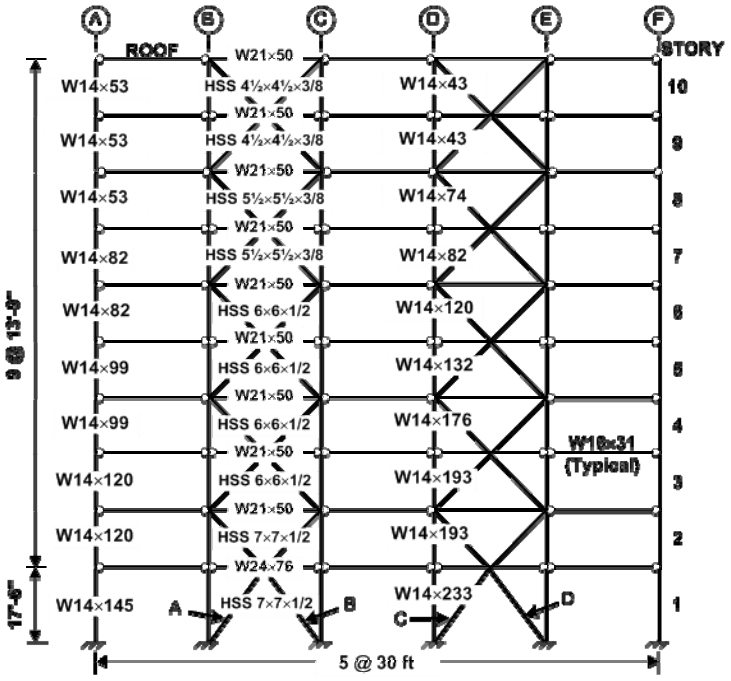

Figure 4.7 SCBF Building Frame (SDC-C): E-W Elevation (Line 6)

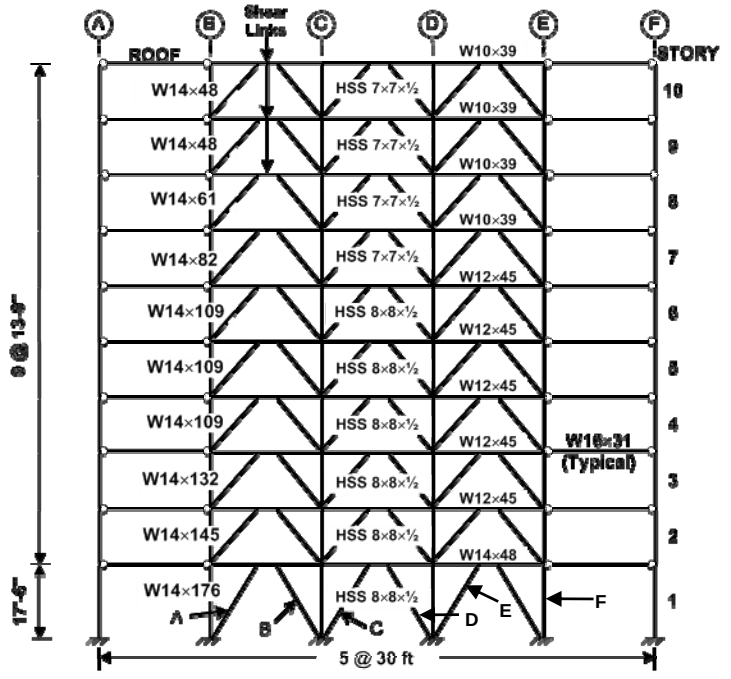

Figure 4.8 EBF Building Frame (SDC-D): E-W Elevation (Line 6)

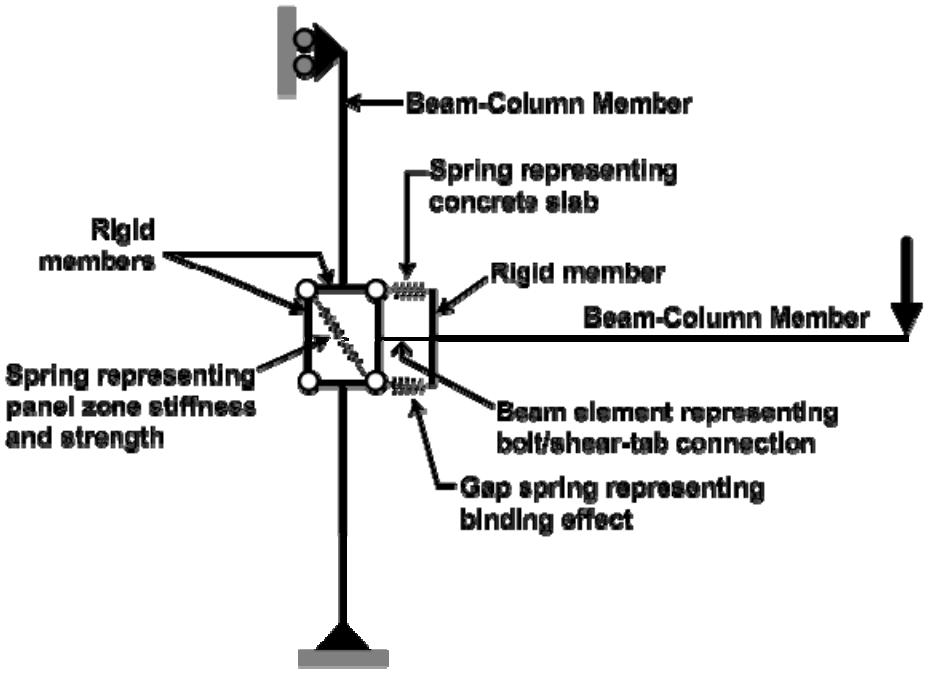

Figure 4.9 Shear (S) connection model

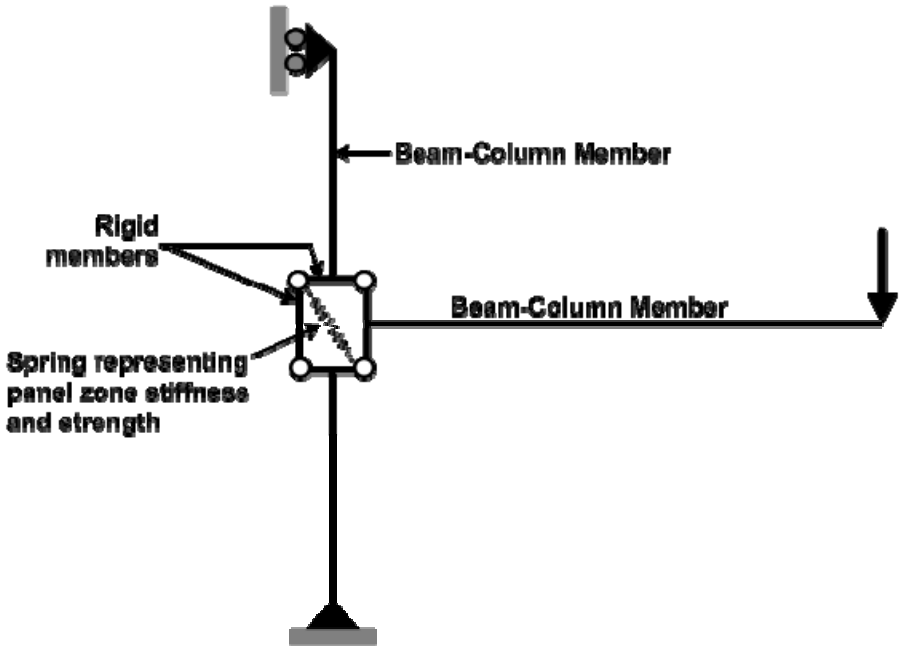

Figure 4.10 Moment connection model

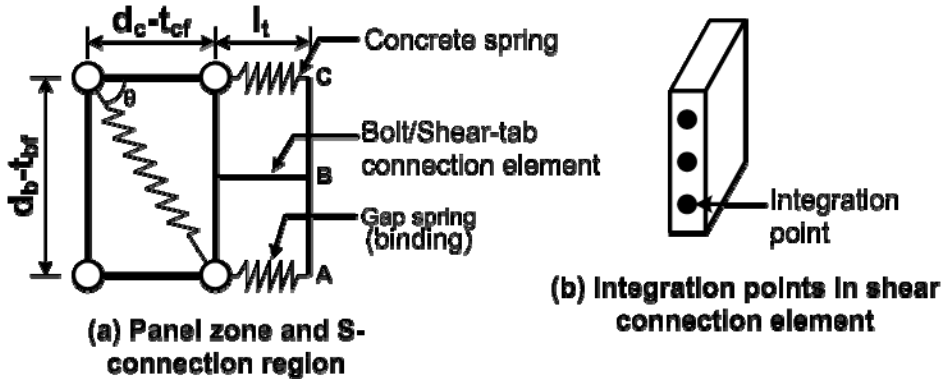

Figure 4.11 Panel zone and S-connection region

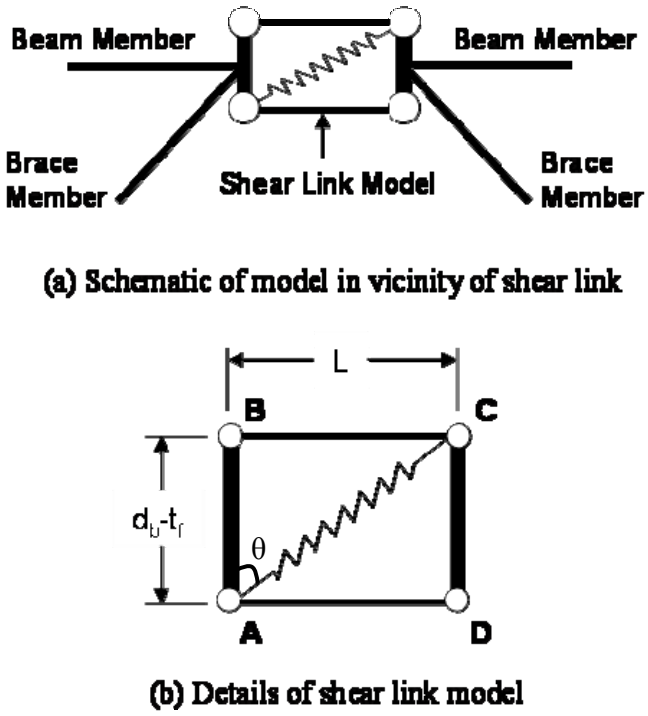

Figure 4.12 Shear Link Model

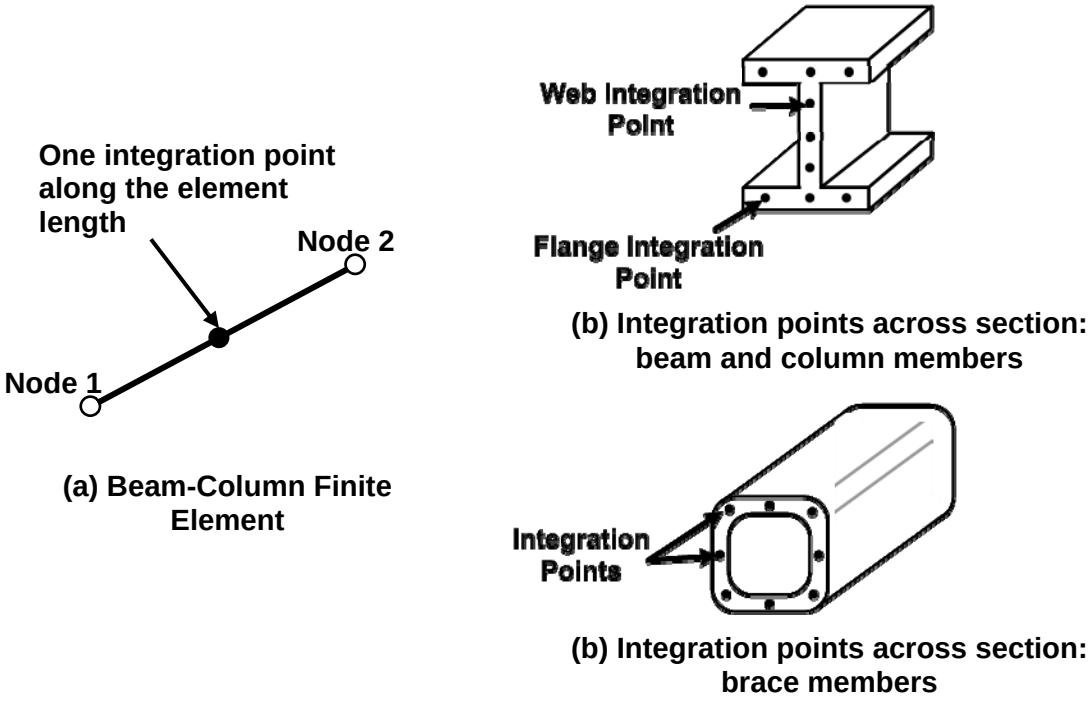

Figure 4.13 Integration points in beam column finite elements

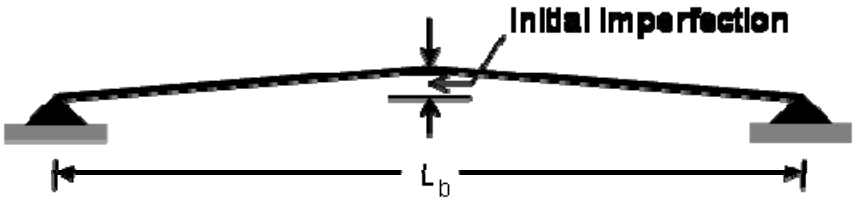

Figure 4.14 Imperfection in brace model

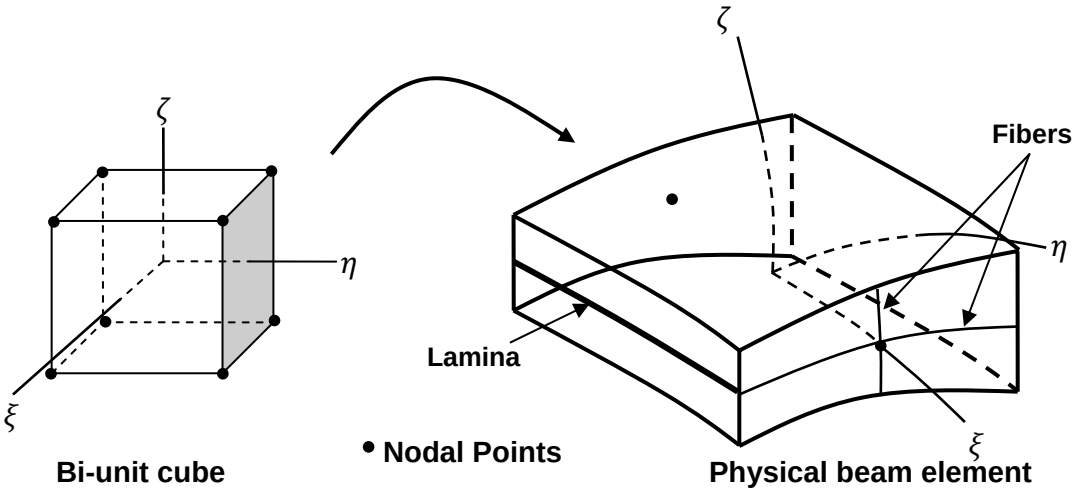

Figure 4.15 Smooth mapping of a bi-unit cube into the physical beam domain

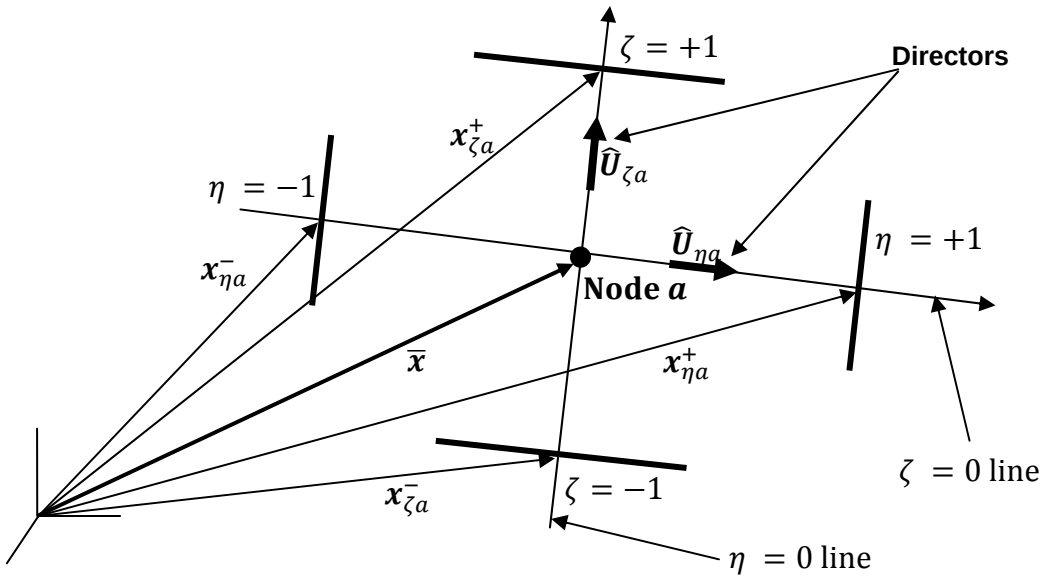

Figure 4.16 Directors at nodal points

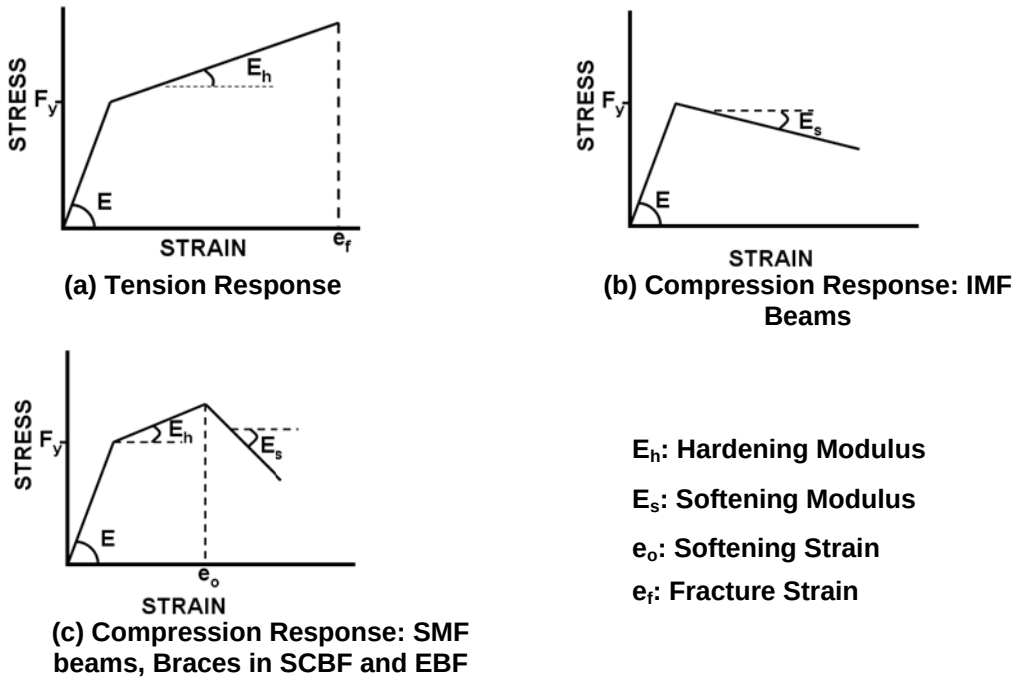

Figure 4.17 Stress strain responses for beam and brace elements

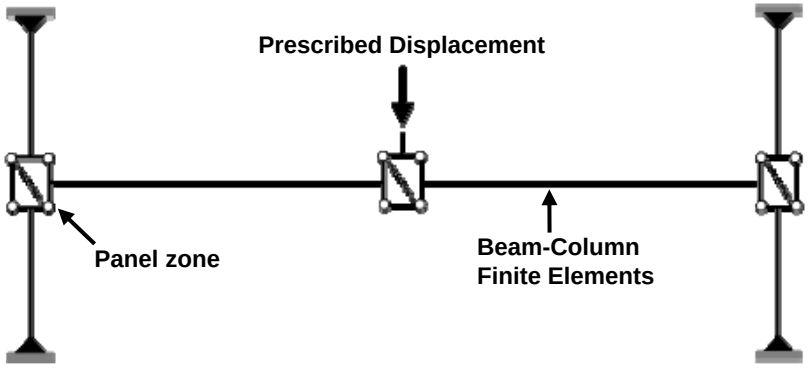

Figure 4.18 Structural scale (SS) model for moment connection calibration

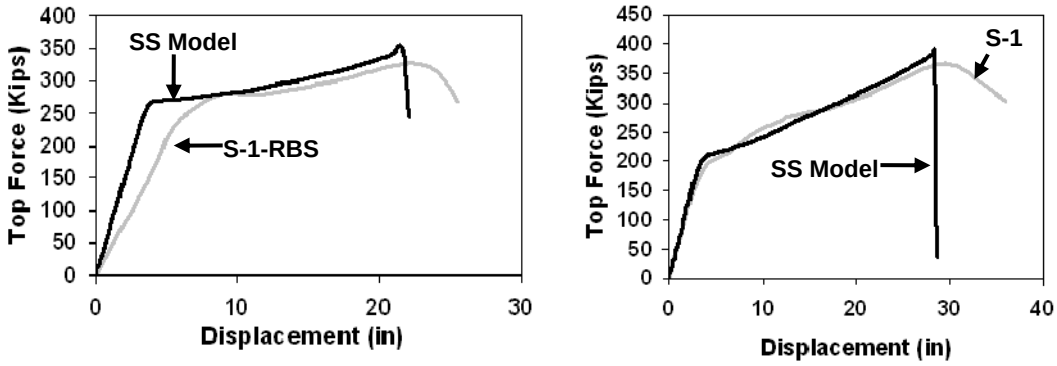

Figure 4.19 Calibration Results: Story-1 sub-assemblages and structural scale (SS) models

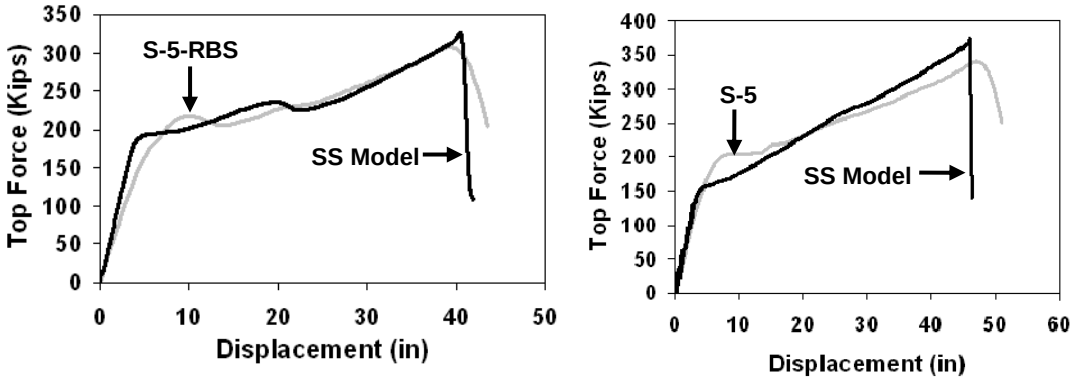

Figure 4.20 Calibration Results: Story-5 sub-assemblages and structural scale (SS) models

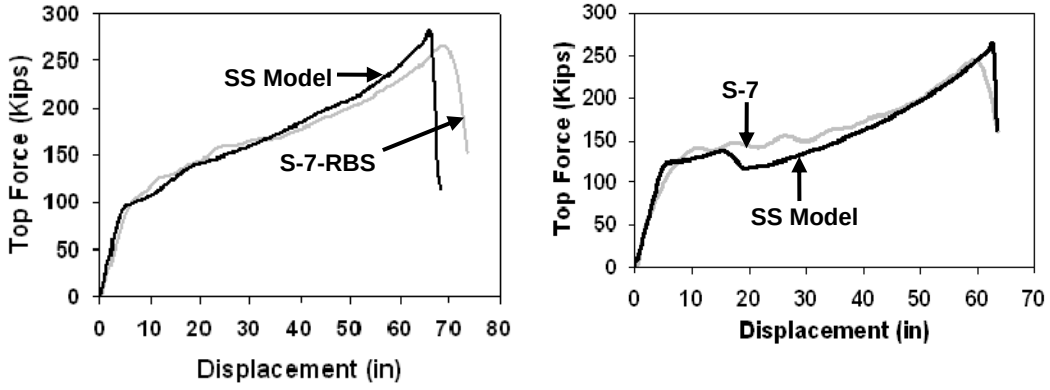

Figure 4.21 Calibration Results: Story-7 sub-assemblages and structural scale (SS) models

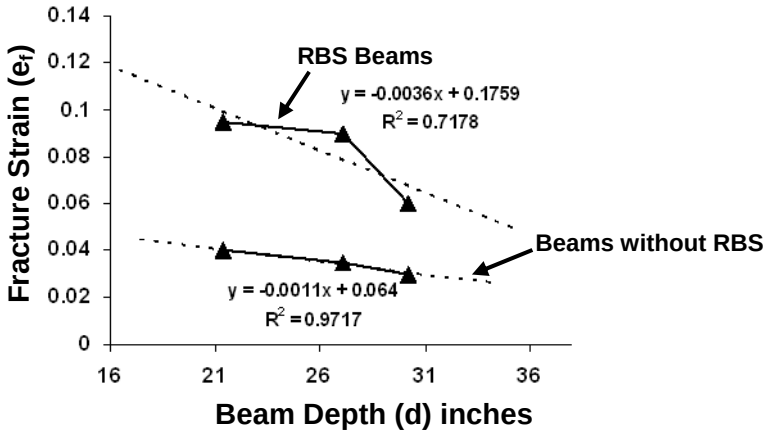

Figure 4.22 Calibration of fracture strain

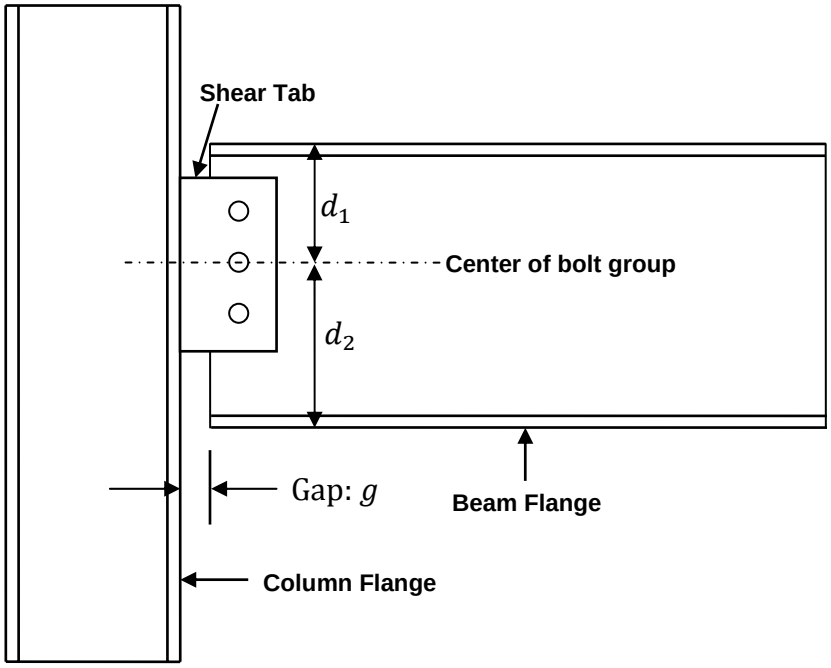

Figure 4.23 Shear connection details

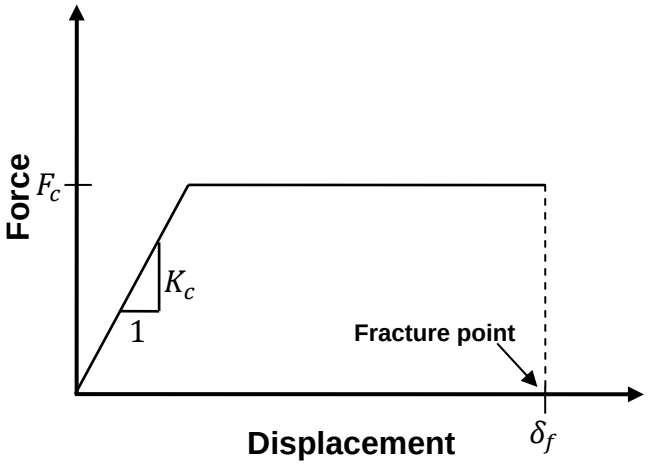

Figure 4.24 Force displacement relationship for concrete spring (compression)

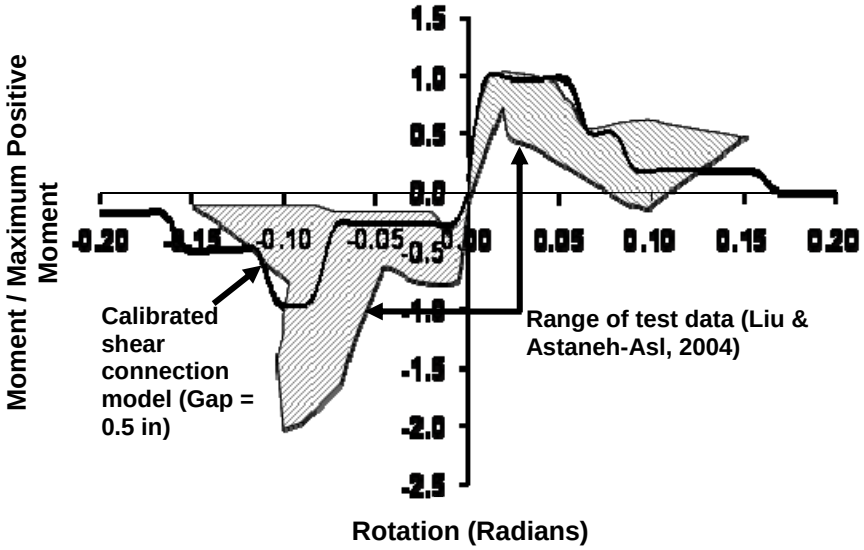

Figure 4.25 Comparison between S-Connection model result and experimental data

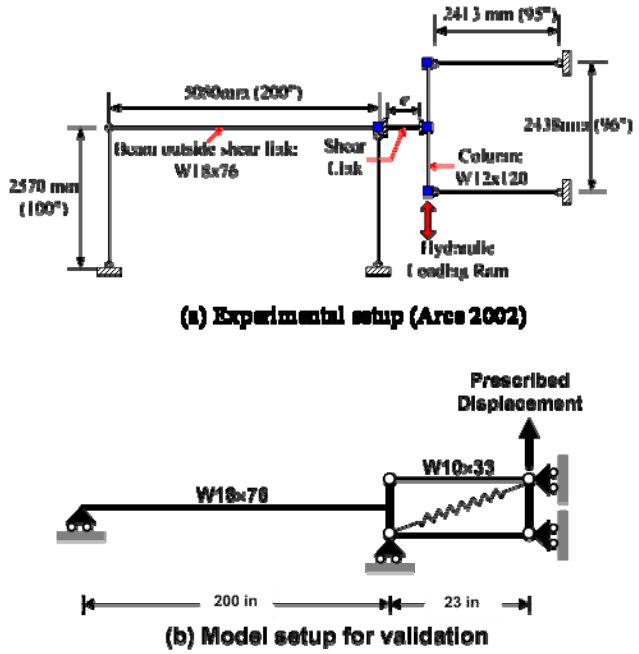

Figure 4.26 Experimental and model setup for validation of shear link model

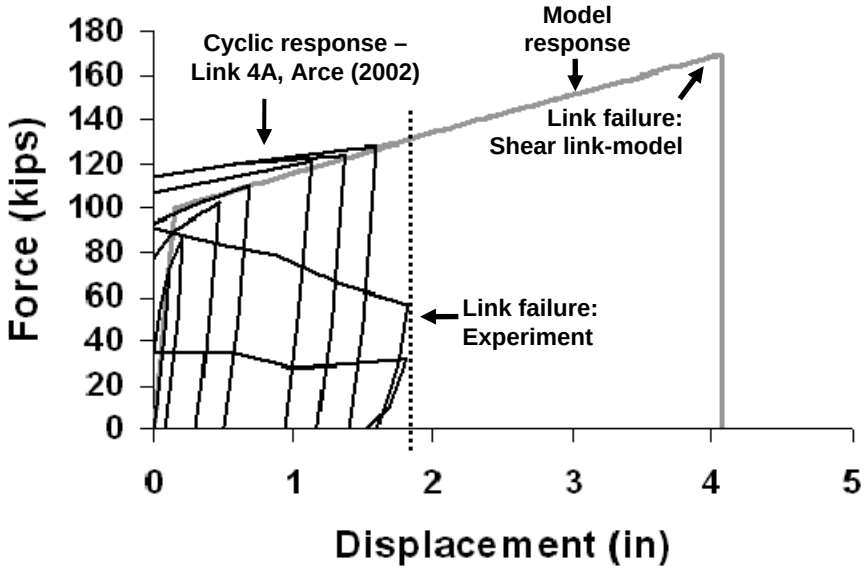

Figure 4.27 Shear link validation- Comparison between test and model data

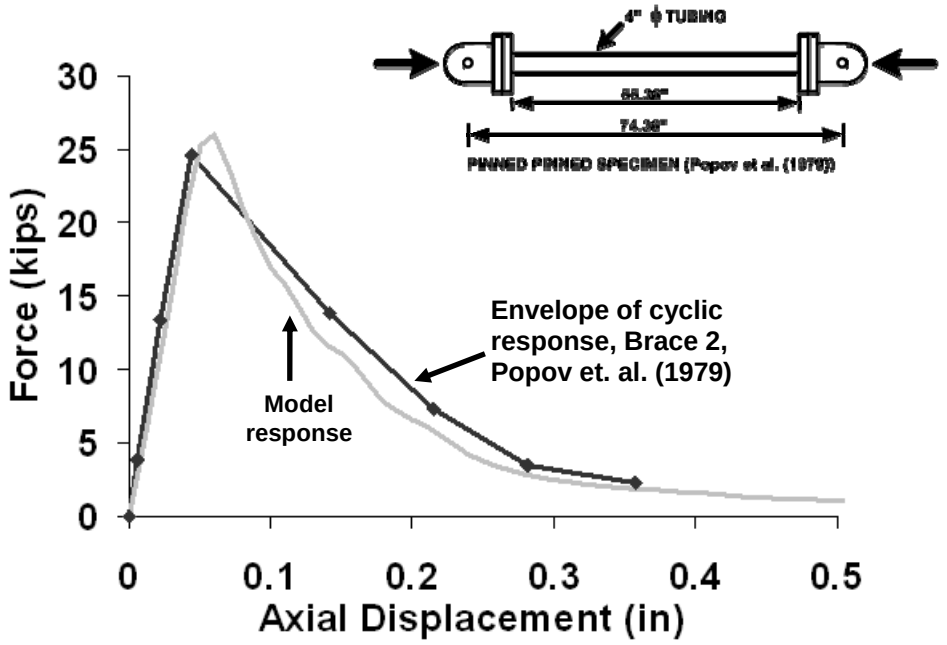

Figure 4.28 Brace validation- Comparison between test and model data

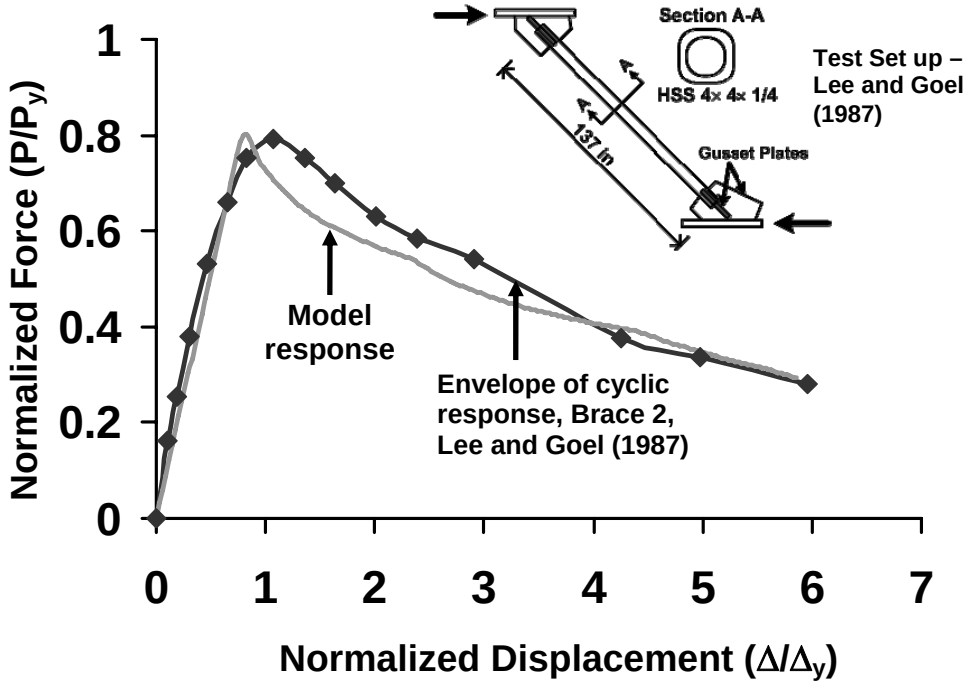

Figure 4.29 Brace validation- Comparison between test and model data

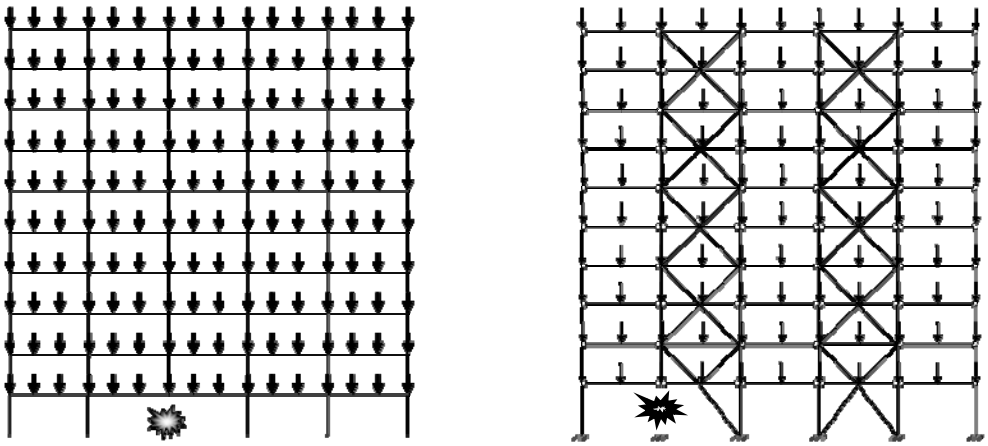

Figure 4.30 Simulation Setup - member/s removed at 7.5 sec

Figure 4.31 Response quantities - APM case-1, IMF F-1 column loss

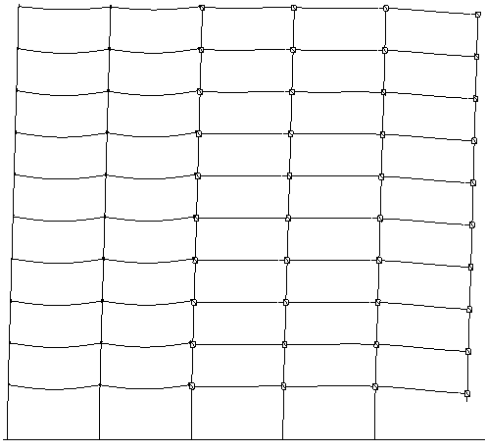

(a) Deformed Shape: Time = 30 sec
Magnification Factor = 10

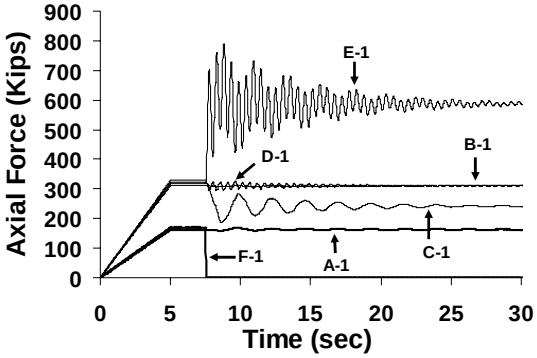

(b) Column Axial Forces

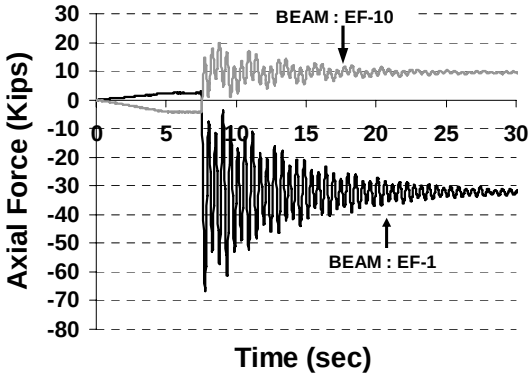

(c) Beam Axial Forces

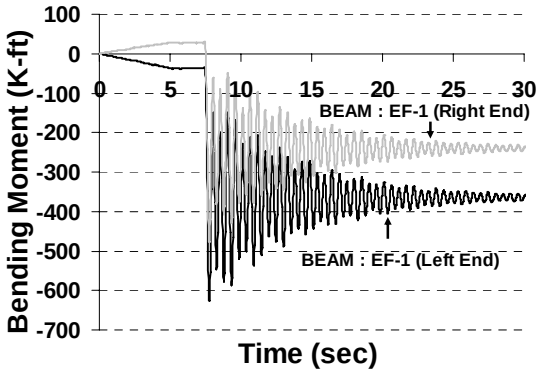

(d) Beam Bending Moments

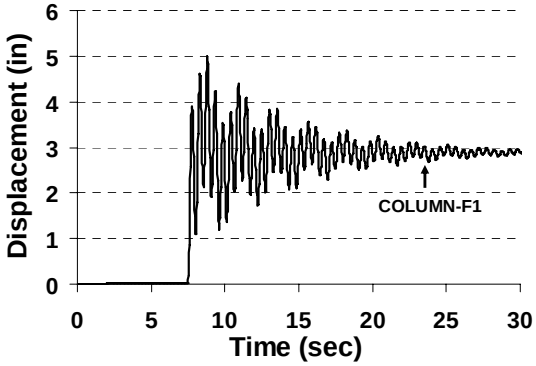

(e) Column Displacement

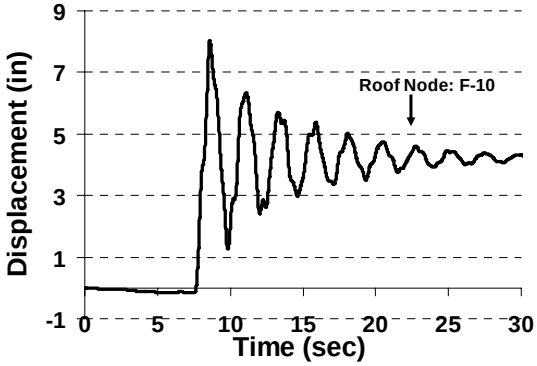

(f) Roof Displacement

Figure 4.32 Response quantities - APM case-2, IMF E-1 column loss

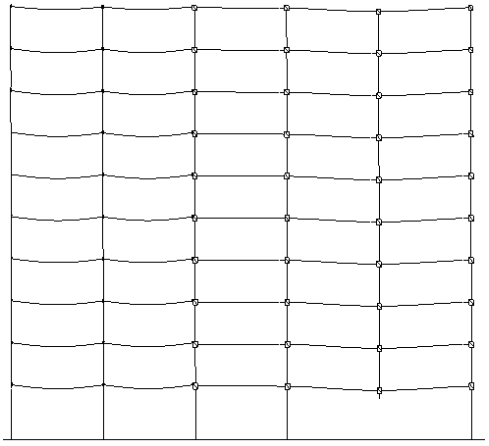

(a) Deformed Shape: Time = 30 sec
Magnification Factor = 10

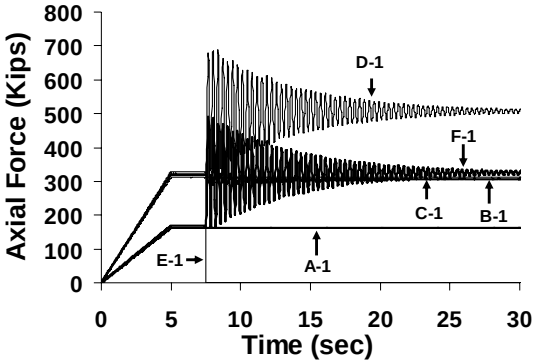

(b) Column Axial Forces

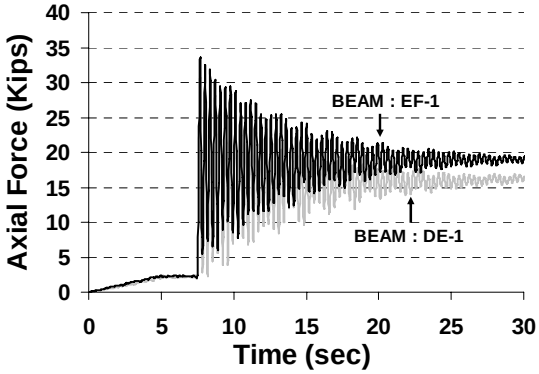

(c) Beam Axial Forces

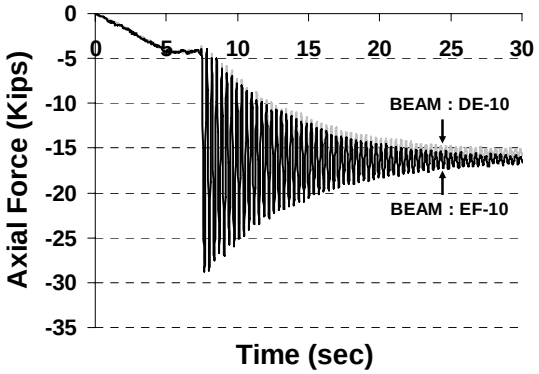

(d) Beam Axial Forces

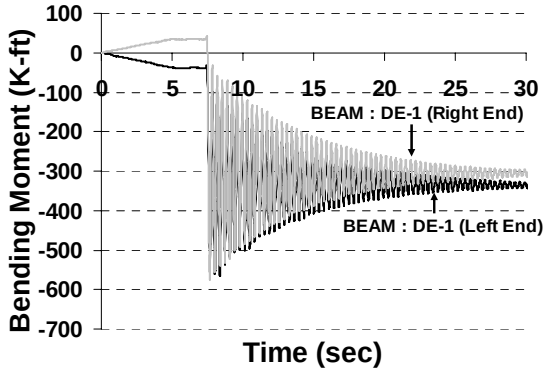

(e) Beam Bending Moments

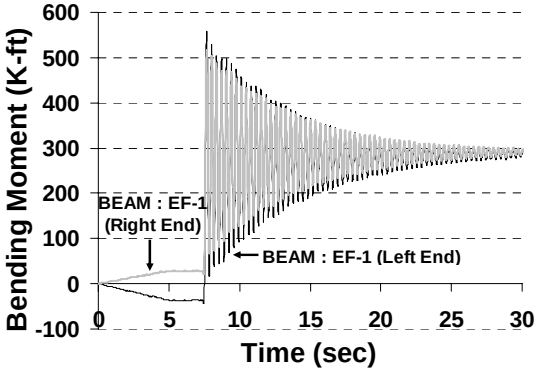

(f) Beam Bending Moments

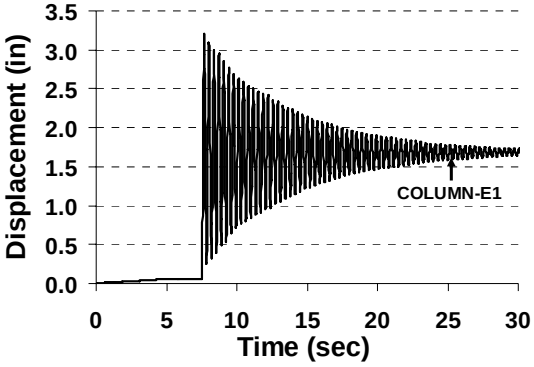

(g) Column Displacement

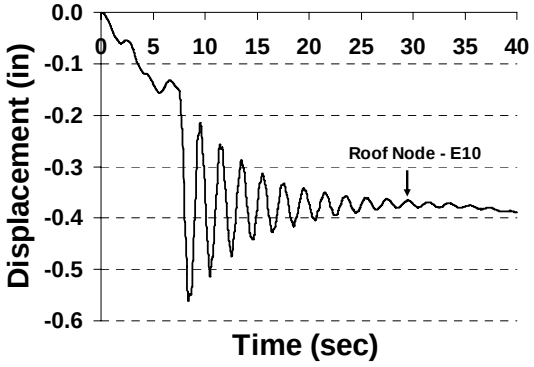

(h) Roof Displacement

Figure 4.33 Response quantities - APM case-3, IMF D-1 column loss

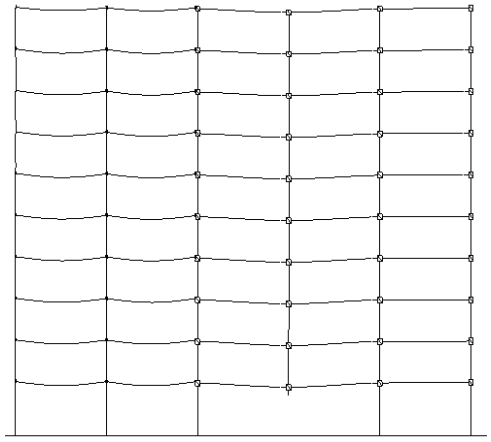

(a) Deformed Shape: Time = 30 sec
Magnification Factor = 10

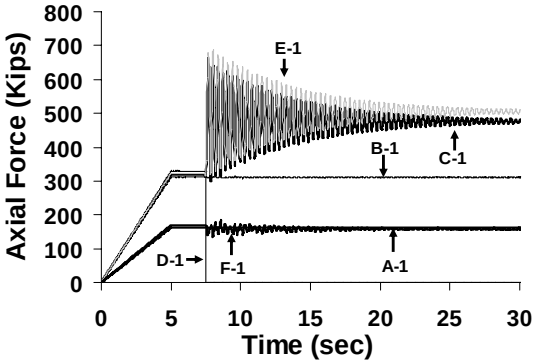

(b) Column Axial Forces

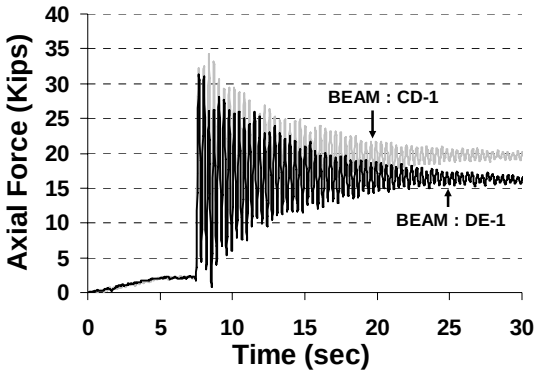

(c) Beam Axial Forces

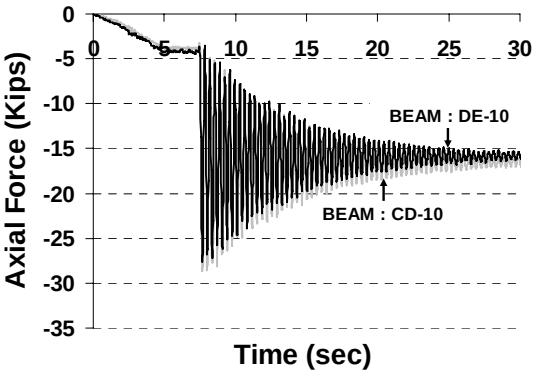

(d) Beam Axial Forces

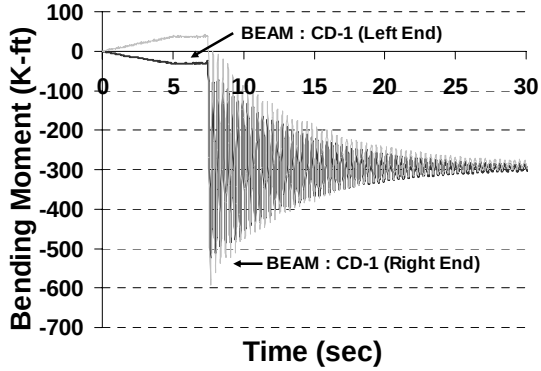

(e) Beam Bending Moments

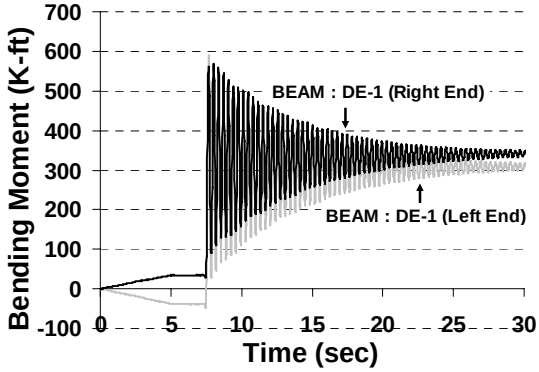

(f) Beam Bending Moments

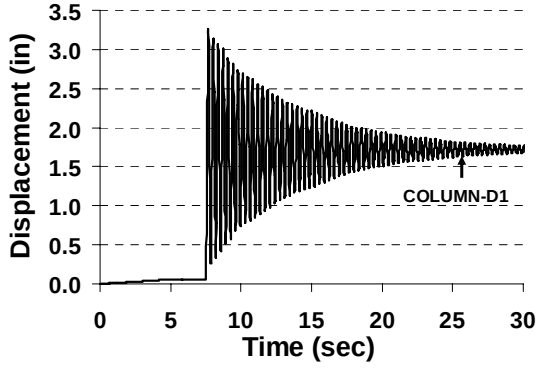

(g) Column Displacement

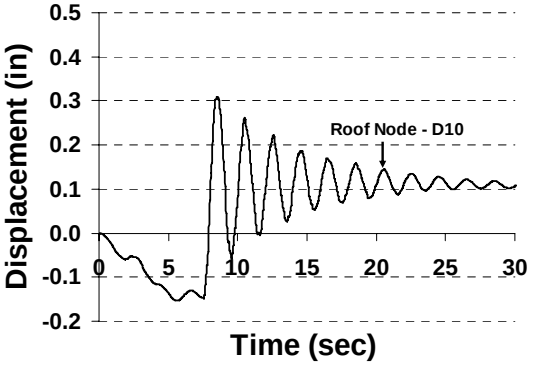

(h) Roof Displacement

Figure 4.34 Response quantities - APM case-4, IMF C-1 column loss

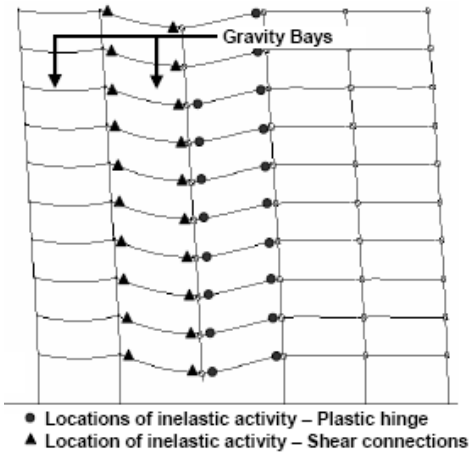

(a) Deformed Shape: Time = 30 sec
Magnification Factor = 10

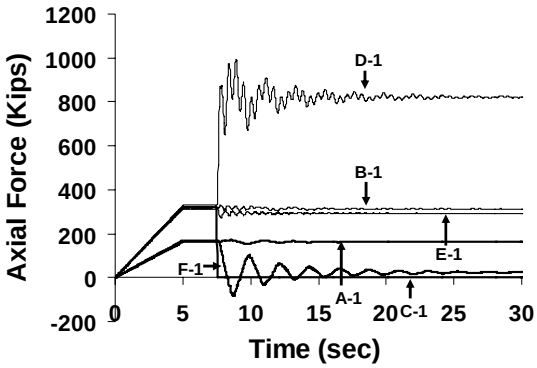

(b) Column Axial Forces

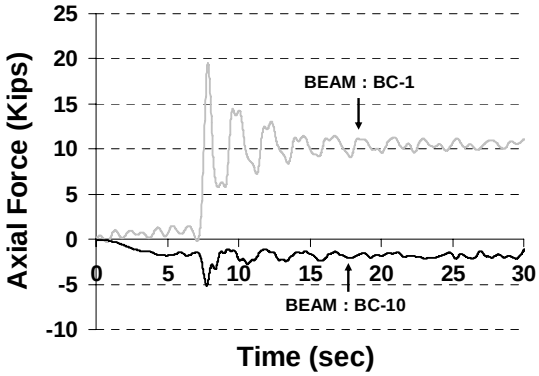

(c) Beam Axial Forces

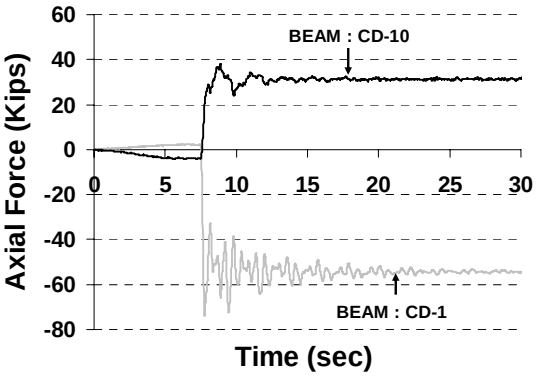

(d) Beam Axial Forces

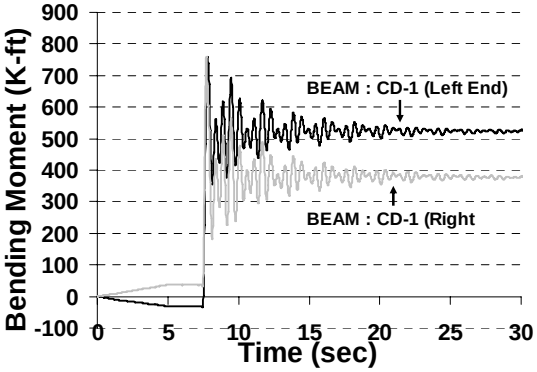

(e) Beam Bending Moments

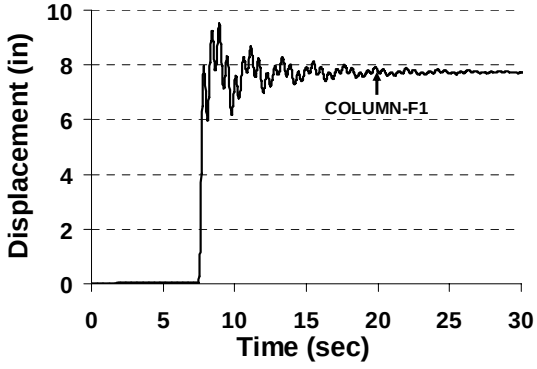

(f) Column Displacement

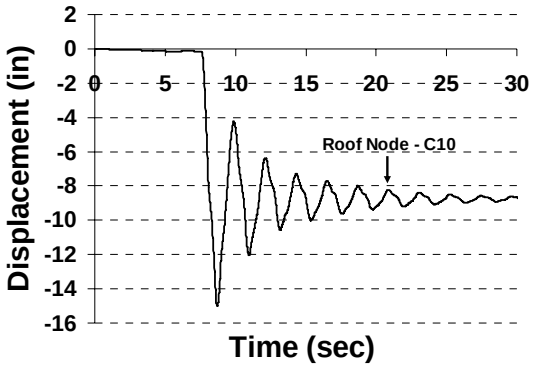

(g) Roof Displacement

Figure 4.35 Response quantities - APM case-5, IMF B-1 column loss

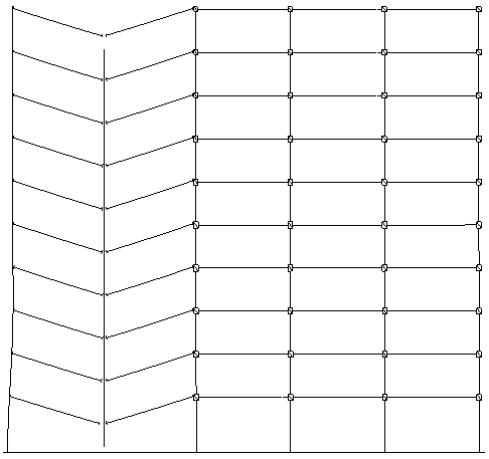

(a) Deformed Shape: Time = 8 sec
Magnification Factor = 1

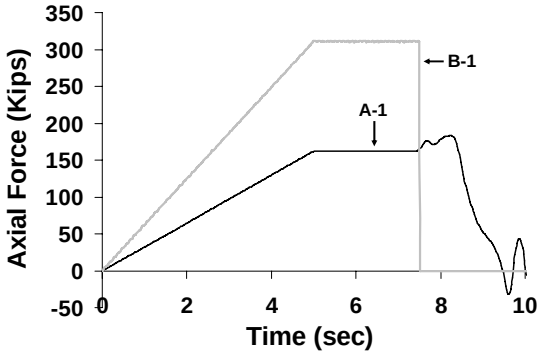

(b) Column Axial Forces

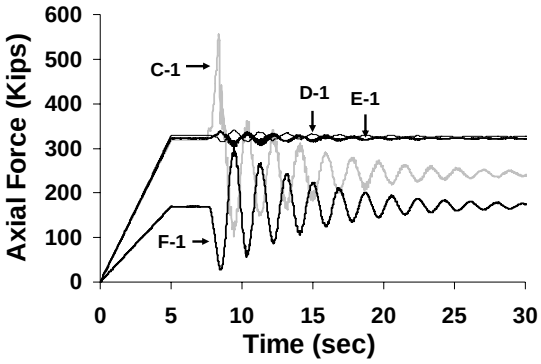

(c) Column Axial Forces

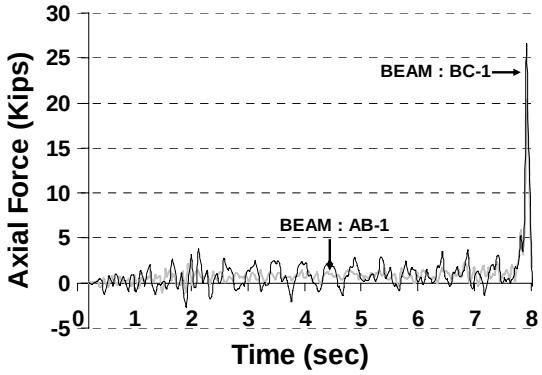

(d) Beam Axial Forces

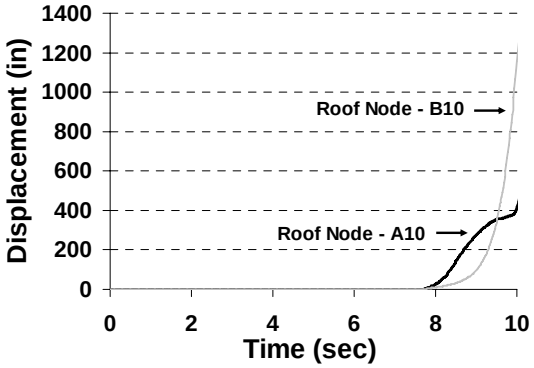

(e) Column Displacement

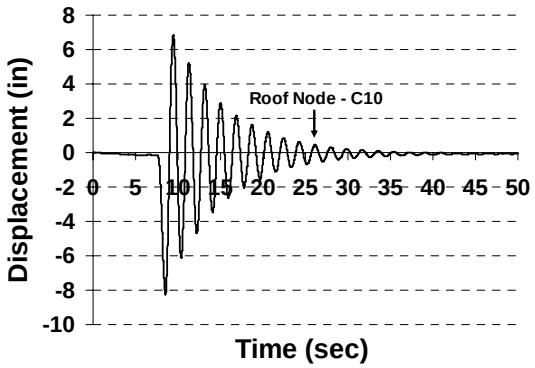

(f) Roof Displacement

Figure 4.36 Response quantities - APM case-6, SMF D-1 column loss

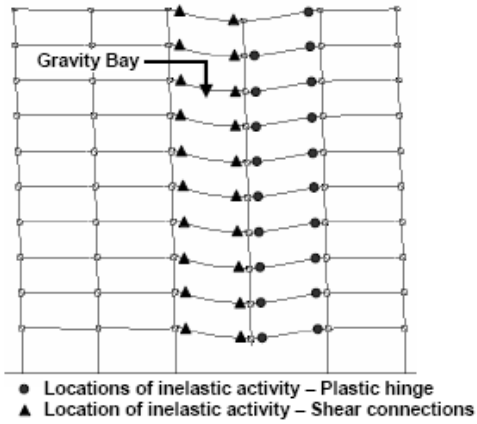

(a) Deformed Shape: Time = 30 sec
Magnification Factor = 10

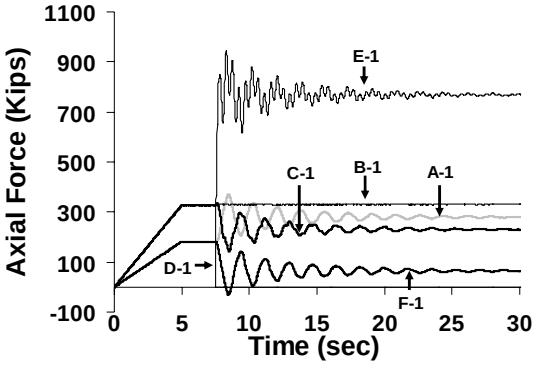

(b) Column Axial Forces

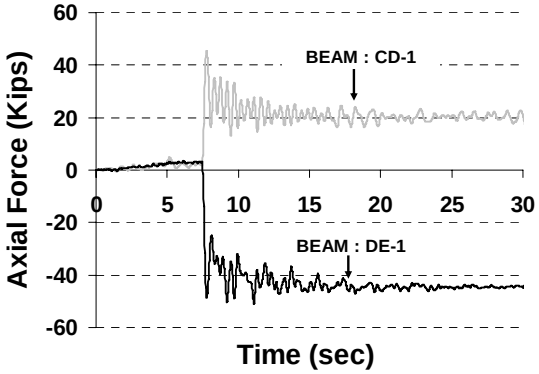

(c) Beam Axial Forces

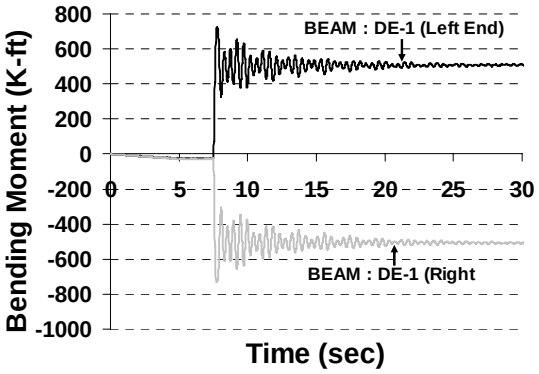

(d) Beam Bending Moments

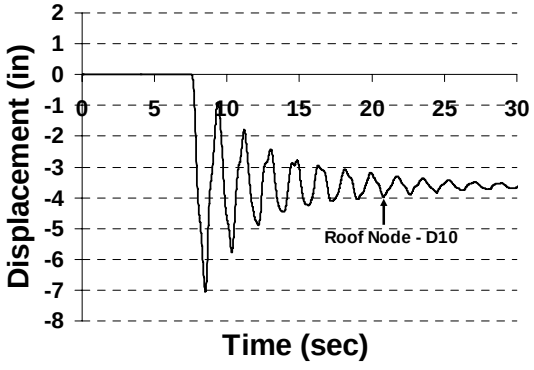

(d) Roof Displacement

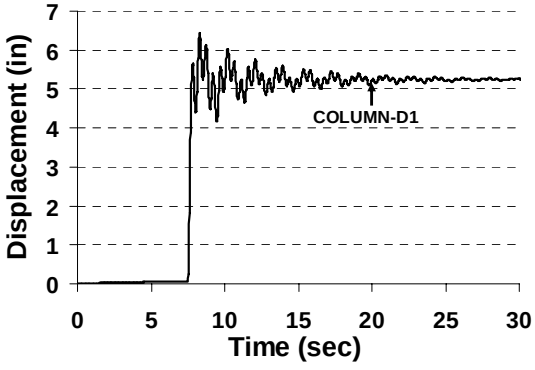

(e) Column Displacement

Figure 4.37 Response quantities - APM case-7, SMF E-1 column loss

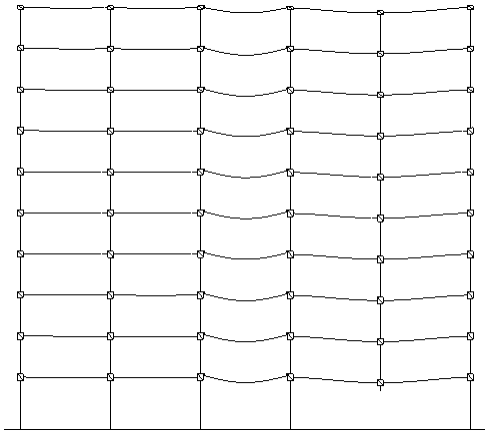

Deformed Shape: Time = 30 sec
Magnification Factor = 20

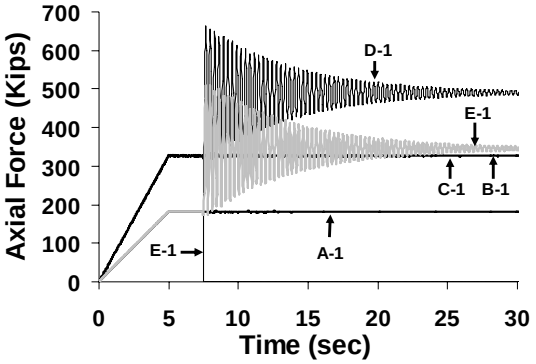

Column Axial Forces

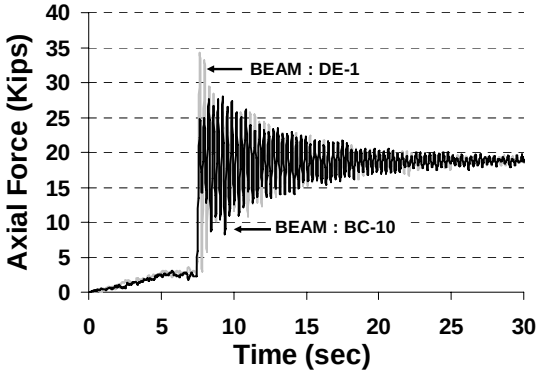

Beam Axial Forces

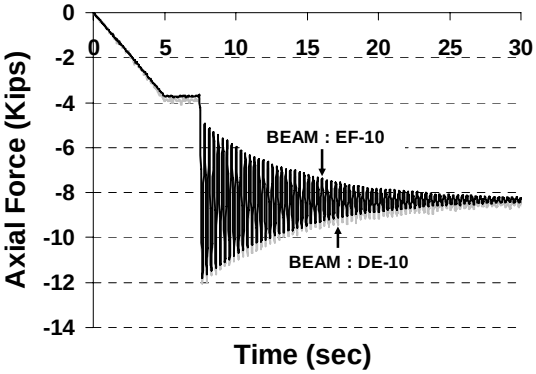

Beam Axial Forces

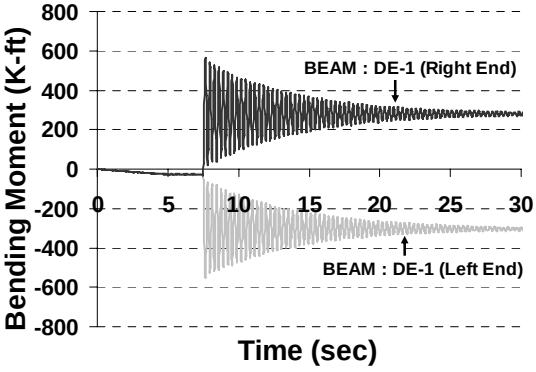

Beam Bending Moments

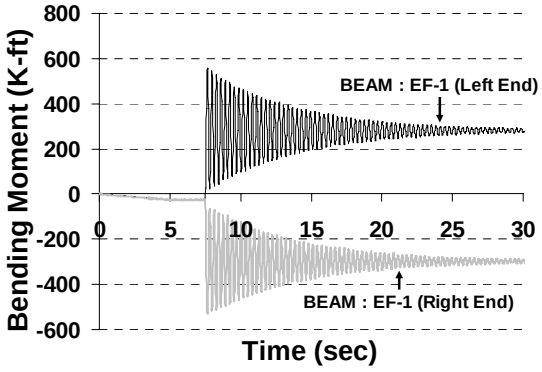

Beam Bending Moments

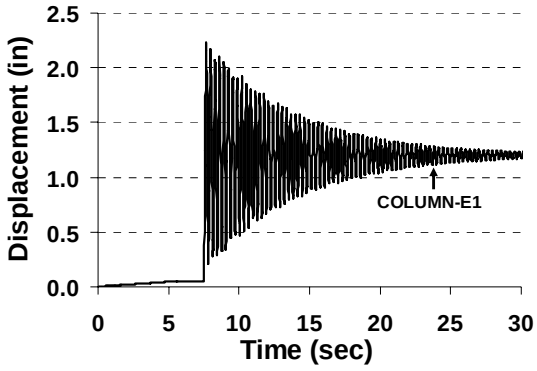

Column Displacement

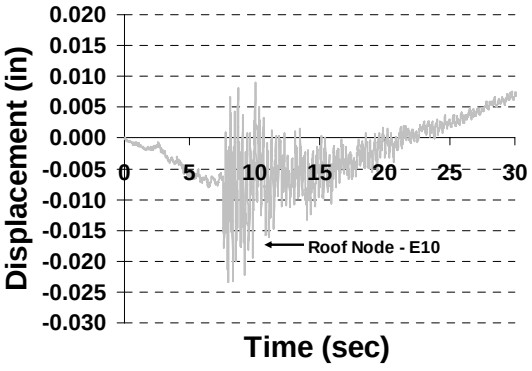

Roof Displacement

Figure 4.38 Response quantities - APM case-8, SMF F-1 column loss

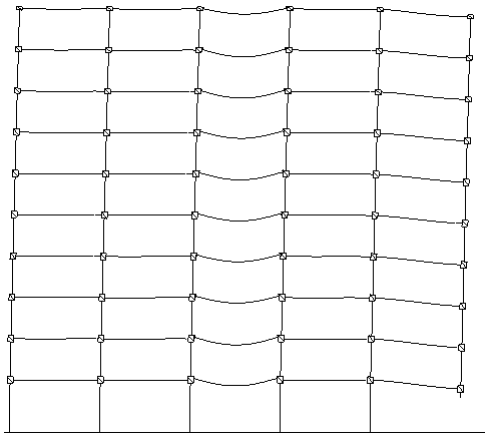

(a) Deformed Shape: Time = 30 sec
Magnification Factor = 20

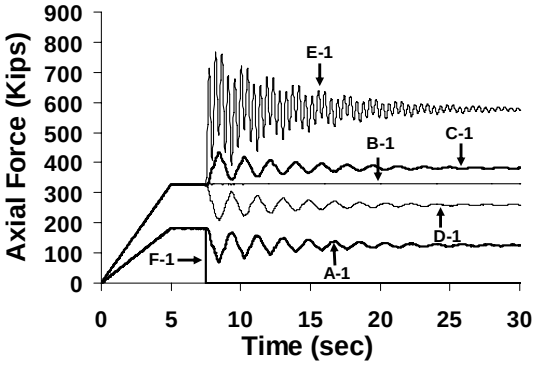

(b) Column Axial Forces

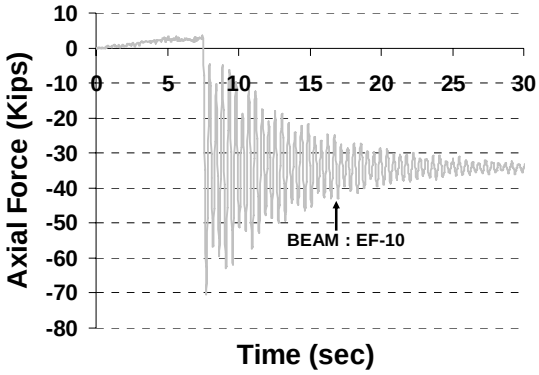

(c) Beam Axial Forces

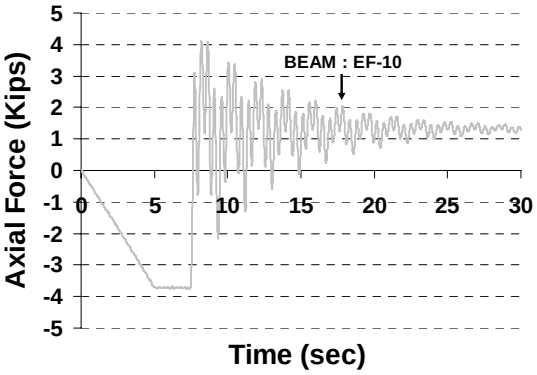

(d) Beam Axial Forces

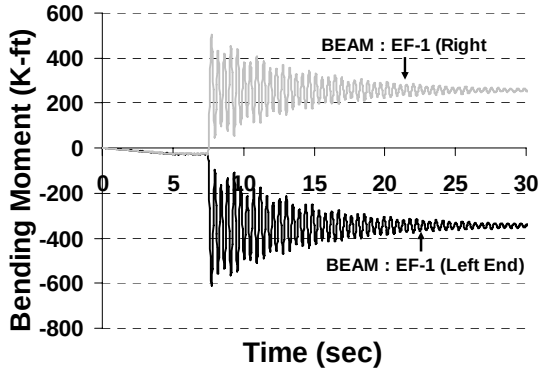

(e) Beam Bending Moments

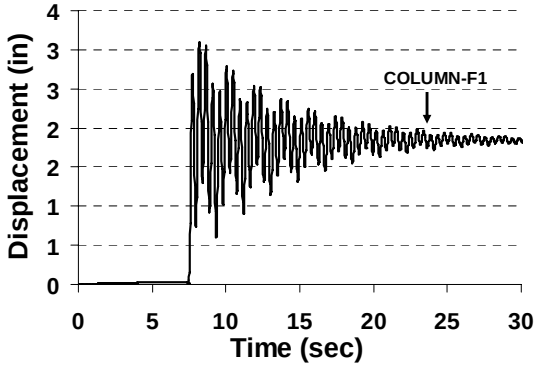

(f) Column Displacement

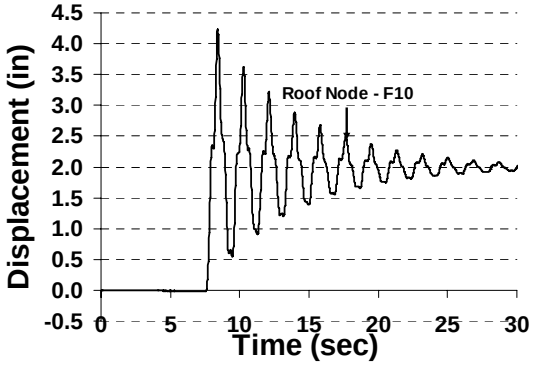

(g) Roof Displacement

Figure 4.39 Response quantities – SCBF APM case I

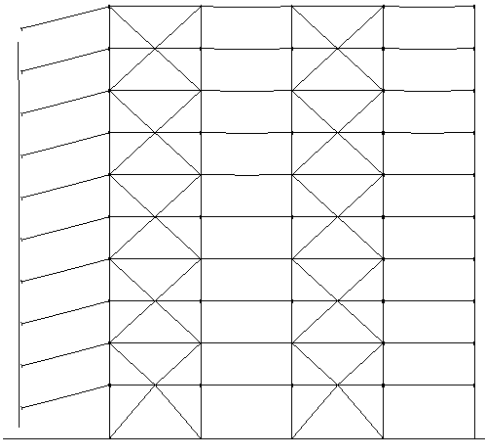

(a) Deformed Shape: Time = 7.9 sec
Magnification Factor = 1

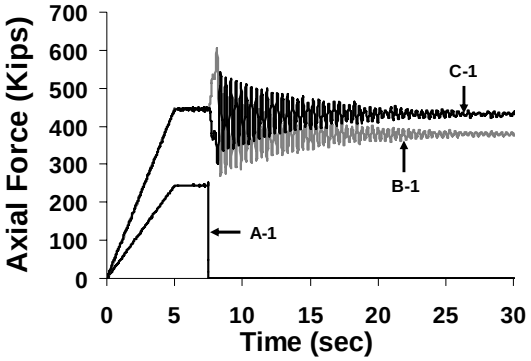

(b) Column Axial Forces

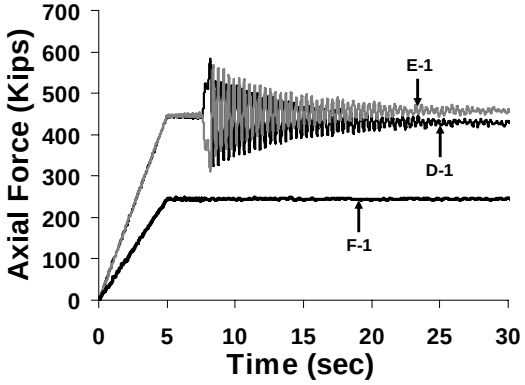

(c) Column Axial Forces

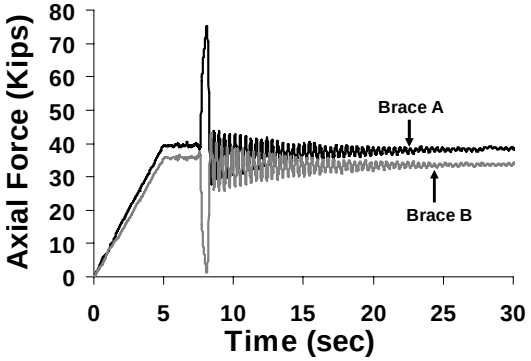

(d) Brace Axial Forces

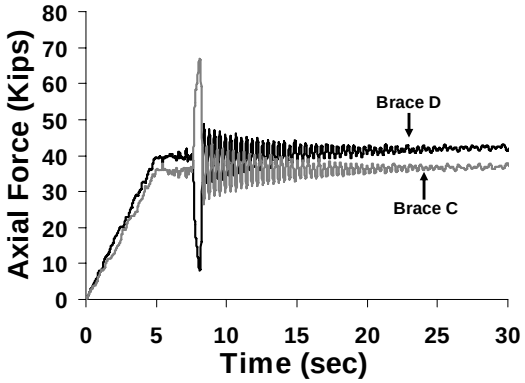

(e) Brace Axial Forces

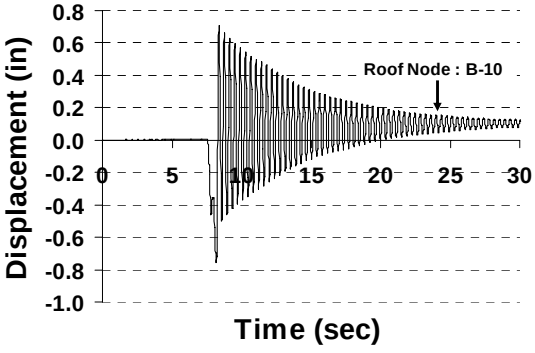

(f) Roof Displacement

Figure 4.40 Response quantities – SCBF APM case II

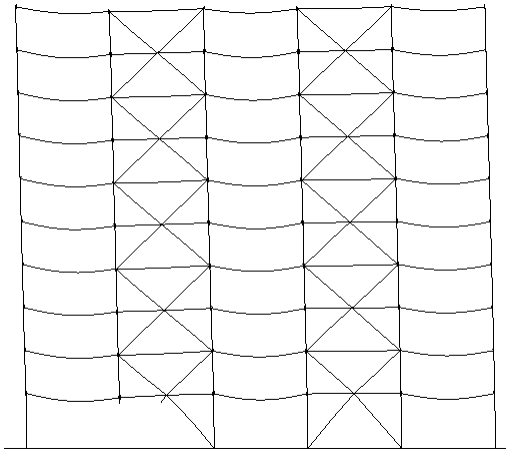

(a) Deformed Shape: Time = 30 sec
Magnification Factor = 20

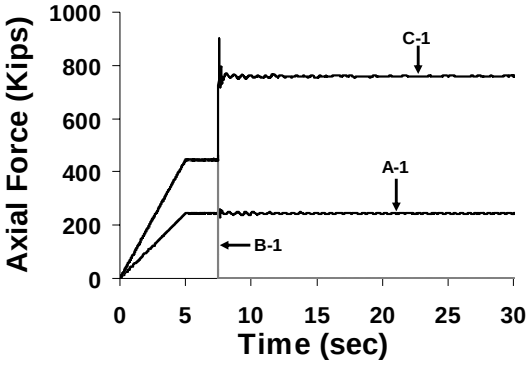

(b) Column Axial Forces

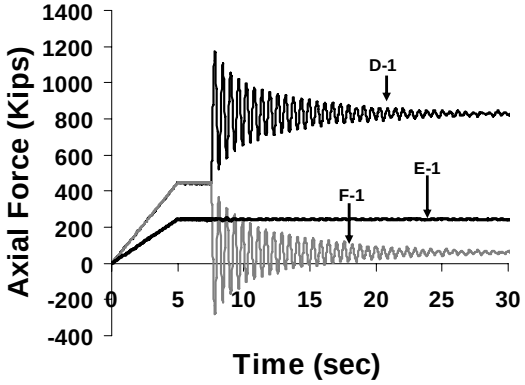

(c) Column Axial Forces

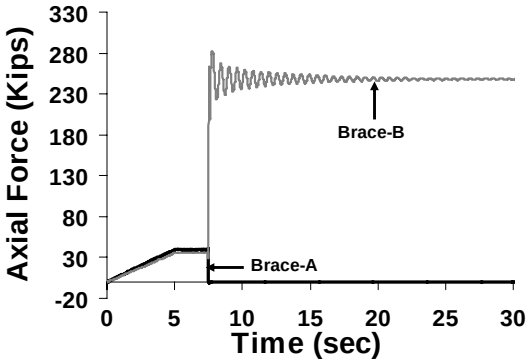

(d) Brace Axial Forces

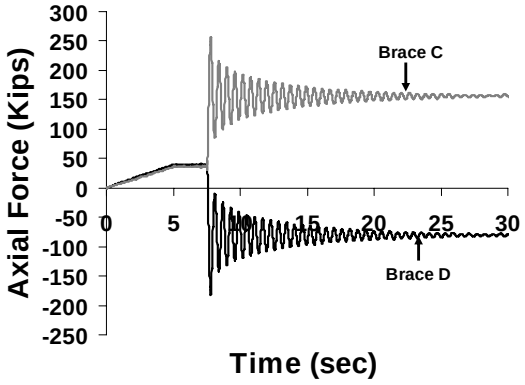

(e) Brace Axial Forces

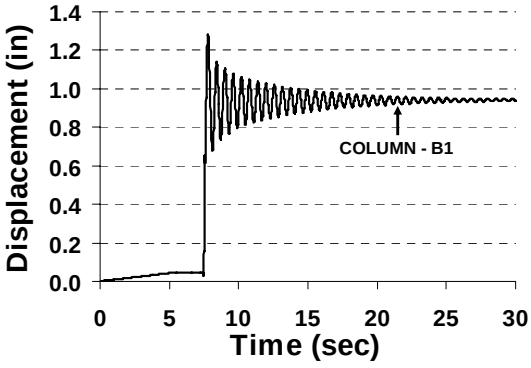

(f) Column Displacement

Figure 4.41 Response quantities – SCBF APM case III

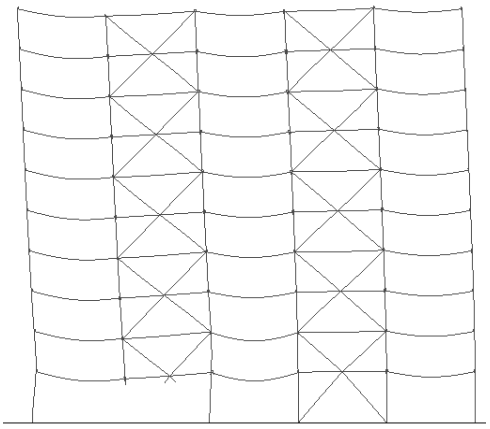

(a) Deformed Shape: Time = 30 sec
Magnification Factor = 20

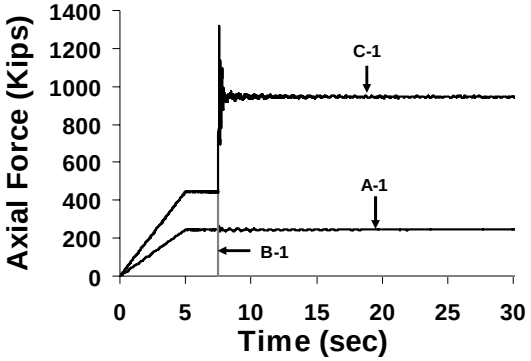

(b) Column Axial Forces

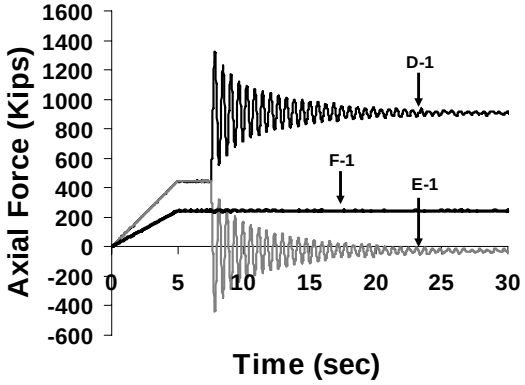

(c) Column Axial Forces

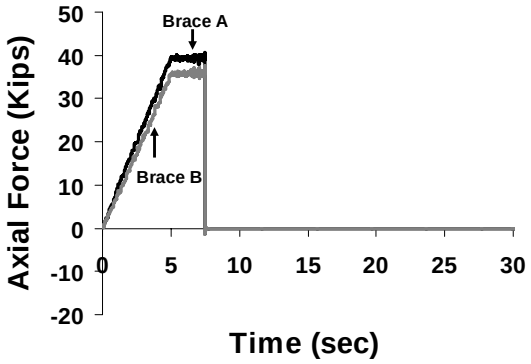

(d) Brace Axial Forces

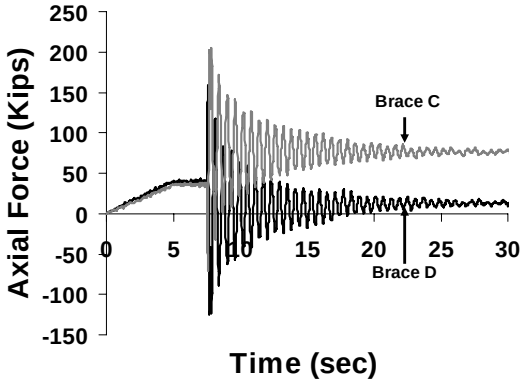

(e) Brace Axial Forces

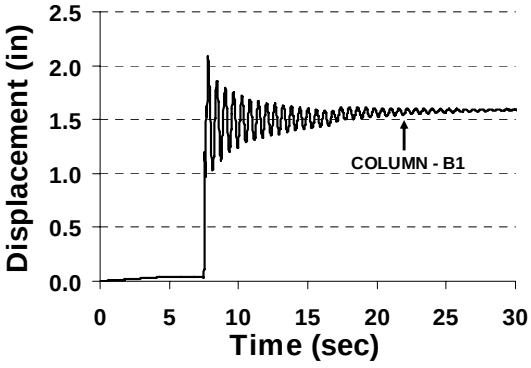

(f) Column Displacement

Figure 4.42 Response quantities – SCBF APM case IV

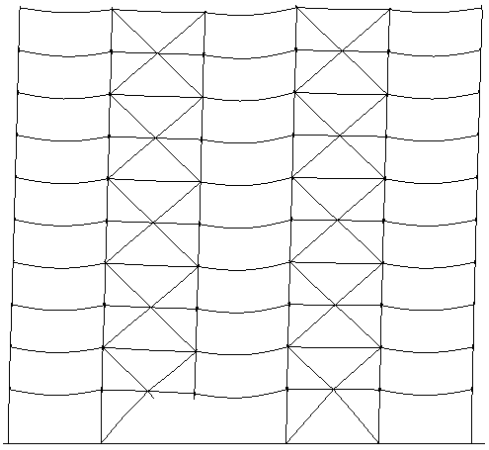

(a) Deformed Shape: Time = 30 sec
Magnification Factor = 20

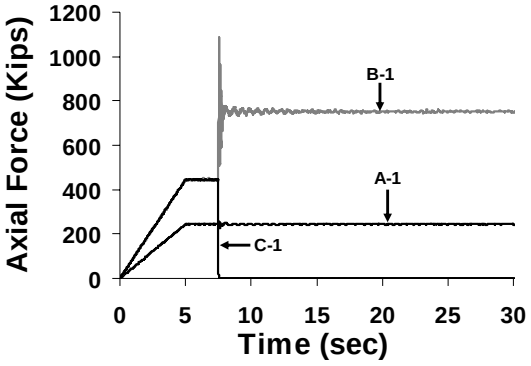

(b) Column Axial Forces

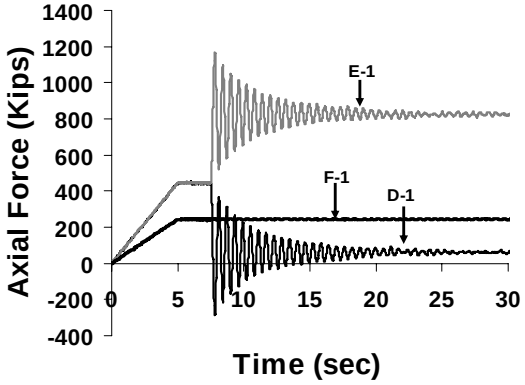

(c) Column Axial Forces

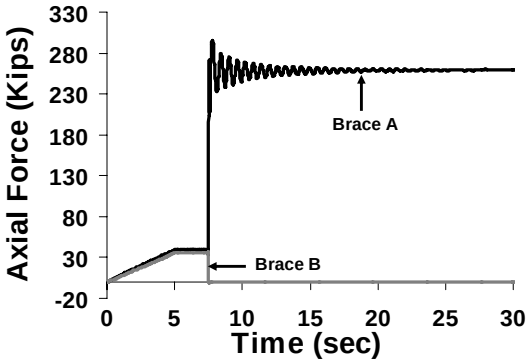

(d) Brace Axial Forces

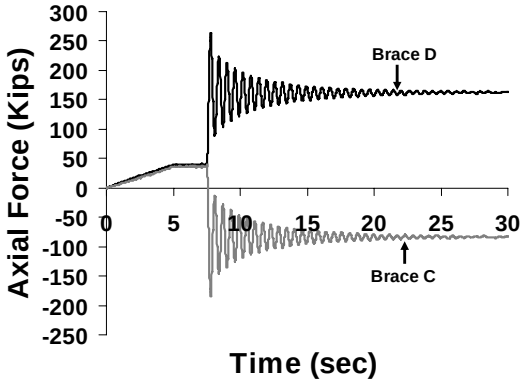

(e) Brace Axial Forces

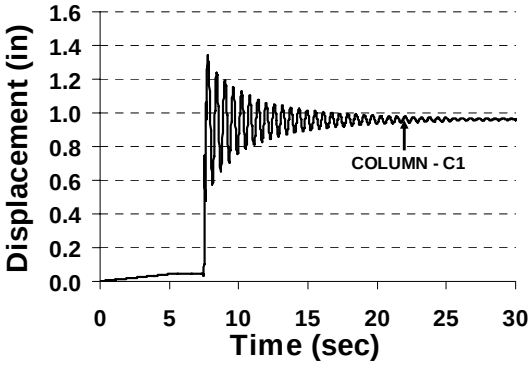

(f) Column Displacement

Figure 4.43 Response quantities – EBF APM case V

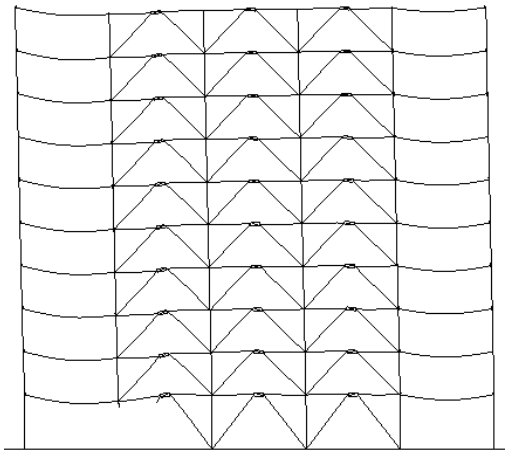

(a) Deformed Shape: Time = 30 sec
Magnification Factor = 20

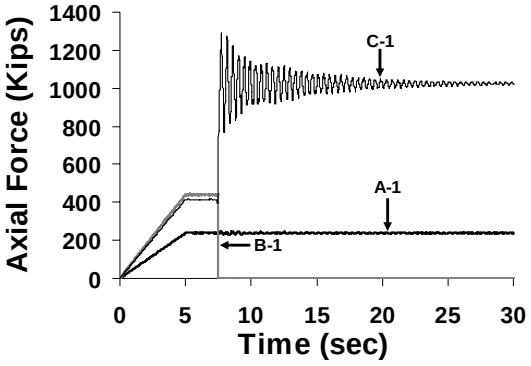

(b) Column Axial Forces

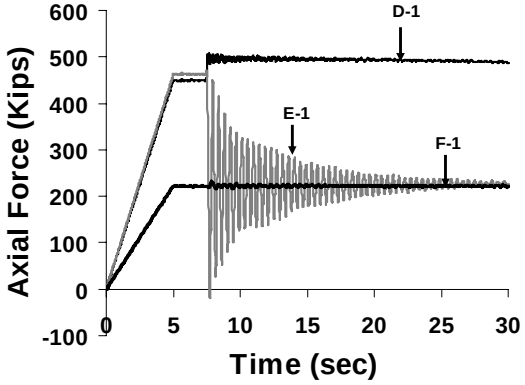

(c) Column Axial Forces

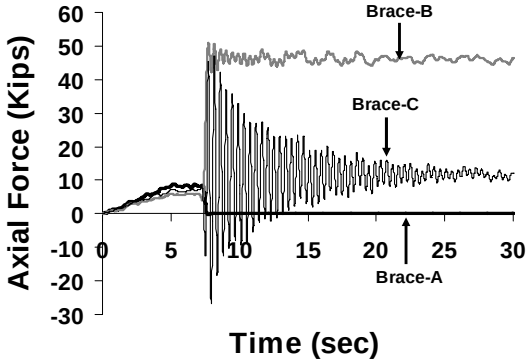

(d) Brace Axial Forces

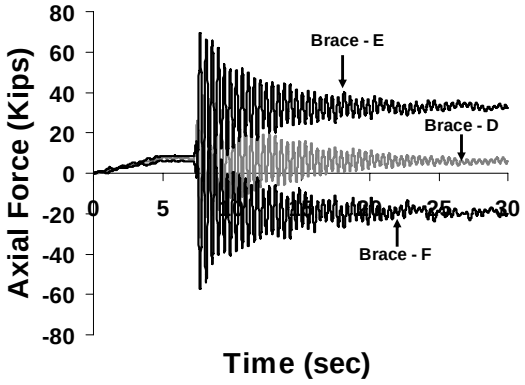

(e) Brace Axial Forces

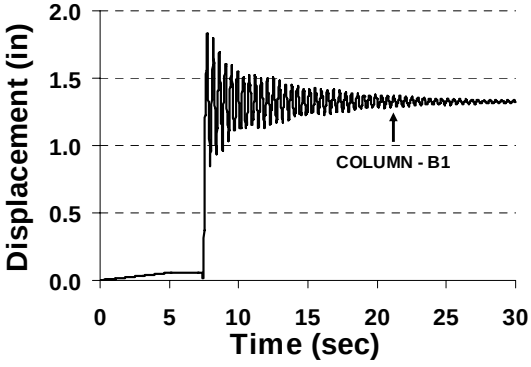

(f) Column Displacement

Figure 4.44 Response quantities – EBF APM case VI

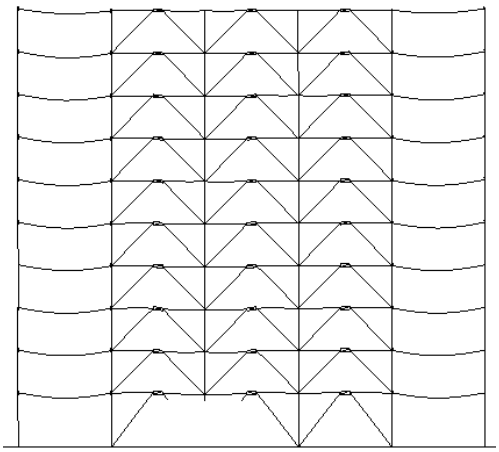

(a) Deformed Shape: Time = 30 sec
Magnification Factor = 20

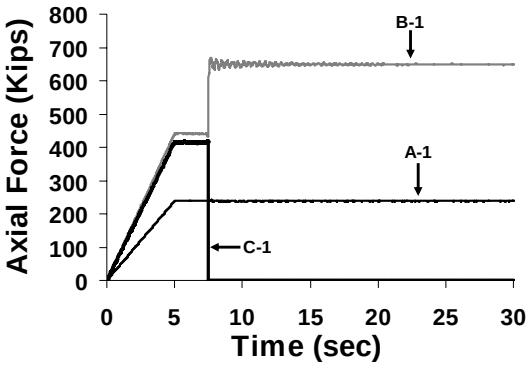

(b) Column Axial Forces

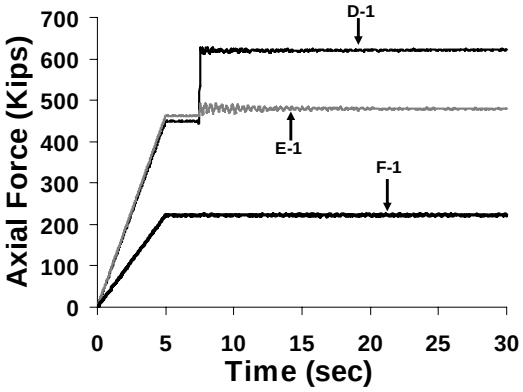

(c) Column Axial Forces

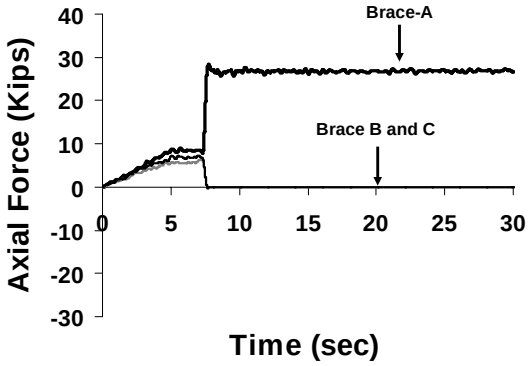

(d) Brace Axial Forces

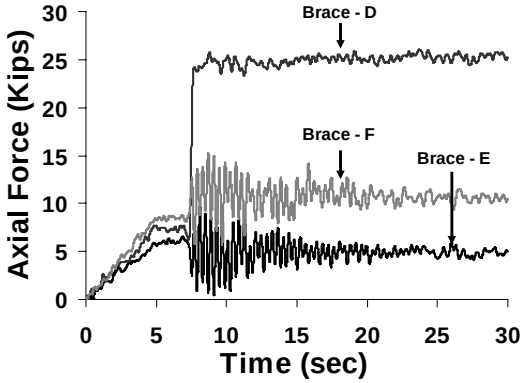

(e) Brace Axial Forces

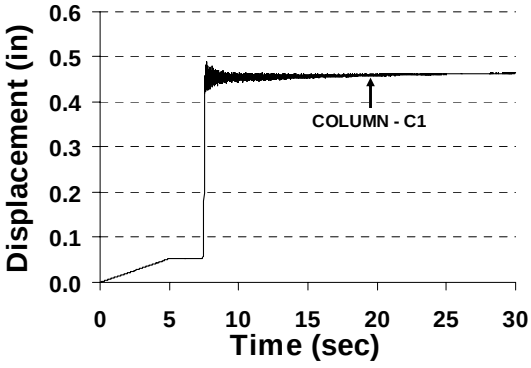

(f) Column Displacement

Figure 4.45 Response quantities – EBF APM case VII

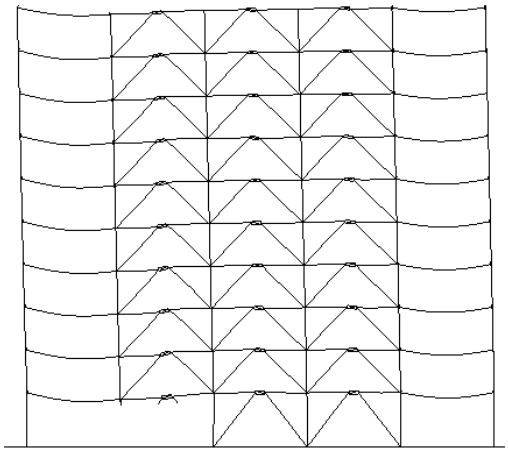

(a) Deformed Shape: Time = 7.8 sec
Magnification Factor = 20

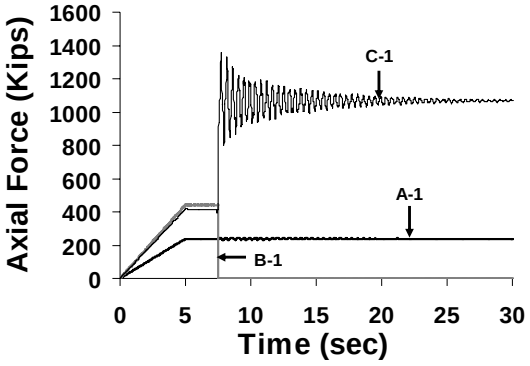

(b) Column Axial Forces

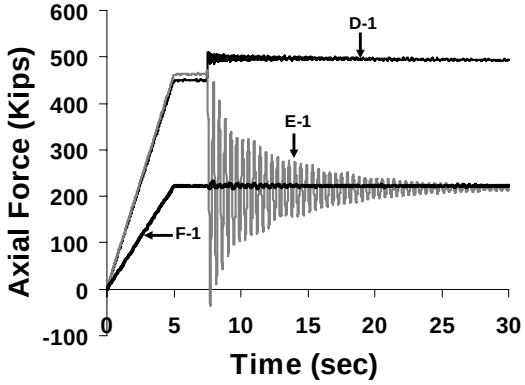

(c) Column Axial Forces

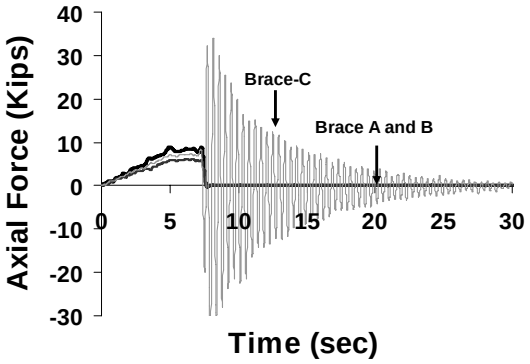

(d) Brace Axial Forces

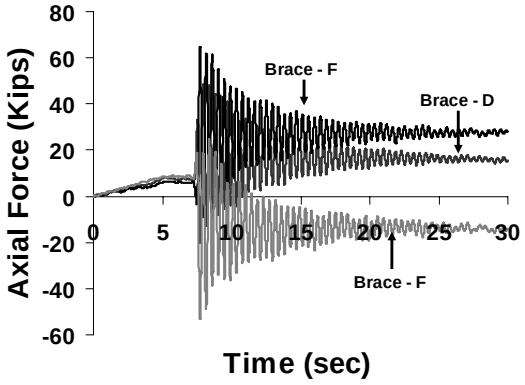

(e) Brace Axial Forces

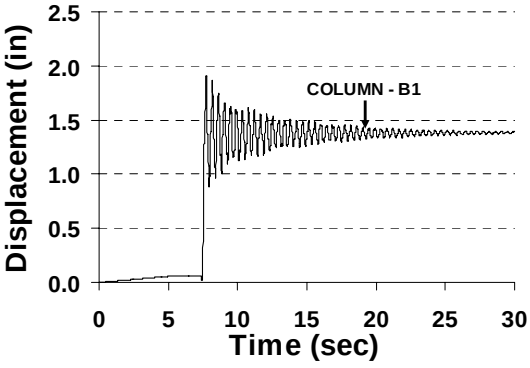

(f) Column Displacement

CHAPTER 5

PUSHDOWN ANALYSIS OF STEEL FRAMES

5.1 Introduction

The alternate path method (APM) was used in Chapter 4 to study the progressive collapse behavior of moment and braced frames. However, as indicated in Chapter 4, APM cannot be used for estimating the residual capacity of a damaged structure and the probable collapse modes in cases where the structural system survives the loss of critical members. Also, as discussed in Chapter 4, APM may indicate no collapse even when a critical member is near capacity, which then leads to questions about the robustness of the system. In other words, will the system fail if the member near capacity fails?

In this chapter a new analysis technique is introduced that can be used to determine the failure load and collapse mechanism of a damaged structure. The presented technique is termed "pushdown analysis" and parallels the pushover method commonly used for assessing the seismic resistance of building structures. The proposed analysis method is used to find the collapse load and the failure modes of steel structural systems using the structural scale models developed in Chapter 4.

The proposed pushdown analysis method is described in Section 5.2. Section 5.3 discusses the structural scale models used for pushdown analysis, while simulation results for various pushdown analysis cases are presented in Section 5.4. Finally, the simulation results are discussed in Section 5.5 and 5.6, and the important conclusions are presented in Section 5.7.

5.2 The Pushdown Analysis Method

The proposed pushdown analysis method consists of analyzing the structure, which has suffered loss of one or more critical members, under increasing gravity loads. Gravity load is increased until failure leading to disproportionate collapse of the structure occurs. The load corresponding to this failure state is defined as the failure load. The overload capacity of the structure is expressed in terms of overload factor (Eq. 5.1), defined as the ratio of failure load to the nominal gravity loads. The proposed pushdown analyses of a damaged structure can be accomplished in three different ways: Uniform pushdown (Fig. 5.1); Bay pushdown (Fig. 5.2); and Incremental dynamic pushdown (Fig. 5.3). These analysis cases are applicable when APM shows that a structure is safe but the residual capacity of the damaged structure has to be determined.

$$Overload\ Factor = \frac{Failure\ load}{Nominal\ gravity\ loads} \tag{5.1}$$

In the uniform pushdown case (Fig. 5.1), gravity loads on the damaged structure are increased proportionally in a nonlinear static analysis framework until the failure limit is reached. This analysis will lead to a collapse state corresponding to failure of the weakest part of the damaged structure. The failure may occur outside the damaged bays, and thus it might not be possible to estimate the residual capacity of the damaged bay. For example, a gravity bay may dominate the collapse response.

To focus the method on the damaged bays, the bay pushdown method is proposed (Fig. 5.2). In this method, the gravity load is increased proportionally only in the bays that suffered damage until failure occurs within the damaged bays. The remaining part of the structure is only subjected to nominal gravity loads. Hence, this analysis will lead to a collapse state corresponding to failure in the damaged bays. As in the previous method, the residual capacity of the damaged bays is measured in terms of an overload factor calculated as the ratio between the load leading to failure and the nominal gravity load.

The incremental dynamic pushdown method (Fig. 5.3) is similar to nonlinear dynamic APM but with one important difference, i.e. the gravity load in the damaged bays is increased incrementally up to a limit where failure occurs. Multiple analyses with increasing gravity loads in damaged bays may be required until a load factor corresponding to the failure in damaged bays is established. This analysis method accounts for dynamic effects, which may be important for some cases and is similar to incremental dynamic analysis used in earthquake engineering. However, this a costly analysis in terms of required computational effort.

5.3 Structural Scale Models for Pushdown Analysis

Pushdown analysis of structural scale models of the 2-D 10 story IMF, SMF, SCBF and EBF building systems developed in Chapter 4 is carried out to investigate their residual capacity after loss of a critical member. As discussed for the collapse analyses in Chapter 4, appropriate structural models that are to be used in pushdown analysis should be able to represent important modes of failure. For instance, in case of steel frames some of the failure modes can be related to instability of the column members and fracture in the structural members or connections. Additionally in the braced frames, the failure may also correspond to buckling of braces. Global collapse of the structural system may involve a combination of these failure modes.

The structural scale models considered herein account for the following failure modes: (a) fracture in beam to column moment connections and shear connections; (b) failure due to column buckling out of plane (weak axis buckling); (c) failure due to buckling of braces; and (d) failure of shear links. The detailed calibration exercises in Chapter 4 ensure that these models are able to represent system behavior with high fidelity. For analysis purpose, only the in-plane response of the frames is considered, however, ground story columns are allowed to deform out of plane to model failure due to column buckling. To allow weak axis buckling of columns to occur, ground story columns are provided with out of plane imperfection of $L/250$ (L = length of column) to model their inelastic buckling and post buckling response. Support conditions at ground story column

bases are modeled as fixed in plane but hinged out of plane. The models are subjected to the limitations discussed in Section 4.10.

5.4 Pushdown Analysis Results

Pushdown analyses of the abovementioned frames are carried out using the three analysis methods described in Section 5.2. Table 5.1 to Table 5.4 show the list of pushdown analysis cases for IMF, SMF, SCBF and EBF systems considered in this study together with the corresponding APM case considered in Chapter 4. For example in Table 5.1 for IMF system, pushdown analysis case 1 corresponds to the APM case 1 in Chapter 4 (Table 4.2) where the column F-1 of the IMF system was removed. In this case, uniform pushdown analysis is carried by removing the column F-1 in the IMF system. The pushdown analysis method, overload factors, and modes of failure are also reported in these tables.

5.4.1 IMF

From the analysis results in Table 5.1, it can be observed that both uniform and bay pushdown cases generally lead to similar collapse modes. However, in uniform pushdown, a lower overload factor is obtained as compared to the corresponding bay pushdown case. This is because of the fact that the structure is under higher overall loads for uniform pushdown cases. It is also observed that moment bays have higher overload factor as compared to the case where one of the bays is a gravity bay. This is due to failure of shear connections in the gravity bay, which limits the overload capacity that can be achieved.

The collapse mode is related to out of plane buckling of the ground story columns for uniform and bay pushdown analysis cases 1, 2, 3, 5 6 and 7. The failure modes for these cases are shown in Fig. 5.4 (a), (b) and (c). The maximum axial load supported by a ground story column in moment bays (W18×119 section) prior to failure by buckling is about 1250 kips. The design capacity of W18×119 column (Fy = 50 ksi, Ky = 1.0 and ϕ

= 1.0) is 1124 kips. Thus, the proposed column model with imperfections produces results that are sufficiently close to the design capacity. For analysis cases 2, 3, 6 and 7, a peak axial force of about 52 kips is developed in the first story beams in the damaged bays, before the collapse occurs by column buckling. In remaining uniform and bay pushdown analyses cases 1 and 8, collapse occurs as a result of shear connection failures in gravity bays as shown in Fig. 5.4 (d) at overload factors of 1.64 and 1.65 respectively. A peak axial tension of about 66 kips develops in the 1st story gravity beam before the shear connection fails.

The collapse modes for the incremental dynamic pushdown cases 10, 11 and 12 are same for as those for the corresponding uniform and bay pushdown cases. For analysis case 9, however, failure occurs by formation of a collapse mechanism over the entire story height where plastic hinges formed at two ends of beams in the bay EF as shown in Fig. 5.4 (e). No fractures were observed during the simulation time of interest i.e. until the column F-1 (top end) hits the ground level, however, rotations obtained at these locations show that fracture of connections is imminent.

Failures due to column buckling (pushdown analyses cases - 1, 2, 3, 5, 6, 7, 10 and 11) result in catastrophic failure of the entire frame in the sense that full collapse occurs as soon as a column buckles. The IMF frame is unable to safely transfer the load shed by the buckling column.

5.4.2 SMF

Analysis results for SMF frame are reported in Table 5.2 and corresponding collapse modes are shown in Fig. 5.5. For analysis cases 1 and 4 (Fig. 5.5 (a)), collapse started as a result of failure of shear connections in gravity bay CD. The shear connection in beam CD-1 (left end) failed first and is followed by failure of shear connections in the upper stories. A peak axial force of 85 Kips is developed in beam CD-1. Failure of shear connections is followed by failure of moment connections in bay DE. An overload factor of 1.82 is achieved in both analyses cases.

For this frame, differences are noted in the collapse modes associated with the uniform and the bay overloading cases. In the uniform overloading analysis case 2, for example, collapse occurred due to shear connection failures in gravity bay CD (Fig. 5.5 (b)), while for the corresponding bay overloading case 5, collapse is due to the fracture in connection regions (RBS zone) in bays DE and EF (Fig. 5.5 (d)). Peak catenary force of 240 kips develops in beams DE-1 and EF-1 for analysis case 5. Similarly, uniform overloading analysis case 3 results in collapse due to buckling of column E-1 (Fig. 5.5 (c)), however, for bay overloading case 6, failure is due to the fracture in connection regions (RBS zones) in bay EF (Fig. 5.5 (e)). The maximum axial load supported by ground story column E-1 (W24×146), prior to failure by buckling is about 1681 kips. The design capacity of this column (Fy = 50 ksi, Ky = 1.0 and ϕ =1.0) is 1506 kips.

Collapse modes for incremental dynamic overloading cases is similar to bay overloading cases except for case 7, where the collapse is triggered by shear connection failure in beam CD-1 (right end) as opposed to shear connection failure in beam CD-1 (left end) for case 4. A peak catenary force of 256 kips is developed in beams DE-1 and EF-1 for the pushdown analysis case 8, at a vertical displacement of about 42 inches.

As shown in Fig. 5.5 (g), for analysis case 7 and for load factor of 1.5 only a partial collapse occurs with failure of shear connections in gravity beams CD-1 and CD-2. The number of shear connection failures in gravity bay CD increases with load factor (Fig. 5.5 (h)) and complete collapse of the bay CD occurs at load factor of 1.7 (Fig. 5.5 (i)).

5.4.3 SCBF

As shown in Table 5.3 and Fig. 5.6, collapse in this frame is initiated by buckling of braces or shear connection failures. Failure modes are also consistent across various analysis cases. For example, in pushdown analysis cases 1, 4 and 7 for uniform, bay and incremental dynamic overloading respectively, the failure is initiated by buckling of brace B as shown in Fig. 5.6 (a). The peak force in brace B (HSS 7×7×½) is 471 kips. Assuming a strength reduction factor of 1.0 and an effective length factor, K = 0.5, the

capacity of this brace is 445 kips. Thus, the proposed brace model with imperfections produces results that are sufficiently close to the design capacity. For pushdown analysis cases 2, 5 and 8 (Fig. 5.6 (b) and (d)), collapse started from failure of shear connections in beam CD-10. A peak axial force of 64 kips is developed in beam CD-10. For pushdown analysis cases 3, 6 and 9, collapse occurred due to buckling of brace A (Fig. 5.6 (c)), which is followed by shear connection failure in bay CD.

The collapse cases associated with brace buckling have a higher overload factor than cases where collapse is initiated by shear connection failures.

5.4.4 EBF

Analysis results for EBF frame are reported in Table 5.4 and corresponding collapse modes are shown in Fig. 5.7. For uniform and bay pushdown cases 1 and 4 (Fig. 5.7 (a)), collapse is initiated by buckling of column C-1 and is followed by shear connection failures in bay AB. Maximum axial load supported by ground story column C-1 (W14×176), prior to failure by buckling is about 2357 kips. The design capacity of column C-1 (Fy = 50 ksi, Ky = 1.0 and ϕ =1.0) is 2122 kips. Peak axial force of 61 kips is developed in beam AB-1. Overload factors of 2.19 and 2.32 are achieved for uniform and bay pushdown cases respectively.

For uniform and bay pushdown cases 2 and 5 (Fig. 5.7 (b)), collapse initiated due buckling of column B-1 and is followed by shear connection failure in bay AB. Overload factors of 3.39 and 3.60 is achieved for uniform and bay pushdown cases respectively. Pushdown analysis cases 3 and 6 (Fig. 5.7 (c)) results in collapse initiated by buckling of column C-1 with overload factors of 2.08 and 2.20 respectively.

For incremental dynamic pushdown case 7, damage increases progressively (Fig. 5.7 (d), (e) and (f)) with the increase in overload factor due to failure of shear connections in bay AB. Complete bay collapse take place at an overload factor of 2.0. Similar results are obtained for incremental dynamic analysis case 9 (Fig. 5.7(h), (i) and (j)), where the

complete bay collapse occur at an overload factor of 1.8. For case 8 (Fig. 5.7(g)), collapse initiate due to buckling of column B-1 at an overload factor of 3.2.

5.5 Discussion of Results for Moment Frames

Results presented in Section 5.4.1 and 5.4.2 shows that the proposed pushdown methods can be successfully used to estimate the residual strength and collapse modes of a damaged structure. APM case 4 for IMF system in Chapter 4 predicts that the loss of column C-1 will not lead to progressive collapse. However, engineering judgment suggested that this is likely a critical situation. This judgment is reaffirmed by the incremental dynamic pushdown analysis, which gives and overload factor of only 1.2 for this case.

The simulation results suggest that the SMF building designed for high seismic risk is generally more resistant to progressive collapse and hence more robust than the IMF building designed for moderate seismic risk. This is evident from the overload factors which for the SMF building range from 1.4 to 3.6 while the IMF building has overload factors in the range of 1.2 to 2.9. Collapse modes across the three pushdown analysis cases are usually consistent, except for few cases where the dynamic pushdown case predicted a different collapse mode than the static cases.

The superior robustness of SMF frames is also manifested by the collapse modes associated with the various analysis cases. Except for analysis case 3, collapse in the SMF frame is associated with failure of shear connections and fracture in RBS zones in connection regions. Such collapse modes are desirable as they limit the failure in the damaged bays while shielding the rest of the structure, thus limiting the extent of collapse. In contrast, most the collapse modes in the IMF frame are associated with buckling of ground story columns. Such collapse modes are undesirable as they jeopardize the stability of the entire structural system. This is evident from pushdown analysis cases for the IMF system where column buckling is followed by instability and collapse of the entire frame.

The better performance of SMF system can be attributed to stronger beams and columns present in this system as compared to IMF frame. This is a result of stringent seismic requirements which the SMF frame has to satisfy. Seismic detailing requirements in SMF system also play an important role as it helps in the formation of catenary action. A peak catenary force of 256 kips is successfully transferred by the reduced beam connections. Moreover, the weaker RBS zones act as structural fuses which fail relatively early, thereby limiting the loads that are transferred to the columns.

5.6 Discussion of Results for Braced Frames

The simulation results suggest that the EBF building designed for high seismic risk is generally more resistant to progressive collapse and hence more robust than the SCBF building designed for moderate seismic risk. This is evident from the overload factors which for EBF building ranges from 1.8 to 3.6 while SCBF building has overload factors in the range of 1.3 to 2.0.

Collapse modes in SCBF system are usually associated with buckling of a brace or failure of shear connections and results in collapse of entire frame. Collapse modes for SCBF across the three pushdown analysis cases are consistent. For EBF frame static pushdown analysis cases results in collapse initiated by column buckling while for incremental dynamic pushdown, collapse is usually due to failure of shear connections.

5.7 Summary and Conclusions

The study in this chapter was concerned with the development of a new analysis technique that can be used for estimating the residual capacity of a damaged structure and the corresponding collapse modes. Specifically, three pushdown methods are proposed - uniform pushdown, bay pushdown and incremental dynamic pushdown. The proposed methods were then used to estimate the residual capacity and collapse modes of 2-dimensional, 10 story SMF, IMF, SCBF and EBF frames, for cases where APM analyses in Chapter 4 predicts no collapse. Based on the simulation studies conducted and within

the assumptions and limitations described in the chapter, the following conclusions can be drawn.

1. The proposed pushdown analysis methods can be used for estimating the residual capacity and collapse modes of a damaged structure.

2. Incremental dynamic pushdown gives a best estimate of residual capacity and collapse modes. Collapse modes across the three pushdown analysis cases usually agree for the building systems considered in this study. However, there are scenarios where dynamic analysis yields a different collapse mode as compared to the static case. For such cases dynamic analysis is indispensable, since the static analyses, even with dynamic impact factors, cannot predict the correct collapse mode.

3. The proposed analyses methods can be used to study the robustness of structural systems and to design new more robust structural systems. Overload factor together with collapse modes is a good indicator of robustness of the system. Simulation results shows that SMF and EBF frames are more robust than the IMF and SCBF systems respectively.

4. Seismic detailing in SMF system play an important role by allowing catenary forces to be developed in beams. Further, the fracture of the RBS connections in this frame limits the maximum force being transferred to the columns. This limits the extent of damage in the frame. It is desirable to have failure in beams rather than in columns. The column failure mode is undesirable as it is more catastrophic than beam failures since it undermines the stability of the entire structural system. Thus, the robustness of the IMF system can be increased by using stronger columns, which might then shift the failure locations to beams connection regions instead of collapse by column buckling.

Pushdown Analysis Case	APM Case	Pushdown Analysis Type	Overload Factor	Failure Mode
1	1	Uniform	2.12	Buckling of Column E-1
2	2	Uniform	2.53	Buckling of Column D-1
3	3	Uniform	2.54	Buckling of Column E-1 and C-1
4	4	Uniform	1.64	Failure of shear connections in bay CD
5	1	Bay	2.33	Buckling of Column E-1
6	2	Bay	2.90	Buckling of Column D-1
7	3	Bay	2.90	Buckling of Column E-1 and C-1
8	4	Bay	1.65	Failure of shear connections in bay CD
9	1	Incremental Dynamic	2.0	Plastic mechanism formation in bay EF
10	2	Incremental Dynamic	2.2	Buckling of Column D-1
11	3	Incremental Dynamic	2.2	Buckling of Column E-1 and C-1
12	4	Incremental Dynamic	1.2	Failure of shear connections in bay CD

Table 5.1 Pushdown Analysis Results - IMF (SDC-C)

Pushdown Analysis Case	APM Case	Pushdown Analysis Type	Overload Factor	Failure Mode
1	6	Uniform	1.82	Failure of shear connections in bay CD
2	7	Uniform	3.23	Failure of shear connections in bay CD
3	8	Uniform	2.93	Buckling of Column E-1
4	6	Bay	1.82	Failure of shear connections in bay CD
5	7	Bay	3.60	Failure of connections (RBS zone) in bay DE and EF
6	8	Bay	3.5	Failure of connections (RBS zone) in bay EF
7	6	Incremental Dynamic	1.7	Failure of shear connections in bay CD
8	7	Incremental Dynamic	3.0	Failure of connections (RBS zone) in bay DE and EF
9	8	Incremental Dynamic	3.0	Failure of connections (RBS zone) in bay EF

Table 5.2 Pushdown Analysis Results - SMF (SDC-D)

Pushdown Analysis Case	APM Case	Pushdown Analysis Type	Overload Factor	Failure Mode
1	II	Uniform	1.91	Buckling of Brace B
2	III	Uniform	1.77	Failure of shear connections in bay CD
3	IV	Uniform	1.87	Buckling of Brace A
4	II	Bay	1.96	Buckling of Brace B
5	III	Bay	1.97	Failure of shear connections in bay CD
6	IV	Bay	2.00	Buckling of Brace A
7	II	Incremental Dynamic	1.8	Buckling of Brace B
8	III	Incremental Dynamic	1.3	Failure of shear connections in bay CD
9	IV	Incremental Dynamic	1.7	Buckling of Brace A

Table 5.3 Pushdown Analysis Results - SCBF (SDC-C)

Pushdown Analysis Case	APM Case	Pushdown Analysis Type	Overload Factor	Failure Mode
1	V	Uniform	2.19	Buckling of column C-1
2	VI	Uniform	3.39	Buckling of column B-1
3	VII	Uniform	2.08	Buckling of column C-1
4	V	Bay	2.32	Buckling of column C-1
5	VI	Bay	3.60	Buckling of column B-1
6	VII	Bay	2.20	Buckling of column C-1
7	V	Incremental Dynamic	2.0	Shear connection failures in bay AB
8	VI	Incremental Dynamic	3.2	Buckling of column B-1
9	VII	Incremental Dynamic	1.8	Shear connection failures in bay AB

Table 5.4 Pushdown Analysis Results - EBF (SDC-D)

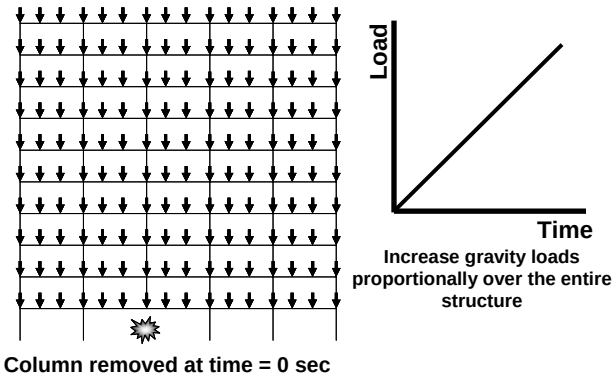

Figure 5.1 Pushdown analysis - case (a) Uniform pushdown

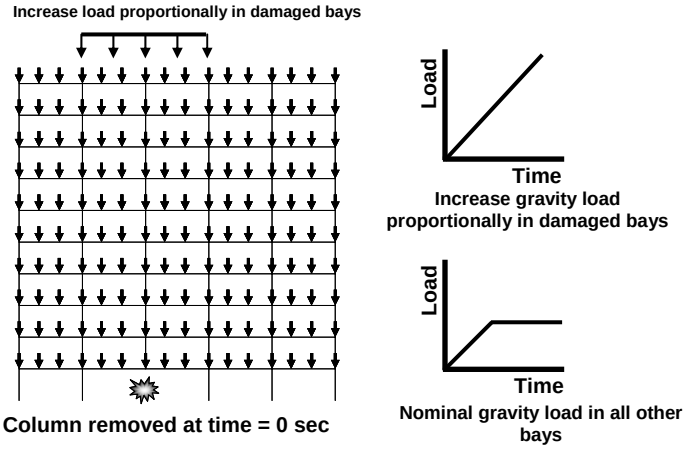

Figure 5.2 Pushdown analysis - case (b) Bay pushdown

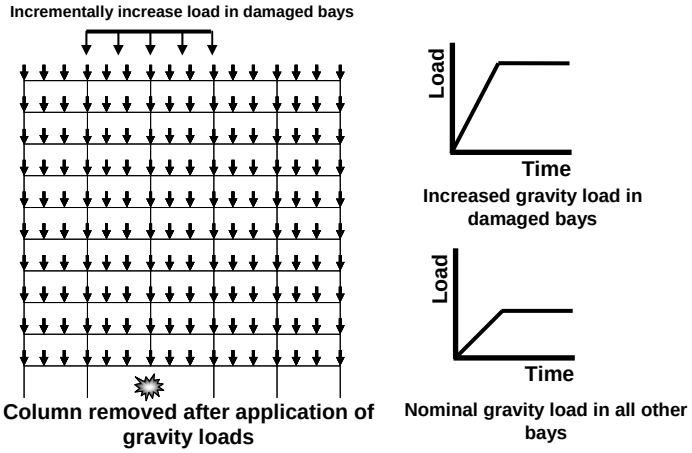

Figure 5.3 Pushdown analysis - case (c) Incremental dynamic pushdown

Figure 5.4 Failure Modes - IMF (SDC-C)

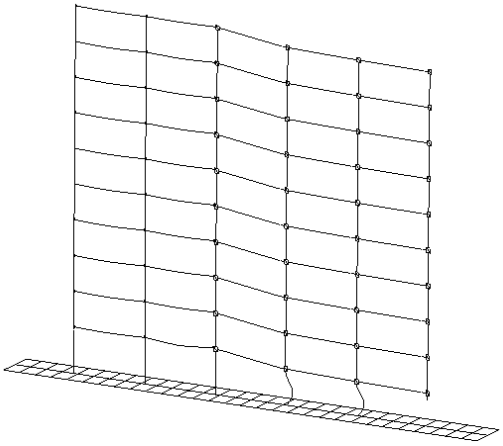

(a) Failure Mode: Pushdown Analysis Case 1 and 5

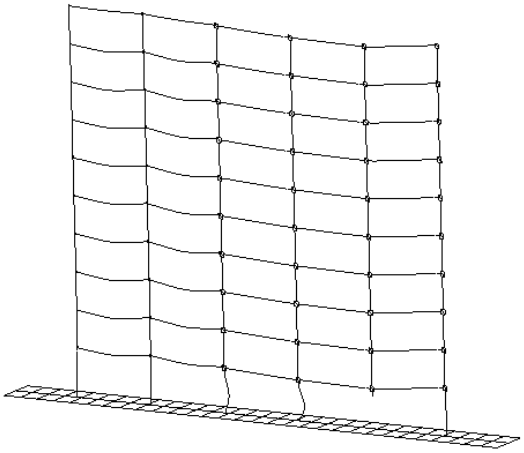

(b) Failure Mode: Pushdown Analysis Case 2, 6 and 10

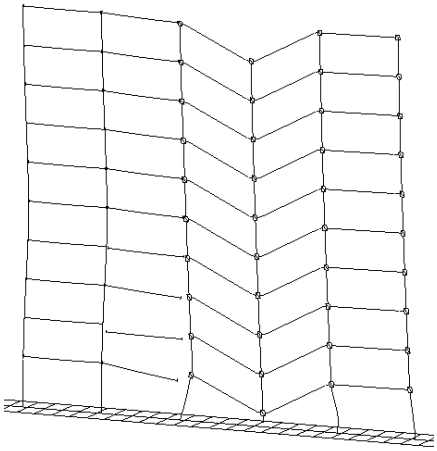

(c) Failure Mode: Pushdown Analysis Case 3, 7 and 11

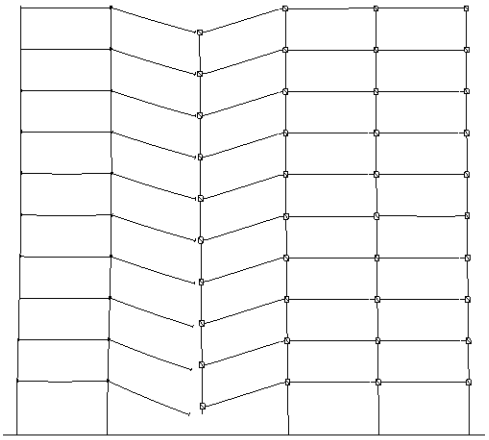

(d) Failure Mode: Pushdown Analysis Case 4, 8 and 12

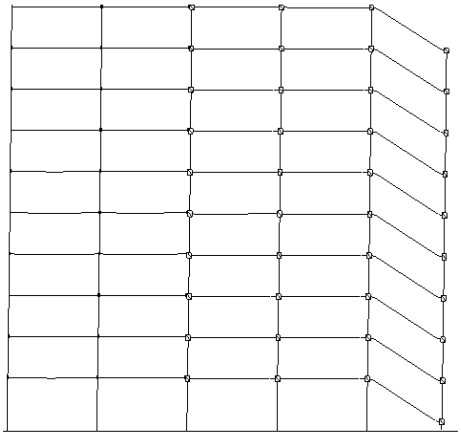

(e) Failure Mode: Pushdown Analysis Case 9

Figure 5.5 Failure Modes - SMF (SDC-D)

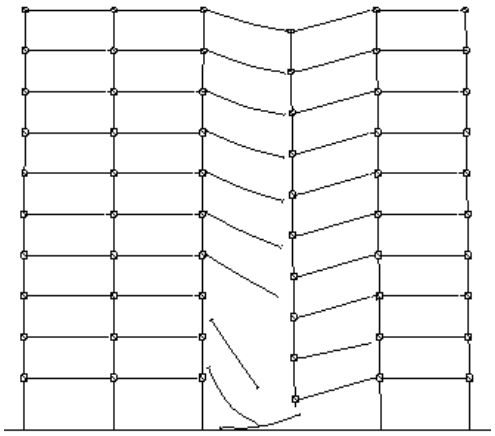

(a) Failure Mode: Pushdown analysis case 1 and 4

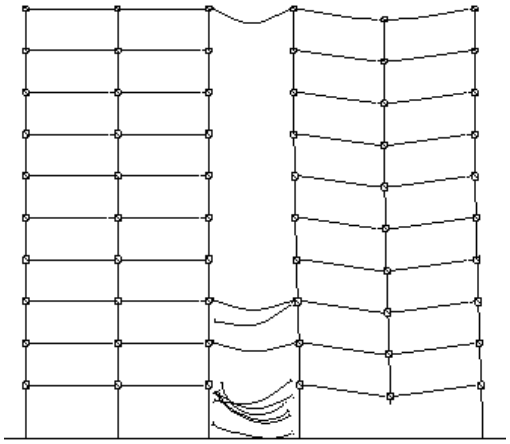

(b) Failure Mode: Pushdown analysis case 2

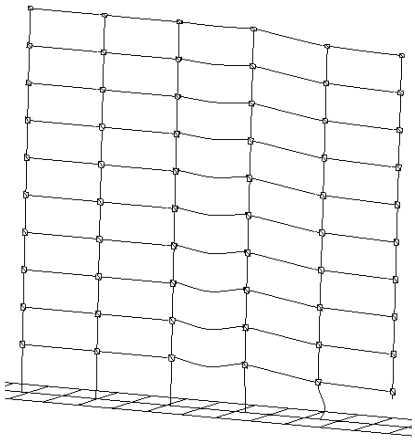

(c) Failure Mode: Pushdown analysis case 3

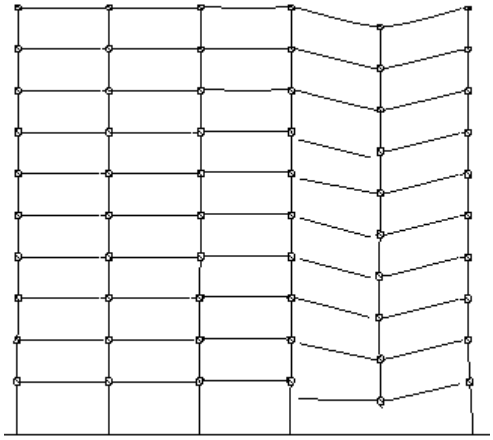

(d) Failure Mode: Pushdown analysis case 5 and 8

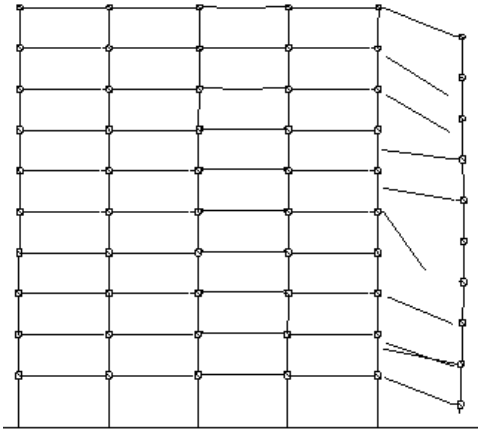

(f) Failure Mode: Pushdown analysis case 6 and 9

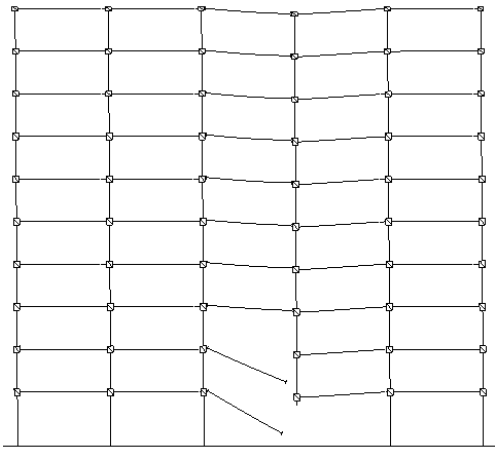

(g) Failure Mode: Pushdown analysis case 7 Load Factor: 1.5

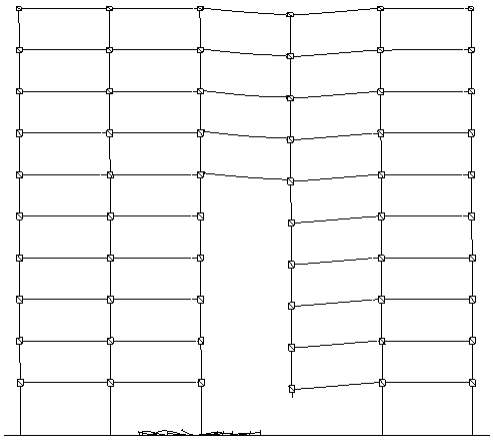

(h) Failure Mode: Pushdown analysis case 7
Load Factor: 1.6

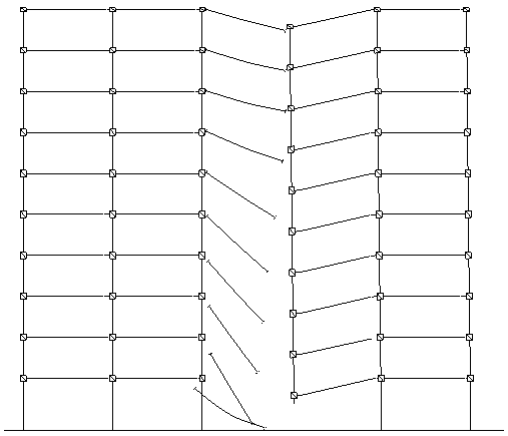

(i) Failure Mode: Pushdown analysis case 7
Load Factor: 1.7

Figure 5.6 Failure Modes - SCBF (SDC-C)

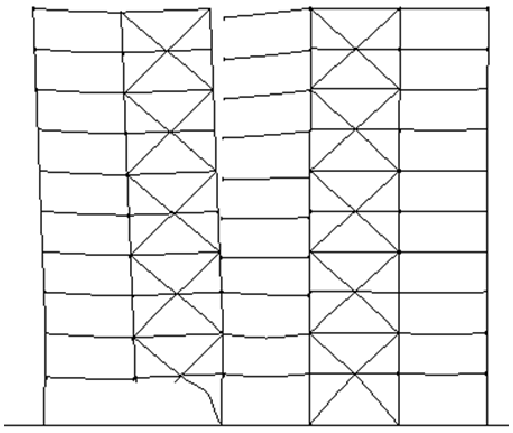

(a) Failure Mode: Pushdown analysis case 1, 4 and 7

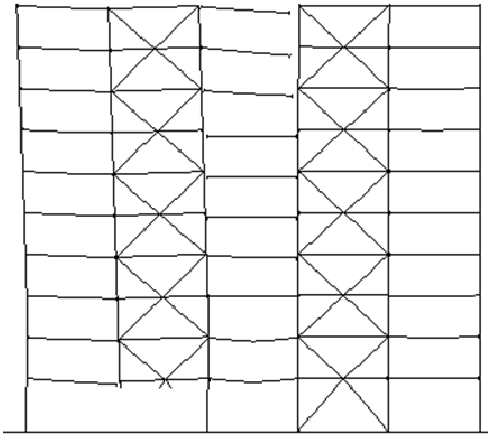

(b) Failure Mode: Pushdown analysis case 2 and 5

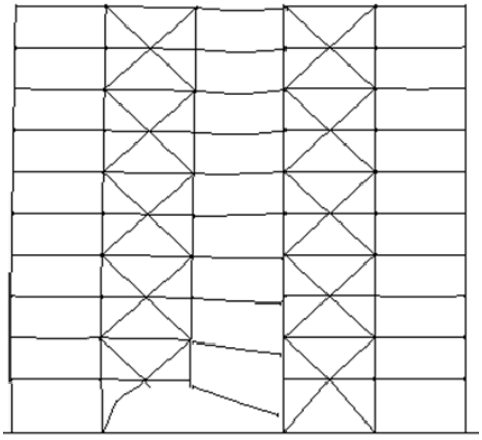

(c) Failure Mode: Pushdown analysis case 3, 6 and 9

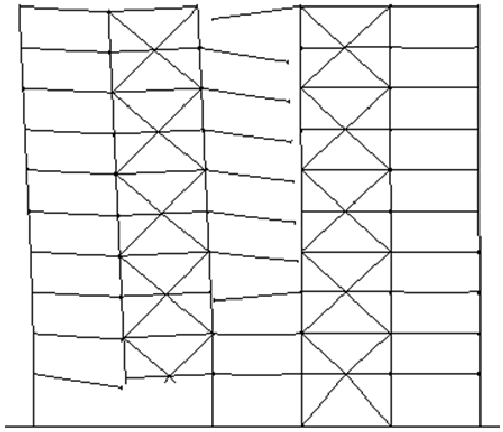

(d) Failure Mode: Pushdown analysis case 8

Figure 5.7 Failure Modes - EBF (SDC-D)

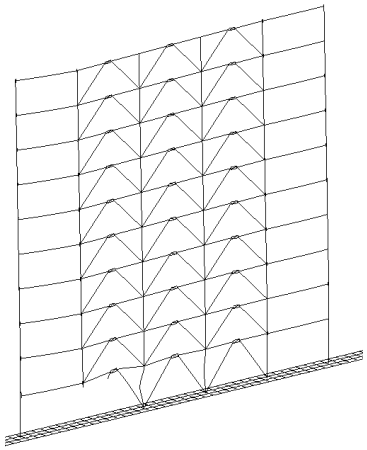

(a) Failure Mode: Pushdown analysis case 1 and 4

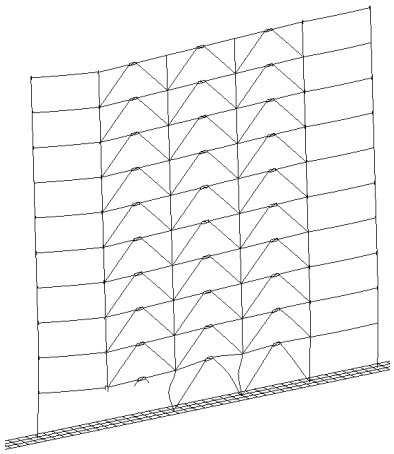

(b) Failure Mode: Pushdown analysis case 2 and 5

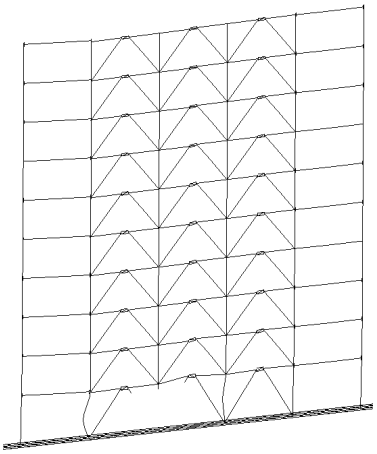

(c) Failure Mode: Pushdown analysis case 3 and 6

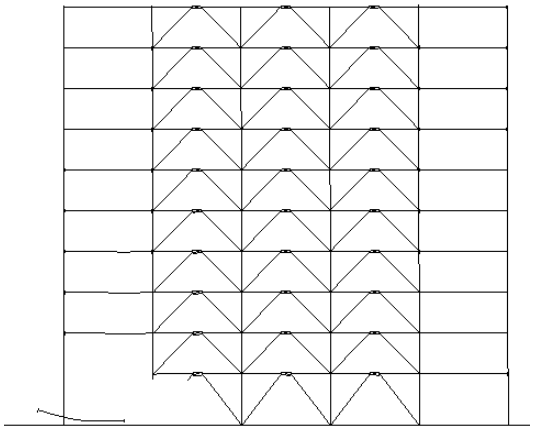

(d) Failure Mode: Pushdown analysis case 7 Load Factor 1.3

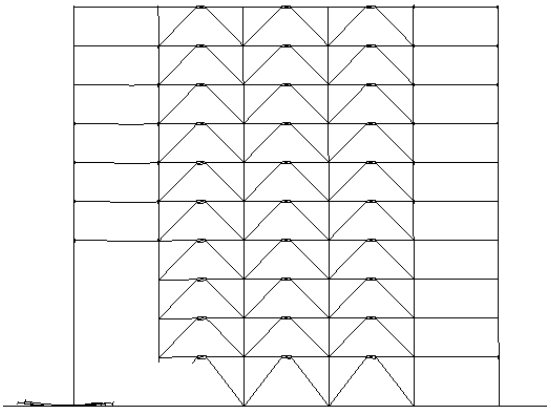

(e) Failure Mode: Pushdown analysis case 7 Load Factor 1.6

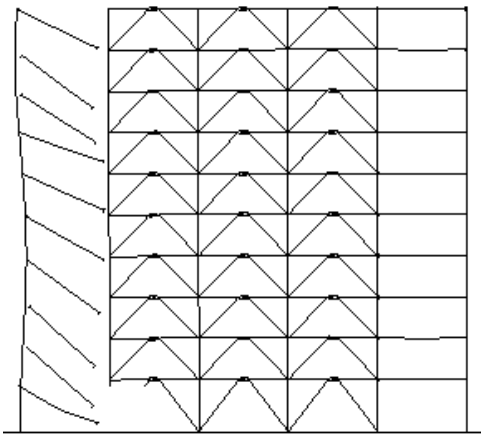

(f) Failure Mode: Pushdown analysis case 7 Load Factor 2.0

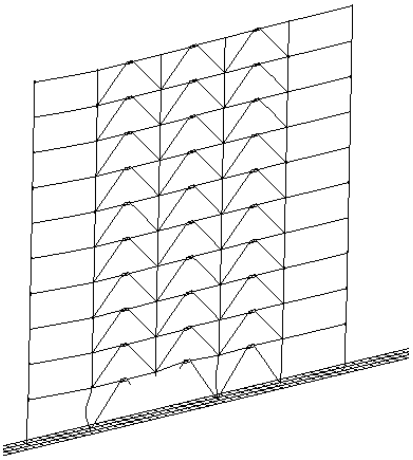

(g) Failure Mode: Pushdown analysis case 8 Load Factor 3.2

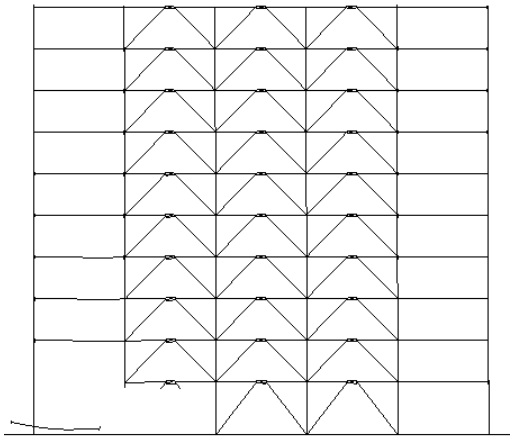

(h) Failure Mode: Pushdown analysis case 9 Load Factor 1.3

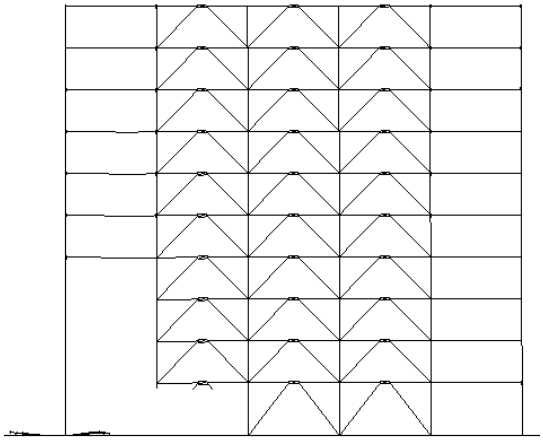

(i) Failure Mode: Pushdown analysis case 9 Load Factor 1.6

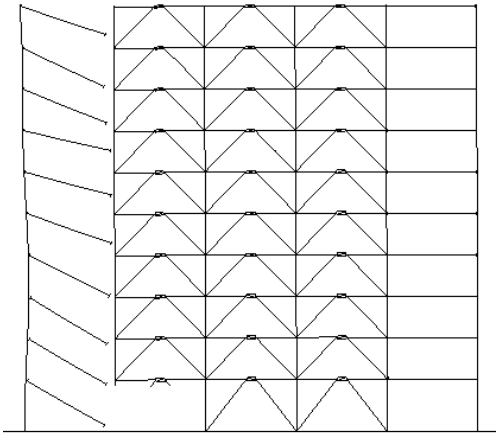

(j) Failure Mode: Pushdown analysis case 9 Load Factor 1.8

CHAPTER 6

MICROMECHANICAL MODEL FOR SIMULATION OF DUCTILE FRACTURE IN STEEL

6.1 Introduction

Ductile fracture in steel is a multi-step process resulting from microvoid nucleation, growth and coalescence of voids in a plastically deforming material. Microvoids typically nucleate at inclusions either by decohesion/debonding of the inclusion matrix interface or by fracture of the inclusion itself. Void nucleation is followed by a void growth stage where voids grow and interact until localized plastic flow and necking of the inter-void matrix occurs. The final phase of ductile fracture occurs when adjacent micro-voids coalesce together into a crack. The micromechanical constitutive model for porous plastic materials proposed by Gurson (1977) and further modified by Tvergaard (1981) and Tvergaard and Needleman (1984), here referred to as Gurson-Tvergaard-Needleman (GTN) model, is frequently used to simulate ductile fracture in steels. Variations of Gurson model such as those proposed by Gologanu et al. (1993, 1994) and Garajeu et al. (2000) also exists, but they are difficult to calibrate and therefore not commonly used in practice.

The GTN model was successfully used in Chapter 3 to simulate the behavior of steel sub-assemblages under collapse conditions. The relative success of the GTN model is primarily due to the incorporation of a sufficient number of adjustable parameters to enable curve fitting of the desired experimental results. However, the chosen parameters are found to be inconsistent with metallurgical results and thus have no physical

significance (Thomason, 1998). Following are important issues that are not address by the GTN model:

a) Void nucleation strain is independent of hydrostatic stress. Void nucleation models proposed by Argon et al. (1975) and Goods et al. (1979), and metallurgical studies (Beremin (1981), Le Roy et al. (1981), Thomson (1990)) have shown that void nucleation strain is sensitive to hydrostatic stress and that the nucleation strain decreases with increase in mean stress.

b) Material damage due to elongation of micro-voids is not considered by the GTN model, which assumes disintegration of material due to only dilation of micro-voids. However, the assumed void coalescence mechanism is not primarily due to micro-void dilations. The very large volumetric dilations needed to bring voids into close proximity are not observed in metallurgical examinations. Metallurgical results (Liu et al. (1968), Hayden et al. (1969), Brown (1976), Le Roy et al. (1981), Wilsdorf (1983), Thomson (1990)) have confirmed that void coalescence is primarily due to plastic limit load failure of the intervoid matrix which is sometimes assisted by micro-void nucleation at second phase particles. An additional parameter known as the critical void volume fraction is introduced in the GTN model to artificially account for the rapid disintegration of material after critical conditions are reached.

c) Most importantly, model parameters in the GTN model that are calibrated to a particular experiment cannot be considered as material properties and cannot be used to simulate ductile fracture in situations which differ largely from the original experiment used for model calibration. This is because the model parameters are dependent on the state of stress within the material and thus cannot be used to simulate fracture under a different state of stress.

In this chapter a damage mechanics-based plasticity model is developed within a finite deformation framework for modeling the micro-mechanical process of ductile fracture in structural steels. Damage mechanics principles of effective stress and strain equivalence

are employed to formulate a constitutive model for simulation of damage due to micro-voids nucleation, growth and coalescence. The micro-scale response of the damage model arises from the addition of history variables known as damage variables that represents the change in micro-structure of the material undergoing a deformation process. In the micro-mechanical model proposed in this work, a scalar damage variable is used to represents the changes that arise due to micro-structural evolution during the ductile fracture process in structural steels. In particular, the three stages of ductile fracture initiation: micro-void nucleation, growth and coalescence are modeled by an appropriate evolution function for the damage variable. Moreover, damage to due to both void elongation and volumetric void growth is modeled. This is a distinct advantage over the existing micro-mechanical models where only one void growth mode is usually represented. Also, the void nucleation strain is taken to be a function of stress triaxiality, thus rendering the model parameters as material properties. This model also belongs to the class of coupled multi-scale models, wherein the response at the macro-scale is directly coupled to the micro-structural evolution via constitutive material models. The model is calibrated and validated by comparing its response to the results obtained from experimental testing of notched steel bar specimens.

The relevant theoretical details of finite deformation continuum theory are first presented in Section 6.2, while other background details of the theory are included in Appendix A. The continuum mechanics framework presented here is based on the work of Van Der et al. (1996) and consistently employs the concepts of dual variables to formulate the theory. Numerical implementation of the proposed model is presented in Section 6.3. The result of parametric studies to investigate the effect of various model parameters on the material response is presented in Section 6.4. Experimental testing of steel specimens and model validation and calibration studies are presented in Section 6.5. and finally the important conclusions are presented in Section 6.6.

6.2 Theoretical Aspects

6.2.1 Kinematics

A continuum body B with a reference configuration $\mathfrak{B}_o$ is considered as a 3-dimensional differentiable manifold. Let $U \subset \mathfrak{B}_o$ be an open set. A coordinate system, $\{X^A\}$, on $\mathfrak{B}$, is a one-to-one mapping between the point's $P \in U$ and the points in an open subset of $\mathbb{R}^3$ i.e. $\{\mathrm{X}^\mathrm{A}\}$: $U \longrightarrow \mathbb{R}^3$. Let t be the time scale with $t \in [0, \infty]$. Motion of the body is considered as a one parameter family of at least C^1 diffeomorphism $\boldsymbol{\varphi}(P,t)\colon \mathfrak{B}_o \rightarrow \mathfrak{B}_t\colon P \mapsto p$, where the parameter t is the time. $\mathfrak{B}_t$ is the actual configuration of the body at time t and is again a manifold. A coordinate system on $\mathfrak{B}_t$ is denoted by $\{x^a\}$. The set of all possible configurations $\mathfrak{B}_p$ is called the configuration space $\mathcal{C}$. The motion of the body B is then simply a curve in configuration space $\mathcal{C}$.

For the following discussion, let $\{\boldsymbol{G}_i\}$ and $\{\boldsymbol{G}^i\}$ be the basis vectors of tangent ($T_P\mathfrak{B}_o$) and cotangent ($T_P^*\mathfrak{B}_o$) spaces, respectively. Also, let $\{\boldsymbol{g}_i\}$ and $\{\boldsymbol{g}^i\}$ be the basis vectors of tangent ($T_p\mathfrak{B}_t$) and cotangent ($T_p^*\mathfrak{B}_t$) spaces, respectively.

Definition 6.1: The material velocity field, $\boldsymbol{V}(P,t)$ is a vector field on $\mathfrak{B}_o$ and is defined as follows:

$$\boldsymbol{V}(P,t)\colon \mathfrak{B}_o \rightarrow T_P\mathfrak{B}_o \qquad \boldsymbol{V}(P,t) \stackrel{\text{def}}{=} \frac{\partial \boldsymbol{\varphi}(P,t)}{\partial t} \tag{6.1}$$

Definition 6.2: The motion $\boldsymbol{\varphi}(t)$ is called C^r-regular if it is a C^r- diffeomorphism for all time t.

Definition 6.3: The spatial velocity field of at least C^1-regular motion is a vector field on $\mathfrak{B}_t$ and is defined as follows:

$$\boldsymbol{v}(p,t)\colon \mathfrak{B}_t \rightarrow T_p\mathfrak{B}_t \qquad \boldsymbol{v}(p,t) \stackrel{\text{def}}{=} \boldsymbol{V}(P,t) \circ \boldsymbol{\varphi}^{-1} \tag{6.2}$$

Definition 6.4: The spatial velocity gradient, $\boldsymbol{l}^{\backslash}$, is defined as mixed (\ ) 2nd order tensor field on $\mathfrak{B}_t$:

$$\boldsymbol{l}^{\backslash}\colon T_p\mathfrak{B}_t \rightarrow T_p\mathfrak{B}_t \qquad \boldsymbol{l}^{\backslash} = \operatorname{grad} \boldsymbol{v}(p,t) \tag{6.3}$$

where the gradient operation is taken with respect to the current configuration.

Definition 6.5: The tangent, $T_P\boldsymbol{\varphi}$, of the map $\boldsymbol{\varphi}(P,t)\colon \mathfrak{B}_o \to \mathfrak{B}_t$, for fixed t, is known as the deformation gradient and is a two point tensor defined as follows:

$$\begin{gathered}\boldsymbol{\mathcal{F}}^{\backslash} = \boldsymbol{\mathcal{F}}^{\backslash}(P,t) = T_P\boldsymbol{\varphi} = \boldsymbol{\mathcal{F}}\colon T_P\mathfrak{B}_o \to T_p\mathfrak{B}_t \\ \ni \boldsymbol{\mathcal{F}} = \mathcal{F}^{a\cdot}_{\cdot A}\boldsymbol{g}_a \otimes \boldsymbol{G}^A \text{ and } \mathcal{F}^{a\cdot}_{\cdot A} = \left.\frac{\partial \varphi^a}{\partial X^A}\right|_P\end{gathered} \tag{6.4}$$

Also, $\boldsymbol{l}^{\backslash}$ is related to the deformation gradient by the following relationship:

$$\boldsymbol{l}^{\backslash} = \dot{\boldsymbol{\mathcal{F}}}\boldsymbol{\mathcal{F}}^{-1} \tag{6.5}$$

Deformation gradient, $\boldsymbol{l}^{\backslash}$, is a mixed tensor and therefore it can be decomposed into symmetric and skew-symmetric parts as follows:

$$\begin{gathered}\boldsymbol{l}^{\backslash} = \boldsymbol{d}^{\backslash} + \boldsymbol{w}^{\backslash} \\ \ni \quad \boldsymbol{d}^{\backslash} = \frac{1}{2}\left(\boldsymbol{l}^{\backslash} + \boldsymbol{l}^{\backslash T}\right) \quad \text{and} \quad \boldsymbol{w}^{\backslash} = \frac{1}{2}\left(\boldsymbol{l}^{\backslash} - \boldsymbol{l}^{\backslash T}\right)\end{gathered} \tag{6.6}$$

where $\boldsymbol{d}^{\backslash}$is known as the rate of deformation tensor and $\boldsymbol{w}^{\backslash}$is known as the spin tensor. The rate of deformation tensor $\boldsymbol{d}^{\backslash}$can also be expressed in terms of Lie derivative of the mixed spatial 2nd order identity tensor $\boldsymbol{i}^{\backslash}\colon T_p\mathfrak{B}_t \to T_p\mathfrak{B}_t$, as follows:

$$\begin{aligned}\frac{1}{2}\boldsymbol{\mathcal{L}}_v\left(\boldsymbol{i}^{\backslash}\right) &= \frac{1}{2}\boldsymbol{\varphi}_*\left(\frac{D}{Dt}\boldsymbol{\varphi}^*\left(\boldsymbol{i}^{\backslash}\right)\right) = \frac{1}{2}\boldsymbol{\mathcal{F}}^{-T}\left[\frac{D}{Dt}\left(\boldsymbol{\mathcal{F}}^T\boldsymbol{i}^{\backslash}\boldsymbol{\mathcal{F}}\right)\right]\boldsymbol{\mathcal{F}}^{-1} \\ &= \frac{1}{2}\boldsymbol{\mathcal{F}}^{-T}\left(\dot{\boldsymbol{\mathcal{F}}}^T\boldsymbol{\mathcal{F}} + \boldsymbol{\mathcal{F}}^T\dot{\boldsymbol{\mathcal{F}}}\right)\boldsymbol{\mathcal{F}}^{-1} = \boldsymbol{d}^{\backslash}\end{aligned} \tag{6.7}$$

In general, the Lie derivative of spatial 2nd order tensor field $\boldsymbol{t}^{\backslash}\colon T_p\mathfrak{B}_t \to T_p\mathfrak{B}_t$, can be obtained as follows:

$$\begin{aligned}\boldsymbol{\mathcal{L}}_v\left(\boldsymbol{t}^{\backslash}\right) &= \boldsymbol{\varphi}_*\left(\frac{D}{Dt}\boldsymbol{\varphi}^*\left(\boldsymbol{t}^{\backslash}\right)\right) = \boldsymbol{\mathcal{F}}^{-T}\left[\frac{D}{Dt}\left(\boldsymbol{\mathcal{F}}^T\boldsymbol{t}^{\backslash}\boldsymbol{\mathcal{F}}\right)\right]\boldsymbol{\mathcal{F}}^{-1} \\ &= \boldsymbol{\mathcal{F}}^{-T}\dot{\boldsymbol{\mathcal{F}}}^T\boldsymbol{t}^{\backslash} + \boldsymbol{t}^{\backslash} + \boldsymbol{t}^{\backslash}\dot{\boldsymbol{\mathcal{F}}}\boldsymbol{\mathcal{F}}^{-1} = \dot{\boldsymbol{t}}^{\backslash} + \boldsymbol{t}^{\backslash}\boldsymbol{l}^{\backslash} + \boldsymbol{l}^{\backslash T}\boldsymbol{t}^{\backslash}\end{aligned} \tag{6.8}$$

6.2.2 Deformation and Strain Measures

Deformations are usually measured in terms of the difference of the square of line elements in the reference configuration ($T_P\mathfrak{B}_o$) and in the current configuration ($T_p\mathfrak{B}_t$).

Let $d\boldsymbol{P} = \boldsymbol{\varphi}^*(d\boldsymbol{p}) \in T_P\mathfrak{B}_o$ and $d\boldsymbol{p} = \boldsymbol{\varphi}_*(d\boldsymbol{P}) \in T_p\mathfrak{B}_t$ be the vectors in reference and current configuration respectively. Then the squared length is expressed in terms of the inner product as follows:

$$\begin{aligned} dP^2 = d\boldsymbol{P}.d\boldsymbol{P} = \boldsymbol{\varphi}^*(d\boldsymbol{p}).\boldsymbol{\varphi}^*(d\boldsymbol{p}) = \boldsymbol{\mathcal{F}}^{-1}d\boldsymbol{p}.\boldsymbol{\mathcal{F}}^{-1}d\boldsymbol{p} \\ = d\boldsymbol{p}.\boldsymbol{\mathcal{F}}^{-T}\boldsymbol{\mathcal{F}}^{-1}d\boldsymbol{p} = d\boldsymbol{p}.\boldsymbol{\varphi}_*\left(\boldsymbol{I}^{\backslash}\right)d\boldsymbol{p} \end{aligned} \tag{6.9}$$

$$\begin{aligned} dp^2 = d\boldsymbol{p}.d\boldsymbol{p} = \boldsymbol{\varphi}_*(d\boldsymbol{P}).\boldsymbol{\varphi}_*(d\boldsymbol{P}) = \boldsymbol{\mathcal{F}}d\boldsymbol{P}.\boldsymbol{\mathcal{F}}d\boldsymbol{P} \\ = d\boldsymbol{P}.\boldsymbol{\mathcal{F}}^{T}\boldsymbol{\mathcal{F}}d\boldsymbol{P} = d\boldsymbol{P}.\boldsymbol{\varphi}^*\left(\boldsymbol{i}^{\backslash}\right)d\boldsymbol{P} \end{aligned} \tag{6.10}$$

where $\boldsymbol{I}^{\backslash}: T_P\mathfrak{B}_o \to T_P\mathfrak{B}_o$ and $\boldsymbol{i}^{\backslash}: T_p\mathfrak{B}_t \to T_p\mathfrak{B}_t$ are 2nd order mixed identity tensors. The following strain tensors are introduced:

Right Cauchy Green Tensor

$$\begin{aligned} &\boldsymbol{C}^{\backslash}: T_P\mathfrak{B}_o \to T_P\mathfrak{B}_o \\ &\boldsymbol{C}^{\backslash} \stackrel{\text{def}}{=} \boldsymbol{\mathcal{F}}^T\boldsymbol{\mathcal{F}} = \boldsymbol{\varphi}^*\left(\boldsymbol{i}^{\backslash}\right) \end{aligned} \tag{6.11}$$

Left Cauchy Green Tensor

$$\begin{aligned} &\boldsymbol{b}^{\backslash}: T_p\mathfrak{B}_t \to T_p\mathfrak{B}_t \qquad \boldsymbol{b}^{\backslash} \stackrel{\text{def}}{=} \boldsymbol{\mathcal{F}}\boldsymbol{\mathcal{F}}^T \\ &\boldsymbol{b}^{\backslash -1} = \boldsymbol{\mathcal{F}}^{-T}\boldsymbol{\mathcal{F}}^{-1} = \boldsymbol{\varphi}_*\left(\boldsymbol{I}^{\backslash}\right) \end{aligned} \tag{6.12}$$

Piola deformation Tensor

$$\begin{aligned} &\boldsymbol{B}^{\backslash}: T_P\mathfrak{B}_o \to T_P\mathfrak{B}_o \\ &\boldsymbol{B}^{\backslash} \stackrel{\text{def}}{=} \boldsymbol{C}^{\backslash -1} = \boldsymbol{\mathcal{F}}^{-1}\boldsymbol{\mathcal{F}}^{-T} \end{aligned} \tag{6.13}$$

Green-Lagrangian Tensor

$$\begin{aligned} &\boldsymbol{E}^{\backslash}: T_P\mathfrak{B}_o \to T_P\mathfrak{B}_o \\ &\boldsymbol{E}^{\backslash} \stackrel{\text{def}}{=} \frac{1}{2}\left(\boldsymbol{C}^{\backslash} - \boldsymbol{I}^{\backslash}\right) = \boldsymbol{\varphi}^*\left(\boldsymbol{e}^{\backslash}\right) \end{aligned} \tag{6.14}$$

Euler-Almansi Tensor

$$\begin{aligned} &\boldsymbol{e}^{\backslash}: T_p\mathfrak{B}_t \to T_p\mathfrak{B}_t \\ &\boldsymbol{e}^{\backslash} \stackrel{\text{def}}{=} \frac{1}{2}\left(\boldsymbol{i}^{\backslash} - \boldsymbol{b}^{\backslash -1}\right) = \boldsymbol{\varphi}_*\left(\boldsymbol{E}^{\backslash}\right) \end{aligned} \tag{6.15}$$

The difference of the squares of line elements can be expressed as follows:

$$dp^2 - dP^2 = 2d\boldsymbol{P}.\boldsymbol{E}^{\backslash}d\boldsymbol{P} = 2d\boldsymbol{p}.\boldsymbol{e}^{\backslash}d\boldsymbol{p} \tag{6.16}$$

Remark 6.1: The strain tensors presented above are some of the common measures of deformation employed in nonlinear solid mechanics. However, these are not the only strain measures that can be defined. A comprehensive review of strain measures can be found in Hill (1968, 1978) and Lubarda (2001).

The material time derivatives of the strain tensors $\boldsymbol{C}$ and $\boldsymbol{E}$, which are defined on the reference configuration, can be computed as follows:

$$\dot{\boldsymbol{C}}^{\backslash} = \dot{\boldsymbol{\mathcal{F}}}^T\boldsymbol{\mathcal{F}} + \boldsymbol{\mathcal{F}}^T\dot{\boldsymbol{\mathcal{F}}} = 2\boldsymbol{\varphi}^*\left(\boldsymbol{d}^{\backslash}\right) \tag{6.17}$$

$$\dot{\boldsymbol{E}}^{\backslash} = \frac{1}{2}\dot{\boldsymbol{C}}^{\backslash} = \boldsymbol{\varphi}^*\left(\boldsymbol{d}^{\backslash}\right) \tag{6.18}$$

where $\boldsymbol{\varphi}^*\left(\boldsymbol{d}^{\backslash}\right) = \boldsymbol{\mathcal{F}}^T\boldsymbol{d}^{\backslash}\boldsymbol{\mathcal{F}} = \frac{1}{2}\boldsymbol{\mathcal{F}}^T\left(\dot{\boldsymbol{\mathcal{F}}}\boldsymbol{\mathcal{F}}^{-1} + \boldsymbol{\mathcal{F}}^{-T}\dot{\boldsymbol{\mathcal{F}}}^T\right)\boldsymbol{\mathcal{F}} = \dot{\boldsymbol{C}}^{\backslash}/2$

The material time derivatives of spatial tensor fields are not objective. However, Lie derivatives of spatial tensors fields are objective tensor fields. Thus, Lie derivatives of spatial strain tensor fields are commonly used in constitutive equations. For instance, Lie derivative of spatial tensor fields $\boldsymbol{e}^{\backslash}$, $\boldsymbol{b}^{\backslash}$ and $\boldsymbol{b}^{-1}$ are given by:

$$\boldsymbol{\mathcal{L}}_v\left(\boldsymbol{e}^{\backslash}\right) = \boldsymbol{\varphi}_*\left(\frac{D}{Dt}\boldsymbol{\varphi}^*\left(\boldsymbol{e}^{\backslash}\right)\right) = \boldsymbol{\varphi}_*\left(\dot{\boldsymbol{E}}^{\backslash}\right) = \boldsymbol{d}^{\backslash} \tag{6.19}$$

$$\boldsymbol{\mathcal{L}}_v\left(\boldsymbol{b}^{\backslash}\right) = \boldsymbol{\mathcal{L}}_v\left(\boldsymbol{b}^{\backslash -1}\right) = \boldsymbol{0} \tag{6.20}$$

6.2.3 Intermediate Configurations

Intermediate configurations are usually introduced in plasticity theories implemented within finite deformation framework (Lee & Liu, 1967; Lee, 1969; Mandel, 1973; Simo and Ortiz, 1985; Simo, 1988 and others). In this section the geometrical aspects of such decompositions are discussed.

Let $\widehat{\mathfrak{B}}_t$ be an intermediate configuration (Fig. 6.1), then the following tangent maps are defined:

$$\begin{aligned} &\boldsymbol{\mathcal{F}}_{\varphi}: T_P\mathfrak{B}_o \to T_p\mathfrak{B}_t \qquad \boldsymbol{\mathcal{F}} = \boldsymbol{\mathcal{F}}_{\varphi} = T_P\boldsymbol{\varphi} \\ &\boldsymbol{\mathcal{F}}_{\varphi_1}: T_P\mathfrak{B}_o \to T_{\hat{p}}\widehat{\mathfrak{B}}_t \qquad \boldsymbol{\mathcal{F}}_1 = \boldsymbol{\mathcal{F}}_{\varphi_1} = T_P\boldsymbol{\varphi}_1 \\ &\boldsymbol{\mathcal{F}}_{\varphi_2}: T_{\hat{p}}\widehat{\mathfrak{B}}_t \to T_p\mathfrak{B}_t \qquad \boldsymbol{\mathcal{F}}_2 = \boldsymbol{\mathcal{F}}_{\varphi_2} = T_{\hat{p}}\,\boldsymbol{\varphi}_2 \end{aligned} \tag{6.21}$$

Also, since $\boldsymbol{\varphi}_1$ and $\boldsymbol{\varphi}_2$ are diffeomorphisms, the tangent $\boldsymbol{\mathcal{F}}_{\varphi}$ can be expressed as the composition of $\boldsymbol{\mathcal{F}}_{\varphi_1}$ and $\boldsymbol{\mathcal{F}}_{\varphi_2}$, i.e.

$$\boldsymbol{\mathcal{F}}_{\varphi} = \boldsymbol{\mathcal{F}}_{\varphi_2}\boldsymbol{\mathcal{F}}_{\varphi_1} \tag{6.22}$$

Unless the deformation is homogeneous, i.e. $\boldsymbol{\mathcal{F}}_{\varphi} \neq Function(P)$, it is not possible to find diffeomorphisms $\boldsymbol{\varphi}_1$ and $\boldsymbol{\varphi}_2$ such that Eq. 6.22 is satisfied for all $P \in \mathfrak{B}_o$ at a fixed time t. However, local diffeomorphisms $\boldsymbol{\varphi}_1 : U_P \to \widehat{U}_{\hat{P}}$ and $\boldsymbol{\varphi}_2 : \widehat{U}_{\hat{p}} \to V_p$ can be defined such that Eq. 6.22 is true in some neighborhoods U_P, $\widehat{U}_{\hat{p}}$ and V_p of P, $\hat{p}$ and p, respectively. For further discussion, intermediate configuration, $\widehat{\mathfrak{B}}_t$, and diffeomorphisms, $\boldsymbol{\varphi}_1$ and $\boldsymbol{\varphi}_2$, are interpreted in this spirit.

Let $d\boldsymbol{P} = \boldsymbol{\varphi}^*(d\boldsymbol{p}) = \boldsymbol{\varphi}_1^*(d\hat{\boldsymbol{p}}) \in T_P\mathfrak{B}_o$, $d\hat{\boldsymbol{p}} = \boldsymbol{\varphi}_*(d\boldsymbol{P}) = \boldsymbol{\varphi}_2^*(d\boldsymbol{p}) \in T_{\hat{p}}\widehat{\mathfrak{B}}_t$ and $d\boldsymbol{p} = \boldsymbol{\varphi}_*(d\boldsymbol{P}) = \boldsymbol{\varphi}_*(d\hat{\boldsymbol{p}}) \in T_p\mathfrak{B}_t$ be the vectors in reference, intermediate and current configurations respectively. Then the following kinematic relationships exist between these configurations:

$$\begin{aligned} dP^2 = d\boldsymbol{P}.d\boldsymbol{P} &= \boldsymbol{\varphi}^*(d\boldsymbol{p}).\boldsymbol{\varphi}^*(d\boldsymbol{p}) = \boldsymbol{\varphi}_1^*(d\hat{\boldsymbol{p}}).\boldsymbol{\varphi}_1^*(d\hat{\boldsymbol{p}}) \\ &= d\boldsymbol{p}.\boldsymbol{\mathcal{F}}^{-T}\boldsymbol{\mathcal{F}}^{-1}d\boldsymbol{p} = d\boldsymbol{p}.\boldsymbol{\varphi}_*\left(\boldsymbol{I}^{\backslash}\right)d\boldsymbol{p} \\ &= d\hat{\boldsymbol{p}}.\boldsymbol{\mathcal{F}}_1^{-T}\boldsymbol{\mathcal{F}}_1^{-1}\,d\hat{\boldsymbol{p}} = d\hat{\boldsymbol{p}}.\boldsymbol{\varphi}_{1*}\left(\boldsymbol{I}^{\backslash}\right)d\hat{\boldsymbol{p}} \end{aligned} \tag{6.23}$$

$$\begin{aligned} dp^2 = d\boldsymbol{p}.d\boldsymbol{p} &= \boldsymbol{\varphi}_*(d\boldsymbol{P}).\boldsymbol{\varphi}_*(d\boldsymbol{P}) = \boldsymbol{\varphi}_{2*}(d\hat{\boldsymbol{p}}).\boldsymbol{\varphi}_{2*}(d\hat{\boldsymbol{p}}) \\ &= d\boldsymbol{P}.\boldsymbol{\mathcal{F}}^{T}\boldsymbol{\mathcal{F}}d\boldsymbol{P} = d\boldsymbol{P}.\boldsymbol{\varphi}^*\left(\boldsymbol{i}^{\backslash}\right)d\boldsymbol{P} \\ &= d\hat{\boldsymbol{p}}.\boldsymbol{\mathcal{F}}_2^{T}\boldsymbol{\mathcal{F}}_2 d\hat{\boldsymbol{p}} = d\hat{\boldsymbol{p}}.\boldsymbol{\varphi}_2^*\left(\boldsymbol{i}^{\backslash}\right)d\hat{\boldsymbol{p}} \end{aligned} \tag{6.24}$$

$$\begin{aligned} d\hat{p}^2 = d\hat{\boldsymbol{p}}.d\hat{\boldsymbol{p}} &= \boldsymbol{\varphi}_{*1}(d\boldsymbol{P}).\boldsymbol{\varphi}_{*1}(d\boldsymbol{P}) = \boldsymbol{\varphi}_2^*(d\boldsymbol{p}).\boldsymbol{\varphi}_2^*(d\boldsymbol{p}) \\ &= d\boldsymbol{P}.\boldsymbol{\mathcal{F}}_1^{T}\boldsymbol{\mathcal{F}}_1 d\boldsymbol{P} = d\boldsymbol{P}.\boldsymbol{\varphi}_1^*\left(\hat{\boldsymbol{\imath}}^{\backslash}\right)d\boldsymbol{P} \\ &= d\boldsymbol{p}.\boldsymbol{\mathcal{F}}_2^{-T}\boldsymbol{\mathcal{F}}_2^{-1}\,d\boldsymbol{p} = d\boldsymbol{p}.\boldsymbol{\varphi}_{2*}\left(\hat{\boldsymbol{\imath}}^{\backslash}\right)d\boldsymbol{p} \end{aligned} \tag{6.25}$$

where $\hat{\boldsymbol{\imath}}^{\backslash} : T_{\hat{p}}\widehat{\mathfrak{B}}_t \to T_{\hat{p}}\widehat{\mathfrak{B}}_t$ is the 2nd order mixed identity tensors on intermediate configuration.

Remark 6.2: In plasticity theories that employ an intermediate configuration, the intermediate configuration $\widehat{\mathfrak{B}}_t$ is considered to be a stress free configuration, i.e. $\widehat{\mathfrak{B}}_t$ is obtained from the current configuration $\mathfrak{B}_t$ by relaxing each particle $p \in \mathfrak{B}_t$

to the stress free state $\hat{p} \in \widehat{\mathfrak{B}}_t$. The tangent map $\boldsymbol{\mathcal{F}}$ is then expressed as $\boldsymbol{\mathcal{F}} = \boldsymbol{\mathcal{F}}_e \boldsymbol{\mathcal{F}}_p$.

6.2.4 Stress Measures

To measure the internal power consumed inside the body due to instantaneous rate of deformation $\boldsymbol{d}^{\backslash}$, stress measures that belongs to the dual space relative to deformation measures are introduced. Cauchy stress tensor field, $\boldsymbol{\sigma}^{/}: T_p^* \mathfrak{B}_t \to T_p^* \mathfrak{B}_t$ and $\boldsymbol{\sigma}^{/} = \boldsymbol{\sigma}^{/}(p,t)$, is defined on the current configuration such that the internal power is given by:

$$\text{Internal Power, } \mathrm{P_{int}} = \int_{\mathfrak{B}_t} \langle \boldsymbol{\sigma}^{/}, \boldsymbol{d}^{\backslash} \rangle_p dv \tag{6.26}$$

The scalar product, $w_{int} = \langle \boldsymbol{\sigma}^{/}, \boldsymbol{d}^{\backslash} \rangle_p$, measures the rate of work per unit volume in the current configuration. Moreover, for non-polar materials, the Cauchy stress tensor is a symmetric tensor, i.e. $\boldsymbol{\sigma}^{/} = \boldsymbol{\sigma}^{/T}$, this result follows from the balance of angular momentum. Other important stress measures that are of interest in solid mechanics are introduced below:

Kirchhoff Stress Tensor	$\boldsymbol{\tau}^{/}: T_p^* \mathfrak{B}_t \to T_p^* \mathfrak{B}_t \qquad \boldsymbol{\tau}^{/} \stackrel{\text{def}}{=} J \boldsymbol{\sigma}^{/}$	(6.27)
Second Piola-Kirchhoff Stress Tensor	$\boldsymbol{S}^{/}: T_P^* \mathfrak{B}_o \to T_P^* \mathfrak{B}_o$ $\boldsymbol{S}^{/} \stackrel{\text{def}}{=} \boldsymbol{\varphi}^*(\boldsymbol{\tau}^{/}) = \boldsymbol{\mathcal{F}}^{*-T} \boldsymbol{\tau}^{/} \boldsymbol{\mathcal{F}}^{*-1}$	(6.28)
First Piola-Kirchhoff Stress Tensor	$\boldsymbol{P}^{/}: T_P^* \mathfrak{B}_o \to T_p^* \mathfrak{B}_t$ $\boldsymbol{P}^{/} \stackrel{\text{def}}{=} \boldsymbol{\mathcal{F}}^{*T} \boldsymbol{S}^{/}$	(6.29)
Mandel Stress Tensor	$\boldsymbol{\Sigma}^{/}: T_P^* \mathfrak{B}_o \to T_P^* \mathfrak{B}_t \qquad \boldsymbol{\Sigma}^{/} \stackrel{\text{def}}{=} \boldsymbol{C}^{\backslash *} \boldsymbol{S}^{/}$	(6.30)

where $J = \det(\boldsymbol{\mathcal{F}})$. In formulating constitutive equations for a pure mechanical theory, i.e. ignoring thermodynamic, magnetic and other related effects, using Coleman-Noll principle, the rate of work per unit reference volume enters into the expression for mechanical energy dissipation. Thus, rate of mechanical work per unit volume in the reference configuration or stress power, W_{int}, is introduced, where $W_{int} = \langle \boldsymbol{\tau}^{/}, \boldsymbol{d}^{\backslash} \rangle_p$.

$\boldsymbol{\tau}^{/}$and $\boldsymbol{d}^{\backslash}$are known as work conjugate pairs. Equivalent expressions of W_{int} in terms of other stress and strain measures can be obtained as follows: $\langle \boldsymbol{\tau}^{/}, \boldsymbol{d}^{\backslash} \rangle_p = \boldsymbol{\varphi}^{*}(\langle \boldsymbol{\tau}^{/}, \boldsymbol{d}^{\backslash} \rangle_p) = \langle \boldsymbol{S}^{/}, \dot{\boldsymbol{E}}^{\backslash} \rangle_P = \langle \boldsymbol{S}^{/}, \frac{1}{2}(\dot{\boldsymbol{\mathcal{F}}}^{T}\boldsymbol{\mathcal{F}} + \boldsymbol{\mathcal{F}}^{T}\dot{\boldsymbol{\mathcal{F}}}) \rangle_P = \langle \boldsymbol{S}^{/}, \boldsymbol{\mathcal{F}}^{T}\dot{\boldsymbol{\mathcal{F}}} \rangle_P = \langle \boldsymbol{\mathcal{F}}^{*T}\boldsymbol{S}^{/}, \dot{\boldsymbol{\mathcal{F}}} \rangle_P = \langle \boldsymbol{P}^{/}, \dot{\boldsymbol{\mathcal{F}}} \rangle_P = \langle \boldsymbol{C}^{\backslash *}\boldsymbol{S}^{/}, \boldsymbol{C}^{\backslash -1}\dot{\boldsymbol{E}}^{\backslash} \rangle_P = \langle \boldsymbol{\Sigma}^{/}, \frac{1}{2}\boldsymbol{C}^{\backslash -1}\dot{\boldsymbol{C}}^{\backslash} \rangle_P$.

Therefore the rate of mechanical work can be expressed as follows:

$$W_{int} = \langle \boldsymbol{\tau}^{/}, \boldsymbol{d}^{\backslash} \rangle_p = \langle \boldsymbol{S}^{/}, \dot{\boldsymbol{E}}^{\backslash} \rangle_P = \langle \boldsymbol{P}^{/}, \dot{\boldsymbol{\mathcal{F}}} \rangle_P = \langle \boldsymbol{\Sigma}^{/}, \frac{1}{2}\boldsymbol{C}^{\backslash -1}\dot{\boldsymbol{C}}^{\backslash} \rangle_P \tag{6.31}$$

6.2.5 Hyperelastic Material

Hyperelastic materials admit existence of a free energy function Ψ. For a purely mechanical theory, Ψ is assumed to be a function of $\boldsymbol{I}^{\backslash}$, $\boldsymbol{i}^{\backslash}$ and $\boldsymbol{\mathcal{F}}^{\backslash}$, i.e. $\Psi = \Psi(\boldsymbol{I}^{\backslash}, \boldsymbol{i}^{\backslash}, \boldsymbol{\mathcal{F}}^{\backslash})$. This is the most general form of free energy function that can be assumed for hyperelastic materials that are assumed to be "local", i.e. derivates of higher order other than the first derivative $\boldsymbol{\mathcal{F}}$ are not used (Marsden & Hughes, 1994). Free energy can be interpreted as the energy stored in the material as it is being deformed. The underlying physical mechanism includes, for example energy stored in elastic atomic lattices for crystalline solids, energy stored in molecular chains in polymers etc.

The functional form of free energy function can be further simplified by assuming the postulate of spatial covariance. Spatial covariance means that the free energy function $\Psi(\boldsymbol{I}^{\backslash}, \boldsymbol{i}^{\backslash}, \boldsymbol{\mathcal{F}})$, expressed per unit volume, should be invariant under any arbitrary superposed spatial diffeomorphism. Let $\boldsymbol{\xi}$ be any diffeomorphism superimposed on current configuration $\mathfrak{B}_t$, with $\boldsymbol{\mathcal{F}}_{\xi} = T\boldsymbol{\xi}$ and $\det(\boldsymbol{\mathcal{F}}_{\xi}) > 0$, (Figure 6.2) such that:

$$\boldsymbol{\mathcal{F}}_{\xi} = T\boldsymbol{\xi}: T_p\mathfrak{B}_t \rightarrow T_{p'}\mathfrak{B}'_t \tag{6.32}$$

Covariance implies that:

$$\Psi\left(\boldsymbol{I}^{\backslash}, \boldsymbol{i}^{\backslash}, \boldsymbol{\mathcal{F}}\right) = \boldsymbol{\xi}_{*}(\Psi) = \Psi\left(\boldsymbol{I}^{\backslash}, \boldsymbol{\xi}_{*}(\boldsymbol{i}^{\backslash}), \boldsymbol{\mathcal{F}}_{\xi}\boldsymbol{\mathcal{F}}\right) \tag{6.33}$$

Now since $\boldsymbol{\xi}$ is arbitrary, assuming $\boldsymbol{\xi} = \boldsymbol{\varphi}^{-1}$, i.e. $\boldsymbol{\mathcal{F}}_{\xi} = \boldsymbol{\mathcal{F}}^{-1} = T\boldsymbol{\varphi}^{-1}$ gives:

$$\Psi = \Psi\left(\boldsymbol{I}^{\backslash}, \boldsymbol{\mathcal{F}}^{*}\boldsymbol{i}^{\backslash}\boldsymbol{\mathcal{F}}, \boldsymbol{\mathcal{F}}^{-1}\boldsymbol{\mathcal{F}}\right) = \Psi\left(\boldsymbol{I}^{\backslash}, \boldsymbol{\varphi}^{*}(\boldsymbol{i}^{\backslash}), \boldsymbol{\mathcal{F}}^{-1}\boldsymbol{\mathcal{F}}\right) = \Psi\left(\boldsymbol{G}^{b}, \boldsymbol{C}^{\backslash}\right)$$
$$\therefore \Psi = \Psi_{C}\left(\boldsymbol{I}^{\backslash}, \boldsymbol{C}^{\backslash}\right) = \Psi_{E}\left(\boldsymbol{I}^{\backslash}, \boldsymbol{E}^{\backslash}\right) \tag{6.34}$$

Thus free energy is expressed as a function of 2nd order mixed identity tensor $\boldsymbol{I}^{\backslash}$ and strain tensor ($\boldsymbol{C}^{\backslash}$ or $\boldsymbol{E}^{\backslash}$) in the reference configuration. For a purely mechanical theory the second law of thermodynamics in form of Clausius-Plank inequality implies the non-negativeness of the internal mechanical energy dissipation rate, D_{int}, per unit reference volume where:

$$D_{int} = W_{int} - \dot{\Psi} \geq 0$$

This inequality represents a simple fact that for any real physical process energy dissipation is always non-negative. The material time derivative of free energy, $\dot{\Psi}$, can be expressed as follows:

$$\dot{\Psi} = \langle \frac{\partial \Psi_{C}}{\partial \boldsymbol{C}^{\backslash}}, \dot{\boldsymbol{C}}^{\backslash} \rangle = \langle \frac{\partial \Psi_{E}}{\partial \boldsymbol{E}^{\backslash}}, \dot{\boldsymbol{E}}^{\backslash} \rangle = \langle \frac{\partial \Psi_{\mathcal{F}}}{\partial \boldsymbol{\mathcal{F}}}, \dot{\boldsymbol{\mathcal{F}}} \rangle \tag{6.35}$$

The gradients $\frac{\partial \Psi_{C}}{\partial \boldsymbol{C}^{\backslash}}$, $\frac{\partial \Psi_{E}}{\partial \boldsymbol{E}^{\backslash}}$ and $\frac{\partial \Psi_{\mathcal{F}}}{\partial \boldsymbol{\mathcal{F}}}$ are 2nd order mixed tensor of type / and $\frac{\partial \Psi_{C}}{\partial \boldsymbol{C}^{\backslash}}$ and $\frac{\partial \Psi_{E}}{\partial \boldsymbol{E}^{\backslash}}$ are symmetric. Also the following relationships exist between them:

$$\frac{\partial \Psi_{C}}{\partial \boldsymbol{C}^{\backslash}} = \frac{1}{2}\frac{\partial \Psi_{E}}{\partial \boldsymbol{E}^{\backslash}} \tag{6.36}$$

$$\frac{\partial \Psi_{\mathcal{F}}}{\partial \boldsymbol{\mathcal{F}}} = 2\boldsymbol{\mathcal{F}}^{*T}\frac{\partial \Psi_{C}}{\partial \boldsymbol{C}^{\backslash}} \tag{6.37}$$

Eq. 6.37 follows from the fact that: $\langle \frac{\partial \Psi_{C}}{\partial \boldsymbol{C}^{\backslash}}, \dot{\boldsymbol{C}}^{\backslash} \rangle = \langle \frac{\partial \Psi_{C}}{\partial \boldsymbol{C}^{\backslash}}, \dot{\boldsymbol{\mathcal{F}}}^{T}\boldsymbol{\mathcal{F}} + \boldsymbol{\mathcal{F}}^{T}\dot{\boldsymbol{\mathcal{F}}} \rangle = \langle \frac{\partial \Psi_{C}}{\partial \boldsymbol{C}^{\backslash}}, 2\boldsymbol{\mathcal{F}}^{T}\dot{\boldsymbol{\mathcal{F}}} \rangle =$
$\langle 2\boldsymbol{\mathcal{F}}^{*T}\frac{\partial \Psi_{C}}{\partial \boldsymbol{C}^{\backslash}}, \dot{\boldsymbol{\mathcal{F}}} \rangle = \langle \frac{\partial \Psi_{\mathcal{F}}}{\partial \boldsymbol{\mathcal{F}}}, \dot{\boldsymbol{\mathcal{F}}} \rangle$

Internal mechanical energy dissipation rate can be expressed using Eq. 6.31 and Eq. 6.35 as follows:

$$D_{int} = \langle \boldsymbol{S}^{/} - \frac{\partial \Psi_{E}}{\partial \boldsymbol{E}}, \dot{\boldsymbol{E}}^{\backslash} \rangle_{P} \geq 0 \text{ or equivalently}$$
$$D_{int} = \langle \boldsymbol{P}^{/} - \frac{\partial \Psi_{\mathcal{F}}}{\partial \boldsymbol{\mathcal{F}}}, \dot{\boldsymbol{\mathcal{F}}} \rangle_{P} \geq 0 \tag{6.38}$$

For a hyperelastic material $D_{int} = 0$, for all admissible strain rates. Therefore, with this restriction Eq. 3.38 gives:

$$\boldsymbol{S}^{/} = \frac{\partial \Psi_{E}}{\partial \boldsymbol{E}} = 2\frac{\partial \Psi_{C}}{\partial \boldsymbol{C}^{\backslash}} \tag{6.39}$$

$$\boldsymbol{P}^{/} = \frac{\partial \Psi_{\mathcal{F}}}{\partial \boldsymbol{\mathcal{F}}} \tag{6.40}$$

Equation 6.39 and 6.40 are the expressions of constitutive relation for the material under consideration. This procedure of deriving constitutive relation is formally known as Coleman-Noll procedure (Coleman & Noll, (1963) and Coleman & Gurtin, (1967)). Other constitutive relationships in terms of stress measures $\boldsymbol{\tau}^{/}$, $\boldsymbol{\sigma}^{/}$ and $\boldsymbol{\Sigma}^{/}$ can be obtained as follows:

$$\boldsymbol{\tau}^{/} = \boldsymbol{\varphi}_{*}(\boldsymbol{S}^{/}) = \; 2\boldsymbol{\mathcal{F}}^{*T}\frac{\partial \Psi_{C}}{\partial \boldsymbol{C}^{\backslash}}\boldsymbol{\mathcal{F}}^{*} = \frac{\partial \Psi_{\mathcal{F}}}{\partial \boldsymbol{\mathcal{F}}}\boldsymbol{\mathcal{F}}^{*} = \boldsymbol{P}^{/}\boldsymbol{\mathcal{F}}^{*} \tag{6.41}$$

$$\boldsymbol{\sigma}^{/} = \frac{1}{J}\boldsymbol{\tau}^{/} = \; \frac{2}{J}\boldsymbol{\mathcal{F}}^{*T}\frac{\partial \Psi_{C}}{\partial \boldsymbol{C}^{\backslash}}\boldsymbol{\mathcal{F}}^{*} = \frac{1}{J}\frac{\partial \Psi_{\mathcal{F}}}{\partial \boldsymbol{\mathcal{F}}}\boldsymbol{\mathcal{F}}^{*} = \frac{1}{J}\boldsymbol{P}^{/}\boldsymbol{\mathcal{F}}^{*} \tag{6.42}$$

$$\boldsymbol{\Sigma}^{/} = \boldsymbol{C}^{\backslash *}\boldsymbol{S}^{/} = 2\boldsymbol{C}^{\backslash *}\frac{\partial \Psi_{C}}{\partial \boldsymbol{C}^{\backslash}} \tag{6.43}$$

Remark 6.3: The material response depends on the specific form of free energy function chosen. In particular, the above described model in terms of free energy is valid for material without any internal constrains. For material with internal constrains, for example incompressible material, the form of free energy function is altered to represent such constraints. Furthers specific examples of free energy models for material with or without internal constraints can be found in Ogden (1997) and Holzapfel (2000) and in the references therein.

Remark 6.4: For isotropic materials, the free energy function can be reduced further in terms of invariants or eigen-values of tensors $\boldsymbol{C}^{\backslash}$ or $\boldsymbol{b}^{\backslash}$. Isotropy implies that the free energy function Ψ should be invariant under any arbitrary superposed isometry on the reference configuration. Consider a diffeomorphism superimposed on reference configuration $\mathfrak{B}_o$, $\boldsymbol{\xi}_{iso}: \mathfrak{B}_o \to \mathfrak{B}'_o$, with tangent $\boldsymbol{\mathcal{F}}_{\xi_{iso}} = T\boldsymbol{\xi}_{iso}$ and $\boldsymbol{\xi}_{iso*}(\boldsymbol{G}^b) = \boldsymbol{G}^b$, such diffeomorphism are known as isometries. The invariance of free energy with respect to isometries is then expressed as follows:

$$\Psi = \boldsymbol{\xi}_{iso*}\left[\Psi\left(\boldsymbol{I}^{\backslash}, \boldsymbol{C}^{\backslash}\right)\right] = \Psi\left(\boldsymbol{I}^{\backslash}, \boldsymbol{\mathcal{F}}_{\xi_{iso}}^{-T}\boldsymbol{C}^{\backslash}\boldsymbol{\mathcal{F}}_{\xi_{iso}}^{-1}\right) \tag{6.44}$$

Choosing $\boldsymbol{\mathcal{F}}_{\xi_{iso}} = \boldsymbol{Q}^{\backslash} \in SO(3)$, Eq. 6.44 implies that

$$\Psi = \Psi\left(\boldsymbol{I}^{\backslash}, \boldsymbol{Q}^{\backslash}\boldsymbol{C}^{\backslash}\boldsymbol{Q}^{\backslash T}\right) \tag{6.45}$$

Thus the free energy function is a rotationally invariant function of $\boldsymbol{C}^{\backslash}$. Since $\boldsymbol{C}^{\backslash}$ is symmetric it can be brought to a diagonal form by an orthogonal transformation, so Ψ is function of only eigen-values or invariants of $\boldsymbol{C}^{\backslash}$.

6.2.6 Multiplicative Plasticity

In multiplicative plasticity model for finite deformation, an intermediate configuration is introduced, which is assumed to be stress free (Figure 6.3).The deformation gradient is decomposed into elastic and plastic parts as follows:

$$\boldsymbol{\mathcal{F}} = \boldsymbol{\mathcal{F}}_e\boldsymbol{\mathcal{F}}_p \tag{6.46}$$

In case of steel plasticity, from the micromechanical point of view, $\boldsymbol{\mathcal{F}}_p$ is an internal variable related to the amount of plastic flow or dislocation movement associated with the underlying crystalline structure. However, from the phenomenological standpoint the intermediate configuration defines the local, stress free unloaded configuration.

The multiplicative decomposition given by Eq. 6.46 is not unique, it is defined up to a rigid body rotation. Indeed for any rotation $\boldsymbol{Q}^{\backslash} \in SO(3)$, the decomposition implies that $\boldsymbol{\mathcal{F}} = (\boldsymbol{\mathcal{F}}_e\boldsymbol{Q}^{\backslash})(\boldsymbol{Q}^{\backslash T}\boldsymbol{\mathcal{F}}_p)$. Based on this decomposition the following strain tensors can be defined:

RC $$\boldsymbol{C}_p^{\backslash}: T_P\mathfrak{B}_o \to T_P\mathfrak{B}_o \quad \boldsymbol{C}_p^{\backslash} \overset{\text{def}}{=} \boldsymbol{\mathcal{F}}_p^T\boldsymbol{\mathcal{F}}_p \tag{6.47}$$

RC $$\boldsymbol{E}_p^{\backslash}: T_P\mathfrak{B}_o \to T_p\mathfrak{B}_o \quad \boldsymbol{E}_p^{\backslash} \overset{\text{def}}{=} \frac{1}{2}\left(\boldsymbol{C}_p^{\backslash} - \boldsymbol{I}^{\backslash}\right) \tag{6.48}$$

RC $$\boldsymbol{E}_e^{\backslash}: T_P\mathfrak{B}_o \to T_p\mathfrak{B}_o \quad \boldsymbol{E}_e^{\backslash} \overset{\text{def}}{=} \boldsymbol{E}^{\backslash} - \boldsymbol{E}_p^{\backslash} = \frac{1}{2}\left(\boldsymbol{C}^{\backslash} - \boldsymbol{C}_p^{\backslash}\right) \tag{6.49}$$

IC $$\begin{gathered}\widehat{\boldsymbol{b}}_p^{\backslash}: T_{\hat{p}}\widehat{\mathfrak{B}}_t \to T_{\hat{p}}\widehat{\mathfrak{B}}_t \quad \widehat{\boldsymbol{b}}_p^{\backslash} \overset{\text{def}}{=} \boldsymbol{\mathcal{F}}_p\boldsymbol{\mathcal{F}}_p^T \\ \widehat{\boldsymbol{b}}_p^{\backslash -1} = \boldsymbol{\mathcal{F}}_p^{-T}\boldsymbol{\mathcal{F}}_p^{-1}\end{gathered} \tag{6.50}$$

IC $$\hat{\boldsymbol{e}}_p^{\backslash}: T_{\hat{p}}\widehat{\mathfrak{B}}_t \to T_{\hat{p}}\widehat{\mathfrak{B}}_t \quad \hat{\boldsymbol{e}}_p^{\backslash} \overset{\text{def}}{=} \frac{1}{2}\left(\hat{\boldsymbol{\imath}}^{\backslash} - \widehat{\boldsymbol{b}}_p^{\backslash -1}\right) \tag{6.51}$$

IC $$\hat{\boldsymbol{c}}_e^{\backslash}: T_{\hat{p}}\widehat{\mathfrak{B}}_t \to T_{\hat{p}}\widehat{\mathfrak{B}}_t \quad \hat{\boldsymbol{c}}_e^{\backslash} \overset{\text{def}}{=} \boldsymbol{\mathcal{F}}_e^T\boldsymbol{\mathcal{F}}_e \tag{6.52}$$

IC $$\hat{\boldsymbol{e}}_e^{\backslash}: T_{\hat{p}}\widehat{\mathfrak{B}}_t \to T_{\hat{p}}\widehat{\mathfrak{B}}_t \quad \hat{\boldsymbol{e}}_e^{\backslash} \stackrel{\text{def}}{=} \frac{1}{2}(\hat{\boldsymbol{c}}_e^{\backslash} - \hat{\boldsymbol{i}}^{\backslash})$$ (6.53)

IC $$\hat{\boldsymbol{e}}^{\backslash}: T_{\hat{p}}\widehat{\mathfrak{B}}_t \to T_{\hat{p}}\widehat{\mathfrak{B}}_t \quad \hat{\boldsymbol{e}}^{\backslash} \stackrel{\text{def}}{=} \hat{\boldsymbol{e}}_e^{\backslash} + \hat{\boldsymbol{e}}_p^{\backslash}$$ (6.54)

CC $$\boldsymbol{b}_e^{\backslash}: T_p\mathfrak{B}_t \to T_p\mathfrak{B}_t \quad \boldsymbol{b}_e^{\backslash} \stackrel{\text{def}}{=} \boldsymbol{\mathcal{F}}_e\boldsymbol{\mathcal{F}}_e^T \qquad \boldsymbol{b}_e^{\backslash -1} = \boldsymbol{\mathcal{F}}_e^{-T}\boldsymbol{\mathcal{F}}_e^{-1}$$ (6.55)

CC $$\boldsymbol{e}_e^{\backslash}: T_p\mathfrak{B}_t \to T_p\mathfrak{B}_t \quad \boldsymbol{e}_e^{\backslash} \stackrel{\text{def}}{=} \frac{1}{2}\left(\boldsymbol{i}^{\backslash} - \boldsymbol{b}_e^{\backslash -1}\right)$$ (6.56)

CC $$\boldsymbol{e}_p^{\backslash}: T_p\mathfrak{B}_t \to T_p\mathfrak{B}_t \quad \boldsymbol{e}_p^{\backslash} \stackrel{\text{def}}{=} \boldsymbol{e}^{\backslash} - \boldsymbol{e}_e^{\backslash} = \frac{1}{2}\left(\boldsymbol{b}_e^{\backslash -1} - \boldsymbol{b}^{\backslash -1}\right)$$ (6.57)

where $T_{\hat{p}}\widehat{\mathfrak{B}}_t$, is the tangent space in intermediate configuration and $\hat{\boldsymbol{i}}^{\backslash}: T_{\hat{p}}\widehat{\mathfrak{B}}_t \to T_{\hat{p}}\widehat{\mathfrak{B}}_t$ is the 2nd order mixed identity tensors on intermediate configuration. Also the following notation is used - RC: reference configuration, IC: intermediate configuration, and CC: current configuration. These tensors are related by push-forward and pull-back operations as follows:

$$\begin{aligned}
\boldsymbol{I}^{\backslash} &= \boldsymbol{\varphi}^*\left(\boldsymbol{b}^{\backslash -1}\right) = \boldsymbol{\varphi}_p^*\left(\boldsymbol{b}_p^{\backslash -1}\right) \\
\boldsymbol{C}^{\backslash} &= \boldsymbol{\varphi}^*\left(\boldsymbol{i}^{\backslash}\right) = \boldsymbol{\varphi}_p^*\left(\hat{\boldsymbol{c}}_e^{\backslash}\right) \\
\boldsymbol{E}^{\backslash} &= \boldsymbol{\varphi}^*\left(\boldsymbol{e}^{\backslash}\right) = \boldsymbol{\varphi}_p^*\left(\hat{\boldsymbol{e}}^{\backslash}\right) \\
\boldsymbol{C}_p^{\backslash} &= \boldsymbol{\varphi}^*\left(\boldsymbol{b}_e^{\backslash -1}\right) = \boldsymbol{\varphi}_p^*\left(\hat{\boldsymbol{i}}^{\backslash}\right) \\
\boldsymbol{E}_p^{\backslash} &= \boldsymbol{\varphi}^*\left(\boldsymbol{e}_p^{\backslash}\right) = \boldsymbol{\varphi}_p^*\left(\hat{\boldsymbol{e}}_p^{\backslash}\right) \\
\boldsymbol{E}_e^{\backslash} &= \boldsymbol{\varphi}^*\left(\boldsymbol{e}_e^{\backslash}\right) = \boldsymbol{\varphi}_p^*\left(\hat{\boldsymbol{e}}_e^{\backslash}\right)
\end{aligned}$$ (6.58)

$$\begin{aligned}
\hat{\boldsymbol{i}}^{\backslash} &= \boldsymbol{\varphi}_{p*}\left(\boldsymbol{C}_p^{\backslash}\right) = \boldsymbol{\varphi}_e^*\left(\boldsymbol{b}_e^{\backslash -1}\right) \\
\widehat{\boldsymbol{b}}_p^{\backslash -1} &= \boldsymbol{\varphi}_{p*}\left(\boldsymbol{I}^{\backslash}\right) = \boldsymbol{\varphi}_e^*\left(\boldsymbol{b}^{\backslash -1}\right) \\
\hat{\boldsymbol{e}}_p^{\backslash} &= \boldsymbol{\varphi}_{p*}\left(\boldsymbol{E}_p^{\backslash}\right) = \boldsymbol{\varphi}_e^*\left(\boldsymbol{e}_p^{\backslash}\right) \\
\hat{\boldsymbol{c}}_e^{\backslash} &= \boldsymbol{\varphi}_{p*}\left(\boldsymbol{C}^{\backslash}\right) = \boldsymbol{\varphi}_e^*\left(\boldsymbol{i}^{\backslash}\right) \\
\hat{\boldsymbol{e}}_e^{\backslash} &= \boldsymbol{\varphi}_{p*}\left(\boldsymbol{E}_e^{\backslash}\right) = \boldsymbol{\varphi}_e^*\left(\boldsymbol{e}_e^{\backslash}\right) \\
\hat{\boldsymbol{e}}^{\backslash} &= \boldsymbol{\varphi}_{p*}\left(\boldsymbol{E}^{\backslash}\right) = \boldsymbol{\varphi}_e^*\left(\boldsymbol{e}^{\backslash}\right)
\end{aligned}$$ (6.59)

$$
\begin{aligned}
\boldsymbol{i}^{\backslash} &= \boldsymbol{\varphi}_{*}\left(\boldsymbol{C}^{\backslash}\right) = \boldsymbol{\varphi}_{e*}\left(\hat{\boldsymbol{c}}_{e}^{\backslash}\right) \\
\boldsymbol{b}^{\backslash -1} &= \boldsymbol{\varphi}_{*}\left(\boldsymbol{I}^{\backslash}\right) = \boldsymbol{\varphi}_{e*}\left(\hat{\boldsymbol{b}}_{p}^{\backslash -1}\right) \\
\boldsymbol{e}^{\backslash} &= \boldsymbol{\varphi}_{*}\left(\boldsymbol{E}^{\backslash}\right) = \boldsymbol{\varphi}_{e*}\left(\hat{\boldsymbol{e}}^{\backslash}\right) \\
\boldsymbol{b}_{e}^{\backslash -1} &= \boldsymbol{\varphi}_{*}\left(\boldsymbol{C}_{p}^{\backslash}\right) = \boldsymbol{\varphi}_{e*}\left(\hat{\boldsymbol{\imath}}^{\backslash}\right) \\
\boldsymbol{e}_{e}^{\backslash} &= \boldsymbol{\varphi}_{*}\left(\boldsymbol{E}_{e}^{\backslash}\right) = \boldsymbol{\varphi}_{e*}\left(\hat{\boldsymbol{e}}_{e}^{\backslash}\right) \\
\boldsymbol{e}_{\boldsymbol{p}}^{\backslash} &= \boldsymbol{\varphi}_{*}\left(\boldsymbol{E}_{p}^{\backslash}\right) = \boldsymbol{\varphi}_{e*}\left(\hat{\boldsymbol{e}}_{p}^{\backslash}\right)
\end{aligned}
\tag{6.60}
$$

The material time derivatives of strain tensor on RC and Lie time derivatives of tensors defined on IC and CC are useful in deriving constitutive relations and are given as follows:

$$
\begin{aligned}
\dot{\boldsymbol{C}}^{\backslash} &= 2\boldsymbol{\varphi}^{*}\left(\boldsymbol{d}^{\backslash}\right) = \boldsymbol{\varphi}_{p}^{*}\left(\boldsymbol{\mathcal{L}}_{v}\left(\hat{\boldsymbol{c}}_{e}^{\backslash}\right)\right) \\
\dot{\boldsymbol{E}}^{\backslash} &= \boldsymbol{\varphi}^{*}\left(\boldsymbol{d}^{\backslash}\right) = \boldsymbol{\varphi}^{*}\left(\boldsymbol{\mathcal{L}}_{v}\left(\boldsymbol{e}^{\backslash}\right)\right) = \boldsymbol{D}^{\backslash} \\
\dot{\boldsymbol{C}}_{p}^{\backslash} &= \dot{\boldsymbol{\mathcal{F}}}_{p}^{T}\boldsymbol{\mathcal{F}}_{p} + \boldsymbol{\mathcal{F}}_{p}^{T}\dot{\boldsymbol{\mathcal{F}}}_{p} = \boldsymbol{\varphi}^{*}\left(\boldsymbol{\mathcal{L}}_{v}\left(\boldsymbol{b}_{e}^{\backslash -1}\right)\right) \\
\dot{\boldsymbol{E}}_{p}^{\backslash} &= \boldsymbol{\varphi}_{p}^{*}\left(\boldsymbol{\mathcal{L}}_{v}\left(\hat{\boldsymbol{e}}_{p}^{\backslash}\right)\right) = \boldsymbol{D}_{p}^{\backslash} \\
\dot{\boldsymbol{E}}_{e}^{\backslash} &= \boldsymbol{\varphi}_{e}^{*}\left(\boldsymbol{\mathcal{L}}_{v}\left(\hat{\boldsymbol{e}}_{e}^{\backslash}\right)\right) = \boldsymbol{D}_{e}^{\backslash}
\end{aligned}
\tag{6.61}
$$

$$
\begin{aligned}
\boldsymbol{\mathcal{L}}_{\boldsymbol{v}}\left(\hat{\boldsymbol{b}}_{p}^{\backslash -1}\right) &= \boldsymbol{0} \\
\boldsymbol{\mathcal{L}}_{\boldsymbol{v}}\left(\hat{\boldsymbol{e}}_{p}^{\backslash}\right) &= \boldsymbol{\varphi}_{p}^{*}\left(\dot{\boldsymbol{E}}_{p}^{\backslash}\right) = \hat{\boldsymbol{d}}_{p}^{\backslash} \\
\boldsymbol{\mathcal{L}}_{\boldsymbol{v}}\left(\hat{\boldsymbol{c}}_{e}^{\backslash}\right) &= \boldsymbol{\varphi}_{p}^{*}\left(\dot{\boldsymbol{C}}^{\backslash}\right) \\
\boldsymbol{\mathcal{L}}_{\boldsymbol{v}}\left(\hat{\boldsymbol{e}}_{e}^{\backslash}\right) &= \boldsymbol{\varphi}_{p}^{*}\left(\dot{\boldsymbol{E}}_{e}^{\backslash}\right) = \hat{\boldsymbol{d}}_{\boldsymbol{e}}^{\backslash} \\
\boldsymbol{\mathcal{L}}_{\boldsymbol{v}}\left(\hat{\boldsymbol{e}}^{\backslash}\right) &= \boldsymbol{\varphi}_{p}^{*}\left(\dot{\boldsymbol{C}}^{\backslash}\right) = \hat{\boldsymbol{d}}^{\backslash}
\end{aligned}
\tag{6.62}
$$

$$
\begin{aligned}
\boldsymbol{\mathcal{L}}_{\boldsymbol{v}}\left(\boldsymbol{b}^{\backslash -1}\right) &= \boldsymbol{0} \\
\boldsymbol{\mathcal{L}}_{\boldsymbol{v}}\left(\boldsymbol{e}^{\backslash}\right) &= \boldsymbol{\varphi}^{*}\left(\dot{\boldsymbol{E}}^{\backslash}\right) = \boldsymbol{d}^{\backslash} \\
\boldsymbol{\mathcal{L}}_{\boldsymbol{v}}\left(\boldsymbol{b}_{e}^{\backslash -1}\right) &= \boldsymbol{\varphi}^{*}\left(\dot{\boldsymbol{C}}_{p}^{\backslash}\right) \\
\boldsymbol{\mathcal{L}}_{\boldsymbol{v}}\left(\boldsymbol{e}_{e}^{\backslash}\right) &= \boldsymbol{\varphi}^{*}\left(\dot{\boldsymbol{E}}_{e}^{\backslash}\right) = \boldsymbol{d}_{e}^{\backslash} \\
\boldsymbol{\mathcal{L}}_{\boldsymbol{v}}\left(\boldsymbol{e}_{p}^{\backslash}\right) &= \boldsymbol{\varphi}^{*}\left(\dot{\boldsymbol{E}}_{p}^{\backslash}\right) = \boldsymbol{d}_{p}^{\backslash}
\end{aligned}
\tag{6.63}
$$

For a pure mechanical theory, the most general form of free energy function is given by $\Psi = \Psi(\boldsymbol{i}^{\backslash}, \boldsymbol{\mathcal{F}}_e^{\backslash}, \boldsymbol{\mathcal{F}}^{\backslash})$. This functional form can be further reduced by assuming the following two axioms (Simo, 1988 (Part-1)): 1) Invariance of free energy under rigid-motion (or isometry) superposed onto the intermediate configuration; and 2) Covariance of free energy with respect to diffeomorphism superposed onto the current configuration. For first axiom, consider an isometry $\boldsymbol{\xi}_{iso}: \widehat{\mathfrak{B}}_t \rightarrow \widehat{\mathfrak{B}}_t'$ with tangent $\boldsymbol{\mathcal{F}}_{\xi_{iso}} = T\boldsymbol{\xi}_{iso}$ superposed on intermediate configuration $\widehat{\mathfrak{B}}_t$, then invariance of free energy requires that:

$$\boldsymbol{\xi}_{iso*}\left[\Psi\left(\boldsymbol{i}^{\backslash}, \boldsymbol{\mathcal{F}}_e^{\backslash}, \boldsymbol{\mathcal{F}}^{\backslash}\right)\right] = \Psi\left(\boldsymbol{i}^{\backslash}, \boldsymbol{\mathcal{F}}_{\xi_{iso}} \boldsymbol{\mathcal{F}}_e^{\backslash}, \boldsymbol{\mathcal{F}}^{\backslash}\right) \tag{6.64}$$

Now choosing $\boldsymbol{\mathcal{F}}_{\xi_{iso}} = \boldsymbol{R}_e^{\backslash}$, where $\boldsymbol{R}_e^{\backslash}$ is the rotation part in the polar decomposition of $\boldsymbol{F}_e^{\backslash}$, that is $\boldsymbol{F}_e = \boldsymbol{v}_e^{\backslash}\boldsymbol{R}_e^{\backslash}$, results in the following functional form of free energy:

$$\Psi\left(\boldsymbol{i}^{\backslash}, \boldsymbol{R}_e^{\backslash}\boldsymbol{\mathcal{F}}_e^{\backslash}, \boldsymbol{\mathcal{F}}^{\backslash}\right) = \widehat{\Psi}\left(\boldsymbol{i}^{\backslash}, \boldsymbol{v}_e^{\backslash}, \boldsymbol{\mathcal{F}}^{\backslash}\right) = \widetilde{\Psi}\left(\boldsymbol{i}^{\backslash}, \boldsymbol{b}_e^{\backslash -1}, \boldsymbol{\mathcal{F}}^{\backslash}\right) \tag{6.65}$$

The covariance of free energy with respect to current configuration can be expressed as follows. Let $\boldsymbol{\xi}$ be any diffeomorphism, with tangent $\boldsymbol{\mathcal{F}}_{\xi} = T\boldsymbol{\xi}$, superposed on current configuration with $\det(\boldsymbol{\mathcal{F}}_{\xi}) > 0$, then covariance implies that $\Psi = \boldsymbol{\xi}_*\left[\Psi\left(\boldsymbol{i}^{\backslash}, \boldsymbol{\mathcal{F}}_e^{\backslash}, \boldsymbol{\mathcal{F}}^{\backslash}\right)\right]$. The related transformations can be then expressed as follows:

$$\Psi = \boldsymbol{\xi}_*\left[\widetilde{\Psi}\left(\boldsymbol{i}^{\backslash}, \boldsymbol{b}_e^{\backslash -1}, \boldsymbol{\mathcal{F}}^{\backslash}\right)\right] = \widetilde{\Psi}\left(\boldsymbol{\xi}_*(\boldsymbol{i}^{\backslash}), \boldsymbol{\xi}_*\left(\boldsymbol{b}_e^{\backslash -1}\right), \boldsymbol{\mathcal{F}}_{\xi}\boldsymbol{\mathcal{F}}^{\backslash}\right) \tag{6.66}$$

Now since $\boldsymbol{\xi}$ is arbitrary, assuming $\boldsymbol{\xi} = \boldsymbol{\varphi}^{-1}$, i.e. $\boldsymbol{\mathcal{F}}_{\xi} = \boldsymbol{\mathcal{F}}^{-1} = T\boldsymbol{\varphi}^{-1}$ gives:

$$\begin{gathered}\Psi = \widetilde{\Psi}\left(\boldsymbol{\xi}_*\left(\boldsymbol{i}^{\backslash}\right), \boldsymbol{\xi}_*\left(\boldsymbol{b}_e^{\backslash -1}\right), \boldsymbol{\mathcal{F}}_{\xi}\boldsymbol{\mathcal{F}}^{\backslash}\right) = \widetilde{\Psi}\left(\boldsymbol{\varphi}^*\left(\boldsymbol{i}^{\backslash}\right), \boldsymbol{\varphi}^*\left(\boldsymbol{b}_e^{\backslash -1}\right), \boldsymbol{\mathcal{F}}^{-1}\boldsymbol{\mathcal{F}}\right) \\ \therefore \Psi = \Psi_C\left(\boldsymbol{C}^{\backslash}, \boldsymbol{C}_p^{\backslash}, \boldsymbol{I}^{\backslash}\right) = \Psi_E\left(\boldsymbol{E}^{\backslash}, \boldsymbol{E}_p^{\backslash}, \boldsymbol{I}^{\backslash}\right)\end{gathered} \tag{6.67}$$

Equation 6.67_2 gives the most general functional form of free energy which can be assumed. Moreover, both isotropic and anisotropic material responses can modeled with the above form of free energy. Further discussions on this form of free energy can be found in Simo (1988 (Part-1)).

Using Eq. 6.67_2, the material time derivative of free energy, $\dot{\Psi}$, can be expressed as follows:

$$\dot{\Psi} = \langle \frac{\partial \Psi_C}{\partial \boldsymbol{C}^{\backslash}}, \dot{\boldsymbol{C}}^{\backslash} \rangle_P + \langle \frac{\partial \Psi_C}{\partial \boldsymbol{C}_p^{\backslash}}, \dot{\boldsymbol{C}}_p^{\backslash} \rangle_P = \langle \frac{\partial \Psi_E}{\partial \boldsymbol{E}^{\backslash}}, \dot{\boldsymbol{E}}^{\backslash} \rangle_P + \langle \frac{\partial \Psi_E}{\partial \boldsymbol{E}_p^{\backslash}}, \dot{\boldsymbol{E}}_p^{\backslash} \rangle_P \tag{6.68}$$

Thus, the internal mechanical energy dissipation rate can be expressed using Eq. 6.67_2 and Eq. 6.68 as follows:

$$D_{int} = \langle \boldsymbol{S}^{/} - \frac{\partial \Psi_E}{\partial \boldsymbol{E}^{\backslash}}, \dot{\boldsymbol{E}}^{\backslash} \rangle_P - \langle \frac{\partial \Psi_E}{\partial \boldsymbol{E}_p^{\backslash}}, \dot{\boldsymbol{E}}_p^{\backslash} \rangle_P \tag{6.69}$$

For elastic process, $\dot{\boldsymbol{E}}_p^{\backslash} = \boldsymbol{0}$ and the non-negativity of D_{int} for all such process gives (Coleman-Noll procedure):

$$\boldsymbol{S}^{/} = \frac{\partial \Psi_E(\boldsymbol{E}^{\backslash}, \boldsymbol{E}_p^{\backslash}, \boldsymbol{I}^{\backslash})}{\partial \boldsymbol{E}^{\backslash}} \tag{6.70}$$

For the case of steel plasticity, free energy can be interpreted as the energy stored in the atomic lattice as the material is deformed. The intermediate configuration is related to plastic deformation, that are a result of dislocation movements and hardening effects are caused by pile-ups and hindrance of these movements. For isotropic hardening, it is assumed that no residual micro-stresses develop in the material. In reality, however, due to various mechanisms caused by cross-slip, mismatch of grain boundaries and other constraints, residual micro-stresses accumulate and manifest themselves in terms of the Bauchinger effect. However, modeling of Bauchinger effect is only important under cyclic loading of material. To model physical behavior related to hardening and Bauchinger effects, additional variables, known as internal variables, are also included in the functional form of free energy. Specifically, for isotropic hardening a spatial scalar field $\alpha^p = \alpha^p(p,t)$ is introduced. The free energy function then becomes:

$$\therefore \Psi = \Psi_C(\boldsymbol{C}^{\backslash}, \boldsymbol{C}_p^{\backslash}, \boldsymbol{I}^{\backslash}, \boldsymbol{\varphi}^*(\alpha^p)) = \Psi_E(\boldsymbol{E}^{\backslash}, \boldsymbol{E}_p^{\backslash}, \boldsymbol{I}^{\backslash}, \boldsymbol{\varphi}^*(\alpha^p)) \tag{6.71}$$

where $\boldsymbol{\varphi}^*(\alpha^p) \overset{\text{def}}{=} \alpha^p \circ \boldsymbol{\varphi}$, is the pull-back of scalar field α^p.

The plasticity model is completed by introducing a yield function to specifying the elastic domain in stress or strain space and by specifying the functional form of flow rules which describes the evolution of internal variables. The yield function and flow rules are specified to describe the important properties of material under consideration. Yield function and flow rules are also subjected to invariance and covariance requirements

similar to free energy function. The commonly used yield function and flow rule for the case of steel plasticity is discussed next.

Remark 6.5: For the case of isotropic response with respect to reference configuration, the functional form of free energy, Eq. 6.67_2, is further reduced as follows:

$$\begin{aligned}\Psi &= \Psi_C\left(\boldsymbol{Q}^{\backslash}\boldsymbol{C}^{\backslash}\boldsymbol{Q}^{\backslash T}, \boldsymbol{Q}^{\backslash}\boldsymbol{C}_p^{\backslash}\boldsymbol{Q}^{\backslash T}, \boldsymbol{I}^{\backslash}, \alpha^p\right) \\ &= \Psi_E\left(\boldsymbol{Q}^{\backslash}\boldsymbol{E}^{\backslash}\boldsymbol{Q}^{\backslash T}, \boldsymbol{Q}^{\backslash}\boldsymbol{E}_p^{\backslash}\boldsymbol{Q}^{\backslash T}, \boldsymbol{I}^{\backslash}, \alpha^p\right) \quad \forall\, \boldsymbol{Q}^{\backslash} \in SO(3)\end{aligned} \tag{6.72}$$

Thus, the free energy for isotropic material depends on strain tensors ($\boldsymbol{C}^{\backslash}, \boldsymbol{C}_p^{\backslash}, \boldsymbol{E}^{\backslash}, \boldsymbol{E}_p^{\backslash}$) only through their invariants or eigen-values. One of the commonly used free energy function is expressed in terms of elastic Finger tensor, $\boldsymbol{b}_e^{\backslash}$, as $\Psi = \Psi(\boldsymbol{b}_e^{\backslash}, \alpha^p)$. Further discussions on the use of this yield function can be in Simo and Hughes (1998). With this free energy function in terms of strain tensor $\boldsymbol{b}_e^{\backslash}$, the rate if energy dissipation can be expressed as:

$$D_{int} = \langle \boldsymbol{\tau}^{/}, \boldsymbol{d}^{\backslash} \rangle_p - \langle \frac{\partial \Psi}{\partial \boldsymbol{b}_e^{\backslash}}, \dot{\boldsymbol{b}}_e^{\backslash} \rangle_p - \frac{\partial \Psi}{\partial \alpha^p}\dot{\alpha}^p \geq 0 \tag{6.73}$$

Now $\dot{\boldsymbol{b}}_e^{\backslash} = \dot{\boldsymbol{\mathcal{F}}}\boldsymbol{C}_p^{\backslash -1}\boldsymbol{\mathcal{F}}^T + \boldsymbol{\mathcal{F}}\dot{\boldsymbol{C}}_p^{\backslash -1}\boldsymbol{\mathcal{F}}^T + \boldsymbol{\mathcal{F}}\boldsymbol{C}_p^{\backslash -1}\dot{\boldsymbol{\mathcal{F}}}^T = \boldsymbol{l}^{\backslash}\boldsymbol{b}_e^{\backslash} + \boldsymbol{b}_e^{\backslash}\boldsymbol{l}^{\backslash} + \boldsymbol{\mathcal{F}}\dot{\boldsymbol{C}}_p^{\backslash -1}\boldsymbol{\mathcal{F}}^T$, thus

$$\begin{aligned}\langle \frac{\partial \Psi}{\partial \boldsymbol{b}_e^{\backslash}}, \dot{\boldsymbol{b}}_e^{\backslash} \rangle_p &= \langle \frac{\partial \Psi}{\partial \boldsymbol{b}_e^{\backslash}}, \boldsymbol{l}^{\backslash}\boldsymbol{b}_e^{\backslash} + \boldsymbol{b}_e^{\backslash}\boldsymbol{l}^{\backslash} + \boldsymbol{\mathcal{F}}\dot{\boldsymbol{C}}_p^{\backslash -1}\boldsymbol{\mathcal{F}}^T \rangle_p \\ &= \langle \boldsymbol{b}_e^{\backslash *}\frac{\partial \Psi}{\partial \boldsymbol{b}_e^{\backslash}}, \boldsymbol{l}^{\backslash} \rangle_p + \langle \boldsymbol{b}_e^{\backslash *}\frac{\partial \Psi}{\partial \boldsymbol{b}_e^{\backslash}}, \boldsymbol{l}^{\backslash T} \rangle_p + \langle \boldsymbol{b}_e^{\backslash *}\frac{\partial \Psi}{\partial \boldsymbol{b}_e^{\backslash}}, \boldsymbol{\mathcal{F}}\dot{\boldsymbol{C}}_p^{\backslash -1}\boldsymbol{\mathcal{F}}^T \rangle_p \\ &= \langle 2\boldsymbol{b}_e^{\backslash *}\frac{\partial \Psi}{\partial \boldsymbol{b}_e^{\backslash}}, \boldsymbol{d}^{\backslash} \rangle_p + \langle 2\boldsymbol{b}_e^{\backslash *}\frac{\partial \Psi}{\partial \boldsymbol{b}_e^{\backslash}}, \frac{1}{2}\boldsymbol{b}_e^{\backslash -1}\boldsymbol{\mathcal{F}}\dot{\boldsymbol{C}}_p^{\backslash -1}\boldsymbol{\mathcal{F}}^T \rangle_p\end{aligned} \tag{6.74}$$

From Eq. 6.73 and Eq. 6.74, D_{int} can be written as follows:

$$\begin{aligned}D_{int} = \langle \boldsymbol{\tau}^{/} - 2\boldsymbol{b}_e^{\backslash *}\frac{\partial \Psi}{\partial \boldsymbol{b}_e^{\backslash}}, \boldsymbol{d}^{\backslash} \rangle_p + \langle 2\boldsymbol{b}_e^{\backslash *}\frac{\partial \Psi}{\partial \boldsymbol{b}_e^{\backslash}}, -\frac{1}{2}\boldsymbol{b}_e^{\backslash -1}\boldsymbol{\mathcal{F}}\dot{\boldsymbol{C}}_p^{\backslash -1}\boldsymbol{\mathcal{F}}^T \rangle_p \\ - \frac{\partial \Psi}{\partial \alpha^p}\dot{\alpha}^p \geq 0\end{aligned} \tag{6.75}$$

Since Eq. 6.75 should be true for all admissible processes Coleman-Noll argument gives:

$$\boldsymbol{\tau}^{/} = 2\boldsymbol{b}_e^{\backslash *}\frac{\partial \Psi}{\partial \boldsymbol{b}_e^{\backslash}} \tag{6.76}$$

Also, the internal energy dissipation rate becomes:

$$D_{int} = \langle \boldsymbol{\tau}', -\frac{1}{2}\boldsymbol{b}_e^{\backslash -1}\boldsymbol{\mathcal{F}}\dot{\boldsymbol{C}}_p^{\backslash -1}\boldsymbol{\mathcal{F}}^T \rangle_p + \zeta^p \dot{\alpha}^p \geq 0 \tag{6.77}$$

Isotropy implies that the tensors $\boldsymbol{b}_e^{\backslash *}$ and $\frac{\partial \Psi}{\partial \boldsymbol{b}_e^{\backslash}}$ are coaxial and hence commutes. Thus, Eq. 6.76 can be written as: $\boldsymbol{\tau}' = 2\boldsymbol{b}_e^{\backslash *}\frac{\partial \Psi}{\partial \boldsymbol{b}_e^{\backslash}} = 2\frac{\partial \Psi}{\partial \boldsymbol{b}_e^{\backslash}}\boldsymbol{b}_e^{\backslash *}$. The scalar variable, $\zeta^p \stackrel{\text{def}}{=} -\frac{\partial \Psi}{\partial \alpha^p}$, is conjugate to $\dot{\alpha}^p$ and is used in to define the yield function of the material.

Remark 6.6: Let $\boldsymbol{A}$ be any symmetric and positive definite 2nd order tensor, therefore it is diagonalizable. Let λ_a and $\boldsymbol{n}_a$ $(a = 1,2,3)$ be the eigen values and eigen vectors of $\boldsymbol{A}$, then its spectral representation is given as follows:

$$\begin{gathered} \boldsymbol{A} = \sum_{a=1}^{3} \lambda_a (\boldsymbol{n}_a \otimes \boldsymbol{n}_a) \quad \text{for } \lambda_1 \neq \lambda_2 \neq \lambda_3 \\ \boldsymbol{A} = \lambda(\boldsymbol{I} - (\boldsymbol{n}_3 \otimes \boldsymbol{n}_3)) + \lambda_3 (\boldsymbol{n}_3 \otimes \boldsymbol{n}_3) \quad \text{for } \lambda = \lambda_1 = \lambda_2 \neq \lambda_3 \\ \boldsymbol{A} = \lambda \boldsymbol{I} \text{ for } \lambda_1 = \lambda_2 = \lambda_3 = \lambda \end{gathered} \tag{6.78}$$

where $\boldsymbol{I}$ is the identity tensor. Now since $\lambda_a = \lambda_a(\boldsymbol{A})$ the following relationships exists (Holzapfel, 2000):

$$\begin{gathered} \frac{\partial \lambda_a}{\partial \boldsymbol{A}} = (\boldsymbol{n}_a \otimes \boldsymbol{n}_a) \quad \text{for } \lambda_1 \neq \lambda_2 \neq \lambda_3 \\ \begin{cases} \dfrac{\partial \lambda}{\partial \boldsymbol{A}} = \boldsymbol{I} - (\boldsymbol{n}_3 \otimes \boldsymbol{n}_3) \\ \dfrac{\partial \lambda_a}{\partial \boldsymbol{A}} = (\boldsymbol{n}_a \otimes \boldsymbol{n}_a) \end{cases} \quad \text{for } \lambda = \lambda_1 = \lambda_2 \neq \lambda_3 \\ \frac{\partial \lambda}{\partial \boldsymbol{A}} = \boldsymbol{I} \qquad \text{for } \lambda_1 = \lambda_2 = \lambda_3 = \lambda \end{gathered} \tag{6.79}$$

Remark 6.7: A quadratic logarithmic model that is frequently used for the description of free energy function in terms of eigen values or principal stretches of elastic Finger tensor $\boldsymbol{b}_e^{\backslash}$ is presented here. For polycrystalline materials like steels, the bulk deviatoric response of the material is different from volumetric response. For application to such materials, the strain tensor $\boldsymbol{b}_e^{\backslash}$ can be decomposed into volume changing ($\boldsymbol{b}_e^{\backslash vc}$) and volume preserving ($\boldsymbol{b}_e^{\backslash vp}$) parts as follows:

$$\boldsymbol{b}_e^{\backslash} = \boldsymbol{b}_e^{\backslash vc}\boldsymbol{b}_e^{\backslash vp} \qquad \boldsymbol{b}_e^{\backslash vp} = J_e^{-\frac{2}{3}}\boldsymbol{b}_e^{\backslash} \qquad \boldsymbol{b}_e^{\backslash vc} = J_e^{\frac{2}{3}}\boldsymbol{i}^{\backslash} \tag{6.80}$$

Note that: $det(\boldsymbol{b}_e^{\backslash vc}) = 1$ and $det(\boldsymbol{b}_e^{\backslash vc}) = J_e^2 = det(\boldsymbol{b}_e^{\backslash})$.

Let the spectral decomposition of $\boldsymbol{b}_e^{\backslash}$ be:

$$\boldsymbol{b}_e^{\backslash} = \sum_{a=1}^{3} \lambda_a^{e^2}(\boldsymbol{n}_a \otimes \boldsymbol{n}_a) \tag{6.81}$$

where λ_a^e and $\boldsymbol{n}_a$ $(a = 1, 2, 3)$ are the eigen values and eigen vectors of tensor $\boldsymbol{b}_e^{\backslash}$ respectively. Then the following relationships exists:

$$J_e = det(\boldsymbol{\mathcal{F}}_e) = \left[det(\boldsymbol{b}_e^{\backslash})\right]^{1/2} = \lambda_1^e\lambda_2^e\lambda_3^e$$
$$\boldsymbol{b}_e^{\backslash vp} = \sum_{a=1}^{3}\left(J_e^{-\frac{1}{3}}\lambda_a^e\right)^2(\underline{n}_a \otimes \underline{n}_a) \qquad \boldsymbol{b}_e^{\backslash vc} = \sum_{a=1}^{3} J_e^{\frac{2}{3}}(\underline{n}_a \otimes \underline{n}_a) \tag{6.82}$$
$$\text{and let } \tilde{\lambda}_a^e = J_e^{-\frac{1}{3}}\lambda_a^e$$

With kinematic assumption (6.46), a unique decoupled representation of free energy function $\Psi = \Psi(\boldsymbol{b}_e^{\backslash}, \alpha^p)$ is postulated such that:

$$\Psi = \Psi(\boldsymbol{b}_e^{\backslash}, \alpha^p) = \Psi_{vol}^e(\boldsymbol{b}_e^{\backslash vc}) + \Psi_{iso}^e(\boldsymbol{b}_e^{\backslash vp}) + \Psi^p(\alpha^p) \tag{6.83}$$

where Ψ_{vol}^e is the energy stored in lattice due to volumetric changes and Ψ_{iso}^e is the energy stored due to isochoric material response. For a quadratic logarithmic energy model, the specific forms of these functions are given by:

$$\Psi_{vol}^e = \frac{1}{2}k(\ln J_e)^2 = \frac{1}{2}k(\ln\lambda_1^e + \ln\lambda_2^e + \ln\lambda_3^e\ )^2$$
$$\Psi_{iso}^e = \mu\left[\left(\ln\tilde{\lambda}_1^e\right)^2 + \left(\ln\tilde{\lambda}_2^e\right)^2 + \left(\ln\tilde{\lambda}_3^e\right)^2\right] \tag{6.84}$$
$$= \mu[(\ln\lambda_1^e)^2 + (\ln\lambda_2^e)^2 + (\ln\lambda_3^e)^2] - \frac{\mu}{3}(\ln J_e)^2$$

$$\text{Linear Hardening: } \Psi^p(\alpha^p) = \frac{1}{2}K^p\alpha^{p^2}, \quad K^p = Hardening\ Modulus$$

$$\text{Saturation Hardening: } \Psi^p(\alpha^p) = (\sigma_{max} - \sigma_Y)\left(\alpha^p + \frac{exp(-a\alpha^p)}{a}\right) \tag{6.85}$$

$$\sigma_{max}, \sigma_Y, a \rightarrow \text{model parameters}$$

where k is the bulk modulus and μ is the shear modulus of the material. This free energy based on logarithmic strain measures satisfies the growth conditions, i.e. $\Psi^e \rightarrow \infty$ as

$J_e \to 0$ and $\Psi^e \to \infty$ as $J_e \to \infty$ where $\Psi^e = \Psi^e_{vol} + \Psi^e_{iso}$. However, Ψ^e is not a convex function of J_e, and therefore cannot be used for problems with very large elastic strains (Simo, 1992). But this model gives excellent approximation for moderately large elastic strains.

Remark 6.8: For formulation of yield function in spatial description, elastic domain in stress space, $\mathbb{E}_\tau$, is frequently introduced in terms of Kirchhoff stress tensor $\boldsymbol{\tau}^{/}$, which restrict the admissible stress fields i.e.

$$\mathbb{E}_\tau = \left\{(\boldsymbol{\tau}^{/}, \zeta^p) \in \mathbb{S} \times \mathbb{R}^n \mid \Phi^p(\boldsymbol{\tau}^{/}, \zeta^p) \leq 0\right\}$$

where $\Phi^p(\boldsymbol{\tau}^{/}, \zeta^p)$ is known as the yield function and the scalar variable $\zeta = \zeta(\alpha^p)$ is known as isotropic hardening parameter and is used model isotropic hardening of material. Principle of objectivity further restricts the function form of yield function as follows:

$$\Phi^p\left(\boldsymbol{\tau}^{\backslash}, \zeta^p\right) = \Phi^p\left(\boldsymbol{Q}^{\backslash}\boldsymbol{\tau}^{\backslash}\boldsymbol{Q}^{\backslash T}, \zeta^p\right) \quad \forall\, \boldsymbol{Q}^{\backslash} \in SO(3) \tag{6.86}$$

Thus if spatial description is employed then Φ^p is necessarily an isotropic function of $\boldsymbol{\tau}^{\backslash}$.

6.2.7 Hyperelastic-Plastic-Damage Model

The hyperelastic-plastic model described above can adequately model material responses related to metal plasticity. However, these models are inadequate to describe the response of metals that undergoes micro-structure changes due to formation, growth and coalescence of micro-voids or micro-defects. To this end continuum models based on damage mechanics are frequently employed. In damage mechanics based models additional history variables are introduced to account for the disintegration or damage of material undergoing deformations.

The concepts of effective stress and/or strain can be found in the literature in the development of damage models. These ideas can be traced back to the pioneering work of Kachanov (1958) in the context of isotropic damage models. The resulting models consider a scalar variable measuring the ratio between damage and intact surfaces on which the stresses act, thus defining the concept of effective stress as the equivalent stress

acting on the intact material. In early development of damage mechanics theory such models have been employed by Krajcinovic (1984), Lemaitre (1985), and Chaboche (1981, 1988, 1995) among others. Other damage mechanics based models in context of small deformation theory also considering plasticity effects, include Simo and Ju (1987a,b), Ju (1989), Lubliner et al. (1989) and Luccioni et al. (1996) among many others. A comprehensive discussion of damage mechanics based models for the case of small deformations can be found in Hansen & Schreyer (1995) and Armero & Oller (2000). Application of damage mechanics based models in context of finite deformation can be found in Kattan & Voyiadjis (1990), Lubarda (1994), Mahnken (2000), Steinmann (1994), Steinmann & Carol (1998), Menzel et al. (2003, 2005), Mediavilla et al. (2006) and Lin & Brocks (2006), among others.

The two important damage mechanics concepts that are used to formulate the proposed damage model are the effective stress concept and the strain equivalence principle. Consider a damage scalar internal variable, α^d, that accounts for damage due to micro-voids nucleation, growth and coalescence then, according to the effective stress concept, the actual stress resisted by the undamaged or intact material surface is expressed as follows:

$$\bar{\boldsymbol{\tau}}^{\backslash} \stackrel{\text{def}}{=} \frac{\boldsymbol{\tau}^{\backslash}}{1-\alpha^d} \tag{6.87}$$

where $\bar{\boldsymbol{\tau}}^{\backslash}$ is known as the effective stress. Together with the strain equivalence principle (Lemaitre, 1971), which states that "any strain constitutive equation for a damaged material may be derived in the same way as for the virgin material except that the usual stress is replaced by the effective stress", the effective stress concept can be used to formulate material constitutive laws. A hyperelastic-plastic-damage model based on these two concepts is derived in this work.

For the proposed hyperelastic-plastic-damage model, the Helmholtz free energy function is defined as follows:

$$\Psi = \Psi\left(\boldsymbol{b}_e^{\backslash}, \alpha^d, \alpha^p\right) \tag{6.88}$$

where α^d is a internal damage variable that describes the damage of material and $\alpha^p$is the strain-like internal variable that describe the state of material at the micro-level induced by dislocation pileups and other micro-defects.

The following functional form of Helmholtz free energy is proposed:

$$\Psi = (1-\alpha^d)\Psi^e\left(\boldsymbol{b}_e^{\backslash}\right) + \Psi^p(\alpha^p) \tag{6.89}$$

A similar free energy decomposition was proposed by Mahnken (2000), however the damage model was formulated at the intermediate configuration in that work. Another form of Helmholtz free energy was proposed by Steinmann (1994) such that $\Psi = \Psi^e_{vol}(\boldsymbol{b}_e^{\backslash vc}) + (1-\alpha^d)\Psi^e_{iso}(\boldsymbol{b}_e^{\backslash vp}) + \Psi^p(\alpha^p)$. In this case, damage was only considered to be a function of the deviatoric component of stress. However, such a formulation is inadequate to model damage due to void growth under high triaxial stresses. With the free energy potential given by Eq. 6.89, the Clausius-Plank inequality becomes:

$$\begin{aligned} D_{int} &= \langle \boldsymbol{\tau}^{/} - 2(1-\alpha^d)\boldsymbol{b}_e^{\backslash *}\frac{\partial \Psi^e}{\partial \boldsymbol{b}_e^{\backslash}}, \boldsymbol{d}^{\backslash}\rangle_p \\ &+ \langle 2(1-\alpha^d)\boldsymbol{b}_e^{\backslash *}\frac{\partial \Psi^e}{\partial \boldsymbol{b}_e^{\backslash}}, -\frac{1}{2}\boldsymbol{b}_e^{\backslash -1}\boldsymbol{\mathcal{F}}\dot{\boldsymbol{C}}_p^{\backslash -1}\boldsymbol{\mathcal{F}}^T\rangle_p + \Psi^e\dot{\alpha}^d + \zeta^p\dot{\alpha}^p \geq 0 \end{aligned} \tag{6.90}$$

Using the Coleman-Noll argument, the Kirchhoff stress tensor which is defined on the current configuration is given by:

$$\boldsymbol{\tau}^{/} = 2(1-\alpha^d)\boldsymbol{b}_e^{\backslash *}\frac{\partial \Psi^e}{\partial \boldsymbol{b}_e^{\backslash}} \tag{6.91}$$

The internal mechanical energy dissipation rate can now be expressed as follows:

$$D_{int} = \langle \boldsymbol{\tau}^{/}, -\frac{1}{2}\boldsymbol{b}_e^{\backslash -1}\boldsymbol{\mathcal{F}}\dot{\boldsymbol{C}}_p^{\backslash -1}\boldsymbol{\mathcal{F}}^T\rangle_p + \Psi^e\dot{\alpha}^d + \zeta^p\dot{\alpha}^p \geq 0 \tag{6.92}$$

Thus for any admissible process, the inequality given in Eq. 6.92 should be satisfied. For describing the evolution of plastic internal variable, α^p, a potential approach is adopted,

wherein a plastic potential function is introduced in terms of the effective Kirchhoff stress $\bar{\boldsymbol{\tau}}^{\backslash} \stackrel{\text{def}}{=} \frac{\boldsymbol{\tau}^{\backslash}}{1-\alpha^d}$ as follows:

$$\phi^p\left(\bar{\boldsymbol{\tau}}^{\backslash}, \zeta^p\right) = \left\|\bar{\boldsymbol{\tau}}^{\backslash dev}\right\| - \sqrt{\frac{2}{3}}(\sigma_y - \zeta^p) \tag{6.93}$$

where σ_y is the yield strength, $\zeta^p = \zeta^p(\alpha^p)$ is the hardening variable and $\bar{\boldsymbol{\tau}}^{\backslash dev}$ is the deviatoric component of effective Kirchhoff stress tensor $\bar{\boldsymbol{\tau}}^{\backslash}$. Thus Eq. 6.93 represents the von Mises yield criteria in terms of the effective Kirchhoff stress tensor $\bar{\boldsymbol{\tau}}^{\backslash}$. Also, $\phi^p\left(\bar{\boldsymbol{\tau}}^{\backslash}, \zeta^p\right)$ is a convex function of $\bar{\boldsymbol{\tau}}^{\backslash dev}$. The evolution of plastic internal variables is then expressed by the following associative flow rules:

$$\dot{\alpha}^p = \gamma \frac{\partial \phi^p}{\partial \zeta^p} = \gamma \sqrt{\frac{2}{3}} \tag{6.94}$$

$$-\frac{1}{2}\boldsymbol{b}_e^{\backslash -1}\boldsymbol{\mathcal{F}}\dot{\boldsymbol{C}}_p^{\backslash -1}\boldsymbol{\mathcal{F}}^T = \frac{\partial \phi^p}{\partial \boldsymbol{\tau}^{\backslash}} = \frac{\gamma}{1-\alpha^d}\frac{\partial \phi^p}{\partial \bar{\boldsymbol{\tau}}^{\backslash}} \tag{6.95}$$

The plasticity part of the model is completed by specifying the following Kuhn-Tucker complementarity conditions:

$$\gamma > 0, \;\; \phi^p < 0 \;\text{ and }\; \gamma\phi^p = 0 \tag{6.96}$$

and the plastic consistency condition:

$$\gamma\dot{\phi}^p = 0 \tag{6.97}$$

For evolution of the damage internal variable, α^d, a typical approach is to introduce an additional potential in terms of variable conjugate to α^d, i.e. $r \equiv \Psi^e$. Such an approach have been suggested by Lemaitre (1985) for small deformation plasticity-damage models, and is also been used by Steinmann (1994) and Mahnken (2000) for large deformation elasto-plastic damage models. In particular a quadratic damage potential in terms of r is introduced in these approaches. Such a model trivially satisfies the dissipation inequality but this model has no micro-mechanical basis to it. The damage evolution laws proposed in this study are based on micro-mechanical theories; and the damage due to micro-void growth in triaxial stress fields and due to elongation of voids in deviatoric stress fields are modeled in a phenomenological sense. The evolution laws that are suggested in this study are given in equation 6.98, and 6.99 below:

$$\dot{\alpha}^d = a_o \mathcal{T}_1(\alpha^p)\dot{\alpha}^p + a_1 T \mathcal{T}_1(\alpha^p)\dot{\alpha}^p + a_2 \exp(a_3 \alpha^p)\, \mathcal{T}_2(\alpha^p)\dot{\alpha}^p \tag{6.98}$$

$$T \overset{\text{def}}{=} \frac{\left\| \boldsymbol{\tau}^{\backslash vol} \right\|}{\left\| \boldsymbol{\tau}^{\backslash dev} \right\|} \tag{6.99}$$

where $\boldsymbol{\tau}^{\backslash vol}$ and $\boldsymbol{\tau}^{\backslash dev}$ are volumetric and deviatoric components of the Kirchhoff stress tensor $\boldsymbol{\tau}^{\backslash}$ and a_o, a_1, a_2, and a_3 are material parameters all ≥ 0.

The first term in the evolution of α^d (Eq. 6.98) represents the material damage due to elongation of void under applied shear. The second terms represents the material damage due to void growth under high triaxiality. In addition, a threshold function, $\mathcal{T}_1(\alpha^p)$, is introduced so that damage is activated only if a certain limit ε_{nuc} is attained for α^p. The value of ε_{nuc}, typically represents the nucleation strain and is equal to the plastic strain at which the micro-voids nucleates. A user-defined relationship between ε_{nuc} and T can be defined, which can be used in Eq. 6.98 above.

Thus the first and second terms of the damage evolution equation model the material damage due to elongation and volumetric growth of micro-voids after void nucleation. The last term represents material damage due to micro-void coalescence. An exponential function is chosen to model the rapid disintegration of material due to micro-voids coalescence in this stage. Again, a threshold function, $\mathcal{T}_2(\alpha^p)$, is introduced so that the void coalescence term is activated only if a certain limit ε_{cl} is attained for α^p. The plastic strain limit ε_{cl} typically represents the plastic strain value at which the micro-voids start to coalesce due to localization in the intervoid matrix.

The functional form of the threshold function is chosen as a Hermitian polynomial to facilitate numerical implementation because of its smoothness. The functional forms of threshold functions are given as follows (Mahnken, 2000):

$$\begin{cases} \mathcal{T}_1(\alpha^p, \varepsilon_{nuc}, \Delta\varepsilon) = 0 \quad \text{if } \alpha^p < \varepsilon_{nuc} \\ \mathcal{T}_1(\alpha^p, \varepsilon_{nuc}, \Delta\varepsilon) = \dfrac{(\alpha^p - \varepsilon_{nuc})^2}{\Delta\varepsilon^2}\left[3 - \dfrac{2(\alpha^p - \varepsilon_{nuc})}{\Delta\varepsilon}\right] \\ \text{if } \varepsilon_{nuc} < \alpha^p < \varepsilon_{nuc} + \Delta\varepsilon \\ \text{and } \mathcal{T}_1(\alpha^p, \varepsilon_{nuc}, \Delta\varepsilon) = 1 \quad \text{if } \alpha^p \geq \varepsilon_{nuc} + \Delta\varepsilon \end{cases} \tag{6.100}$$

$$\begin{cases} \mathcal{T}_2(\alpha^p, \varepsilon_{cl}, \Delta\varepsilon) = 0 \quad \text{if } \alpha^p < \varepsilon_{cl} \\ \mathcal{T}_2(\alpha^p, \varepsilon_{cl}, \Delta\varepsilon) = \dfrac{(\alpha^p - \varepsilon_{cl})^2}{\Delta\varepsilon^2}\left[3 - \dfrac{2(\alpha^p - \varepsilon_{cl})}{\Delta\varepsilon}\right] \\ \text{if } \varepsilon_{cl} < \alpha^p < \varepsilon_{cl} + \Delta\varepsilon \\ \text{and } \mathcal{T}_2(\alpha^p, \varepsilon_{cl}, \Delta\varepsilon) = 1 \quad \text{if } \alpha^p \geq \varepsilon_{cl} + \Delta\varepsilon \end{cases} \tag{6.101}$$

The parameter, $\Delta\varepsilon$, represents the range over which the damage activation process is smoothened out and can be regarded as a material parameter.

6.3 Numerical Implementation

The above described hyperelastic-plastic-damage model is implemented in the commercial finite element program LS-DYNA. Further details and the integration algorithm for elastic-plastic damage model presented above are described in this section. For the purpose of model implementation, Cartesian coordinates are used. Following are the important properties of the Cartesian coordinates system:

Covariant and contravariant basis are identical and are given by standard Euclidean basis vectors of: $\{\boldsymbol{g_1} = \boldsymbol{G^1} = \boldsymbol{e}_1, \boldsymbol{g_2} = \boldsymbol{G^2} = \boldsymbol{e}_2, \boldsymbol{g_3} = \boldsymbol{G^3} = \boldsymbol{e}_3\}$. Thus symbol distinguishing, contravariant, covariant and mixed tensors, i.e., $b, \#, \backslash \text{ and} /$, are not used.
The metric tensors $\boldsymbol{g}$ and $\boldsymbol{G}$ are equal to the identity tensor, $\boldsymbol{I} = \delta_{ij}\boldsymbol{e}_i \otimes \boldsymbol{e}_j$.
The dual of a tensor is equal to its transpose, and scalar product can be identified with the inner product.

Thus, in Cartesian coordinate systems, standard rules of tensor algebra are applicable. An introduction to tensor algebra in Cartesian system can be found in Holzapfel (2000).
A quadratic logarithmic model for free energy, Ψ^e, in terms of eigen values of tensor $\boldsymbol{b}_e$ is assumed (Remark 5.7), with the following functional form:

$$\begin{aligned} \Psi^e(\boldsymbol{b}_e) = \frac{1}{2}k(\ln\lambda_1^e + \ln\lambda_2^e + \ln\lambda_3^e\ )^2 \\ + \mu[(\ln\lambda_1^e)^2 + (\ln\lambda_2^e)^2 + (\ln\lambda_3^e)^2] - \frac{\mu}{3}(\ln J_e)^2 \end{aligned} \tag{6.102}$$

Chain rule of differentiation of free energy function (Eq. 6.102) with respect to $\boldsymbol{b}^e$ gives:

$$\frac{\partial \Psi^e}{\partial \boldsymbol{b}^e} = \sum_{a=1}^{3} \frac{\partial \Psi^e}{\partial (\ln \lambda_a^e)} \frac{\partial \ln \lambda_a^e}{\partial \lambda_a^e} \frac{\partial \lambda_a^e}{\partial \lambda_a^{e^2}} \frac{\partial \lambda_a^{e^2}}{\partial \boldsymbol{b}^e} = \sum_{a=1}^{3} \frac{1}{2\lambda_a^{e^2}} \frac{\partial \Psi^e}{\partial (\ln \lambda_a^e)} (\boldsymbol{n}_a \otimes \boldsymbol{n}_a) \tag{6.103}$$

Also differentiating, Ψ^e, with respect to $\ln \lambda_a^e$ gives:

$$\frac{\partial \Psi^e}{\partial (\ln \lambda_a^e)} = k \ln J^e + 2\mu \ln \lambda_a^e - \frac{2\mu}{3} \ln J^e \tag{6.104}$$

Combining Eq. 6.91, 6.103, and 6.104, Kirchhoff stress tensor, $\boldsymbol{\tau}$, is given by:

$$\boldsymbol{\tau} = (1 - \alpha^d) 2 \left[\sum_{r=1}^{3} \lambda_a^{e^2} (\boldsymbol{n}_r \otimes \boldsymbol{n}_r) \right] \left[\sum_{a=1}^{3} \frac{1}{2\lambda_a^{e^2}} \left(k \ln J^e + 2\mu \ln \lambda_a^e - \frac{2\mu}{3} \ln J^e \right) (\boldsymbol{n}_a \otimes \boldsymbol{n}_a) \right] \tag{6.105}$$

$$\therefore \ \boldsymbol{\tau} = \sum_{a=1}^{3} (1 - \alpha^d) \left(\left(k - \frac{2}{3}\mu \right) \ln J^e + 2\mu \ln \lambda_a^e \right) (\boldsymbol{n}_a \otimes \boldsymbol{n}_a)$$

Introducing the 4th order identity tensor, $\mathbb{I} = \boldsymbol{e}_i \otimes \boldsymbol{e}_j \otimes \boldsymbol{e}_i \otimes \boldsymbol{e}_j$ and the 4th order volumetric ($\mathbb{P}_{\text{vol}}$) and 4th order deviatoric ($\mathbb{P}_{\text{dev}}$) tensors where:

$$\mathbb{P}_{\text{vol}} \stackrel{\text{def}}{=} \frac{1}{3} \boldsymbol{I} \otimes \boldsymbol{I} \tag{6.106}$$

$$\mathbb{P}_{\text{dev}} \stackrel{\text{def}}{=} \mathbb{I} - \frac{1}{3} \boldsymbol{I} \otimes \boldsymbol{I} \tag{6.107}$$

$\mathbb{P}_{\text{vol}}$ and $\mathbb{P}_{\text{dev}}$ are the volumetric and deviatoric subspace projectors on $\mathcal{L}(\mathbb{E} \otimes \mathbb{E}, \mathbb{R})$ respectively, in the sense that $\forall \ \boldsymbol{A} \in \mathcal{L}(\mathbb{E} \otimes \mathbb{E}, \mathbb{R})$:

$$\begin{aligned} \mathbb{P}_{\text{vol}}: &\quad \boldsymbol{A} \to dev(\boldsymbol{A}) \\ \mathbb{P}_{\text{dev}}: &\quad \boldsymbol{A} \to vol(\boldsymbol{A}) \end{aligned} \tag{6.108}$$

and $\boldsymbol{A} = \boldsymbol{A}^{vol} + \boldsymbol{A}^{dev}$, where $\boldsymbol{A}^{vol} \stackrel{\text{def}}{=} \mathbb{P}_{\text{vol}} : \boldsymbol{A}$ =and $\boldsymbol{A}^{dev} \stackrel{\text{def}}{=} \mathbb{P}_{\text{dev}} : \boldsymbol{A}$. In principal basis system, $\{\boldsymbol{n}_1, \boldsymbol{n}_2, \boldsymbol{n}_3\}$, $\mathbb{I} = \boldsymbol{n}_i \otimes \boldsymbol{n}_j \otimes \boldsymbol{n}_i \otimes \boldsymbol{n}_j$ and $\boldsymbol{I} = \boldsymbol{n}_1 \otimes \boldsymbol{n}_1 + \boldsymbol{n}_2 \otimes \boldsymbol{n}_2 + \boldsymbol{n}_3 \otimes \boldsymbol{n}_3$.

From Eq. 6.105_2, deviatoric ($\boldsymbol{s}$) and volumetric ($\boldsymbol{p}$) components of Kirchhoff stress tensor can be obtained as follows:

$$\boldsymbol{p} = \mathbb{P}_{\text{vol}}\colon\boldsymbol{\tau} = (1-\alpha^d)\sum_{a=1}^{3} k\ln J^e(\boldsymbol{n}_a \otimes \boldsymbol{n}_a) \tag{6.109}$$

$$\boldsymbol{s} = \mathbb{P}_{\text{dev}}\colon\boldsymbol{\tau} = (1-\alpha^d)\sum_{a=1}^{3}\left(2\mu\ln\lambda_a^e - \frac{2}{3}\mu\ln J^e\right)(\boldsymbol{n}_a \otimes \boldsymbol{n}_a) \tag{6.110}$$

The yield function (Eq. 6.93), $\phi^p(\bar{\boldsymbol{\tau}}, \zeta^p)$, can be written in terms of $\boldsymbol{s}$ as follows:

$$\phi^p(\bar{\boldsymbol{\tau}}, \zeta^p) = \|\bar{\boldsymbol{s}}\| - \sqrt{\frac{2}{3}}(\sigma_y - \zeta^p) \tag{6.111}$$

Since $\frac{\partial\phi^p}{\partial\bar{\boldsymbol{\tau}}\backslash} = \frac{\partial\|\mathbb{P}_{\text{dev}}\colon\bar{\boldsymbol{\tau}}\|}{\partial\bar{\boldsymbol{\tau}}\backslash} = \frac{\mathbb{P}_{\text{dev}}\colon\bar{\boldsymbol{\tau}}}{\|\mathbb{P}_{\text{dev}}\colon\bar{\boldsymbol{\tau}}\|} = \frac{\bar{\boldsymbol{s}}}{\|\bar{\boldsymbol{s}}\|}$, the flow rule (Eq. 6.95) can written as:

$$-\frac{1}{2}\boldsymbol{b}_e^{-1}\boldsymbol{\mathcal{F}}\dot{\boldsymbol{C}}_p^{-1}\boldsymbol{\mathcal{F}}^T = \frac{\partial\phi^p}{\partial\boldsymbol{\tau}} = \frac{\gamma}{1-\alpha^d}\frac{\bar{\boldsymbol{s}}}{\|\bar{\boldsymbol{s}}\|} \tag{6.112}$$

The free energy, $\Psi^p(\alpha^p)$, due plastic hardening is taken as a sum linear and saturation hardening terms (Eq. 6.85) as follows:

$$\Psi^p(\alpha^p) = \frac{1}{2}K^p\alpha^{p2} + (\sigma_{max} - \sigma_Y)\left(\alpha^p + \frac{exp(-a\alpha^p)}{a}\right) \tag{6.113}$$

Using the above model the plastic hardening variable, ζ^p, is given by:

$$\zeta^p = -\frac{\partial\Psi^p}{\partial\alpha^p} = -K^p\alpha^p - (\sigma_{max} - \sigma_Y)(1 - exp(-a\alpha^p)) \tag{6.114}$$

With the above assumed functional forms the internal energy dissipation rate, (Eq. 6.92) can be expressed as follows:

$$D_{int} = \gamma\left(\|\bar{\boldsymbol{s}}\| + \zeta^p\sqrt{\frac{2}{3}}\right)$$
$$+\gamma\sqrt{\frac{2}{3}}\left((a_o + a_1T)\mathcal{T}_1(\alpha^p) + a_2\exp(+a_3\alpha^p)\,\mathcal{T}_2(\alpha^p)\right) \geq 0 \tag{6.115}$$

Combining Eq. 6.111 and 6.115 gives:

$$D_{int} = \gamma\sqrt{\frac{2}{3}}\left[\sigma_y + \left((a_o + a_1 T)\mathcal{T}_1(\alpha^p) + a_2\exp(a_3\alpha^p)\,\mathcal{T}_2(\alpha^p)\right)\right] \geq 0 \qquad (6.116)$$

Now since $\gamma \geq 0$, $\sigma_y > 0$ and all the other terms entering in Eq. 6.116 are also positive, the internal energy dissipation rate is greater than zero for any process. This shows that the dissipation inequality is satisfied for the proposed damage model.

Another important feature of the above described elasto-plastic damage model is that no volume change is associated with the plastic deformations. This is an important result which is used in the numerical implementation of the model and can be obtained as follows. With $J = \det(\boldsymbol{\mathcal{F}}) = \det(\boldsymbol{\mathcal{F}}_e\boldsymbol{\mathcal{F}}_p) = J_e J_p$, the total and elastic volume changes are given by $J = \det(\boldsymbol{\mathcal{F}}) > 0$ and $J_e = [\det(\boldsymbol{b}_e)]^{1/2} > 0$, respectively. So the rate of change J is given by: $\dot{J} = \dot{J}_e J_p + J_e\dot{J}_p$. Now the expression for $\dot{J}_e$ can be obtained as follows:

$$\begin{aligned} \dot{J}_e &= \frac{1}{2}[\det(\boldsymbol{b}_e)]^{-1/2}\frac{\partial\det(\boldsymbol{b}_e)}{\partial\boldsymbol{b}_e}:\dot{\boldsymbol{b}}_e \\ \Rightarrow \dot{J}_e &= \frac{1}{2}J_e\boldsymbol{b}_e^{-1}:\dot{\boldsymbol{b}}_e = \frac{1}{2}J^e\boldsymbol{b}_e^{-1}:\left[\boldsymbol{l}\boldsymbol{b}_e + \boldsymbol{b}_e\boldsymbol{l}^{\mathrm{T}} + \boldsymbol{\mathcal{F}}\dot{\boldsymbol{C}}_p^{-1}\boldsymbol{\mathcal{F}}^T\right] \\ \Rightarrow \dot{J}_e &= J_e\left[\boldsymbol{I}:\boldsymbol{d} - \frac{\gamma}{1-\alpha^d}\boldsymbol{I}:\frac{\bar{\boldsymbol{s}}}{\|\bar{\boldsymbol{s}}\|}\right] \end{aligned} \qquad (6.117)$$

Now since $\boldsymbol{I}:\frac{\bar{\boldsymbol{s}}}{\|\bar{\boldsymbol{s}}\|} = 0$, Eq. 6.117_3 gives:

$$\dot{J}_e = J_e\boldsymbol{I}:\boldsymbol{d} \qquad (6.118)$$

Similarly, an expression for $\dot{J}_p$ can be obtained as follows:

$$\begin{aligned} \dot{J}_p &= \frac{1}{2}\left[\det(\boldsymbol{C}_p)\right]^{-1/2}\frac{\partial\det(\boldsymbol{C}_p)}{\partial\boldsymbol{C}_p}:\dot{\boldsymbol{C}}_p \\ \Rightarrow \dot{J}_p &= \frac{1}{2}J_p\boldsymbol{C}_p^{-1}:\dot{\boldsymbol{C}}_p \end{aligned} \qquad (6.119)$$

Now since, $-\frac{1}{2}\boldsymbol{b}_e^{-1}\boldsymbol{\mathcal{F}}\dot{\boldsymbol{C}}_p^{-1}\boldsymbol{\mathcal{F}}^T = \frac{\partial\phi^p}{\partial\boldsymbol{\tau}}$, this implies that: $\dot{\boldsymbol{C}}_p = 2\gamma\boldsymbol{C}_p\boldsymbol{\mathcal{F}}^{-1}\frac{\partial\phi^p}{\partial\boldsymbol{\tau}}\boldsymbol{\mathcal{F}}$. Therefore, $\boldsymbol{C}_p^{-1}:\dot{\boldsymbol{C}}_p = \boldsymbol{C}_p^{-1}:2\gamma\boldsymbol{C}_p\boldsymbol{\mathcal{F}}^{-1}\frac{\partial\phi^p}{\partial\boldsymbol{\tau}}\boldsymbol{\mathcal{F}} = \boldsymbol{I}:2\gamma\boldsymbol{\mathcal{F}}^{-1}\frac{\partial\phi^p}{\partial\boldsymbol{\tau}}\boldsymbol{\mathcal{F}} = 2\gamma\boldsymbol{I}:\frac{\partial\phi^p}{\partial\boldsymbol{\tau}}$. Combining this relation with Eq. 6.119_2 gives:

$$\dot{J}_p = \gamma J_p\boldsymbol{I}:\frac{\partial\phi^p}{\partial\boldsymbol{\tau}} = \gamma J_p\boldsymbol{I}:\frac{\bar{\boldsymbol{s}}}{\|\bar{\boldsymbol{s}}\|} = 0 \text{ and } J_p = 1 \qquad (6.120)$$

Combining, the relation $\dot{J} = \dot{J}_e J_p + J_e\dot{J}_p$ and Eq. 6.120, gives:

$$\dot{J} = \dot{J}_e \tag{6.121}$$

Thus the plastic volume is conserved for the case when the yield function is pressure independent i.e. plastic deformation is isochoric and all the volume change is due to the elastic part of the deformation.

To advance the solution within an incremental solution scheme in a finite element (FE) framework, the flow rule (Eq. 6.112) and the evolution equations for the hardening and damage variables (Eq. 6.94 and 6.98) have to be integrated over a finite time step $\Delta t = t_{n+1} - t_n$. Such a computation is typically carried out at an integration point. The known values at time t_n include Cauchy stress tensor ($\boldsymbol{\sigma}_n$), deformation gradient $\boldsymbol{\mathcal{F}}_n$ and internal variables (α_n^p, α_n^d). The known values at time t_{n+1} includes deformation gradient ($\boldsymbol{\mathcal{F}}_{n+1}$), which is found from the global FE formulation. Global FE formulation can be an implicit or an explicit scheme. The objective of the integration scheme is to compute the Cauchy stress tensor ($\boldsymbol{\sigma}_{n+1}$) and internal variables ($\alpha_{n+1}^p, \alpha_{n+1}^d$) at time t_{n+1}. The main difference between implicit and explicit FE formulations is that for implicit scheme a consistent algorithmic tangent is required to assemble the global tangent stiffness matrix, however for explicit FE formulation such an algorithmic tangent is not required. The proposed elasto-plastic-damage model is implemented in the commercial explicit finite element code LS-DYNA. Thus an algorithmic tangent is not computed in this work. Moreover, the integration of the flow rule is carried out using an exponential map integrator first proposed by Weber and Anand (1990) and was advocated by Eterovic and Bathe (1990) and Simo (1992). In the context of damage based models such integrators have been used by Steinmann (1994, 2005) and Mahnken (2000). The integration of damage and plastic internal evolution laws is carried via the Euler backward method.

The following additional terms are introduced to facilitate the implementation of the algorithm:

$$\boldsymbol{\varepsilon}^e = \begin{Bmatrix} \varepsilon_1^e \\ \varepsilon_2^e \\ \varepsilon_3^e \end{Bmatrix} = \begin{Bmatrix} \ln\lambda_1^e \\ \ln\lambda_2^e \\ \ln\lambda_3^e \end{Bmatrix} \quad \boldsymbol{\beta} = \begin{Bmatrix} \beta_1 \\ \beta_2 \\ \beta_3 \end{Bmatrix} \quad \tilde{\boldsymbol{\eta}} = \begin{Bmatrix} \tilde{\eta}_1 \\ \tilde{\eta}_2 \\ \tilde{\eta}_3 \end{Bmatrix} \quad \boldsymbol{\eta} = \begin{Bmatrix} \eta_1 \\ \eta_2 \\ \eta_3 \end{Bmatrix} \tag{6.122}$$

$$\boldsymbol{a} \stackrel{\text{def}}{=} k\mathbf{1} \otimes \mathbf{1} + 2\mu\left(\boldsymbol{I} - \frac{1}{3}\mathbf{1} \otimes \mathbf{1}\right) \tag{6.123}$$

$$\boldsymbol{\beta} \stackrel{\text{def}}{=} \boldsymbol{a}\boldsymbol{\varepsilon}^{e} \quad \therefore \boldsymbol{\tau} = (1 - \alpha^{d}) \sum_{a=1}^{3} \beta_a (\boldsymbol{n}_a \otimes \boldsymbol{n}_a) \tag{6.124}$$

$$\boldsymbol{\eta} \stackrel{\text{def}}{=} 2\mu\left(\boldsymbol{I} - \frac{1}{3}\mathbf{1} \otimes \mathbf{1}\right)\boldsymbol{\varepsilon}^{e} = \boldsymbol{\beta} - \frac{1}{3}(\mathbf{1}.\boldsymbol{\beta})\mathbf{1} \tag{6.125}$$

$$\therefore \bar{\boldsymbol{s}} = \sum_{a=1}^{3} \eta_a (\boldsymbol{n}_a \otimes \boldsymbol{n}_a) \tag{6.126}$$

$$\|\bar{\boldsymbol{s}}\|^2 = \boldsymbol{\eta}^T\boldsymbol{\eta} = 2\mu\boldsymbol{\varepsilon}^{e^T}\left(\boldsymbol{I} - \frac{1}{3}\mathbf{1} \otimes \mathbf{1}\right)\boldsymbol{\varepsilon}^{e} \tag{6.127}$$

$$\tilde{\boldsymbol{\eta}} \stackrel{\text{def}}{=} \frac{\boldsymbol{\eta}}{\|\boldsymbol{\eta}\|} = \frac{1}{\sqrt{\boldsymbol{\eta}^T\boldsymbol{\eta}}}\boldsymbol{\eta} \tag{6.128}$$

$$\boldsymbol{n} \stackrel{\text{def}}{=} \frac{\bar{\boldsymbol{s}}}{\|\bar{\boldsymbol{s}}\|} = \sum_{a=1}^{3} \tilde{\eta}_a (\boldsymbol{n}_a \otimes \boldsymbol{n}_a) \tag{6.129}$$

$$\phi^{p}(\boldsymbol{\tau}, \zeta^{p}) = \|\boldsymbol{\eta}\| - \sqrt{\frac{2}{3}}[\sigma_Y - \zeta^{p}(\alpha^{p})] \tag{6.130}$$

The integration of the plasticity models is usually carried out in two steps (Simo and Hughes, 1998). In the first step known as "elastic" or "trial" step, all inelasticity is frozen. If the yielding condition is not exceeded then the trial step gives the correct state. However, if the yielding condition is exceeded the algorithm proceeds to "plastic" step where further computations are carried out assuming that plastic flow occur and the consistency condition is enforced in this step. A two step algorithm based on the above concept is described next.

Step -1: Trial Step (Freeze Plastic Flow)

No plastic flow implies:

$$\gamma_{n+1} = 0, \;\; \boldsymbol{C}_{p_{n+1}}^{-1^{TR}} = \boldsymbol{C}_{p_n}^{-1}, \;\; \alpha_{n+1}^{p^{TR}} = \alpha_n^{p}, \;\; \alpha_{n+1}^{d^{TR}} = \alpha_n^{d} \tag{6.131}$$

$$\boldsymbol{b}_{e_{n+1}}^{TR} = \boldsymbol{\mathcal{F}}_{n+1}\boldsymbol{C}_{p_{n+1}}^{-1^{TR}}\boldsymbol{\mathcal{F}}_{n+1}^{T} \tag{6.132}$$

$$J_{n+1}^{e^{TR}} = \det(\boldsymbol{\mathcal{F}}_{n+1}) \qquad J_{n+1}^{p^{TR}} = 1 \tag{6.133}$$

Let $\left\{\lambda_{a_{n+1}}^{e^{2^{TR}}}, \widehat{\boldsymbol{n}}_{a_{n+1}}^{TR}\right\}$ be the eigen pairs of $\boldsymbol{b}_{e_{n+1}}^{TR}$, then using Eq. 6.122 to 6.130, the following relationships can be obtained:

$$\boldsymbol{\varepsilon}_{n+1}^{e^{TR}} = \begin{Bmatrix} \ln\lambda_{1_{n+1}}^{e^{TR}} \\ \ln\lambda_{2_{n+1}}^{e^{TR}} \\ \ln\lambda_{3_{n+1}}^{e^{TR}} \end{Bmatrix} \tag{6.134}$$

$$\boldsymbol{\beta}_{n+1}^{TR} = \boldsymbol{a}\boldsymbol{\varepsilon}_{n+1}^{e^{TR}} \text{ and } \boldsymbol{\eta}_{n+1}^{TR} = \boldsymbol{\beta}_{n+1}^{TR} - \frac{1}{3}(\mathbf{1}.\boldsymbol{\beta}_{n+1}^{TR})\mathbf{1} \tag{6.135}$$

$$\|\boldsymbol{\eta}_{n+1}^{TR}\|^2 = 2\mu\left(\boldsymbol{\varepsilon}_{n+1}^{e^{TR}}\right)^T \left(\boldsymbol{I} - \frac{1}{3}\mathbf{1}\otimes\mathbf{1}\right)\boldsymbol{\varepsilon}_{n+1}^{e^{TR}}$$

$$\phi_{n+1}^{p^{TR}} = \|\boldsymbol{\eta}_{n+1}^{TR}\| - \sqrt{\frac{2}{3}}[\sigma_Y - \zeta^p\left(\alpha_{n+1}^{p^{TR}}\right)] \tag{6.136}$$

$$\overline{\boldsymbol{p}}_{n+1} = \sum_{a=1}^{3} k\mathbf{1}.\boldsymbol{\varepsilon}_{n+1}^{e^{TR}}(\widehat{\boldsymbol{n}}_{a_{n+1}}^{TR}\otimes\widehat{\boldsymbol{n}}_{a_{n+1}}^{TR}) \tag{6.137}$$

$$\boldsymbol{\eta}_{n+1}^{TR} = 2\mu\left(\boldsymbol{I} - \frac{1}{3}\mathbf{1}\otimes\mathbf{1}\right)\boldsymbol{\varepsilon}_{n+1}^{e^{TR}}$$

$$\bar{\boldsymbol{s}}_{n+1}^{TR} = \sum_{a=1}^{3} \eta_{a_{n+1}}^{TR}(\widehat{\boldsymbol{n}}_{a_{n+1}}^{TR}\otimes\widehat{\boldsymbol{n}}_{a_{n+1}}^{TR}) \tag{6.138}$$

$$\bar{\boldsymbol{\tau}}_{n+1}^{TR} = \bar{\boldsymbol{s}}_{n+1}^{TR} + \overline{\boldsymbol{p}}_{n+1} \tag{6.139}$$

$$\boldsymbol{\tau}_{n+1}^{TR} = (1 - \alpha_{n+1}^{d^{TR}})\bar{\boldsymbol{\tau}}_{n+1}^{TR} \tag{6.140}$$

If $\phi_{n+1}^{p^{TR}} \leq 0$, this implies that the trial step is admissible and the following updates are carried out.

ELASTIC UPDATES

$$\alpha_{n+1}^{p} = \alpha_{n+1}^{p^{TR}} \quad \text{and} \quad \alpha_{n+1}^{d} = \alpha_{n+1}^{d^{TR}} \tag{6.141}$$

$$\boldsymbol{C}_{p_{n+1}}^{-1} = \boldsymbol{C}_{p_{n+1}}^{-1^{TR}} \tag{6.142}$$

$$\boldsymbol{\tau}_{n+1} = \boldsymbol{\tau}_{n+1}^{TR} \tag{6.143}$$

$$\boldsymbol{\sigma}_{n+1} = \frac{1}{J_{n+1}^{e^{TR}}}\boldsymbol{\tau}_{n+1} \tag{6.144}$$

If $\phi_{n+1}^{p^{TR}} > 0$, this implies that the trial step is not admissible and the algorithm proceeds to the second step, i.e. the plastic step.

Step -2: Plastic Step

In this step, the integration of flow rules is carried out and the consistency condition is enforced as described next.

(a) Integration of flow rule using exponential integrator:

$$-\frac{1}{2}\boldsymbol{b}_e^{-1}\boldsymbol{\mathcal{F}}\dot{\boldsymbol{C}}_p^{-1}\boldsymbol{\mathcal{F}}^T=\frac{\gamma}{1-\alpha^d}\boldsymbol{n}$$

$$\Rightarrow \dot{\boldsymbol{C}}_p^{-1}=-\frac{2\gamma}{1-\alpha^d}\boldsymbol{\mathcal{F}}^{-1}\boldsymbol{n}\boldsymbol{b}_e\boldsymbol{\mathcal{F}}^{-T}=-\frac{2\gamma}{1-\alpha^d}\boldsymbol{\mathcal{F}}^{-1}\boldsymbol{n}\boldsymbol{\mathcal{F}}\boldsymbol{C}_p^{-1}\,\boldsymbol{\mathcal{F}}^T\boldsymbol{\mathcal{F}}^{-T} \tag{6.145}$$

$$\Rightarrow \dot{\boldsymbol{C}}_p^{-1}=\frac{2\gamma}{1-\alpha^d}\boldsymbol{\mathcal{F}}^{-1}\boldsymbol{n}\boldsymbol{\mathcal{F}}\boldsymbol{C}_p^{-1}$$

Using the exponential integrator, the integration of Eq. 6.145_3 over the time period $\Delta t=t_{n+1}-t_n$, yields the following expression:

$$\begin{aligned}\boldsymbol{C}_{p_{n+1}}^{-1}&=\exp\left(-\frac{2\Delta\gamma_{n+1}}{1-\alpha_{n+1}^d}\boldsymbol{\mathcal{F}}_{n+1}^{-1}\boldsymbol{n}_{n+1}\boldsymbol{\mathcal{F}}_{n+1}\right)\boldsymbol{C}_{p_n}^{-1}\\ \Rightarrow \boldsymbol{C}_{p_{n+1}}^{-1}&=\boldsymbol{\mathcal{F}}_{n+1}^{-1}\exp\left(-\frac{2\Delta\gamma_{n+1}}{1-\alpha_{n+1}^d}\boldsymbol{n}_{n+1}\right)\boldsymbol{\mathcal{F}}_{n+1}\boldsymbol{C}_{p_n}^{-1}\end{aligned} \tag{6.146}$$

where $\Delta\gamma_{n+1}\equiv\Delta t\gamma_{n+1}$. Now combining Eq. 6.146 with the relationships: $\boldsymbol{b}_{e_{n+1}}=\boldsymbol{\mathcal{F}}_{n+1}\boldsymbol{C}_{p_{n+1}}^{-1}\boldsymbol{\mathcal{F}}_{n+1}^T$, gives:

$$\begin{aligned}\boldsymbol{b}_{e_{n+1}}&=\exp\left(-\frac{2\Delta\gamma_{n+1}}{1-\alpha_{n+1}^d}\boldsymbol{n}_{n+1}\right)\boldsymbol{\mathcal{F}}_{n+1}\boldsymbol{C}_{p_n}^{-1}\boldsymbol{\mathcal{F}}_{n+1}^T\\ \Rightarrow \boldsymbol{b}_{e_{n+1}}&=\exp\left(-\frac{2\Delta\gamma_{n+1}}{1-\alpha_{n+1}^d}\boldsymbol{n}_{n+1}\right)\boldsymbol{b}_{e_{n+1}}^{TR}\end{aligned} \tag{6.147}$$

where $\boldsymbol{b}_{e_{n+1}}^{TR}=\boldsymbol{\mathcal{F}}_{n+1}\boldsymbol{C}_{p_n}^{-1}\boldsymbol{\mathcal{F}}_{n+1}^T$.

Using the following spectral forms for $\boldsymbol{n}_{n+1}$and $\boldsymbol{b}_{e_{n+1}}$:

$$\begin{aligned}\boldsymbol{n}_{n+1}&=\sum_{a=1}^{3}\tilde{\eta}_{a_{n+1}}(\hat{\boldsymbol{n}}_{a_{n+1}}\otimes\hat{\boldsymbol{n}}_{a_{n+1}})\\ \boldsymbol{b}_{e_{n+1}}&=\lambda_{a_{n+1}}^{e^2}(\hat{\boldsymbol{n}}_{a_{n+1}}\otimes\hat{\boldsymbol{n}}_{a_{n+1}})\end{aligned} \tag{6.148}$$

and combining with Eq. 6.147_2 gives:

$$\begin{aligned}\boldsymbol{b}_{e_{n+1}}^{TR} &= \boldsymbol{b}_{e_{n+1}} \exp\left(\frac{2\Delta\gamma_{n+1}}{1-\alpha_{n+1}^{d}}\boldsymbol{n}_{n+1}\right) \\ &= \sum_{a=1}^{3}\left[\exp\left(\frac{2\Delta\gamma_{n+1}}{1-\alpha_{n+1}^{d}}\tilde{\eta}_{a_{n+1}}\right)\lambda_{a_{n+1}}^{e^2}\right](\widehat{\boldsymbol{n}}_{a_{n+1}} \otimes \widehat{\boldsymbol{n}}_{a_{n+1}})\end{aligned} \tag{6.149}$$

Also, $\boldsymbol{b}_{e_{n+1}}^{TR} = \lambda_{a_{n+1}}^{e^2{}^{TR}}(\widehat{\boldsymbol{n}}_{a_{n+1}}^{TR} \otimes \widehat{\boldsymbol{n}}_{a_{n+1}}^{TR})$, thus the uniqueness of the spectral decomposition of $\boldsymbol{b}_{e_{n+1}}^{TR}$ yields:

$$\begin{aligned}\lambda_{a_{n+1}}^{e^2{}^{TR}} &= \exp\left(\frac{2\Delta\gamma_{n+1}}{1-\alpha_{n+1}^{d}}\tilde{\eta}_{a_{n+1}}\right)\lambda_{a_{n+1}}^{e^2} \\ \widehat{\boldsymbol{n}}_{a_{n+1}} &= \widehat{\boldsymbol{n}}_{a_{n+1}}^{TR} \\ a &= 1,2,3\end{aligned} \tag{6.150}$$

Taking the logarithm of both sides of Eq. 6.150_1 gives:

$$\boldsymbol{\varepsilon}_{n+1}^{e} = \boldsymbol{\varepsilon}_{n+1}^{e^{TR}} - \frac{\Delta\gamma_{n+1}}{1-\alpha_{n+1}^{d}}\tilde{\boldsymbol{\eta}}_{n+1} \tag{6.151}$$

Combining Eq. 6.124 and 6.151 gives:

$$\begin{aligned}\boldsymbol{\beta}_{n+1} &= \boldsymbol{a}\boldsymbol{\varepsilon}_{n+1}^{e} \\ \Rightarrow \boldsymbol{\beta}_{n+1} &= \boldsymbol{a}\boldsymbol{\varepsilon}_{n+1}^{e^{TR}} - \frac{\Delta\gamma_{n+1}}{1-\alpha_{n+1}^{d}}\boldsymbol{a}\tilde{\boldsymbol{\eta}}_{n+1} \\ \Rightarrow \boldsymbol{\beta}_{n+1} &= \boldsymbol{\beta}_{n+1}^{TR} - \frac{2\mu\Delta\gamma_{n+1}}{1-\alpha_{n+1}^{d}}\boldsymbol{a}\tilde{\boldsymbol{\eta}}_{n+1}\end{aligned} \tag{6.152}$$

Now Eq. 6.152_3 together with Eq. 6.124 gives:

$$\begin{aligned}\boldsymbol{\eta}_{n+1} &= 2\mu\left(\boldsymbol{I} - \frac{1}{3}\mathbf{1}\otimes\mathbf{1}\right)\boldsymbol{\varepsilon}_{n+1}^{e} \\ \Rightarrow \boldsymbol{\eta}_{n+1} &= \left(\boldsymbol{I} - \frac{1}{3}\mathbf{1}\otimes\mathbf{1}\right)\left[\boldsymbol{\varepsilon}_{n+1}^{e^{TR}} - \frac{\Delta\gamma_{n+1}}{1-\alpha_{n+1}^{d}}\tilde{\boldsymbol{\eta}}_{n+1}\right] \\ \Rightarrow \boldsymbol{\eta}_{n+1} &= \boldsymbol{\eta}_{n+1}^{TR} - \frac{2\mu\Delta\gamma_{n+1}}{1-\alpha_{n+1}^{d}}\tilde{\boldsymbol{\eta}}_{n+1} \\ \Rightarrow \frac{\boldsymbol{\eta}_{n+1}}{\|\boldsymbol{\eta}_{n+1}\|}\|\boldsymbol{\eta}_{n+1}\| &= \frac{\boldsymbol{\eta}_{n+1}^{TR}}{\|\boldsymbol{\eta}_{n+1}^{TR}\|}\|\boldsymbol{\eta}_{n+1}^{TR}\| - \frac{2\mu\Delta\gamma_{n+1}}{1-\alpha_{n+1}^{d}}\tilde{\boldsymbol{\eta}}_{n+1} \\ \Rightarrow \tilde{\boldsymbol{\eta}}_{n+1}\left(\|\boldsymbol{\eta}_{n+1}\| + \frac{2\mu\Delta\gamma_{n+1}}{1-\alpha_{n+1}^{d}}\right) &= \tilde{\boldsymbol{\eta}}_{n+1}^{TR}\|\boldsymbol{\eta}_{n+1}^{TR}\|\end{aligned} \tag{6.153}$$

Equation 6.153_5 implies that:

$$\|\boldsymbol{\eta}_{n+1}\| + \frac{2\mu\Delta\gamma_{n+1}}{1-\alpha_{n+1}^{d}} = \|\boldsymbol{\eta}_{n+1}^{TR}\| \tag{6.154}$$

$$\widetilde{\boldsymbol{\eta}}_{n+1} = \widetilde{\boldsymbol{\eta}}_{n+1}^{TR} \tag{6.155}$$

(b) Consistency Condition

Enforcing the consistency condition at time $t = t_{n+1}$ gives:

$$\phi_{n+1}^{p} = \|\boldsymbol{\eta}_{n+1}\| - \sqrt{\frac{2}{3}}[\sigma_y - \zeta^{p}(\alpha_{n+1}^{p})] = 0 \tag{6.156}$$

Using Eq. 6.154, the consistency condition can be written as follows:

$$\phi_{n+1}^{p} = \|\boldsymbol{\eta}_{n+1}^{TR}\| - \frac{2\mu\Delta\gamma_{n+1}}{1-\alpha_{n+1}^{d}} - \sqrt{\frac{2}{3}}[\sigma_y - \zeta^{p}(\alpha_{n+1}^{p})] = 0 \tag{6.157}$$

(c) Integration of damage and plastic internal variables

Integrating Eq. 6.94 using Euler backward method gives:

$$\alpha_{n+1}^{p} = \alpha_{n}^{p} + \sqrt{\frac{2}{3}}\Delta\gamma_{n+1} \tag{6.158}$$

Integrating Eq. 6.98 using Euler backward method gives:

$$\alpha_{n+1}^{d} = \alpha_{n}^{d} + \sqrt{\frac{2}{3}}\Delta\gamma_{n+1}\big[(a_o + a_1 T_{n+1})\mathcal{T}_1(\alpha_{n+1}^{p}) + a_2 \exp(a_3\alpha_{n+1}^{p})\,\mathcal{T}_2(\alpha_{n+1}^{p})\big] \tag{6.159}$$

where $T_{n+1} = \frac{\|\bar{\boldsymbol{p}}_{n+1}\|}{\|\boldsymbol{\eta}_{n+1}\|} = \frac{\|\bar{\boldsymbol{p}}_{n+1}\|}{\|\boldsymbol{\eta}_{n+1}^{TR}\| - \frac{2\mu\Delta\gamma_{n+1}}{1-\alpha_{n+1}^{d}}}$

(d) Solution by Newton Raphson Method

Equations 6.157 and 6.159 are nonlinear equations in $\Delta\gamma_{n+1}$ and α_{n+1}^{d}. These equations are solved together with the Eq. 6.158 to obtain $\Delta\gamma_{n+1}$ and α_{n+1}^{d}. For solution of these equations, writing Eq. 6.157 as follows:

$$F_1(k_{n+1}^{d}, \Delta\gamma_{n+1}) = \|\boldsymbol{\eta}_{n+1}^{TR}\| - \frac{2\mu\Delta\gamma_{n+1}}{1-\alpha_{n+1}^{d}} - \sqrt{\frac{2}{3}}\big[\sigma_y - \zeta^{p}(\alpha_{n+1}^{p})\big] = 0 \tag{6.160}$$

Similarly, writing Eq. 6.159 as follows:

$$F_2\left(\alpha_{n+1}^d, \Delta\gamma_{n+1}\right) = \alpha_{n+1}^d - \alpha_n^d$$

$$-\sqrt{\frac{2}{3}}\Delta\gamma_{n+1}\left[(a_o + a_1 T_{n+1})\mathcal{T}_1\left(\alpha_{n+1}^p\right) + a_2 \exp\left(a_3\alpha_{n+1}^p\right)\mathcal{T}_2\left(\alpha_{n+1}^p\right)\right] \tag{6.161}$$

$$= 0$$

Thus, Eq. 6.160 and 6.161 can be considered as two equations in two variables α_{n+1}^d and $\Delta\gamma_{n+1}$, and therefore can be solved by the standard Newton-Raphson method. Starting with the initial values of $\Delta\gamma_{n+1}^{(0)} = 0$ and $\alpha_{n+1}^{d(0)} = \alpha_n^d$, the following iterations are carried out to obtain the solution:

$$\begin{bmatrix}\delta(\Delta\gamma_{n+1}^{(k+1)}) \\ \delta(\alpha_{n+1}^{d(k+1)})\end{bmatrix} = \begin{bmatrix}\dfrac{\partial F_1}{\partial\Delta\gamma_{n+1}} & \dfrac{\partial F_1}{\partial\alpha_{n+1}^d} \\ \dfrac{\partial F_2}{\partial\Delta\gamma_{n+1}} & \dfrac{\partial F_2}{\partial\alpha_{n+1}^d}\end{bmatrix}^{-1}_{\left(\Delta\gamma_{n+1}^{(k)}, \alpha_{n+1}^{d(k)}\right)} \begin{bmatrix}F_1\left(\alpha_{n+1}^{d(k)}, \Delta\gamma_{n+1}^{(k)}\right) \\ F_2\left(\alpha_{n+1}^{d(k)}, \Delta\gamma_{n+1}^{(k)}\right)\end{bmatrix} \tag{6.162}$$

The incremental updates are obtained as follows:

$$\begin{aligned}\Delta\gamma_{n+1}^{(k+1)} &= \Delta\gamma_{n+1}^{(k)} + \delta(\Delta\gamma_{n+1}^{(k+1)}) \\ \alpha_{n+1}^{d(k+1)} &= \alpha_{n+1}^{d(k)} + \delta(\alpha_{n+1}^{d(k+1)})\end{aligned} \tag{6.163}$$

The derivatives entering in Eq. 6.162 are given as follows:

$$\frac{\partial F_1}{\partial\Delta\gamma_{n+1}} = -\frac{2\mu}{1-\alpha_{n+1}^d} - \frac{2}{3}\left[K^p + a(\sigma_{max} - \sigma_Y)\exp\left(-a\alpha_{n+1}^p\right)\right] \tag{6.164}$$

$$\frac{\partial F_1}{\partial\alpha_{n+1}^d} = -\frac{2\mu\Delta\gamma_{n+1}}{\left(1-\alpha_{n+1}^d\right)^2} \tag{6.165}$$

$$\begin{aligned}\frac{\partial F_2}{\partial\Delta\gamma_{n+1}} = &-\sqrt{\frac{2}{3}}\left[(a_o + a_1 T_{n+1})\mathcal{T}_1\left(\alpha_{n+1}^p\right)\right. \\ &\left. + a_2 \exp\left(a_3\alpha_{n+1}^p\right)\mathcal{T}_2\left(\alpha_{n+1}^p\right)\right] \\ &-\sqrt{\frac{2}{3}}\Delta\gamma_{n+1}\left[(a_o + a_1 T_{n+1})\frac{\partial\mathcal{T}_1}{\partial\Delta\gamma_{n+1}}\right. \\ &+ a_1\mathcal{T}_1\left(\alpha_{n+1}^p\right)\frac{\partial T_{n+1}}{\partial\Delta\gamma_{n+1}} + a_2\exp\left(a_3\alpha_{n+1}^p\right)\frac{\partial\mathcal{T}_2}{\partial\Delta\gamma_{n+1}} \\ &\left. + \sqrt{\frac{2}{3}}a_2 a_3 \exp\left(a_3\alpha_{n+1}^p\right)\mathcal{T}_2\left(\alpha_{n+1}^p\right)\right]\end{aligned} \tag{6.166}$$

$$\frac{\partial \mathcal{T}_1}{\partial \Delta\gamma_{n+1}} = 0 \quad \text{if } \alpha^p_{n+1} < \varepsilon_{nuc}$$

$$\frac{\partial \mathcal{T}_1}{\partial \Delta\gamma_{n+1}} = 2\sqrt{\frac{2}{3}}\frac{\left(\alpha^p_{n+1} - \varepsilon_{nuc}\right)}{\Delta\varepsilon^2}\left[3 - \frac{2\left(\alpha^p_{n+1} - \varepsilon_{nuc}\right)}{\Delta\varepsilon}\right]$$

$$+ \frac{\left(\alpha^p_{n+1} - \varepsilon_{nuc}\right)^2}{\Delta\varepsilon^2}\left[3 - 2\sqrt{\frac{2}{3}}\frac{1}{\Delta\varepsilon}\right] \quad \text{if } \varepsilon_{nuc} < \alpha^p_{n+1} < \varepsilon_{nuc} + \Delta\varepsilon \tag{6.167}$$

$$\text{and } \frac{\partial \mathcal{T}_1}{\partial \Delta\gamma_{n+1}} = 0 \quad \text{if } \alpha^p_{n+1} \geq \varepsilon_{nuc} + \Delta\varepsilon$$

$$\frac{\partial \mathcal{T}_2}{\partial \Delta\gamma_{n+1}} = 0 \quad \text{if } \alpha^p_{n+1} < \varepsilon_{cl}$$

$$\frac{\partial \mathcal{T}_2}{\partial \Delta\gamma_{n+1}} = 2\sqrt{\frac{2}{3}}\frac{\left(\alpha^p_{n+1} - \varepsilon_{cl}\right)}{\Delta\varepsilon^2}\left[3 - \frac{2\left(\alpha^p_{n+1} - \varepsilon_{cl}\right)}{\Delta\varepsilon}\right]$$

$$+ \frac{\left(\alpha^p_{n+1} - \varepsilon_{cl}\right)^2}{\Delta\varepsilon^2}\left[3 - 2\sqrt{\frac{2}{3}}\frac{1}{\Delta\varepsilon}\right] \quad \text{if } \varepsilon_{cl} < \alpha^p_{n+1} < \varepsilon_{cl} + \Delta\varepsilon \tag{6.168}$$

$$\text{and } \frac{\partial \mathcal{T}_2}{\partial \Delta\gamma_{n+1}} = 0 \quad \text{if } \alpha^p_{n+1} \geq \varepsilon_{cl} + \Delta\varepsilon$$

$$\frac{\partial T_{n+1}}{\partial \Delta\gamma_{n+1}} = \frac{\|\overline{\boldsymbol{p}}_{n+1}\|}{\left(\|\boldsymbol{\eta}^{TR}_{n+1}\| - \frac{2\mu\Delta\gamma_{n+1}}{1-\alpha^d_{n+1}}\right)^2}\left(\frac{2\mu}{1-\alpha^d_{n+1}}\right) \tag{6.169}$$

$$\frac{\partial F_2}{\partial \alpha^d_{n+1}} = 1 - \sqrt{\frac{2}{3}}\Delta\gamma_{n+1}a_1\mathcal{T}_1\left(\alpha^p_{n+1}\right)\frac{\partial T_{n+1}}{\partial \alpha^d_{n+1}} \tag{6.170}$$

$$\frac{\partial T_{n+1}}{\partial \alpha^d_{n+1}} = \frac{2\mu\Delta\gamma_{n+1}\|\overline{\boldsymbol{p}}_{n+1}\|}{\left(\|\boldsymbol{\eta}^{TR}_{n+1}\| - \frac{2\mu\Delta\gamma_{n+1}}{1-\alpha^d_{n+1}}\right)^2}\frac{1}{\left(1-\alpha^d_{n+1}\right)^2} \tag{6.171}$$

After solving these equations, the relevant updates are obtained using Eq. 6.150_2, 6.151, 6.152, 6.155, 6.159 and 6.158.

6.4 Model Results

6.4.1 Single Element Response

To investigate the effect of various parameters entering in the model, a parametric study is carried out using a single element of size 0.25×0.25×0.25 inches, with one point integration. The model set up is shown in Fig. 6.4. The bulk modulus and shear modulus are taken as follows: $k = 24167\ Ksi$, and $\mu = 11154\ Ksi$. A critical value of the damage parameter, α_{cr}^{d}, is introduced and the element is removed (is assumed to have failed) when this critical damage parameter is reached. For this parametric study α_{cr}^{d} is taken as 0.9. The various cases considered for this parametric study are given in Table 6.1. and the results are shown in Fig. 6.5 to Fig. 6.10. The figures show that a wide range of material responses can be simulated and that the model has the flexibility to address micro-structural changes due to void growth and coalescence. For example as shown in Fig. 6.10, the two stages of material response can be modeled; the first descending branch of the curve corresponds to the damage due to void growth processes, while the second descending branch corresponds to the rapid disintegration of the material due to the void coalescence processes. Clearly, the rate of damage growth can be controlled by appropriate selection of parameters.

6.5 Experimental Verification of the Proposed Model

6.5.1 Experimental Testing

To validate and calibrate the proposed micro-mechanical model an experimental program is carried out as a part of this research. The experimental study involved tension tests of Grade A36 steel specimens that were notched to a desired geometry. Figures 6.11 and 6.12 show the geometry of the two steel specimens used in this work. The specimen shown in Fig. 6.11 has symmetric notches while the specimen in Fig. 6.12 has asymmetric notches. Specimens are prepared from flat hot rolled bars of dimension 18×4

inches. These two different notch patterns are chosen to promote different stress conditions in the material. In particular, specimens with symmetrical notches are subjected to higher triaxial stresses as compared to specimens with asymmetrical notches which are subjected to lower triaxiality. Thus these specimens will experience different modes and rates of damage, and are chosen to calibrate the proposed micromechanical model to represent damage modes due to both dilation and elongation of micro-voids. Two different thicknesses of 0.25 inch and 0.5 inch are used for each of the test specimens and two specimens of each type are tested. Specimens are tested to failure and the data of interest from the tension test is the force versus displacement response of the specimens.

The notched bars are tested in a 50 kip servo-hydraulic MTS load frame under displacement control. The data channels acquired from the test are time, extensometer displacement, and force. An extensometer of 1.5 inch gage length is used for measuring displacement. Figure 6.13 shows a photo of the test setup. A loading rate 0.03 in/min is used in the tests.

To facilitate further discussions, symmetrically notched specimens are designated as SN-X-Y, where X represents the thickness (in inches) of the specimen, while asymmetrically notch specimens are designated as ASN-X-Y. The appended letter Y represents the specimen number in the same series and is either 1 or 2. Figure 6.14 shows one of the fractured specimens at the end of the test. Load displacement curves for SN-0.25, SN-0.5, ASN-0.25 and ASN-0.5 specimens are shown in Fig. 6.15, 6.16, 6.17 and 6.18, respectively.

6.5.2 Model Calibration

Calibration of the developed constitutive material model is carried out using finite element analysis of the notched specimens used in the experimental part of this study. Failure of steel members results in softening response and is characterized by formation of localization zones or bands associated with high deformations and most of the energy

dissipation occurs in these zones. The size of such localization zones cannot be resolved by classical continuum mechanics theories due to the lack of an intrinsic length scale in these theories. This leads to finite element results that are mesh dependent. Indeed, the finite element results fail to converge no matter how small an element size is used. Various theories are proposed in the literature that are used to regularize the localization behavior including: (a) higher order gradient based theories (Aifantis (1984,1987)); (b) nonlocal theories (Bazant et al., (1984)) (b) rate dependent constitutive models (Needleman (1988)); (c) Cosserat continua (deBorst et al., (1991)); and (d) mesh size dependent constitutive models (Hillerborg et al., 1976). In this work, this pathology is addressed by making the material parameters mesh size dependent and the constitutive model is calibrated for finite elements of size 0.025 in.

Model parameters are obtained from finite element simulations of specimen SN-0.25, wherein multiple simulations are carried out to adjust the model parameters in order to match the experimental results. Finite element models of the notched bar employ selectively reduced fully integrated eight node isoparametric solid elements (Hallquist, 2006). Table 6.2 shows the material parameters, obtained by trial and error, which give a good match to the experimental results obtained for SN-0.25. The yield strength of the steel is 42 ksi and the hardening curve is shown in Fig. 6.19. The void nucleation strain, ε_{nul}, is taken as a function of stress triaxiality. Figure 6.20 shows the bilinear relationship that is used to model void nucleation strain as a function of stress triaxiality. This relationship is modeled after the results obtained by Bandstra et al. (1998), where it was shown that the effective strain to failure first decreases rapidly with triaxiality and then at higher triaxiality the decrease is at a slower rate. Fracture is simulated by removing affected elements when the damage variable, α^d, reaches a value of 0.9. Figure 6.21 shows the finite element mesh of SN-0.25. As shown in Fig. 6.23, with the above model parameters a good match is obtained between experimental and finite element results for this specimen.

6.5.3 Model Validation

Model validation is carried out by using the model parameters obtained in Section 6.5.2 to simulate the response for other test cases i.e. for specimens SN-0.5, ASN-0.25 and ASN-0.5. Figure 6.21 and 6.22 shows the finite element meshes of SN-0.25 and ASN-0.5. Figure 6.24 to 6.26 show comparisons between finite element and experimental results. A good match between the finite element and experimental results is obtained for all the cases.

6.5.4 Discussion of Results

Validation studies presented in Section 6.5.3 shows that the model parameters obtained in Section 6.5.2 can be considered as material properties and therefore can be used to represent material response under a variety of stress states. Plots of stress triaxiality at various locations of the specimens are shown in Fig. 6.27 to Fig 6.30. The average triaxiality on the fracture plane (as defined in Fig. 6.31 and Fig. 6.32), together with the triaxiality value at the center and the edge of the fractured plane are plotted in these figures. It can be observed that stress triaxiality varies from an average value of about 1.5 for symmetric notches to an average of about 0.9 for asymmetric notches. A large variation of triaxiality within the section can also be observed. The locations of fracture initiation for various cases are shown in Fig 6.33 and Fig 6.34. Failure initiation occurs at the edge of specimens near the notch where triaxiality is high during the initial loading stage leading to smaller values of void nucleation strain in these regions. The location of fracture initiation is consistent with the results reported by Kuwamura et al. (1997), which showed that for sharp notched steel specimens fracture initiation occurred just under the surface of the notch where the triaxiality was highest. Fracture initiation is also consistent with the results reported by Toribio et al. (2003), who carried out mechanical and scanning electron micrograph testing of 27 notched samples of high-strength pearlitic steel bars and noted that fracture initiates at locations of highest triaxiality. Thus, the proposed damage evolution law is able to successfully model the ductile fracture process under various states of stress.

6.5.5 Summary and Conclusions

The study in this chapter was concerned with the development of a damage mechanics based micro-mechanical model which can be used to simulate ductile fracture in structural steels. Specifically, a damage model based on the concept of effective stress and strain equivalence principle in a finite deformation framework was proposed. The damage evolution law was designed to take into account the changes that arise due to micro-structural evolution during the ductile fracture process. In particular, damage due to the three stages of ductile fracture initiation: micro-void nucleation, growth and coalescence were modeled. Damage evolution due to void elongation and dilation were also modeled and a triaxiality based void nucleation criterion was included. The algorithm for numerical integration of the proposed damage model was presented and implemented in the explicit finite element code LS-DYNA. A parametric study showing the effect of various model parameters was also presented.

Experimental testing of symmetrically and asymmetrically notched steel bars was carried out and results from the tests were used to calibrate and verify the proposed model. A set of model parameters were proposed for the developed micro-mechanical model. Simulation results from the finite element analysis showed that the proposed damage model can be used to model the ductile fracture process in steel.

Analysis Case	Parameters
Case 1	$a = a_0 = a_1 = a_2 = a_3 = 0, \quad \sigma_y = 50\ Ksi$ $K^p(Ksi) = 1450, 72.5, 29.0, 3.625$
Case 2	$K^p = a_0 = a_1 = a_2 = a_3 = 0, \sigma_y = 50\ Ksi, \sigma_{max} = 85\ Ksi$ $a = 5, 10, 20, 50$
Case 3	$K^p = a_0 = a_1 = a_2 = a_3 = 0, \sigma_y = 50\ Ksi, a = 40$ $\sigma_{max} = 65, 75, 85, 100$
Case 4	$a_1 = a_2 = a_3 = 0, \sigma_y = 50\ Ksi\ , \sigma_{max} = 65\ Ksi, a = 40, K^p = 29\ Ksi$ $\varepsilon_{nuc} = 0.2, \quad \Delta\varepsilon = 0.05 \quad \alpha_{cr}^d = 0.9$ $a_0 = 0, 0.25, 0.5, 1, 2.5, 5, 10$
Case 5	$a_o = a_2 = a_3 = 0, \sigma_y = 50\ Ksi\ , \sigma_{max} = 65\ Ksi, a = 40, K^p = 29\ Ksi$ $\varepsilon_{nuc} = 0.2 \quad \Delta\varepsilon = 0.05 \quad \alpha_{cr}^d = 0.9$ $a_1 = 0, 0.25, 0.5, 1, 2.5, 5, 10$
Case 6	$\sigma_y = 50\ Ksi\ , \quad \sigma_{max} = 65\ Ksi, \quad a = 40, \quad K^p = 29\ Ksi$ $\varepsilon_{nuc} = 0.2\ \ \varepsilon_{cl} = 0.4\ \ \Delta\varepsilon = 0.05, \ \ a_o = a_1 = 0.5\ \ a_2 = 1.0\ \ \alpha_{cr}^d = 0.9$ $a_3 = \ 1, 5, 10, 15$

Table 6.1 Analyses cases

Model parameters	
Bulk Modulus	24167 ksi
Shear Modulus	11154 ksi
Hardening-curve	Fig. 6.15
Yield Stress σ_y	42 ksi
a_o	0.175
a_1	0.325
a_2	1.75
a_3	2.5
ε_{cl}	0.5
ε_{nuc}	Fig. 6.16

Table 6.2 Model parameters

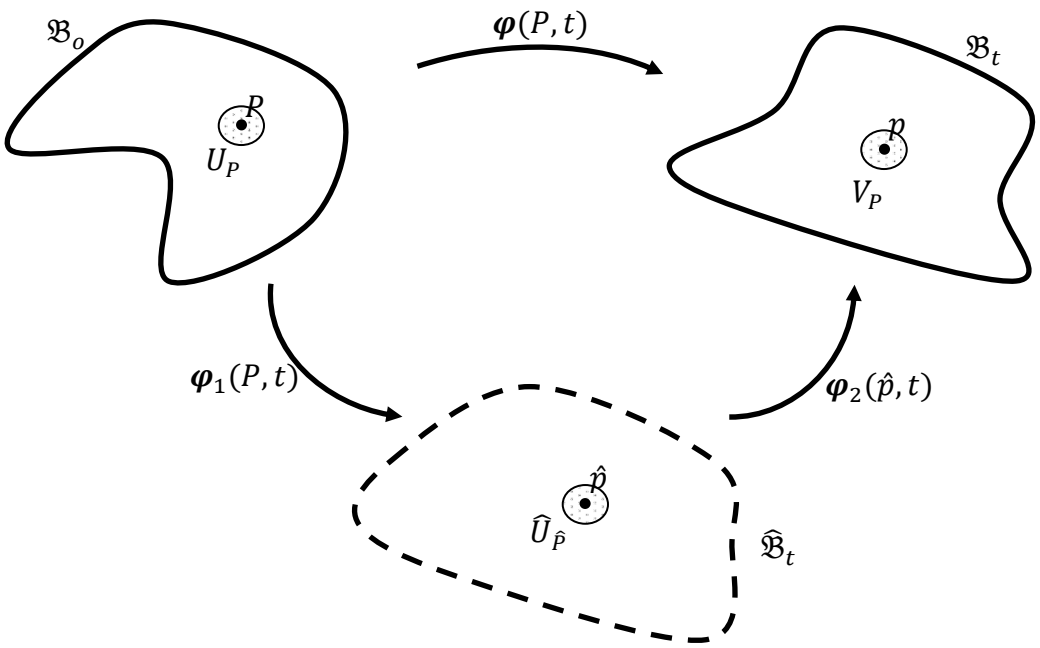

Figure 6.1 Intermediate configuration

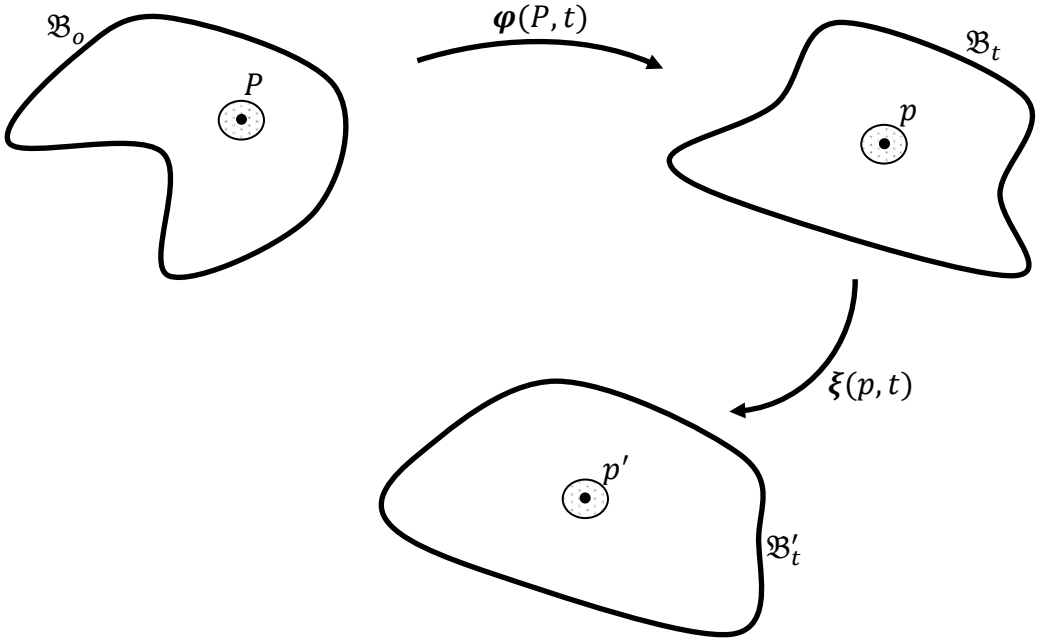

Figure 6.2 Covariance with respect to superposed diffeomorphism

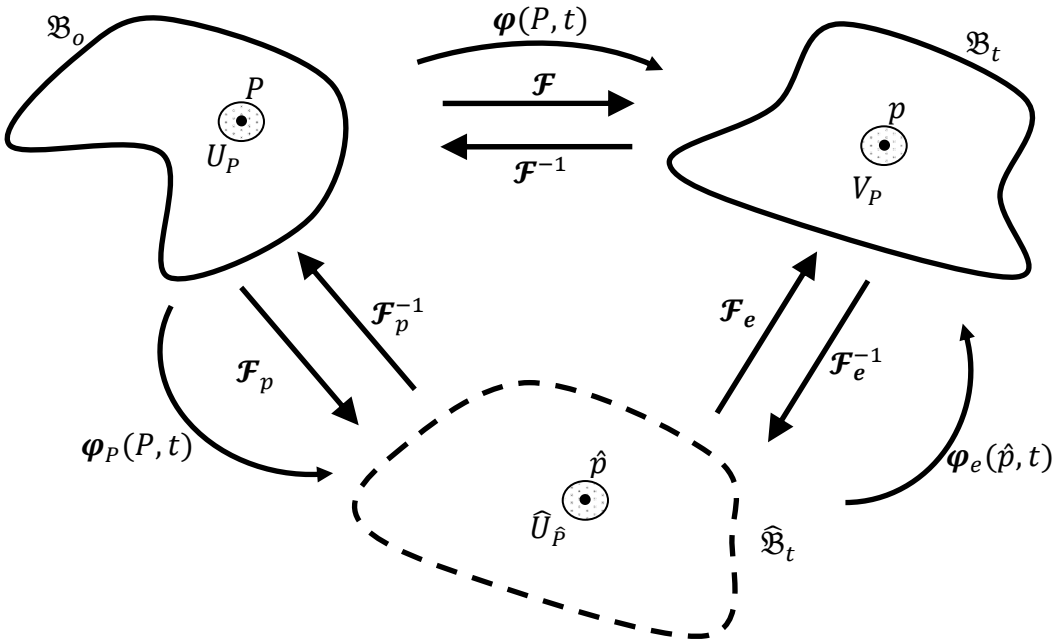

Figure 6.3 Multiplicative plasticity with intermediate configuration

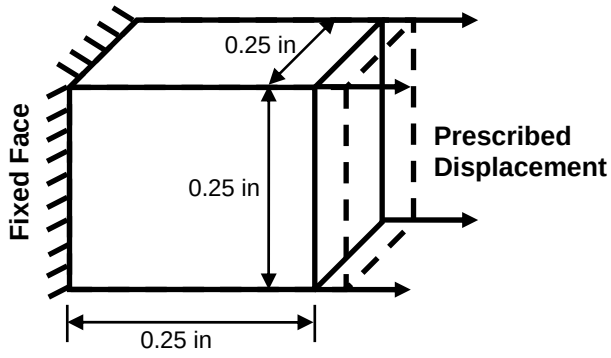

Figure 6.4 Model setup for parametric study

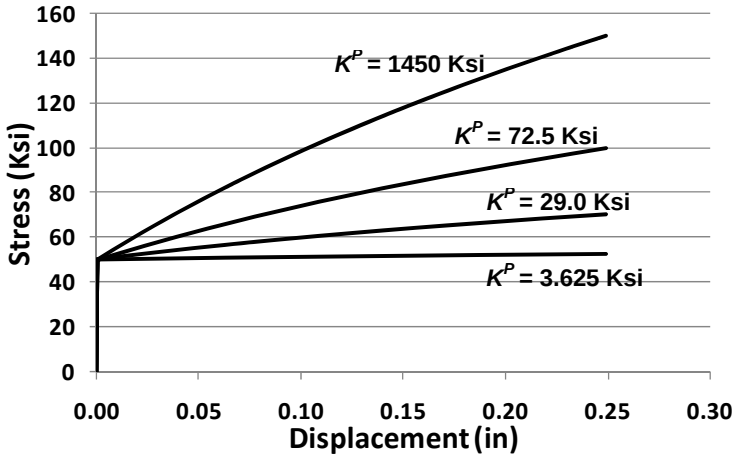

Figure 6.5 Effect of K^p

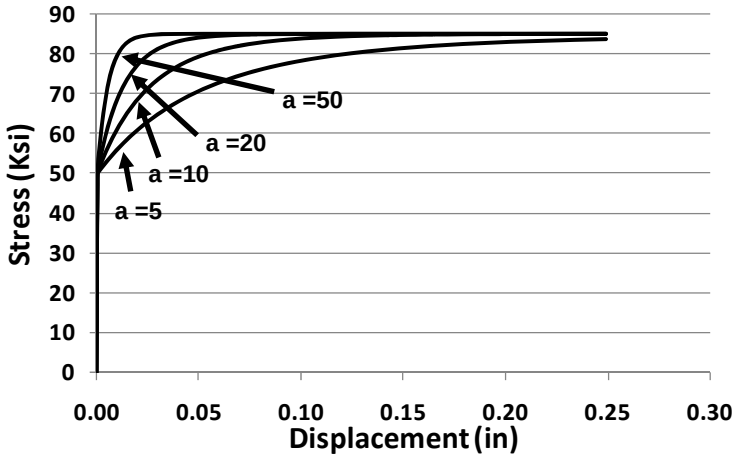

Figure 6.6 Effect of parameter "a"

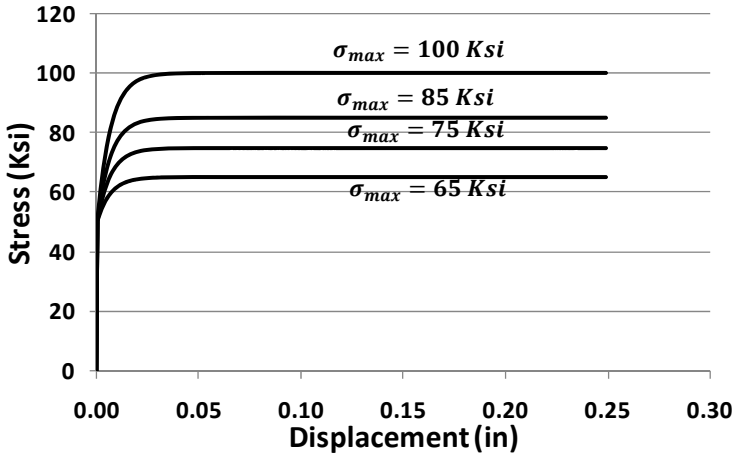

Figure 6.7 Effect of parameter σ_{max}

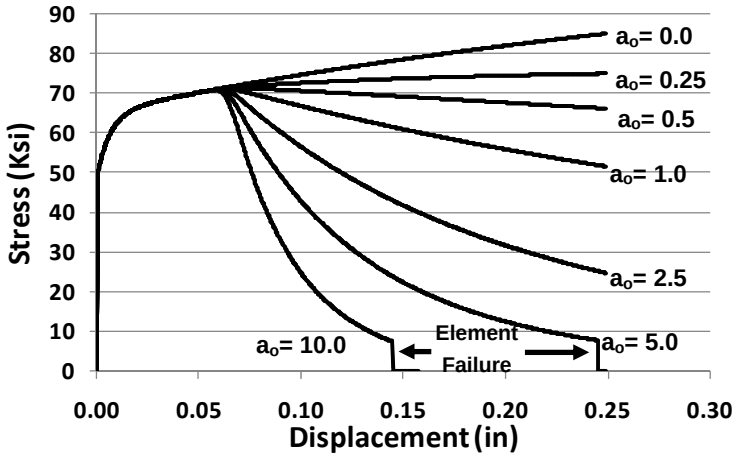

Figure 6.8 Effect of parameter a_o

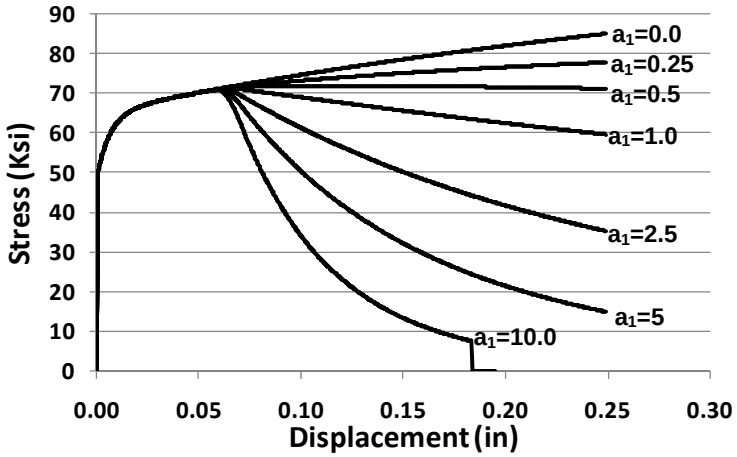

Figure 6.9 Effect of parameter a_1

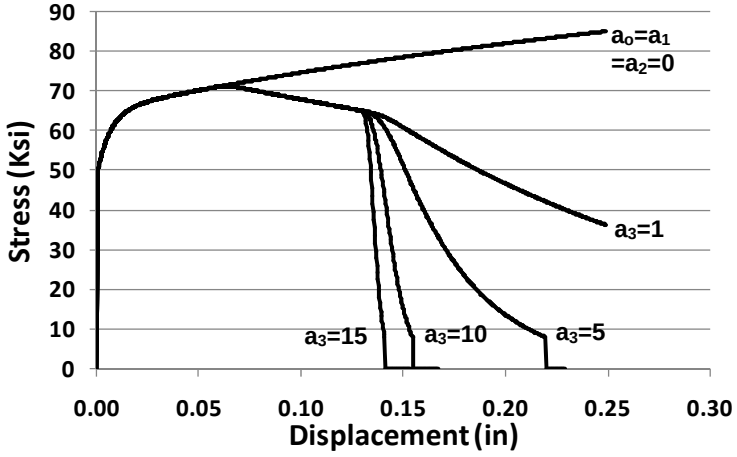

Figure 6.10 Effect of parameter a_3

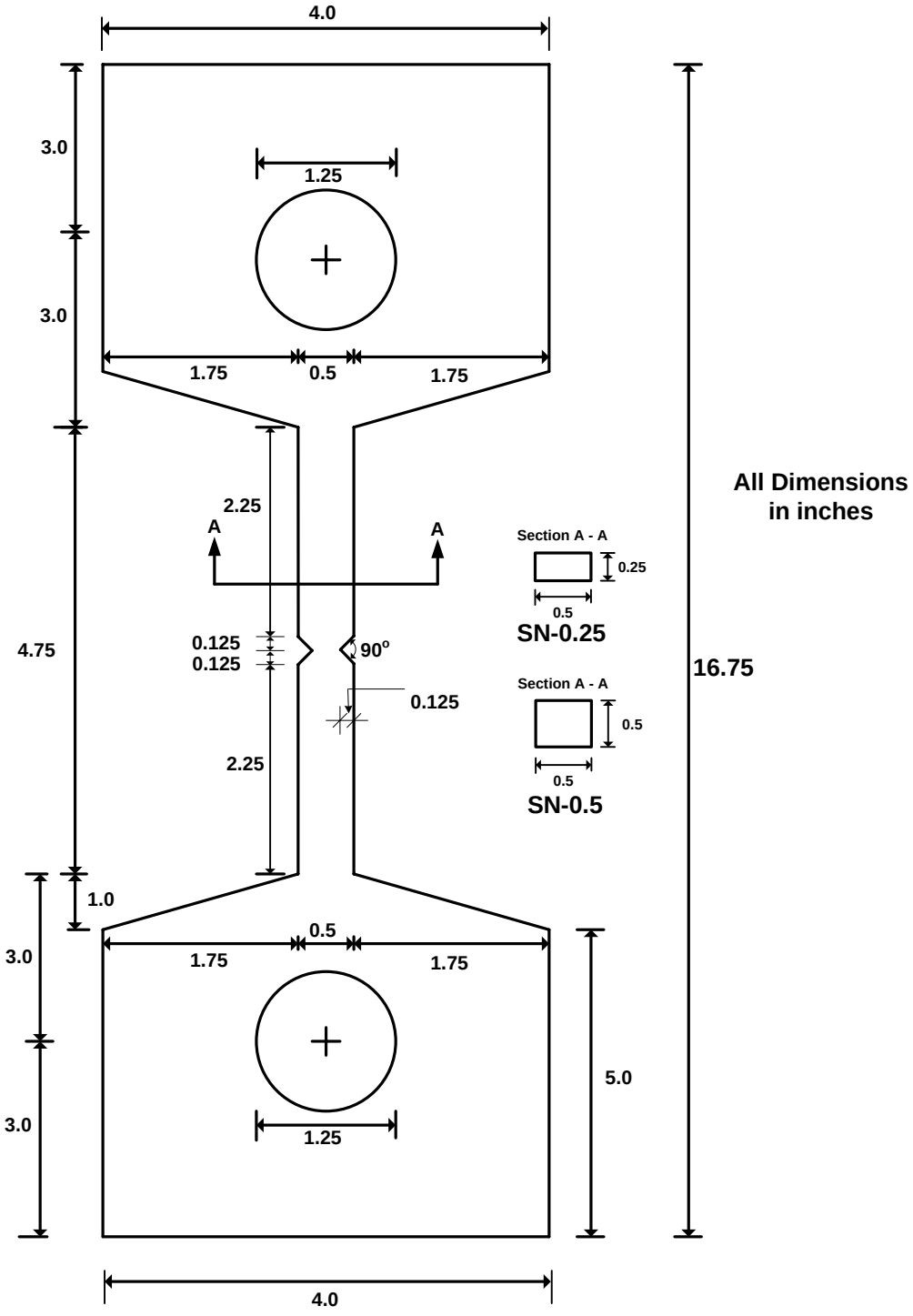

Figure 6.11 Geometry of specimen with symmetric notch

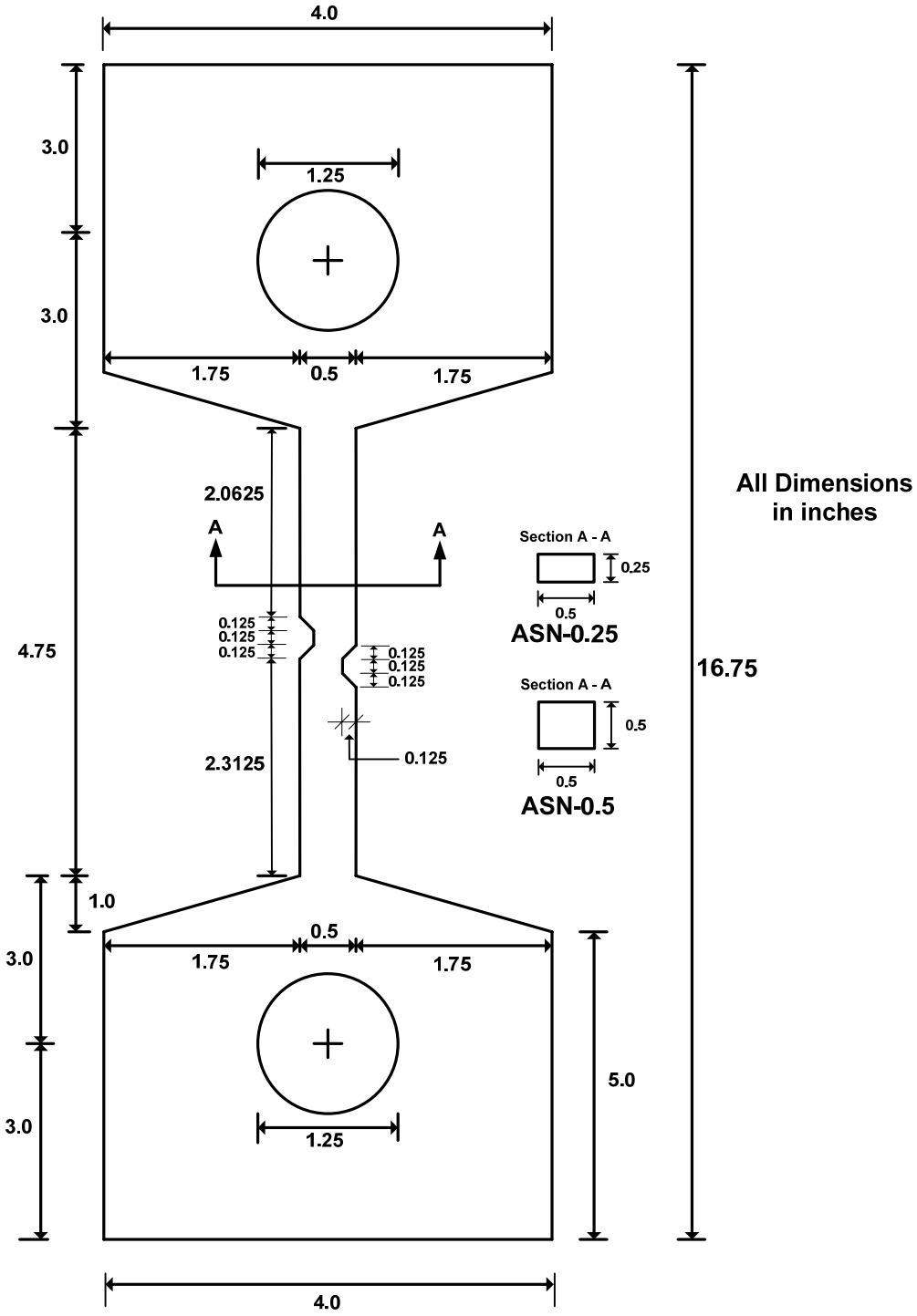

Figure 6.12 Geometry of specimen with asymmetric notch

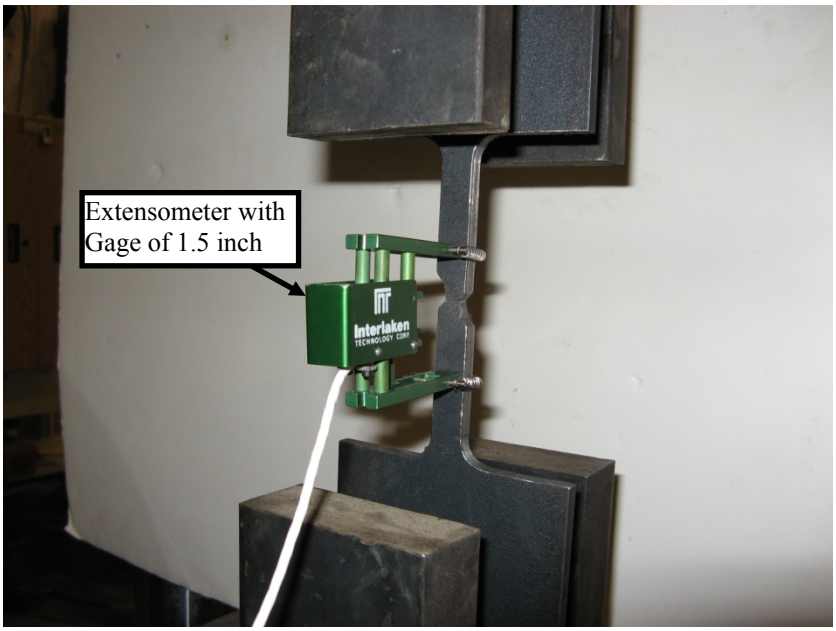

Figure 6.13 Photo of the test setup

Figure 6.14 Specimen fractured after the test

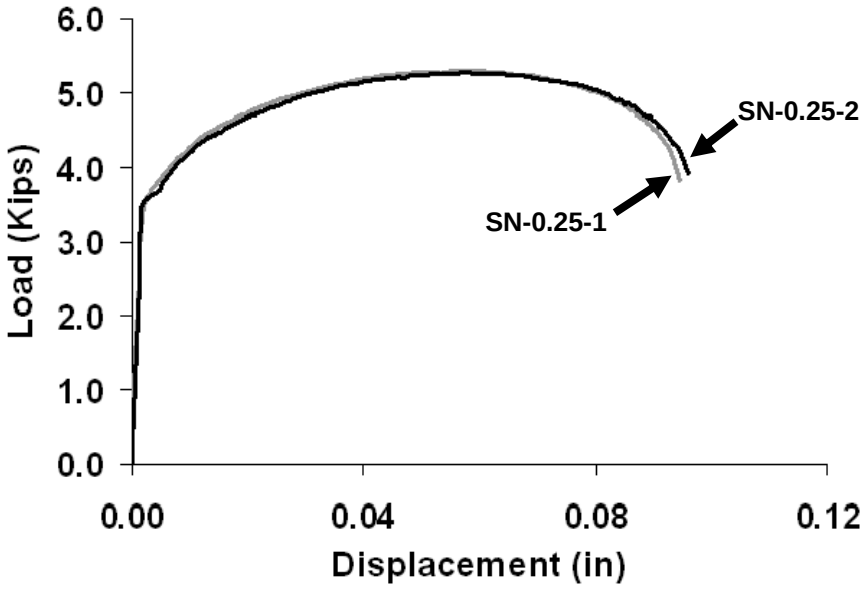

Figure 6.15 Load displacement curve for specimens SN-0.25

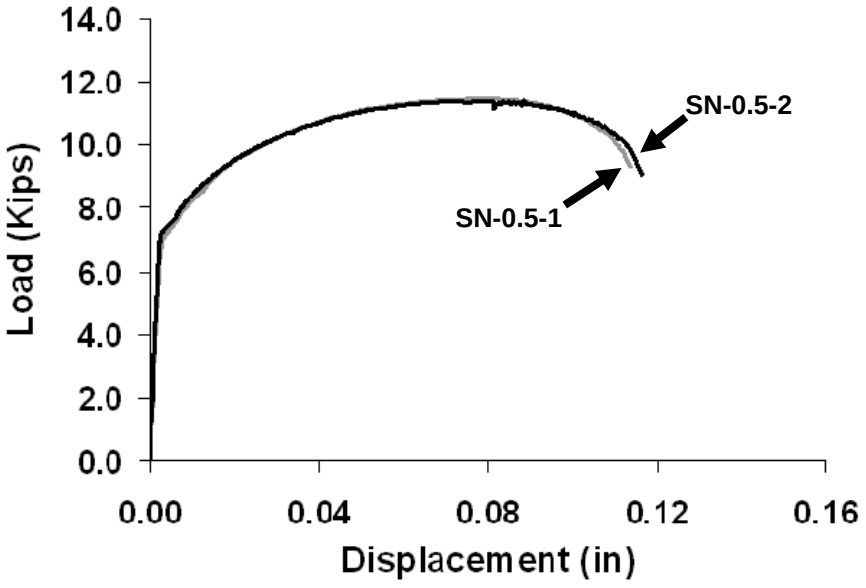

Figure 6.16 Load displacement curve for specimens SN-0.5

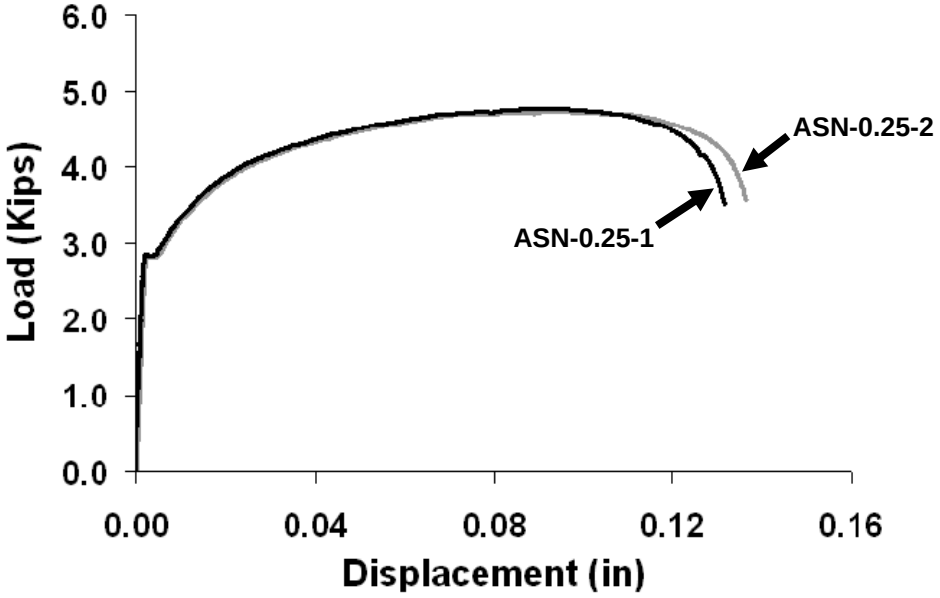

Figure 6.17 Load displacement curve for specimens ASN-0.25

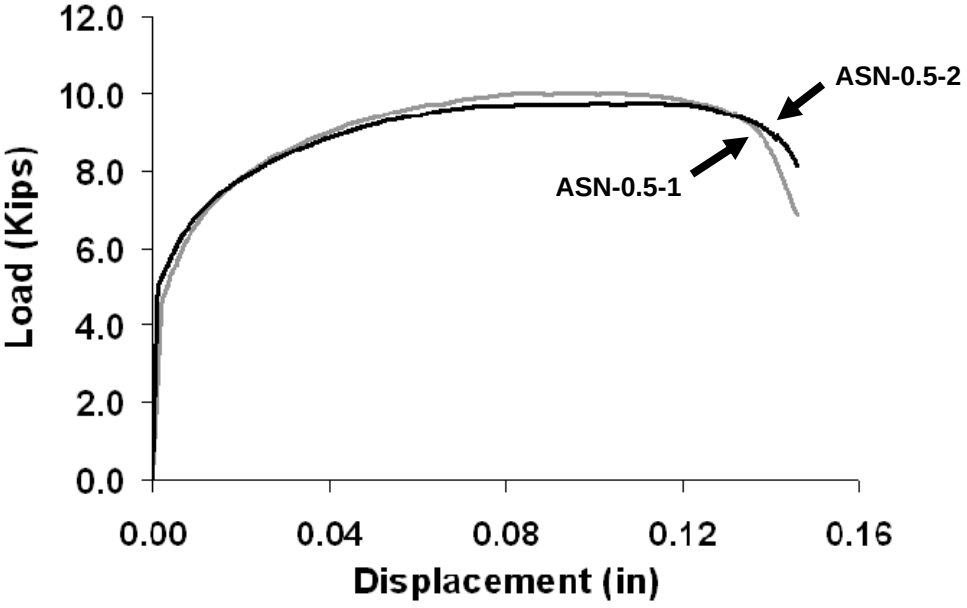

Figure 6.18 Load displacement curve for specimens ASN-0.5

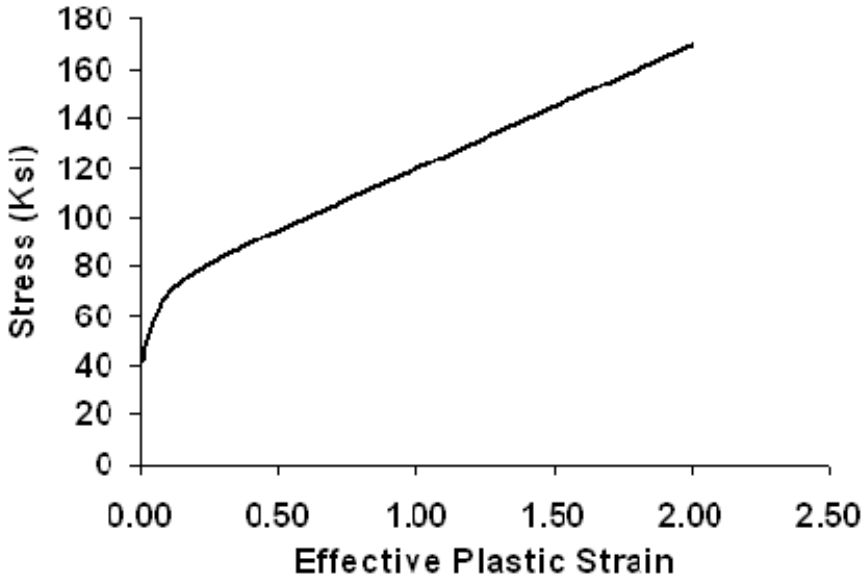

Figure 6.19 Hardening curve for steel

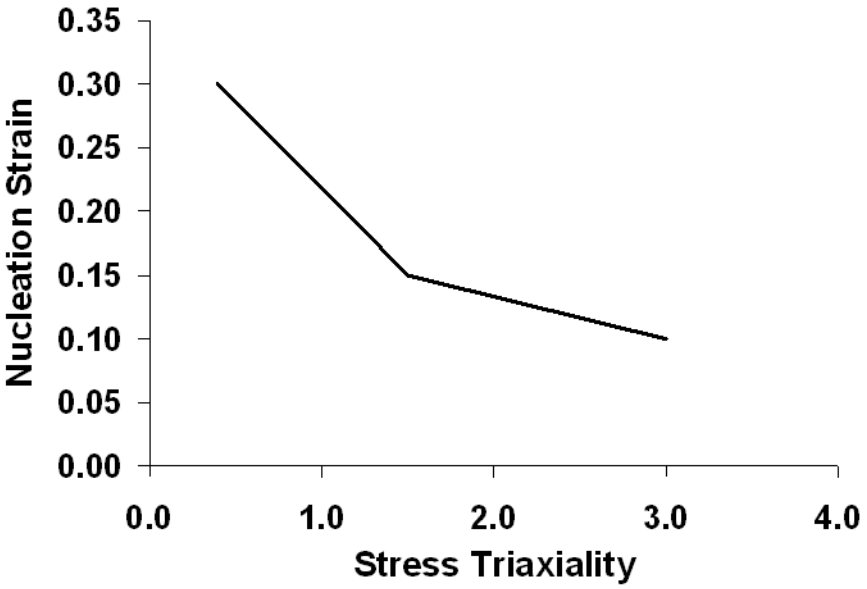

Figure 6.20 Nucleation strain vs stress triaxiality

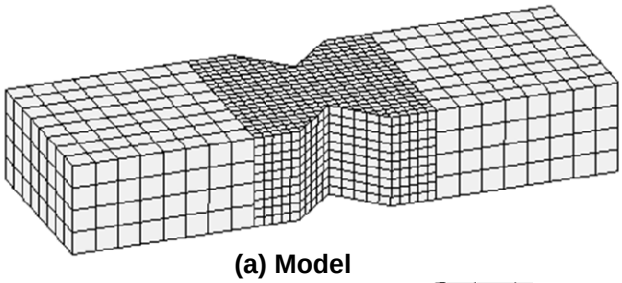

(a) Model

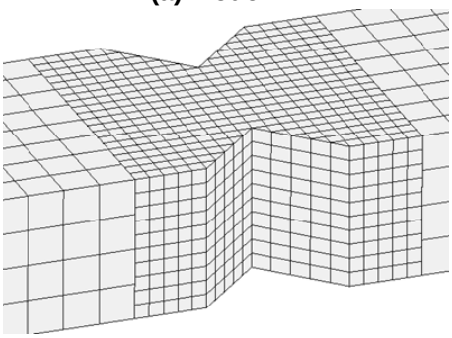

(b) Mesh in notch region

Figure 6.21 Finite element model for specimen SN-0.25

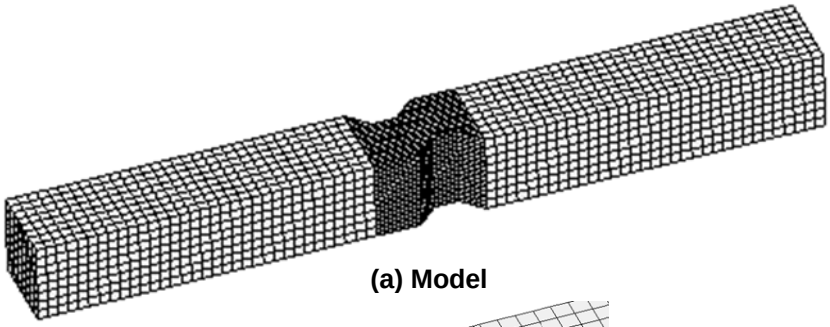

(a) Model

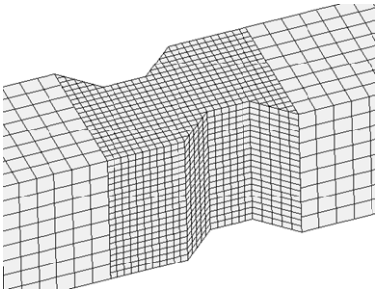

(b) Mesh in notch region

Figure 6.22 Finite element model for specimen ASN-0.5

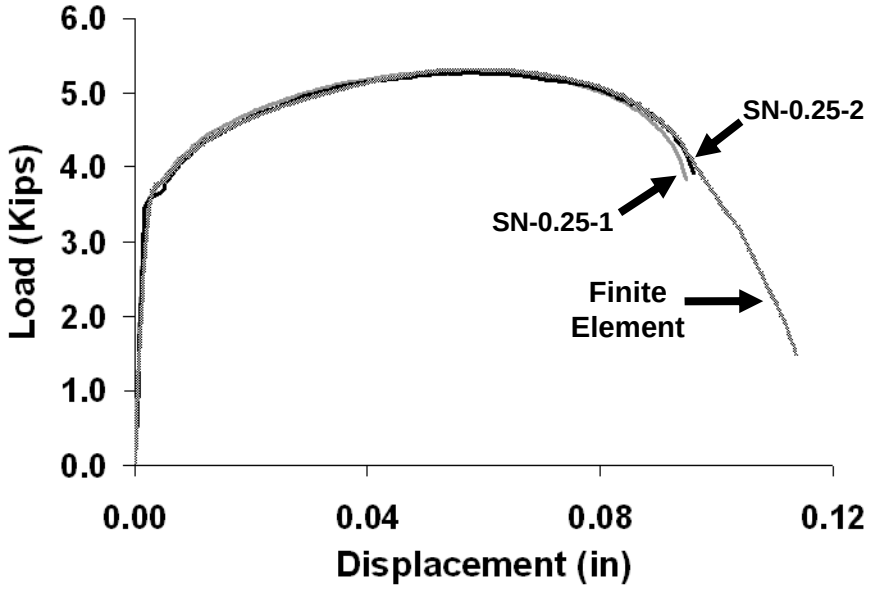

Figure 6.23 Comparison of simulation and experimental results (SN-0.25)

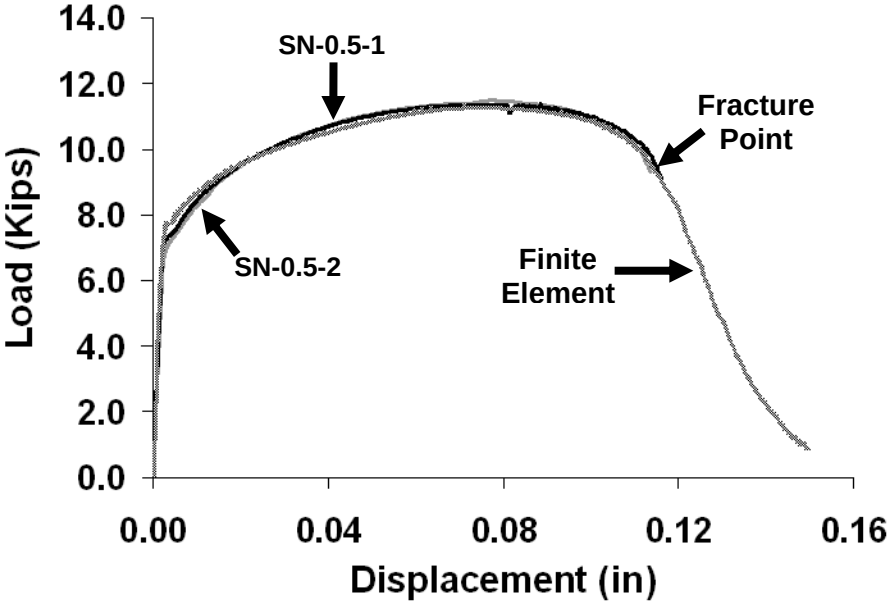

Figure 6.24 Comparison of simulation and experimental results (SN-0.5)

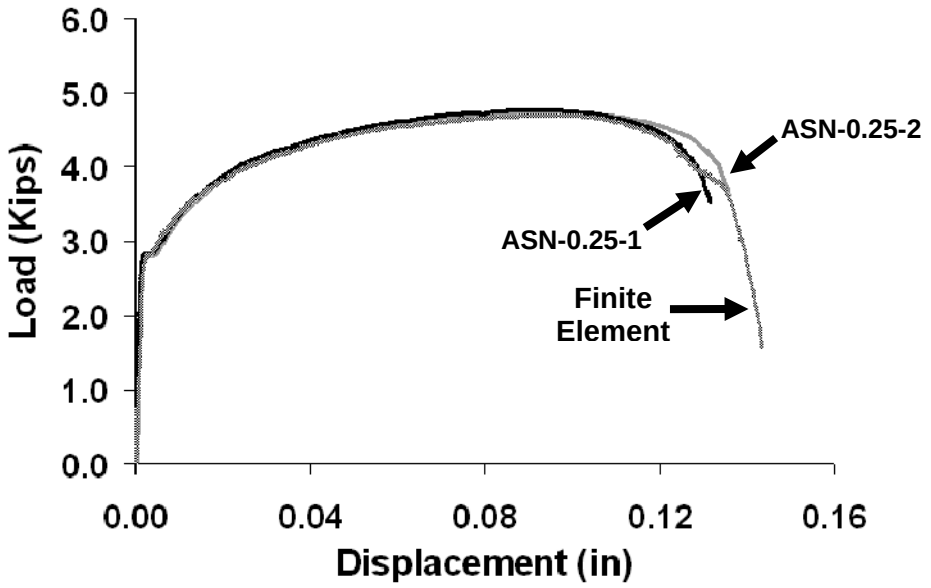

Figure 6.25 Comparison of simulation and experimental results (ASN-0.25)

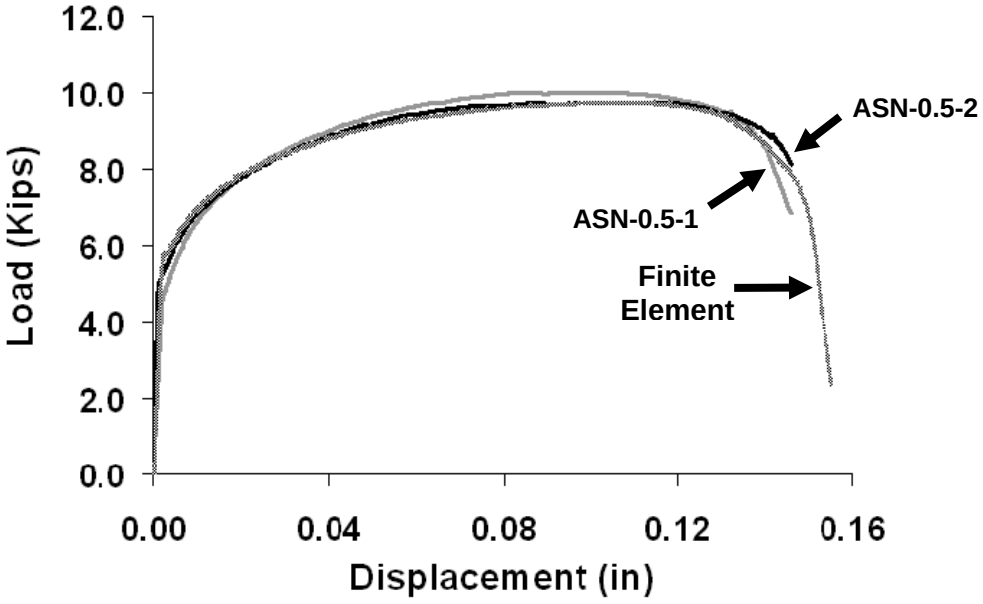

Figure 6.26 Comparison of simulation and experimental results (ASN-0.5)

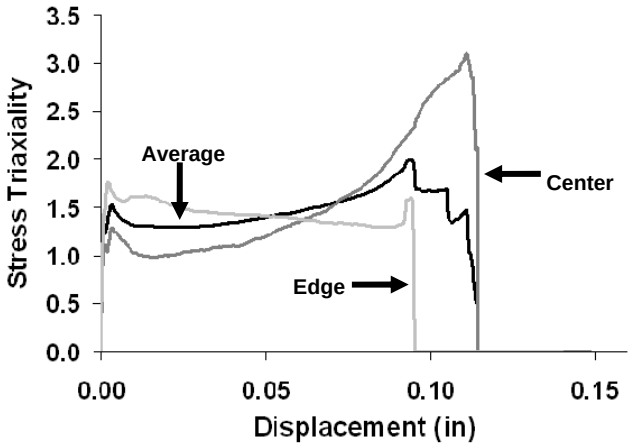

Figure 6.27 Variation of stress triaxiality (SN-0.25)

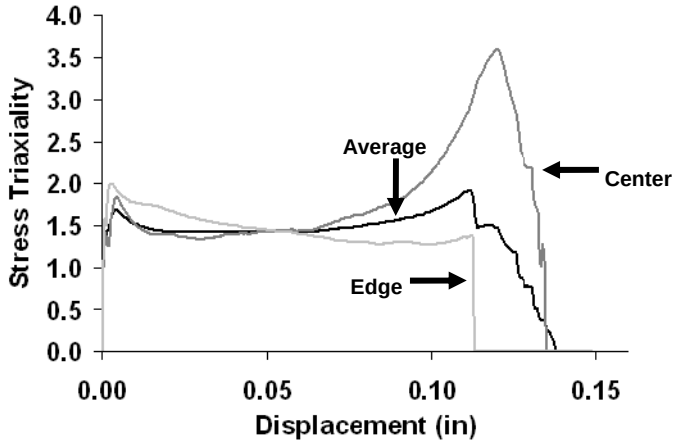

Figure 6.28 Variation of stress triaxiality (SN-0.5)

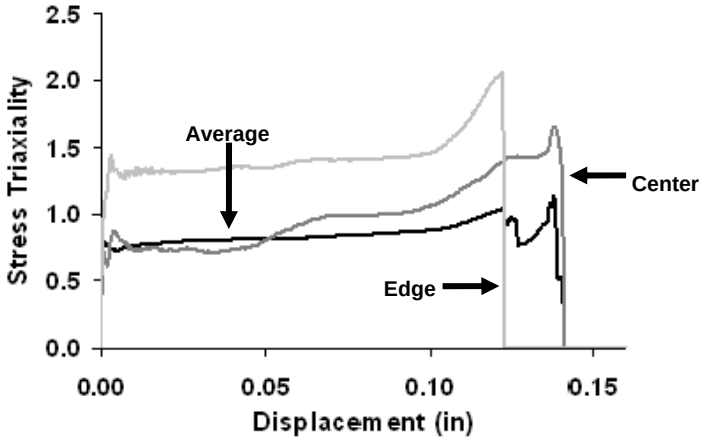

Figure 6.29 Variation of stress triaxiality (ASN-0.25)

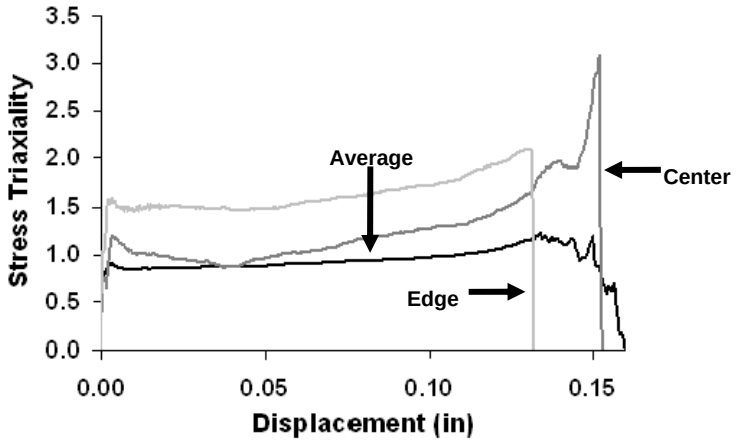

Figure 6.30 Variation of stress triaxiality (ASN-0.5)

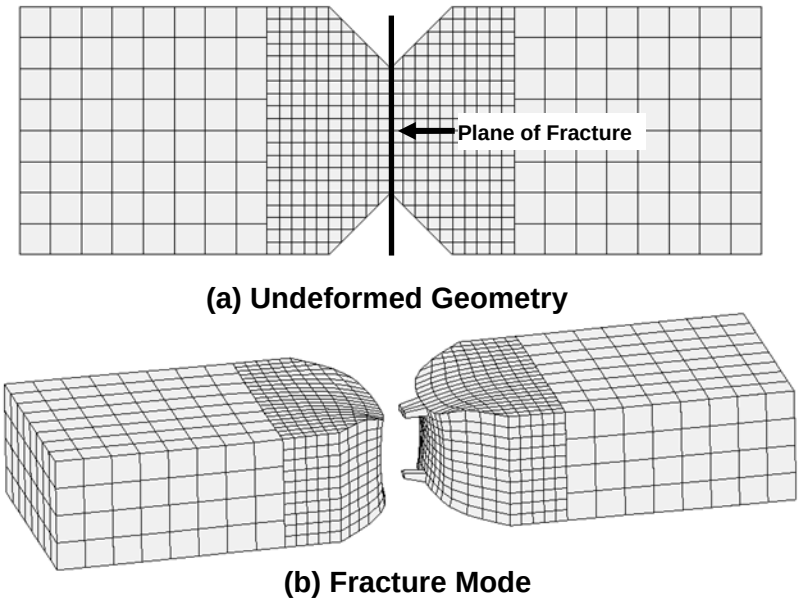

Figure 6.31 Fracture mode in symmetric notches

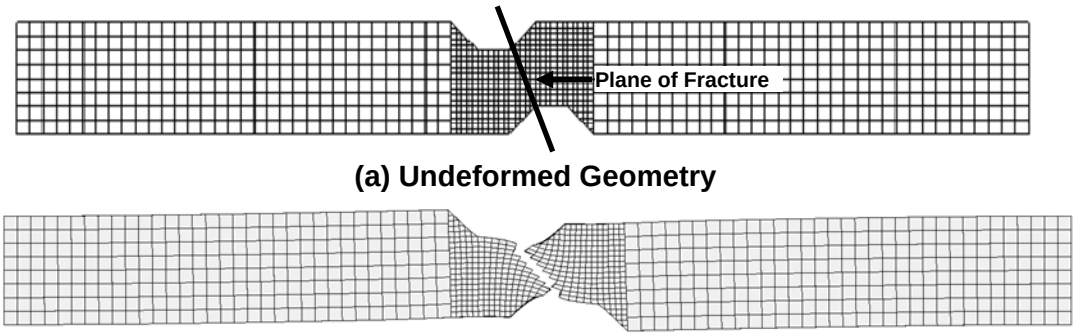

(a) Undeformed Geometry

(b) Fracture Mode

Figure 6.32 Fracture mode in asymmetric notches

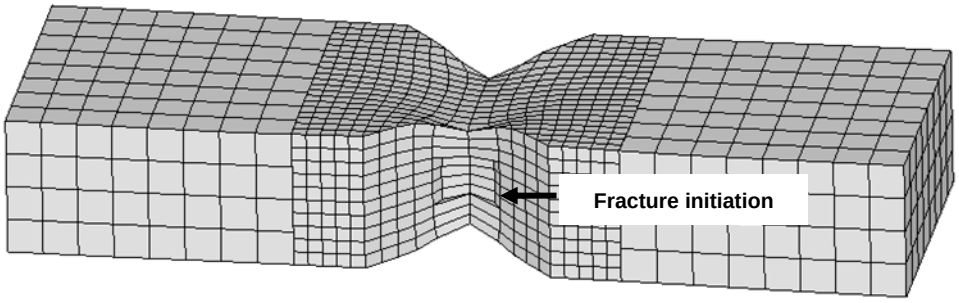

(a) SN-0.25

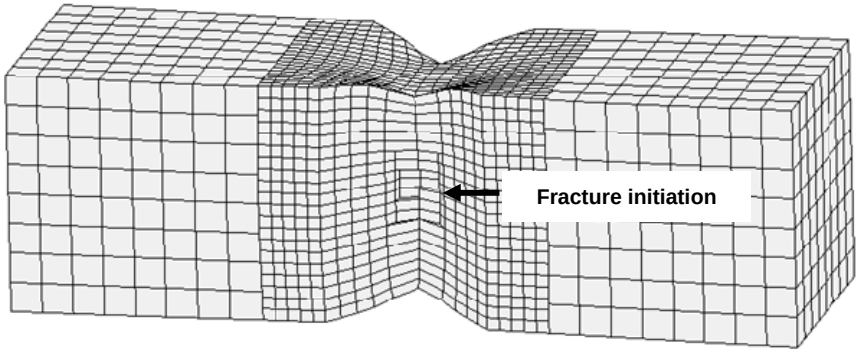

(b) SN-0.5

Figure 6.33 Location of fracture initiation (SN)

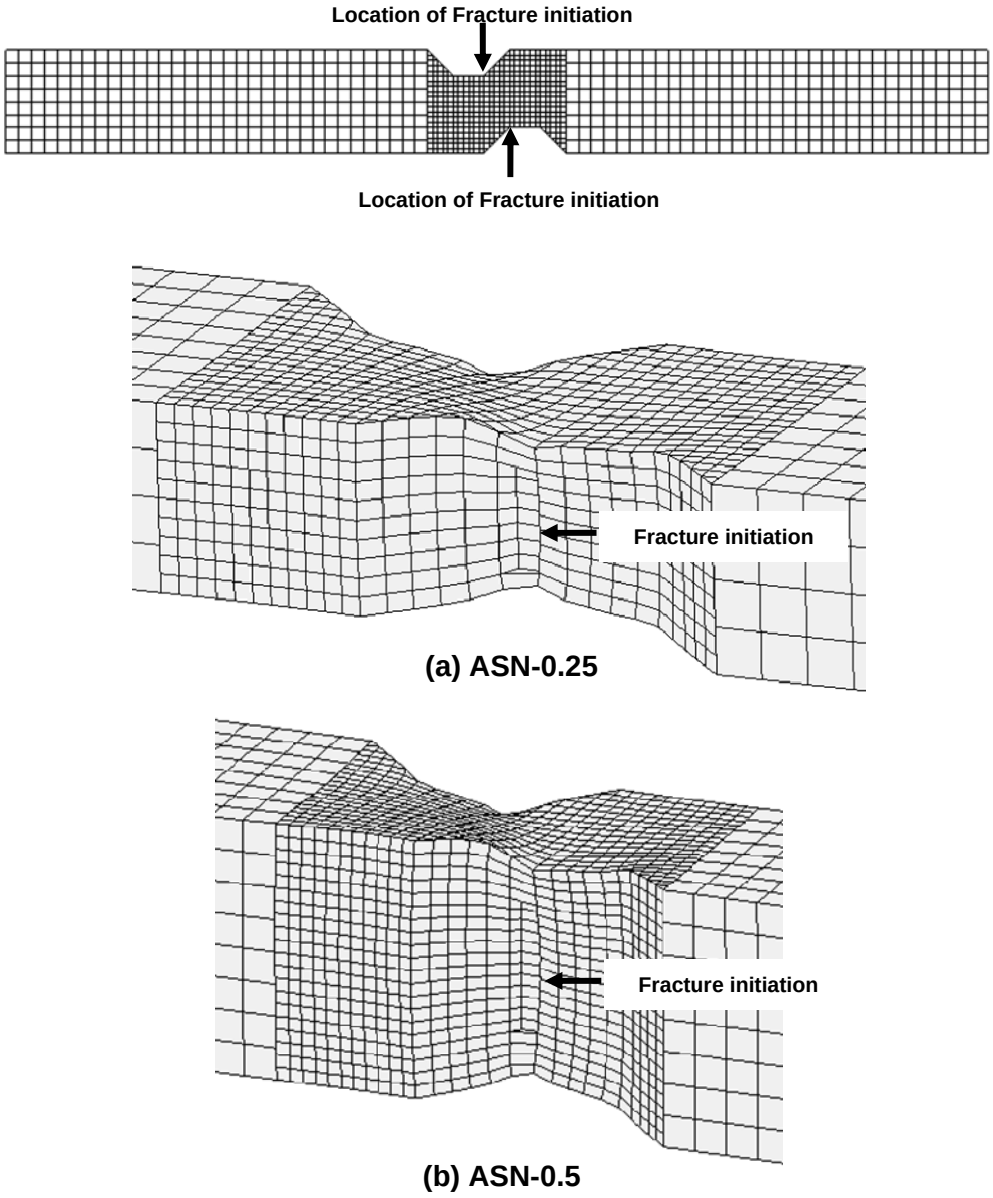

Figure 6.34 Location of fracture initiation (ASN)

CHAPTER 7

SUMMARY AND CONCLUSIONS

7.1 Summary

This dissertation focused on the progressive collapse response of seismically designed steel frames. It dealt with a variety of critical issues that influence the collapse of steel structures within a multi-scale computational framework. The dissertation starts with a discussion of past studies related to progressive collapse of structural systems. Current design requirements and the mechanisms of ductile fracture processes in steels together with the available methods for simulation of these processes were also reviewed. In particular, models based on quantum mechanics, molecular dynamics, continuum mechanics and multi-scale methods for linking models at various scales were discussed.

In the first phase of the study, finite element computational simulation was used to investigate the collapse behavior of moment resisting steel frame sub-assemblages. An existing micro-mechanical constitutive model for porous plastic materials was calibrated using available test data and employed for simulation of micro through structural-scale behavior of the sub-assemblages. Termed coupled multi-scale simulation, this approach ties micro-structural changes that occur during the ductile fracture process, such as micro-void nucleation, growth and coalescence, to macro-scale response via the micro-mechanical constitutive model. A history-like variable in the constitutive model, known as void volume fraction, took into account the disintegration of material at the micro-scale due to nucleation, growth and coalescence of voids. The micromechanical model

was calibrated to experimental results available in literature. Finite element mesh sensitivity studies were then conducted and the simulation model was used to investigate the catenary behavior of a number of steel subassemblies taken from a seismically designed special moment frame. Important parameters that influence behavior were identified and studied. In particular, the effect of out-of-plane pulling action imposed by a transverse beam, yield stress to ultimate strength ratio (YUSR), heat effected zone (HAZ) and web connection details such as shear tab thickness were investigated.

Computationally efficient structural-scale models, which can be used for progressive collapse analysis of steel moment and braced frames systems using nonlinear dynamic APM, were also proposed in this dissertation. The developed structural scale models used a combination of beam-column finite elements and nonlinear spring elements to represent important physical processes of interest at the structural scale. Micro-scale behavior, such as fracture, and macro-scale behavior such as local buckling was also taken into accounted by using appropriate constitutive material properties. The developed models fall in the category of uncoupled multi-scale models, wherein the structural scale models are calibrated to represent micro and macro scale processes. Using the developed structural scale models, models for three popular connections types: reduced beam sections for special moment frames (SMF), welded unreinforced flange - welded web moment resisting connections for intermediate moment frames (IMF) and shear connections, were proposed in this work. In addition, models for braces and shear links were also proposed for special concentrically braced frames (SCBF) and eccentrically braced frames (EBF). A brief overview of nonlinear beam elements together with numerical implementation of the J_2 plasticity model employed in this research was presented. The proposed structural scale models were calibrated and validated and then utilized within the context of APM to study the progressive collapse resistance of 2-dimensional, 10-story SMF, IMF, SCBF and EBF buildings designed according to contemporary seismic design specifications and practices.

A new analysis technique was proposed in this dissertation that can be used to determine the failure load and collapse mechanism of a damaged structure. The proposed technique

was termed “pushdown analysis” and it parallels the pushover method commonly used for assessing the seismic resistance of building structures. The new method was used to examine the robustness of structural systems. In particular, the residual capacity and collapse modes of 2-dimensional, 10 story SMF, IMF, SCBF and EBF frames were investigated.

Motivated by a number of deficiencies in existing fracture models for steel, a new micro-mechanical constitutive model which can be used for simulation of ductile fracture in steel was also proposed. The proposed model employed a scalar damage variable to represents the changes that arise due to micro-structural evolution during the ductile fracture process in structural steels. In particular, the three stages of ductile fracture initiation: micro-void nucleation, growth and coalescence were modeled by prescribing appropriate evolution functions for the damage variable. The model belongs to the class of coupled multi-scale models, wherein the response at macro-scale is directly coupled to the micro-structural evolution via a constitutive material model. The proposed constitutive model was implemented within a finite deformation framework using effective stress and strain equivalence principles. Numerical implementation of the proposed model was also presented and parametric studies were conducted to investigate the effect of various model parameters on the material response. The model was calibrated and validated by comparing its response to the results obtained from experimental testing of symmetrically and asymmetrically notched steel specimens.

7.2 Conclusions

The following conclusions can be drawn from the limited analytical, computational and experimental studies conducted in this dissertation:

1) From the simulation results of steel sub-assemblages it can be concluded that seismically designed special moment frame assemblies are ductile enough to permit catenary mode to fully develop. Simulation results also established that the out-of-plane pulling action induced by transverse beams has no adverse effect on system behavior, but

that ductility and strength were adversely influenced by an increase in beam depth and an increase in the yield to ultimate strength ratio. It can also be concluded that subassemblies with reduced beam sections are stronger and more ductile than corresponding subassemblies without RBS. Furthermore, the heat affected zone in beam flanges did not have a significant deleterious influence on system behavior while an increase in shear tab strength shifted the location of ductile fracture resulting in better overall system behavior.

2) Nonlinear dynamic analysis using APM of seismically designed structural systems show that the SMF designed for high seismic risk is less vulnerable to gravity-induced progressive collapse than the IMF designed for moderate seismic risk. The relative success of SMF versus IMF stems from improved layout that consists of more as well as generally stronger moment bays.

3) The results further showed that ductility demands associated with column loss in the moment bays of IMF and SMF buildings systems considered in this work are rather small and therefore the advantage of using ductile seismic detailing for mitigating progressive collapse is not evident.

4) APM also suggest that while SCBF and EBF systems benefited from locating the seismic systems on the perimeter of the buildings, the EBF designed for high seismic risk is less vulnerable to gravity-induced progressive collapse than the SCBF designed for moderate seismic risk. The relative success of EBF versus SCBF stems essentially from an improved system layout rather than mobilization of ductile detailing.

5) The proposed pushdown analysis method can be used for estimating the residual capacity and collapse modes of a damaged structure. Of the three techniques investigated, incremental dynamic pushdown gives a best estimate of residual capacity and collapse modes.

6) The proposed pushdown analysis method can be used to study the robustness of structural systems and to design structural systems that are more resistant to collapse. Simulation results shows that SMF and EBF frames are more robust than the IMF and SCBF systems respectively. The results also show that failure associated with beams is a preferable failure mode when compared to column failure.

7) The proposed micromechanical model can be used for simulation of ductile fracture in steel. Parametric study shows that a variety of responses needed to represent the physical process of interest can be obtained by choosing appropriate model parameters. Comparisons with the experimental results show that the proposed model is able to represent damage under a variety of stress states.

7.3 Practical Implications

Following are important conclusions with practical implications that can be drawn from the studies conducted in this dissertation:

1) As indicated in Section 7.2, the simulation studies of steel sub-assemblages shows that the out-of-plane pulling action imposed by a transverse beam does not significantly influence sub-assemblage structural behavior. This results suggest that it is conservative to conduct simulations and tests that do not model the out-of-plane pulling effect, which considerably simplifies testing and analysis. Another observation is that system ductility is adversely influenced by an increase in beam depth and an increase in the yield to ultimate strength ratio. This implies that designers should strive to use a larger number of smaller beam members rather than concentrate resistance in a few larger members, which is common practice in earthquake-resistant construction. In addition, designers should specify ASTM A-992 steel (which has a specified maximum YUSR of 0.85) for collapse resistant construction rather than specifying generic steels which could have a detrimentally high YUSR. The simulation results further suggest that improving the beam web connection by either increasing the shear tab thickness or directly welding the beam web to the column can better protect the beam-column interface by shifting ductile

fracture initiation to the reduced flange region thereby making the connection stronger and more ductile.

2) The APM frame studies show that shear tab connections, which are used in gravity bays, have the necessary ductility to develop catenary action. However, for the system designs considered herein, they do not have the strength to resist progressive collapse once a gravity column is lost. If such columns are necessary, structural designers should carefully evaluate collapse resistance of perimeter gravity bays through refined analysis models or detailed simulations methods of the sort proposed here.

3) Pushdown analysis shows that it is desirable to have failures in beams rather than in columns. The column failure mode is undesirable as it is more catastrophic since it undermines the stability of the entire structural system. Thus, designers should strive to use stronger columns to facilitate a more benign collapse mode that limits the extent of damage in the system and reduces the risk of total collapse.

7.4 Recommendations for Future Research

The following research topics are recommended for further research to better understand the progressive collapse behavior of structural systems:

1) Collapse studies of moment sub-assemblages with welded web connections were considered in this study. Research is needed to study collapse behavior of sub-assemblages with other types of moment connections such as flange plate bolted/welded moment connections, extended end-plate moment connections, etc.

2) Collapse behavior of only seismically designed 2-D steel frames was investigated in this research. Research is needed to study the progressive collapse behavior of gravity systems in a 3-D framework where slabs can play an important role in providing resistance to collapse.

3) Further research is also needed to study the collapse behavior of different shear connections in gravity systems prone to collapse, such as double angle connections, stiffened/unstiffened seated connections. These connections are frequently used in beam to column connections in gravity systems.

4) A micro-mechanical model for ductile fracture initiation in steels was developed in this dissertation. After the crack starts it can propagate in either a ductile manner or in a brittle manner, i.e. sometimes the propagation mode switches from ductile to brittle fracture mode, where the brittle mode is associated with cleavage or intergranular fracture. Conditions under which such ductile to brittle transitions occur are not well understood. Therefore, further research is needed to address the issue of ductile fracture to cleavage fracture or inter-granular fracture transitions.

5) A micromechanical model proposed in this study is intended for monotonic loading only. Steel structures may also be subjected to cyclic loading, for example, during earthquakes. However, there is a limited understanding of ductile fracture process under cyclic loading conditions and high fidelity constitutive models for simulating fracture under cyclic loading are not available. Further research is needed to develop constitutive models for simulating ductile fracture process under cyclic loading conditions.

6) The model parameters for the proposed micro-mechanical model are mesh dependent and are calibrated to a particular mesh size. Further research is needed to regularize the model by incorporating a length scale in the model. Regularization methods such as nonlocal theories, gradient plasticity theories and other related methods can be exploited for this purpose.

APPENDICES

APPENDIX A

A.1 Introduction

In this appendix chapter an introduction to geometric concepts related to continuum mechanics concepts is presented in a differential manifold framework. This framework is adopted from the work done by Giessen & Koffmann (1996). The salient features of this framework are that the importance of dual variables is emphasized, and a distinction between inner product and scalar product is made.

A.2 Theoretical Aspects

A.2.1 Body

A continuum body B with configuration $\mathfrak{B}$ is considered as a 3-dimensional differentiable manifold. Let $U \subset \mathfrak{B}$ be an open set. A coordinate system, $\boldsymbol{\Psi}$, on $\mathfrak{B}$, is a one-to-one mapping between the point's $P \in U$ and the points in an open subset of $\mathbb{R}^3$ i.e. $\boldsymbol{\Psi}$: $U \longrightarrow \mathbb{R}^3$.

A.2.2 Tangent and Cotangent Spaces

The covariant basis vectors $\boldsymbol{G}_i (i = 1,2,3)$ on $\mathfrak{B}$ are defined as:

$$\boldsymbol{G}_i \stackrel{\text{def}}{=} \frac{\partial P}{\partial \Psi^i}, \quad i = 1,2,3 \quad \forall\, P \in U \tag{A.1}$$

Definition A.1: The tangent space $T_P\mathfrak{B}$ at a point $P \in \mathfrak{B}$ is the linear vector space of all vectors $\boldsymbol{V} \in \mathbb{R}^3$, such that

$$\boldsymbol{V} = V^i \boldsymbol{G}_i, \; V^i \in \mathbb{R}, \text{ emanating at point } P \in \mathfrak{B} \tag{A.2}$$

Definition A.2: A vector field $\boldsymbol{V}(P)$ on the manifold $\mathfrak{B}$ is the map

$$\boldsymbol{V}(P): \mathfrak{B} \to T_P\mathfrak{B} \quad \forall\, P \in \mathfrak{B} \tag{A.3}$$

Definition A.3: The cotangent space $T_P^*\mathfrak{B}$ at a point $P \in \mathfrak{B}$ is the linear vector space $\mathcal{L}(T_P\mathfrak{B}, \mathbb{R})$ of all linear maps $\boldsymbol{\alpha}$: $T_P\mathfrak{B} \to \mathbb{R}$ emanating at $P \in \mathfrak{B}$, i.e.

$$T_P^*\mathfrak{B} = \mathcal{L}(T_P\mathfrak{B}, \mathbb{R}) \tag{A.4}$$

Remark A.1: Tangent and cotangent spaces are dual spaces. The elements of the tangent space are called vectors while those of cotangent space are called one-forms or covectors.

A.2.3 Scalar Product

A scalar product is a bilinear mapping, $\langle \cdot\,,\ \cdot \rangle_P: T_P^*\mathfrak{B} \times T_P\mathfrak{B} \to \mathbb{R}$ such that

$$\begin{gathered} \langle \boldsymbol{\alpha}, \boldsymbol{V} \rangle_P: T_P^*\mathfrak{B} \times T_P\mathfrak{B} \to \mathbb{R}, \quad \boldsymbol{\alpha} \in T_P^*\mathfrak{B} \; and \; \boldsymbol{V} \in T_P\mathfrak{B} \\ \langle \boldsymbol{\alpha}, \boldsymbol{V} \rangle_P \overset{\text{def}}{=} \boldsymbol{\alpha}(\boldsymbol{V}) \end{gathered} \tag{A.5}$$

Remark A.2: The dual of the cotangent space $T_P^*\mathfrak{B}$ is identical (isomorphic) to tangent space $T_P\mathfrak{B}$. Therefore, a vector $\boldsymbol{V} \in T_P\mathfrak{B}$ can be considered as a linear function on $T_P^*\mathfrak{B}$, thus scalar product acts as a symmetric bilinear form, i.e. $\langle \boldsymbol{\alpha}, \boldsymbol{V} \rangle_P = \langle \boldsymbol{V}, \boldsymbol{\alpha} \rangle_P$. The basis of the cotangent space $T_P^*\mathfrak{B}$ is known as dual basis and is denoted by $\boldsymbol{G}^i$, i $= 1,2,3$. The dual basis is given by the requirement:

$$\langle \boldsymbol{G}^i, \boldsymbol{G}_j \rangle_P = \delta_j^i \tag{A.6}$$

where δ_j^i is the Kronecker symbol.

For one-form $\boldsymbol{\alpha} \in T_P^*\mathfrak{B}$ the following representation in terms of basis vectors can be obtained:

$$\boldsymbol{\alpha} = \alpha_i \boldsymbol{G}^i \tag{A.7}$$

Therefore, in component form the inner-product is given by:

$$\langle \boldsymbol{\alpha}, \boldsymbol{V} \rangle_P = \langle \alpha_i \boldsymbol{G}^i, V^j \boldsymbol{G}_j \rangle_P = \alpha_i V^i \tag{A.8}$$

A.2.4 Tensors

Definition A.4: Tensors are defined as multi-linear mappings on product spaces of tangent and/or cotangent spaces, for example a second order tensors can be defined as follows:

$$\begin{aligned} \boldsymbol{T}^{\backslash}&: T_P^*\mathfrak{B} \times T_P\mathfrak{B} \to \mathbb{R} \\ \boldsymbol{T}^{/}&: T_P\mathfrak{B} \times T_P^*\mathfrak{B} \to \mathbb{R} \\ \boldsymbol{T}^{b}&: T_P\mathfrak{B} \times T_P\mathfrak{B} \to \mathbb{R} \\ \boldsymbol{T}^{\#}&: T_P^*\mathfrak{B} \times T_P^*\mathfrak{B} \to \mathbb{R} \end{aligned} \tag{A.9}$$

In component form, for example:

$$\begin{gathered} \boldsymbol{T}^{\backslash}(\boldsymbol{\alpha}, \boldsymbol{V}) = \boldsymbol{T}^{\backslash}\left(\alpha_i \boldsymbol{G}^i, V^j \boldsymbol{G}_j\right) = \alpha_i V^j \boldsymbol{T}^{\backslash}\left(\boldsymbol{G}^i, \boldsymbol{G}_j\right) = \alpha_i V^j T_{\cdot j}^{i \cdot} \\ \text{where } T_{\cdot j}^{i \cdot} \stackrel{\text{def}}{=} \boldsymbol{T}^{\backslash}\left(\boldsymbol{G}^i, \boldsymbol{G}_j\right) \end{gathered} \tag{A.10}$$

Similarly, for other 2nd order tensors:

$$\begin{aligned} \boldsymbol{T}^{/}(\boldsymbol{V}, \boldsymbol{\alpha}) &= V^i \alpha_j T_{i \cdot}^{\cdot j} \text{ and } T_{i \cdot}^{\cdot j} \stackrel{\text{def}}{=} \boldsymbol{T}^{/}\left(\boldsymbol{G}_i, \boldsymbol{G}^j\right) \\ \boldsymbol{T}^{b}(\boldsymbol{U}, \boldsymbol{V}) &= U^i V^j T_{ij} \text{ and } T_{ij} \stackrel{\text{def}}{=} \boldsymbol{T}^{b}\left(\boldsymbol{G}_i, \boldsymbol{G}_j\right) \\ \boldsymbol{T}^{\#}(\boldsymbol{\alpha}, \boldsymbol{\beta}) &= \alpha_i \beta_j T^{ij} \text{ and } T^{ij} \stackrel{\text{def}}{=} \boldsymbol{T}^{\#}\left(\boldsymbol{G}^i, \boldsymbol{G}^j\right) \end{aligned} \tag{A.11}$$

The symbols \ (mixed tensor), / (mixed tensor), b (covariant tensor) and # (contravariant tensor) indicates the position of spaces $T_P\mathfrak{B}$ and $T_P^*\mathfrak{B}$. The space of all the multi-linear mappings on product spaces themselves forms linear vector spaces. For example, 2nd order tensors belong to the linear spaces as follows:

$$\begin{aligned} \boldsymbol{T}^{\backslash} \in \mathcal{S}_{\cdot 1}^{1 \cdot} &= \mathcal{L}(T_P^*\mathfrak{B}, T_P\mathfrak{B}, \mathbb{R}) \\ \boldsymbol{T}^{/} \in \mathcal{S}_{1 \cdot}^{\cdot 1} &= \mathcal{L}(T_P\mathfrak{B}, T_P^*\mathfrak{B}, \mathbb{R}) \\ \boldsymbol{T}^{b} \in \mathcal{S}_{2}^{0} &= \mathcal{L}(T_P\mathfrak{B}, T_P\mathfrak{B}, \mathbb{R}) \\ \boldsymbol{T}^{\#} \in \mathcal{S}_{0}^{2} &= \mathcal{L}(T_P^*\mathfrak{B}, T_P^*\mathfrak{B}, \mathbb{R}) \end{aligned} \tag{A.12}$$

Similarly, higher order tensors and tensor-spaces can be defined.

Remark A.3: Vectors and one-forms can be considered as tensors on spaces $\mathcal{S}_0^1 = \mathcal{L}(T_P^*\mathfrak{B}, \mathbb{R})$ and $\mathcal{S}_1^0 = \mathcal{L}(T_P\mathfrak{B}, \mathbb{R})$ respectively.

Definition A.5: A second order tensor field on the manifold $\mathfrak{B}$ is a map

$$\boldsymbol{T}(P): \mathfrak{B} \to T_P\mathfrak{B} \quad \forall\, P \in \mathfrak{B} \tag{A.13}$$

where $\boldsymbol{T}$ is any 2nd order tensor. Similarly any other tensor field on a manifold can be defined.

Definition A.6: Tensor product, $\boldsymbol{T}_1 \otimes \boldsymbol{T}_2$, of two tensors $\boldsymbol{T}_1$ and $\boldsymbol{T}_2$ is illustrated by an example. Let $\boldsymbol{T}_1 \in \mathcal{S}_2^0$ and $\boldsymbol{T}_2 \in \mathcal{S}_{1\cdot}^{\cdot 1}$

$$\begin{gathered}(\boldsymbol{T}_1 \otimes \boldsymbol{T}_2) \in \mathcal{S}_2^0 \otimes \mathcal{S}_{1\cdot}^{\cdot 1} = \mathcal{S}_{3\cdot}^{\cdot 1} = \mathcal{L}(T_P\mathfrak{B}, T_P\mathfrak{B}, T_P\mathfrak{B}, T_P^*\mathfrak{B}, \mathbb{R}) \text{ and} \\ (\boldsymbol{T}_1 \otimes \boldsymbol{T}_2)(\boldsymbol{U}_1, \boldsymbol{V}_1 | \boldsymbol{U}_2, \boldsymbol{\alpha}^2) \stackrel{\text{def}}{=} \boldsymbol{T}_1(\boldsymbol{U}_1, \boldsymbol{V}_1)\, \boldsymbol{T}_2(\boldsymbol{U}_2, \boldsymbol{\alpha}^2)\end{gathered} \tag{A.14}$$

Remark A.4: Tensor product of tensors is a higher order tensor. For example, second order tensors can also be defined as tensor product of vectors and one-forms as follows:

Let $\boldsymbol{U}, \boldsymbol{V} \in T_P\mathfrak{B}$ and $\boldsymbol{\alpha}, \boldsymbol{\beta} \in T_P^*\mathfrak{B}$, then

$$\begin{aligned}\boldsymbol{U}\otimes\boldsymbol{V} \in \mathcal{S}_0^2 \ni (\boldsymbol{U}\otimes\boldsymbol{V})(\boldsymbol{\alpha}, \boldsymbol{\beta}) &\stackrel{\text{def}}{=} \langle \boldsymbol{U}, \boldsymbol{\alpha}\rangle_p \langle \boldsymbol{V}, \boldsymbol{\beta}\rangle_p \\ \boldsymbol{U}\otimes\boldsymbol{\alpha} \in \mathcal{S}_{1\cdot}^{1\cdot} \ni (\boldsymbol{U}\otimes\boldsymbol{\alpha})(\boldsymbol{\beta}, \boldsymbol{V}) &\stackrel{\text{def}}{=} \langle \boldsymbol{U}, \boldsymbol{\beta}\rangle_p \langle \boldsymbol{\alpha}, \boldsymbol{V}\rangle_p \\ \boldsymbol{\alpha}\otimes\boldsymbol{U} \in \mathcal{S}_{1\cdot}^{\cdot 1} \ni (\boldsymbol{\alpha}\otimes\boldsymbol{U})(\boldsymbol{V}, \boldsymbol{\beta}) &\stackrel{\text{def}}{=} \langle \boldsymbol{\alpha}, \boldsymbol{V}\rangle_p \langle \boldsymbol{U}, \boldsymbol{\beta}\rangle_p \\ \boldsymbol{\alpha}\otimes\boldsymbol{\beta} \in \mathcal{S}_2^0 \ni (\boldsymbol{\alpha}\otimes\boldsymbol{\beta})(\boldsymbol{U}, \boldsymbol{V}) &\stackrel{\text{def}}{=} \langle \boldsymbol{\alpha}, \boldsymbol{U}\rangle_p \langle \boldsymbol{\beta}, \boldsymbol{V}\rangle_p\end{aligned} \tag{A.15}$$

Similarly, higher order tensor products can be defined.

Remark A.5: In terms of tensor products of basis vectors, 2nd order tensors can be represented as follows:

$$\begin{aligned}\text{Mixed: } \boldsymbol{T}^{\backslash} &= T_{\cdot j}^{i\cdot}(\boldsymbol{G}_i \otimes \boldsymbol{G}^j) \\ \text{Mixed: } \boldsymbol{T}^{/} &= T_{i\cdot}^{\cdot j}(\boldsymbol{G}^i \otimes \boldsymbol{G}_j) \\ \text{Covaraint: } \boldsymbol{T}^b &= T_{ij}(\boldsymbol{G}^i \otimes \boldsymbol{G}^j) \\ \text{Contravariant: } \boldsymbol{T}^{\#} &= T^{ij}(\boldsymbol{G}_i \otimes \boldsymbol{G}_j)\end{aligned} \tag{A.16}$$

Remark A.6: Tensors can also be considered as linear maps on appropriate spaces. For example, $\boldsymbol{\alpha}\otimes\boldsymbol{U} \in \mathcal{S}^{1}_{1\cdot}$ and $\boldsymbol{T}^{\backslash} \in \mathcal{S}^{1\cdot}_{1}$ can be defined as linear operators as follows:

$$\begin{gathered}\boldsymbol{\alpha}\otimes\boldsymbol{U}: T_P^*\mathfrak{B} \to T_P^*\mathfrak{B} \ni (\boldsymbol{\alpha}\otimes\boldsymbol{U})\boldsymbol{\beta} \stackrel{\text{def}}{=} \boldsymbol{\alpha}\langle \boldsymbol{U}, \boldsymbol{\beta}\rangle_p \ \forall\ \boldsymbol{\beta} \in T_p^*\mathfrak{B}, \\ \boldsymbol{T}^{\backslash}: T_P\mathfrak{B} \to T_P\mathfrak{B} \ni \boldsymbol{T}^{\backslash}(\boldsymbol{U}) = \boldsymbol{T}^{\backslash}\boldsymbol{U} \stackrel{\text{def}}{=} T^{i\cdot}_{\cdot j}\left(\boldsymbol{G}_i\otimes\boldsymbol{G}^j\right)\left(U^q\boldsymbol{G}_q\right) \\ = T^{i\cdot}_{\cdot j}U^q\boldsymbol{G}_i\langle \boldsymbol{G}^j, \boldsymbol{G}_q\rangle_p = T^{i\cdot}_{\cdot j}U^j\boldsymbol{G}_i\end{gathered} \tag{A.17}$$

Since tensor space is a linear vector space itself, the dual space of tensor space can be defined. For example, the dual of tensor space $\mathcal{L}(T_P^*\mathfrak{B}, T_P\mathfrak{B}, \mathbb{R})$ is the tensor space $\mathcal{L}(T_P\mathfrak{B}, T_P^*\mathfrak{B}, \mathbb{R})$.

Definition A.7: The scalar product of two tensor which live in dual tensor spaces is illustrated by an example as follows:

$$\begin{gathered}\text{Let } \boldsymbol{A}^{\backslash} = A^{i\cdot}_{\cdot j}\boldsymbol{G}_i\otimes\boldsymbol{G}^j \in \mathcal{S}^{1\cdot}_{1} \wedge \boldsymbol{B}^{/} = B^{\cdot q}_{p\cdot}\boldsymbol{G}^p\otimes\boldsymbol{G}_q \in \mathcal{S}^{1}_{1\cdot} \\ \langle \boldsymbol{A}^{\backslash}, \boldsymbol{B}^{/}\rangle_p = \langle \boldsymbol{B}^{\backslash}, \boldsymbol{A}^{/}\rangle_p \stackrel{\text{def}}{=} \langle A^{i\cdot}_{\cdot j}\boldsymbol{G}_i\otimes\boldsymbol{G}^j, B^{\cdot q}_{p\cdot}\boldsymbol{G}^p\otimes\boldsymbol{G}_q\rangle_p \\ = A^{i\cdot}_{\cdot j}B^{\cdot q}_{p\cdot}\langle \boldsymbol{G}_i, \boldsymbol{G}^p\rangle_p\langle \boldsymbol{G}^j, \boldsymbol{G}_q\rangle_p = A^{i\cdot}_{\cdot j}B^{\cdot j}_{i\cdot}\end{gathered} \tag{A.18}$$

Similarly, scalar products of higher order tensors living in the dual tensor spaces can be defined.

Remark A.7: Following is the duality relationships for 2nd order tensor spaces:

$$\begin{gathered}\mathcal{S}^{2}_{0} \overset{Dual}{\Longleftrightarrow} \mathcal{S}^{0}_{2} \\ \mathcal{S}^{1\cdot}_{1} \overset{Dual}{\Longleftrightarrow} \mathcal{S}^{1}_{1\cdot}\end{gathered} \tag{A.19}$$

Remark A.8: If U and V are two vector spaces with duals $U^*$and V^*, respectively. Then the dual, $(U\otimes V)^*$ of vector space $U\otimes V$ is naturally isomorphic to $U^*\otimes V^*$.

Definition A.8: Let $\boldsymbol{T}^{\backslash}, \boldsymbol{T}^{/}, \boldsymbol{T}^{b}$ and $\boldsymbol{T}^{\#}$be second order tensors, then their dual or adjoint are denoted by $\boldsymbol{T}^{\backslash *}, \boldsymbol{T}^{/*}, \boldsymbol{T}^{b*}$ and $\boldsymbol{T}^{\#*}$, respectively and are defined as follows:

$$\begin{gathered}\boldsymbol{T}^{\backslash *}: T_P^*\mathfrak{B} \to T_P^*\mathfrak{B} \ni \langle \boldsymbol{T}^{\backslash}\boldsymbol{U}, \boldsymbol{\alpha}\rangle_p = \langle \boldsymbol{U}, \boldsymbol{T}^{/*}\boldsymbol{\alpha}\rangle_p \text{ or } T^{\cdot j^*}_{i\cdot} = T^{i\cdot}_{\cdot j} \\ \boldsymbol{T}^{/*}: T_P\mathfrak{B} \to T_P\mathfrak{B} \ni \langle \boldsymbol{T}^{\backslash}\boldsymbol{\alpha}, \boldsymbol{U}\rangle_p = \langle \boldsymbol{\alpha}, \boldsymbol{T}^{\backslash *}\boldsymbol{U}\rangle_p \text{ or } T^{i\cdot^*}_{\cdot j} = T^{\cdot j}_{i\cdot} \\ \boldsymbol{T}^{b*}: T_P\mathfrak{B} \to T_P^*\mathfrak{B} \ni \langle \boldsymbol{T}^{b}\boldsymbol{U}, \boldsymbol{V}\rangle_p = \langle \boldsymbol{U}, \boldsymbol{T}^{b*}\boldsymbol{V}\rangle_p \text{ or } T^{ij^*} = T^{ji} \\ \boldsymbol{T}^{\#*}: T_P^*\mathfrak{B} \to T_P\mathfrak{B} \ni \langle \boldsymbol{T}^{\#}\boldsymbol{\alpha}, \boldsymbol{\beta}\rangle_p = \langle \boldsymbol{\alpha}, \boldsymbol{T}^{\#*}\boldsymbol{\beta}\rangle_p \text{ or } T^*_{ij} = T_{ji} \\ \forall\ \boldsymbol{U}, \boldsymbol{V} \in T_p\mathfrak{B} \wedge \boldsymbol{\alpha}, \boldsymbol{\beta} \in T_p^*\mathfrak{B}\end{gathered} \tag{A.20}$$

Remark A.9: The matrix components of dual of a tensor are identical to the transpose of component matrix of original tensor.

Remark A.10: Mixed 2nd order tensors, $\boldsymbol{T}^{\backslash *} \in \mathcal{S}_1^{\cdot 1}$, but $\boldsymbol{T}^{\backslash} \in \mathcal{S}_{\cdot 1}^{1\cdot}$, similarly $\boldsymbol{T}^{/*} \in \mathcal{S}_{\cdot 1}^{1\cdot}$but $\boldsymbol{T}^{/} \in \mathcal{S}_1^{\cdot 1}$. However, $\boldsymbol{T}^{b*} \wedge \boldsymbol{T}^{b} \in \mathcal{S}_2^0$ and $\boldsymbol{T}^{\#*} \wedge \boldsymbol{T}^{\#} \in \mathcal{S}_0^2$, belongs to the same tensor spaces. Thus for covariant and contravariant 2nd order tensors self-duality or self-adjointness can be defined.

Definition A.9: A map $\boldsymbol{T}^b: T_p\mathfrak{B} \to T_p^*\mathfrak{B}$ is called self-dual or self-adjoint if $\boldsymbol{T}^{b*} = \boldsymbol{T}^b$. Similarly, a map $\boldsymbol{T}^{\#}: T_P^*\mathfrak{B} \to T_p\mathfrak{B}$ is called self-dual or self-adjoint if $\boldsymbol{T}^{\#*} = \boldsymbol{T}^{\#}$.

A.2.5 Riemannian Metric

In solid mechanics, manifolds that are of interests are Riemannian manifolds, i.e. the manifold $\mathfrak{B}$ is endowed with a Riemannian metric. The Riemannian metric can then be used to define inner product of tensors.

Definition A.10: A Riemannian metric $\boldsymbol{G}(P) \equiv \boldsymbol{G}_P$ on $\mathfrak{B}$ is a C^∞ 2nd order covariant tensor field on $\mathfrak{B}$ such that:

$$\begin{gathered} \boldsymbol{G}_P(\boldsymbol{V}_1, \boldsymbol{V}_2) = \boldsymbol{G}_P(\boldsymbol{V}_2, \boldsymbol{V}_1) \ \forall \ \boldsymbol{V}_2, \boldsymbol{V}_1 \in T_P\mathfrak{B} \\ \boldsymbol{G}_P(\boldsymbol{V}, \boldsymbol{V}) > 0 \ \forall \ \boldsymbol{V} \in T_P\mathfrak{B} \text{ with } \boldsymbol{V} \neq \boldsymbol{0} \end{gathered} \tag{A.21}$$

Definition A.11: The inner product on tangent space $T_P\mathfrak{B}$ at P is the mapping:

$$\boldsymbol{U}.\boldsymbol{V}: T_P\mathfrak{B} \times T_P\mathfrak{B} \to \mathbb{R} \ni \boldsymbol{U}.\boldsymbol{V} \stackrel{\text{def}}{=} \boldsymbol{G}_P(\boldsymbol{U}, \boldsymbol{V}) \ \forall \ \boldsymbol{U}, \boldsymbol{V} \in T_P\mathfrak{B} \tag{A.22}$$

Remark A.11: $\boldsymbol{G}_P$ is a covariant tensor field ($\boldsymbol{G}_P \equiv \boldsymbol{G}_P^b \equiv \boldsymbol{G}^b$) and belongs to $\mathcal{S}_2^0$. In component form, $\boldsymbol{G}_P = G_{ij}(\boldsymbol{G}^i \otimes \boldsymbol{G}^j)$. $\boldsymbol{G}_P$ can also be considered as linear map: $\boldsymbol{G}_P^b: T_P\mathfrak{B} \to T_P^*\mathfrak{B}$. The inverse map $\boldsymbol{G}_P^{b-1}: T_P^*\mathfrak{B} \to T_P\mathfrak{B}$ can also be defined where $\boldsymbol{G}_P^{b-1} \equiv \boldsymbol{G}_P^{\#} \equiv \boldsymbol{G}^{\#}$, is a contravariant metric tensor, $\boldsymbol{G}^{\#} = G^{ij}(\boldsymbol{G}_i \otimes \boldsymbol{G}_j)$.

Definition A.12: The contravariant metric tensor, $\boldsymbol{G}^{\#}$, defines an inner product on cotangent space $T_P^*\mathfrak{B}$ at P as follows:

$$\boldsymbol{\alpha}.\boldsymbol{\beta}: T_P^*\mathfrak{B} \times T_P^*\mathfrak{B} \to \mathbb{R} \ni \boldsymbol{\alpha}.\boldsymbol{\beta} \stackrel{\text{def}}{=} \boldsymbol{G}_P^{\#}(\boldsymbol{\alpha},\boldsymbol{\beta}) \quad \forall\ \boldsymbol{\alpha},\boldsymbol{\beta} \in T_P^*\mathfrak{B} \tag{A.23}$$

Remark A.12: Both covariant and contravariant metric tensors are self-dual or self-adjoint, i.e. $\boldsymbol{G}^{b} = \boldsymbol{G}^{b*}$ and $\boldsymbol{G}^{\#} = \boldsymbol{G}^{\#*}$.

Remark A.13: In component form, $\boldsymbol{U}.\boldsymbol{V} = G_{ij}U^iV^j$ and $\boldsymbol{\alpha}.\boldsymbol{\beta} = G^{ij}\alpha_i\beta_i$. Also, it can be shown that: $\boldsymbol{U}.\boldsymbol{V} = \langle \boldsymbol{G}^b\boldsymbol{U},\boldsymbol{V}\rangle_P = \langle \boldsymbol{U},\boldsymbol{G}^b\boldsymbol{V}\rangle_P$, $\boldsymbol{\alpha}.\boldsymbol{\beta} = \langle \boldsymbol{G}^{\#}\boldsymbol{\alpha},\boldsymbol{\beta}\rangle_P = \langle \boldsymbol{\alpha},\boldsymbol{G}^{\#}\boldsymbol{\beta}\rangle_P$, $\boldsymbol{G}^b(\boldsymbol{G}_i,\boldsymbol{G}_j) = G_{ij}$ and $\boldsymbol{G}^{\#}(\boldsymbol{G}^i,\boldsymbol{G}^j) = G^{ij}$.

A.2.6 Transpose

Let $\boldsymbol{T}^{\backslash},\boldsymbol{T}^{/},\boldsymbol{T}^{b}$ and $\boldsymbol{T}^{\#}$ be second order tensors, then their transpose are denoted by $\boldsymbol{T}^{\backslash T},\boldsymbol{T}^{/T},\boldsymbol{T}^{bT}$ and $\boldsymbol{T}^{\#T}$, respectively and are defined as follows:

$$\begin{aligned}
&\boldsymbol{T}^{\backslash T}: T_P\mathfrak{B} \to T_P\mathfrak{B} \ \ni \boldsymbol{T}^{\backslash}\boldsymbol{U}.\boldsymbol{V} = \boldsymbol{T}^{\backslash T}\boldsymbol{V}.\boldsymbol{U} \text{ or } T^{i\cdot T}_{\cdot j} = G^{iq}T^{p\cdot}_{\cdot q}G_{pj}\\
&\boldsymbol{T}^{/T}: T_P^*\mathfrak{B} \to T_P^*\mathfrak{B} \ \ni \boldsymbol{T}^{/}\boldsymbol{\alpha}.\boldsymbol{\beta} = \boldsymbol{T}^{/T}\boldsymbol{\beta}.\boldsymbol{\alpha} \text{ or } T^{\cdot jT}_{i\cdot} = G_{iq}T^{\cdot q}_{p\cdot}G^{pj}\\
&\boldsymbol{T}^{bT}: T_P^*\mathfrak{B} \to T_P\mathfrak{B} \ \ni \boldsymbol{T}^{b}\boldsymbol{U}.\boldsymbol{\alpha} = \boldsymbol{T}^{bT}\boldsymbol{\alpha}.\boldsymbol{U} \text{ or } T^{ijT} = G^{ip}T_{pq}G^{qj}\\
&\boldsymbol{T}^{\#T}: T_P\mathfrak{B} \to T_P^*\mathfrak{B} \ \ni \boldsymbol{T}^{\#}\boldsymbol{\alpha}.\boldsymbol{U} = \boldsymbol{T}^{\#T}\boldsymbol{U}.\boldsymbol{\alpha} \text{ or } T^T_{ij} = G_{ip}T^{pq}G_{qj}\\
&\forall\ \boldsymbol{U},\boldsymbol{V} \in T_P\mathfrak{B} \wedge \boldsymbol{\alpha},\boldsymbol{\beta} \in T_P^*\mathfrak{B}
\end{aligned} \tag{A.24}$$

A.2.7 Mapping Between Manifolds: Diffeomorphism and Two-point Tensors

Definition A.13: A C^r- diffeomorphism between manifolds $\mathfrak{B}_1$ and $\mathfrak{B}_2$ is a C^rmap, $\boldsymbol{\varphi}: \mathfrak{B}_1 \to \mathfrak{B}_2$, such that the inverse map $\boldsymbol{\varphi}^{-1}: \mathfrak{B}_1 \to \mathfrak{B}_2$ exists and is also C^r. Two manifolds are considered to be diffeomorphic if there exists a diffeomorphism between them.

Definition A.14: A map, $\boldsymbol{\varphi}: \mathfrak{B}_1 \to \mathfrak{B}_2$, between manifolds is called a local diffeomorphism if every point $P \in \mathfrak{B}_1$ has a neighborhood U such that $\varphi(U)$ is open in $\mathfrak{B}_2$ and $\boldsymbol{\varphi}: U \to \boldsymbol{\varphi}(U)$ is a diffeomorphism.

Let $P \in \mathfrak{B}_1$ and $\boldsymbol{\varphi}$ be a C^r- diffeomorphism such that $\boldsymbol{\varphi}(P) = p \in \mathfrak{B}_2$, then define the following spaces:

$T_P\mathfrak{B}_1$: Tangent space at $P \in \mathfrak{B}_1$ with basis $\{\boldsymbol{G}_i\}$ and $\boldsymbol{V} \in T_P\mathfrak{B}_1$

$T_P^*\mathfrak{B}_1$: Cotangent space at $P \in \mathfrak{B}_1$ with basis $\{\boldsymbol{G}^j\}$

$T_p\mathfrak{B}_2$: Tangent space at $p \in \mathfrak{B}_2$ with basis $\{\boldsymbol{g}_i\}$ and $\boldsymbol{v} \in T_p\mathfrak{B}_2$

$T_p^*\mathfrak{B}_2$: Cotangent space at $p \in \mathfrak{B}_2$ with basis $\{\boldsymbol{g}^j\}$ and $\boldsymbol{\beta} \in T_p^*\mathfrak{B}_2$

Now a mixed two point tensor is defined as follows:

Definition A.15: A mixed two point tensor $\boldsymbol{\mathcal{T}}^{\backslash}$ over the map $\boldsymbol{\varphi}$ is a linear map

$$\boldsymbol{\mathcal{T}}^{\backslash}: T_P\mathfrak{B}_1 \to T_p\mathfrak{B}_2 : \boldsymbol{V} \mapsto \boldsymbol{v} = \boldsymbol{\mathcal{T}}\boldsymbol{V} \tag{A.25}$$

Coordinates representation: $\boldsymbol{\mathcal{T}}^{\backslash} = \mathcal{T}_{\cdot A}^{a\cdot}\boldsymbol{g}_a \otimes \boldsymbol{G}^A$. Since \ is the only type of 2-point tensors considered in this study, this symbol is dropped, and 2-point tensors are written as $\boldsymbol{\mathcal{T}} \equiv \boldsymbol{\mathcal{T}}^{\backslash}$.

Definition A.16: The dual of a two point tensor, $\boldsymbol{\mathcal{T}}$, is defined as:

$$\boldsymbol{\mathcal{T}}^*: T_p^*\mathfrak{B}_2 \to T_P^*\mathfrak{B}_1 \ni \langle \boldsymbol{\mathcal{T}}\boldsymbol{V}, \boldsymbol{\beta} \rangle_p = \langle \boldsymbol{V}, \boldsymbol{\mathcal{T}}^*\boldsymbol{\beta} \rangle_P \; \forall \, \boldsymbol{V} \in T_P\mathfrak{B}_1, \boldsymbol{\beta} \in T_p^*\mathfrak{B}_2 \tag{A.26}$$

Coordinates representation: $\boldsymbol{\mathcal{T}}^* = \mathcal{T}_{A\cdot}^{\cdot a*}\boldsymbol{G}^A \otimes \boldsymbol{g}_a = \mathcal{T}_{\cdot a}^{A\cdot}\boldsymbol{G}^A \otimes \boldsymbol{g}_b$

Definition A.17: The transpose of a two point tensor, $\boldsymbol{\mathcal{T}}$, is defined as:

$$\boldsymbol{\mathcal{T}}^T: T_p\mathfrak{B}_2 \to T_P\mathfrak{B}_1 \ni \boldsymbol{\mathcal{T}}\boldsymbol{V}.\boldsymbol{\beta} = \boldsymbol{\mathcal{T}}^T\boldsymbol{\beta}.\boldsymbol{V} \; \forall \, \boldsymbol{V} \in T_P\mathfrak{B}_1, \boldsymbol{\beta} \in T_p^*\mathfrak{B}_2 \tag{A.27}$$

Coordinates representation: $\boldsymbol{\mathcal{T}}^T = \mathcal{T}_{\cdot a}^{A\cdot T}\boldsymbol{G}_A \otimes \boldsymbol{g}^a = g_{ab}\mathcal{T}_{\cdot B}^{b\cdot}G^{BA}\boldsymbol{G}_A \otimes \boldsymbol{g}^a$

Definition A.18: The tangent or differential, $T\boldsymbol{\varphi} = \boldsymbol{\mathcal{F}}_{\varphi} = \boldsymbol{\mathcal{F}}$, of the map $\boldsymbol{\varphi}: \mathfrak{B}_1 \to \mathfrak{B}_2$ is defined as:

$$\boldsymbol{\mathcal{F}}: T_P\mathfrak{B}_1 \to T_p\mathfrak{B}_2 \ni \boldsymbol{\mathcal{F}} = \mathcal{F}_{\cdot A}^{a\cdot}\boldsymbol{g}_a \otimes \boldsymbol{G}^A \text{ and } \mathcal{F}_{\cdot A}^{a\cdot} = \left.\frac{\partial \varphi^a}{\partial \Psi^A}\right|_P$$
$$\boldsymbol{\mathcal{F}} \stackrel{\text{def}}{=} T_P\boldsymbol{\varphi} \tag{A.28}$$

where $\boldsymbol{\Psi}$ are the coordinates on $\mathfrak{B}_1$. Thus, $\boldsymbol{\mathcal{F}}$ is a two point tensor.

Definition A.19: The tangent of the inverse map $\boldsymbol{\varphi}^{-1}: \mathfrak{B}_2 \to \mathfrak{B}_1$, that is $\boldsymbol{\mathcal{F}}^{-1}$,is defined as:

$$\boldsymbol{\mathcal{F}}^{-1}: T_p\mathfrak{B}_2 \to T_P\mathfrak{B}_1 \ni \boldsymbol{\mathcal{F}}^{-1} = \mathcal{F}_{\cdot a}^{A\cdot^{-1}} \boldsymbol{G}_A \otimes \boldsymbol{g}^a \text{ and } \mathcal{F}_{\cdot a}^{A\cdot^{-1}} = \left.\frac{\partial \varphi^{A^{-1}}}{\partial \phi^a}\right|_p \tag{A.29}$$

$$\boldsymbol{\mathcal{F}}^{-1} \stackrel{\text{def}}{=} T_p \boldsymbol{\varphi}^{-1}$$

where $\boldsymbol{\phi}$ are the coordinates on $\mathfrak{B}_2$.

A.2.8 Invariant transformations

The main concern in application of manifold structure to solid mechanics is the study of properties of differentiable manifolds that are preserved by diffeomorphisms. In this section the important transformation under a diffeomorphism are considered.

Definition A.20: The push-forward, $\boldsymbol{\varphi}_*(\cdot)$, of a vector field $\boldsymbol{V}(P): \mathfrak{B}_1 \to T_P\mathfrak{B}_1$under the diffeomorphism $\boldsymbol{\varphi}: \mathfrak{B}_1 \to \mathfrak{B}_2$ is defined as:

$$\boldsymbol{\varphi}_*(\boldsymbol{V}): T_P\mathfrak{B}_1 \to T_p\mathfrak{B}_2: \boldsymbol{V} \mapsto \boldsymbol{v} = \boldsymbol{\mathcal{F}}\boldsymbol{V} \text{ where } \boldsymbol{\mathcal{F}} = T_P\boldsymbol{\varphi} \tag{A.30}$$

Definition A.21: The pull-back, $\boldsymbol{\varphi}^*(\cdot)$, of a vector field $\boldsymbol{v}(p): \mathfrak{B}_2 \to T_p\mathfrak{B}_2$under the diffeomorphism $\boldsymbol{\varphi}: \mathfrak{B}_1 \to \mathfrak{B}_2$ is defined as:

$$\boldsymbol{\varphi}^*(\boldsymbol{v}): T_p\mathfrak{B}_2 \to T_P\mathfrak{B}_1: \boldsymbol{v} \mapsto \boldsymbol{V} = \boldsymbol{\mathcal{F}}^{-1}\boldsymbol{v} \text{ where } \boldsymbol{\mathcal{F}}^{-1} = T_p\boldsymbol{\varphi}^{-1} \tag{A.31}$$

Definition A.22: The push-forward, $\boldsymbol{\varphi}_*(\cdot)$, of a one-form field $\boldsymbol{\alpha}(P): \mathfrak{B}_1 \to T_P^*\mathfrak{B}_1$under the diffeomorphism $\boldsymbol{\varphi}: \mathfrak{B}_1 \to \mathfrak{B}_2$ is defined by the requirement that the scalar product, $\langle \boldsymbol{V}, \boldsymbol{\alpha} \rangle_P$, remains invariant under the diffeomorphism $\boldsymbol{\varphi}$, i.e. $\langle \boldsymbol{V}, \boldsymbol{\alpha} \rangle_P = \langle \boldsymbol{\varphi}_*(\boldsymbol{V}), \boldsymbol{\varphi}_*(\boldsymbol{\alpha}) \rangle_p$.

$$\boldsymbol{\varphi}_*(\boldsymbol{\alpha}): T_P^*\mathfrak{B}_1 \to T_p^*\mathfrak{B}_2: \boldsymbol{\alpha} \mapsto \boldsymbol{\beta} = \boldsymbol{\mathcal{F}}^{*-1}\boldsymbol{\alpha} \tag{A.32}$$

Definition A.23: The pull-back, $\boldsymbol{\varphi}^*(\cdot)$, of a one-form field $\boldsymbol{\beta}(p): \mathfrak{B}_2 \to T_p^*\mathfrak{B}_2$under the diffeomorphism $\boldsymbol{\varphi}: \mathfrak{B}_1 \to \mathfrak{B}_2$ is defined by the requirement that the scalar product,

$\langle \boldsymbol{v}, \boldsymbol{\beta} \rangle_p$, remains invariant under the diffeomorphism $\boldsymbol{\varphi}$, i.e. $\langle \boldsymbol{v}, \boldsymbol{\beta} \rangle_p = \langle \boldsymbol{\varphi}^*(\boldsymbol{v}), \boldsymbol{\varphi}^*(\boldsymbol{\beta}) \rangle_P$.

$$\boldsymbol{\varphi}^*(\boldsymbol{\beta}): T_p^* \mathfrak{B}_2 \to T_P^* \mathfrak{B}_1 : \boldsymbol{\beta} \mapsto \boldsymbol{\alpha} = \boldsymbol{\mathcal{F}}^* \boldsymbol{\beta} \tag{A.33}$$

For application to continuum mechanics, the push-forward and pull-back operations on second order tensor fields are formed to preserve symmetry and self duality of 2nd order tensors. To this end invariance of quadratic forms are employed. For example, push-forward of 2nd order tensor $\boldsymbol{T}^{\backslash}$ is defined by the invariance of $\boldsymbol{T}^{\backslash}\boldsymbol{V}.\boldsymbol{U} = \boldsymbol{\varphi}_*\left(\boldsymbol{T}^{\backslash}\boldsymbol{V}.\boldsymbol{U}\right) = \boldsymbol{\varphi}_*\left(\boldsymbol{T}^{\backslash}\right)\boldsymbol{\varphi}_*(\boldsymbol{V}).\boldsymbol{\varphi}_*(\boldsymbol{U}) = \boldsymbol{\mathcal{F}}^T\boldsymbol{\varphi}_*\left(\boldsymbol{T}^{\backslash}\right)\boldsymbol{\mathcal{F}}\boldsymbol{V}.\boldsymbol{U} \Longrightarrow \boldsymbol{\varphi}_*\left(\boldsymbol{T}^{\backslash}\right) = \boldsymbol{\mathcal{F}}^{-T}\boldsymbol{T}^{\backslash}\boldsymbol{\mathcal{F}}^{-1}$. Table A-1 gives the summary of important push-forward and pull-back operations.

A.2.9 Objective Time Derivatives

Definition A.24: Let $\boldsymbol{\varphi}: \mathfrak{B}_1(p) \to \mathfrak{B}_2(p')$, be a diffeomorphism and let $\boldsymbol{t}(p)$ be a spatial tensor field of arbitrary order defined on $\mathfrak{B}_1$. Further, let $\boldsymbol{t}'(p')$ be the transformed tensor field under the diffeomorphism $\boldsymbol{\varphi}: \mathfrak{B}_1(p) \to \mathfrak{B}_2(p')$. The tensor field $\boldsymbol{t}(p)$ transforms objectively under the transformation $\boldsymbol{\varphi}$ if:

$$\boldsymbol{t}' = \boldsymbol{\varphi}_*(\boldsymbol{t}) \tag{A.34}$$

where $\boldsymbol{\varphi}_*(\boldsymbol{t})$ is the push-forward of $\boldsymbol{t}$ under the diffeomorphism $\boldsymbol{\varphi}$.

Remark A.14: A tensor field $\boldsymbol{t}(p)$is said to be spatially covariant if A.43 hold for every diffeomorphism $\boldsymbol{\varphi}: \mathfrak{B}_1(p) \to \mathfrak{B}_2(p')$.

Remark A.15: An isometry is a diffeomorphism which leave the metric tensor invariant, i.e. $\boldsymbol{\varphi}_*(\boldsymbol{G}) = \boldsymbol{G}$, where $\boldsymbol{G}$ is a metric on $\mathfrak{B}_1$.

Definition A.25: Let Ψ be a an object defined on the reference configuration $\mathfrak{B}$, where Ψ can be a scalar , a vector, a one form or a tensor of arbitrary order. The material time derivative of this object is defined as:

$$\dot{\Psi} \stackrel{\text{def}}{=} \frac{D\Psi}{Dt} = \left.\frac{\partial \Psi}{\partial t}\right|_P \tag{A.35}$$

where the index P indicates that the particle P is held fixed during differentiation.

Definition A.26: The Lie derivative of an object Ψ (scalar , vector or tensor) defined on current configuration $\mathfrak{B}_t$ is defined as follows:

$$\mathcal{L}_v(\Psi) = \boldsymbol{\varphi}_* \left(\frac{D}{Dt} \boldsymbol{\varphi}^* [\Psi] \right) \tag{A.36}$$

Remark A.16: Material time derivative of any spatial tensor field (field defined on the current configuration) is not an objective tensor field. However, Lie derivatives of spatial tensor field are objective tensor fields.

	Push-forward $\boldsymbol{\varphi_*(\cdot)}$	**Pull-back** $\boldsymbol{\varphi^*(\cdot)}$
Scalar	$\boldsymbol{\varphi_*(S) = S \circ \varphi^{-1}}$	$\boldsymbol{\varphi^*(S) = S \circ \varphi}$
Vector	$\boldsymbol{\varphi_*(V) = \mathcal{F}V}$	$\boldsymbol{\varphi^*(v) = \mathcal{F}^{-1}\, v}$
One-form	$\boldsymbol{\varphi_*(\alpha) = \mathcal{F}^{*-1}\alpha}$	$\boldsymbol{\varphi^*(\beta) = \mathcal{F}^{*}\beta}$
2nd Order Tensors	$\boldsymbol{\varphi_*(T^{\backslash}) = \mathcal{F}^{-T}T\backslash\mathcal{F}^{-1}}$ $\boldsymbol{\varphi_*(T^{/}) = \mathcal{F}^{*T}T/\mathcal{F}^{*}}$ $\boldsymbol{\varphi_*(T^{b}) = \mathcal{F}^{*-1}T^{b}\mathcal{F}^{-1}}$ $\boldsymbol{\varphi_*(T^{\#}) = \mathcal{F}T^{\#}\mathcal{F}^{*}}$	$\boldsymbol{\varphi^*(t^{\backslash}) = \mathcal{F}^{T}t\backslash\mathcal{F}}$ $\boldsymbol{\varphi^*(t^{/}) = \mathcal{F}^{*-T}t/\mathcal{F}^{*-1}}$ $\boldsymbol{\varphi^*(t^{b}) = \mathcal{F}^{*}t^{b}\mathcal{F}}$ $\boldsymbol{\varphi^*(t^{\#}) = \mathcal{F}^{-1}t^{\#}\mathcal{F}^{*-1}}$

Table A-1: Push-forward and Pull-back Operations

BIBLIOGRAPHY

Abedi, K., and Parke, G.A.R. (1996). "Progressive collapse of single-layer braced domes," *International Journal of Space Structures*, Vol. 11, No 3, 291-306.

Abraham, F.F., Broughton, J., Bernstein, N., and Kaxiras, E. (1998). "Spanning the continuum to quantum length scales in a dynamic simulation of brittle fracture," *Europhysics Letters*, Vol. 44, No. 6, 783-787.

Abraham, F.F., Broughton, J.Q., Bernstein, N., and Kaxiras, E. (1998). "Spanning the length scales in dynamic simulation," *Computers in Physics*, Vol. 12, Issue 6, 538-546.

Aifantis, E.C. (1984). "On the microstructural origin of certain inelastic models," *Journal of Engineering Materials and Technology - transactions of the ASME*, Vol. 106, 326-330.

Aifantis, E.C. (1987). "The physics of plastic deformation," *International Journal of Plasticity*, Vol. 3, No. 3, 211-247.

AISC (1997). Seismic Provisions for Structural Steel Buildings, ANSI/AISC 341-97, *American Institute of Steel Construction*, Chicago, Illinois.

AISC (2002). Seismic Provisions for Structural Steel Buildings, ANSI/AISC 341-02, *American Institute of Steel Construction*, Chicago, Illinois.

AISC (2005). Seismic Provisions for Structural Steel Buildings, ANSI/AISC 341-05, *American Institute of Steel Construction*, Chicago, Illinois.

AISC-LRFD (1999). Manual of Steel Construction –Load and Resistant Factor Design, Third Edition, *American Institute of Steel Construction,* Chicago.

AISC (2005). Steel Construction Manual, 13th Edition, *American Institute of Steel Construction*, Chicago.

ANSI/AISC 360-05 (2005). Specifications for Structural Steel Buildings. *American Institute of Steel Construction*, Chicago.

Arce, G. (2002). Impact of Higher Strength Steels on Local Buckling and Overstrength of Links in Eccentrically Braced Frames. Master's Thesis, *Dept. of Civil Engineering*, Univ. of Texas at Austin, Austin, TX.

Argon, A.S., Im, J., and Safoglu, R. (1975). "Cavity formation from inclusions in ductile fracture," *Metallurgical Transactions*, Vol. 6A, 825-837.

Armero, F., and Oller, S. (2000). "A general framework for continuum damage models. I. Infinitesimal plastic damage models in stress space," *International Journal of Solids and Structures*, Volume 37, Issues 48-50, 7409-7436.

Armero, F., and Oller, S. (2000). "A general framework for continuum damage models. II. Integration algorithms, with applications to the numerical simulation of porous metals," *International Journal of Solids and Structures*, Volume 37, Issues 48-50, 7437-7464.

Arora, J.S., Haskell, D.F., and Govil, A.K. (1980), "Optimal design of large structures for damage tolerance," *AIAA Journal*, Vol. 18, No. 5, 563-570.

Anderson, T.L. (2004). Fracture Mechanics: fundamentals and applications, CRC Press, Boca Raton, FL, 3rd ed.

Antman, S. (2005). Nonlinear Problems of Elasticity, Springer, 2nd ed.

ASCE Standard 7-02, Minimum Design Loads for Buildings and Other Structures (ASCE 7-02/ANSI A58) (2002), American Society of Civil Engineers, Reston, VA.

ASCE Standard 7-05, Minimum Design Loads for Buildings and Other Structures (ASCE 7-05/ANSI A58) (2005), American Society of Civil Engineers, Reston, VA.

Astaneh-Asl, A. (2003). "Progressive Collapse Prevention in New and Existing Buildings", Proceedings, *9th Arab Structural Engineering Conference*, November 29-December 1, Abu Dhabi, United Arab Emirates (UAE).

Astaneh-Asl, A., Jones, B, Zhao, Y., and Hwa, R., (2002), Progressive collapse resistance of steel building floors", Report number: UCB/CEE-STEEL-2001/03, University of California at Berkeley.

Atkins, P., and Friedman, R. (2005). Molecular Quantum Mechanics, Oxford University Press, USA, 4th ed.

Attard, P. (2002), Thermodynamics and Statistical Mechanics, Academic Press, 1st ed.

Baldridge S.M. and Humay F.K. (2003). "Preventing progressive collapse in concrete buildings," *Concrete International*, November 2003, 73-79.

Bandstra, J. P., Goto, D. M. and Koss, D. A. (1998). "Ductile failure as a result of a void-sheet instability: Experiment and computational modeling," *Material Science and Engineering*, A249, 46-54.

Bathe, K.J. (1995). Finite Element Procedures, Prentice Hall.

Bathe, K.J., and Chapelle, D. (2003). The Finite Element Analysis of Shells: Fundamentals, Springer; 1st ed.

Bazant, Z.P., Belytschko, M., and Chang, T.P. (1984), "Continuum theory for strain-softening," *ASCE Journal of Engineering Mechanics*, Vol. 110, 1666-1691.

Belytschko, T., Fish, J. and Bayliss, A. (1990). "The Spectral Overlay on Finite Elements for Problems with High Gradients," *Computer Methods in Applied Mechanics and Engineering*, Vol. 81, No. 1, 71-89.

Belytschko, T., Liu, W.K., and Moran, B. (2000). Nonlinear Finite Elements for Continua and Structures, Wiley, 1st ed.

Benzerga, A.A., Besson, J., and Pineau, A. (1999). "Coalescence-controlled anisotropic ductile fracture," *Journal of Engineering Materials and Technology*, Vol. 121(2), 221-229.

Benzerga, A. A. and Besson, J. (2001). "Plastic potentials for anisotropic porous solids," *European Journal of Mechanics A/Solids*, 20(3), 397–434.

Beremin, F.M. (1981). "Cavity formation from inclusions in ductile fracture of A508 steel," *Metallurgical Transactions A*, Vol. 12(5), 723-731.

Bonet, J., and Wood, R.D. (2008). Nonlinear Continuum Mechanics for Finite Element Analysis, Cambridge University Press, 2nd ed.

Bridgman, P.W., (1952). *Studies in Large Flow and Fracture.* McGraw Hill, NewYork.

Broughton, J.Q., Abraham, F.F., Bernstein, N., and Kaxiras, E. (1999). "Concurrent coupling of length scales: methodology and applications," *Physics Review B*, Vol. 60, Issue 4, 2391-2403.

Brown, L.M., and Stobbs, W.M. (1976). "The work hardening of copper silica vs equilibrium plastic relaxation by secondary dislocations," *Philosophical Magazine*, Vol. 34, 351-372.

Casciati, F., and Faravelli, L. (1984). "Progressive Failure for Seismic Reliability Analysis", *Engineering Structures*, Vol. 6, No. 2, 97-103.

Castaneda, P., and Zaidman, M. (1994). "Constitutive models for porous materials with evolving microstructure," *J. Mech. Phys. Solids*, Vol. 42, No. 9, 1459–1497.

Chaboche, J.L. (1981). "Continous damage mechanics - a tool to describe phenomena before crack initiation," *Nuclear Engineering and Design*, Vol. 64, No. 2, 233-247.

Chaboche, J.L. (1988). "Continuum damage mechanics. Part-I General concepts," Journal of Applied Mechanics," Vol. 55, No. 1, 59-64.

Chaboche, J.L. (1988). "Continuum damage mechanics. Part-II Damage growth, crack initiation, and crack growth," Journal of Applied Mechanics," Vol. 55, No. 1, 65-72.

Chaboche, J.L., Lesne, P.M., and Maire, J.F. (1995). "Continuum damage mechanics, anisotropy and damage deactivation for brittle materials like concrete and ceramic composites," *International Journal of Damage Mechanics*, Vol. 4, No. 1, 5-22.

Chaboche, J.L. (1995). "A continuum damage theory with anisotropic and unilateral damage," La Recherche Aerospatiale 2, 139-147.

Coleman, B.D., and Gurtin, M.E. (1967). "Thermodynamics with internal state variables," *The Journal of Chemical Physics*, Vol. 47, 597-613.

Coleman, B.D., and Noll, W. (1963). "The thermodynamics of elastic materials with heat conduction and. Viscosity," *Archives for Rational Mechanics and Analysis*, Vol. 13, 167-178.

Cook, D.B. (2005). Handbook of Computational Quantum Chemistry, Dover Publications.

Crisfield M.A. (1991). Non-Linear Finite Element Analysis of Solids and Structures, Volume 1, Wiley.

Crisfield M.A. (1997). Non-Linear Finite Element Analysis of Solids and Structures, Volume 2 - Advanced Topics, Wiley, 1st ed.

de Borst, R., and Sluys, L.J. (1991). "Localization in a cosserat continuum under static and loading conditions," *Computer Methods in Applied Mechanics and Engineering*, Vol. 90, Issue 1-3, 805-827.

Dhar, S., Sethuraman, R., and Dixit, P.M. (1996). "A continuum damage mechanics model for void growth and micro crack initiation," *Engineering fracture mechanics*, Vol. 53, No. 6, 917-928.

Dong, S. B. (1983). "Global-Local Finite Element Methods," Chapter 14 In: Noor, A. K., and Pilkey, W. D. (ed.), *State of the Art Surveys on Finite Element Technology*, pp. 451-474. American Society of Mechanical Engineers (ASME), New York.

Dos Santos, F.F. and Ruggieri, C. (2003). "Micromechanics modelling of ductile fracture in tensile specimens using computational cells," *Fatigue and Fracture of Engineering Materials and Structures*, 26(2), 173-181.

Dusenberry, D.O., and Hamburger, R.O. (2006). "Practical Means for Energy-Based Analyses of Disproportionate Collapse Potential," *Journal of Performance of Constructed Facilities*, Volume 20, Issue 4, 336-348.

Ellingwood, B.R., and Dusenberry D.O. (2005). "Building design for abnormal load and progressive collapse," *Computer-Aided Civil and Infrastructure Engineering*, Vol. 20, 2005, 194-205.

Ellingwood, B.R. (2006). Mitigating Risk from Abnormal Loads and Progressive Collapse," *Journal of Performance of Constructed Facilities*, Vol. 20, Issue 4, 315-323.

Ellingwood, B., and Leyendecker, E.V. (1978). "Approaches for design against progressive collapse," *Journal of the Structural Division*, ASCE, 104(3), 413-423.

El-Tawil, S. and Deierlein, G. G. (1998). "An Examination for Stress Resultant Plasticity for Frame Structures," *Journal of Engineering Mechanics*, ASCE, Vol. 124, No. 12, pp. 1360-1370.

El-Tawil, S., and Deierlein, G.G. (2001). "Nonlinear analysis of mixed steel concrete frames I: Element formulation," *Journal of Structural Engineering*, ASCE, Vol. 127, No. 6, 647-655.

El-Tawil, S., and Deierlein, G.G. (2001). "Nonlinear analysis of mixed steel concrete frames II: Implementation and Verification," *Journal of Structural Engineering*, ASCE, Vol. 127, No. 6, 647-655.

El-Tawil S., Vidarsson, E., Mikesell, T., and Kunnath, S.K. (1999). "Inelastic behavior and design of steel panel zones," *Journal of Structural Engineering*, ASCE, Vol. 125, No. 2, 183-193.

Eterovic, A.L., and Bathe, K.J. (1990). "Hyperelastic-based large strain elasto-plastic constitutive formulation with combined isotropic-kinematic hardening using the logarithmic stress and strain measures," *International Journal for Numerical Methods in Engineering*, Vol. 30, Issue 6, 1099-1114.

FEMA 273 (1997). NEHRP Guidelines for the Seismic Rehabilitation of Buildings, *Federal Emergency Management Agency*, Washington, DC.

FEMA 302 (1997). Recommended Provisions for Seismic Regulations for New Buildings, *Federal Emergency Management Agency*, Washington, DC.

FEMA 350 (2000). Recommended Seismic Design Criteria for New Steel Moment-Frame Bulidings, *Federal Emergency Management Agency*, Washington, DC.

FEMA 355D (2000). State of the Art Report on Connection Performance, *Federal Emergency Management Agency*, Washington, DC.

FEMA 356 (2000). Prestandard and Commentary for the Seismic Rehabilitation of Buildings, *Federal Emergency Management Agency*, Washington, DC.

FEMA 369 (2000). NEHRP Recommended Provisions for Seismic Regulations for New Buildings and Other Structures. Part 2: Commentary, *Federal Emergency Management Agency*, Washington, DC.

Ferahian, R.H. (1972). "Buildings: Design for prevention of progressive collapse", *Civil Engineering- ASCE,* February 1972, pp. 66-69.

Fish, J., Nayak, P., and Holmes, M.H. (1994). "Microscale Reduction Error Indicators and Estimators for a Periodic Heterogeneous Medium," *Computational Mechanics*, Vol. 14, No. 4, 323-338.

Fish, J., Shek, K., Pandheeradi, M., and Shephard, M.S. (1997). "Computational Plasticity for Composite Structures Based on Mathematical Homogenization: Theory and Practice," *Computer Methods in Applied Mechanics and Engineering*, Vol. 148, No. 1, 53-73.

Fish J., and Wagiman A. (1993). "Multiscale finite element method for a locally nonperiodic heterogeneous medium," *Computational Mechanics*, Vol. 12, No. 3, 164-180.

Frenkel, D., and Smit, B. (2001). Understanding Molecular Simulation, Academic Press, 2nd ed.

Garajeu, M., Michel, J. C., and Suquet, P. (2000). "A micromechanical approach of damage in viscoplastic materials by evolution size, shape and distribution of voids," *Computer Methods in Applied Mechanics and Engineering*, 183(3-4), 223–246.

Ghosh, S.K. (2006). Assessing Ability of Seismic Structural Systems to Withstand Progressive Collapse: Design of Steel Braced Frame Buildings. *Report - SK Ghosh and Associates*, 334 E Colfax, Unit E, Palatine, IL 60067.

Ghosh S., Lee K., and Moorthy S. (1995). "Multiple scale analysis of heterogeneous elastic structures using homogeneization theory and Voronoi cell finite element method," *International Journal of Solids and Structures*, Vol. 32, No. 1, 1995, 27-42.

Ghosh, S., Lee, K., and Moorthy, S. (1996). "Two scale analysis of heterogeneous elastic-plastic materials with asymptotic homogenization and Voronoi cell finite element model," *Computer Methods in Applied Mechanics and Engineering*, Vol. 132, Issue 1-2, 63-116.

Gologanu, M., Leblond, J. B., and Devaux, J. (1993). "Approximate models for ductile metals containing non-spherical voids - case of axisymmetric prolate ellipsoidal cavities," *Journal of the Mechanics and Physics of Solids*, 41(11), 1723–1754.

Gologanu, M., Leblond, J. B., and Devaux, J. (1994). "Approximate models for ductile metals containing non-spherical voids - case of axisymmetric oblate ellipsoidal cavities," *Journal of Engineering Materials and Technology*, Transactions of the ASME, 116(3), 290–297.

Goldstein, H., Poole, C.P., and Safko, J.L. (2001). Classical Mechanics, Addison Wesley, 3rd ed.

Goods, S.H., and Brown, L.M., (1979). "The nucleation of cavities by plastic deformation," *Acta Metallurgica*, Vol. 27, No. 1, 1-15.

Govindjee, S.D, Kay, G.J., and Simo, J.C. (1995). "Anisotropic modeling and numerical simulation of brittle damage in concrete," *International Journal of Numerical Methods in Engineering*, Vol. 38, Issue 21, 3611-3633.

Gross, J.L., and McGuire, W. (1983). "Progressive collapse resistant design," *Journal of Structural Engineering*, ASCE, 109(1), 1-14.

Grierson, D.E., Xu, L., and Liu, Y. (2005). "Progressive-failure analysis of buildings subjected to abnormal loading," *Computer-Aided Civil and Infrastructure Engineering*, Vol. 20, No. 3, 155-171.

Griffiths, D.J. (2004). Introduction to Quantum Mechanics, Benjamin Cummings, 2nd ed.

Gurson, A. L. (1977). "Continuum theory of ductile rupture by void nucleation and growth. Part I: Yield criteria and flow rules for porous ductile media," *Journal of Engineering Materials and Technology*, 99(1), 2-15.

Gurtin, M.E. (1981). An Introduction to Continuum Mechanics, Academic Press.

Haile, J.M. (1997), Molecular Dynamics Simulation, Wiley-Interscience, 1st ed.

Hajjar, J.F., and Molodan. A. (1998). "A distributed plasticity model for cyclic analysis of concrete-filled steel tube beam-columns and composite frames," *Engineering Structures*, Vol. 20(4-6), 398-412.

Hallquist, J. (2006), "*LS-DYNA*", Livermore Software Technology Corp, Livermore, CA.

Hamburger, R., and Whittaker, A. (2004), "Design of steel structures for blast-related progressive collapse resistance," *Modern Steel Construction*, AISC, March 2004, 45-51.

Hancock, J.W., and Mackenzie, A. C., (1976). "On the mechanics of ductile failure in high-strength steel subjected to multi-axial stress-states," *Journal of Mechanics and Physics of Solids*, Vol. 24, 147-169.

Hao, S., Liu, W.K., Olson, G.B., and Moran, B., (2004). "Multi-scale constitutive model and computational framework for the design of ultra-high strength, high toughness steels," *Computer Method in Applied Mechanics and Engineering*, Vol. 193, Issue 17-20, 1865-1908.

Hansen, N.R., and Schreyer, H.L. (1994). "A thermodynamically consistent framework for theories of elastoplasticity coupled with damage," *International Journal of Solids and Structures*, Vol. 31, Issue 3, 359-389.

Hayden, H.W., and Floreen, S. (1969). "Observations of localized deformation during ductile fracture," *Acta Metallurgica*, Vol. 17, 213-214.

Hill, R. (1956). "The mechanics of quasi-static plastic deformation in metals," In: Batchelor," *Surveys in Mechanics: The G.I. Taylor 70th Anniversary Volume*, G.K., Davies, R.M. (Eds.), Cambridge University Press, Cambridge, 7-31.

Hill, R. (1968). "On constitutive inequalities for simple materials-I," *Journal of Mechanics and Physics of Solids*, Vol. 16(4), 229-242.

Hill, R. (1978). "Aspects of invariance in solid mechanics," in: C.-S. Yih (ed.), *Advances in Applied Mechanics*, Vol. 18, Academic Press, New York, 1-75.

Hill, R. (1998), The Mathematical Theory of Plasticity, Oxford University Press, USA

Hillerborg, A., Modeer, M., and Petersson, P.E. (1976). "Analysis of crack formation and crack growth in concrete by means of fracture mechanics and finite elements," Cement and Concrete Research, Vol. 6, 773-782.

Hollister, S.J., and Kikuchi, N. (1992). "A comparison of homogenization and standard mechanics analyses for periodic porous composites," *Computational Mechanics*, Vol. 10, No. 2, 73-95.

Holzapfel G.A. (2000). Nonlinear Solid Mechanics: A Continuum Approach for Engineering, Wiley, 1st ed.

Horstemeyer, M.F., Baskes, M.I., and Plimpton, S.J. (2001). "Computational nanoscale plasticity simulations using embedded atom potentials," *Theoretical and Applied Fracture Mechanics*, Vol. 37, No. 1-3, 49-98.

Huang, Y. (1991). "Accurate dilation rates for spherical voids in triaxial stress fields," *Journal of Applied Mechanics,* Vol. 58, 1084-1086.

Hughes T.J.R (2000). The Finite Element Method: Linear Static and Dynamic Finite Element Analysis, Dover Publications.

Hughes, T.J.R., Feijoo, G.R., Mazzei, L. and Quincy, J.B. (1998). "The variational multiscale method - a paradigm for computational mechanics," *Computer Methods in Applied Mechanics and Engineering*, Vol. 166, No. 1, 3-24.

IBC (2003). International Building Code, International Code Council, Washington, D.C

IBC (2006). International Building Code, International Code Council, Washington, D.C

Interagency Security Committee (ISC) (2004). ISC Security Design Criteria for New Federal Office Buildings and Major Modernization Projects, Washington, DC.

Isobe, D., and Tsuda, M. (2003). "Seismic collapse analysis of reinforced concrete framed structures using the finite element method," *Earthquake Engineering and Structural Dynamics*, 32(13), 2027-2046.

Jin, J., and El-Tawil, S. (2005). "Evaluation of FEMA-350 Seismic provisions for steel panel zones," *Journal of Structural Engineering*, ASCE, 131(2), 250-258.

Ju, J.W., (1989). "On energy-based coupled elastoplastic damage theories: constitutive modeling and computation aspects," *International Journal of Solids and Structures*, Vol. 25, Issue 7, 803-833.

Kaewkulchai, G., and Williamson, E.B. (2004). "Beam element formulation and solution procedure for dynamic progressive collapse analysis," *Computers & Structures*, Vol. 82, Issue 7-8, 639-651.

Kachanov, L.M., (1958). "Time rupture process under creep conditions," Izv. ARad. SSSR Teckh. Nauk 8, 26-31, (in Russian).

Kachanov, L.M., (1986). Introduction to Continuum Damage Mechanics, Springer, 1st ed.

Kanvinde A.M. (2004), "Micromechanical simulation of earthquake induced fracture in steel structures," *PhD Thesis*, Stanford University.

Kattan, P.I., and Voyiadjis G.Z. (1990). "A coupled theory of damage mechanics and finite strain elasto-plasticity. I: Damage and elastic deformations," *International Journal of Engineering Science*, Vol. 28, No. 5, 421-435.

Kim, K.D., and Engelhardt, M.D. (2000). "Beam-coulmn element for nonlinear seismic analysis of steel frames," *Journal of Structural Engineering*, ASCE, Vol. 126, No. 8, 916-924.

Krajcinovic, D. (1984). "Continuum damage mechanics," *Applied Mechanics Review*, Vol. 37, 397-402.

Kuwamura, H., and Yamamoto, K. (1997). "Ductile crack as a trigger of brittle fracture in steel," *Journal of Structural Engineering*, ASCE, Vol. 123, No. 6, 729-735.

Leach, A. (2001). Molecular Modeling: Principles and Applications, Prentice Hal, 2nd ed.

Leblond, J. B., Perrin, G., and Devaux, J. (1995). "An improved Gurson-type model for hardenable ductile metals," *European Journal of Mechanics A/Solids*, 14(4), 499-527.

Lee, B. J., and Mear, M. E. (1999). "Evolution of elliptical voids in power-law viscous solids," *Mechanics of Materials*, 31(1), 9-28.

Lee, E.H. (1969), "Elastic-plastic deformation at finite strains," *Journal of Applied Mechanics*, Vol. 36(1), 1-6.

Lee, E.H., and Liu, D.T. (1967). "Finite-strain elastic-plastic theory with application to plane-wave analysis," *Journal of Applied Physics*, Vol. 38(1), 19-27.

Lee, S., and Goel, S.C. (1987). Seismic behavior of hollow and concrete-filled square tubular bracing members, *Research report UMCE 87-11*, CEE Department - University of Michigan, Ann Arbor, MI 48109-2125.

Lemaitre, J. (1971). "Evaluation of dissipation and damage in metals submitted dynamic loading," In: *Proceedings of ICM1*, Kyoto, Japan.

Lemaitre, J. (1985). "A continuous damage mechanics model for ductile fracture," *Journal of Engineering Materials and Technology*, Trans. ASME, Vol. 107(1), 83-89.

LeRoy, G., Embury, J. D., Edward, G., and Ashby, M. F. (1981). "A model of ductile fracture based on the nucleation and growth of voids," *Acta Metallurgica*, Vol. 29, No. 8, 1509-1522.

Lewars, E.G. (2003). Computational Chemistry: Introduction to the Theory and Applications of Molecular and Quantum Mechanics, Springer, 1st ed.

Lewicki, B. and Olesen, S.O. (1974). "Limiting the possibility of progressive collapse," *Building Reseacrh & Practice,* Vol. 2, No.1, 10-13.

Leyendecker, E.V. and Ellingwood, B.R. (1977). "Design to reduce the risk of progressive collapse," *Building Science Series 98*, National Bureau of Standards, Washington, D.C.

Liang, X., Shen, Q., and Ghosh, S.K. (2006). "Assessing ability of seismic structural systems to withstand progressive collapse: seismic design and progressive collapse analysis of steel frame buildings." Report, SK Ghosh and Associates, 334 E Colfax, Unit E, Palatine, IL 60067.

Liew, J.Y.R. and Chen, H. (2004). "Explosion and fire element analysis of frames using fiber element approach," *Journal of Structural Engineering*, ASCE, Vol. 130, No. 7, 991-1000.

Lin, R.C., and Brocks, W. (2006). "On a finite-strain viscoplastic law coupled with anisotropic damage: theoretical formulations and numerical applications," *Archive of Applied Mechanics*, Vol. 75, No. 6-7,

Liu, C.T., and Gurland, J. (1968). "Fracture behavior of spheroidized carbon steels," *Transactions of the American Society of Metals*, Vol. 61, 156-157.

Liu, J., and Astaneh-Asl, A. (2003). "Moment-Rotation Parameters for Composite Shear Tab Connections," *Journal of Structural Engineering*, ASCE, 130(9), 1371-1380.

Liu, W.K., Park, H.S., Qian, D., Karpov, E.G., Kadowaki, H., and Wagner, G.J. (2006). "Bridging scale methods for nanomechanics and materials," *Computer Methods in Applied Mechanics and Engineering*, Vol. 195, Issue 13-16, 1407-1421.

Lubarda, V.A. (2001). Elastoplasticity Theory, CRC Press, 1st ed.

Lubarda, V.A. (1994). "An analysis of large-strain damage elastoplasticity," *International Journal of Solids and Structures*, Vol. 31, No. 21, 2951-2964.

Lubliner, J. (2008). PlasticityTheory, Dover Publications.

Lubliner, J., Oliver, J., Oller, S., and Onate, E. (1989). "Plastic-damage model for concrete," *International Journal of Solids and Structures*, Vol. 25, No. 3, 299-326.

Luccioni, B., Oller, S., and Danesi, R. (1996). "Coupled plastic-damaged model," *Computer Methods in Applied Mechanics and Engineering*, Vol. 129, Issue 1-2, 81-89.

Mackenzie, A.C., Hancock, J.W., and Brown, D.K., (1977). "On the influence of state of stress on the ductile failure initiation in high strength steels," *Engineering Fracture Mechanics*, Vol. 9, 167-188.

Magnusson J. (2004). "Learning from structures subjected to loads extremely beyond design," *Modern Steel Construction*, AISC, March 2004, 31-34.

Mahnken, R. (1999). "Aspects on the finite-element implementation of the Gurson model including parameter identification," *International Journal of Plasticity*, Volume 15, Issue 11, Pages 1111-1137.

Mahnken, R. (2000). "A comprehensive study of a multiplicative elastoplasticity model coupled to damage including parameter identification," *Computers and Structures*, Vol. 74, No. 2, 179-200.

Mahnken, R. (2002). "Theoretical, numerical and identification aspects of a new model class for ductile damage," *International Journal of Plasticity*, Volume 18, Issue 7, July 2002, Pages 801-831.

Mahnken, R. (2005). "Void growth in finite deformation elasto-plasticity due to hydrostatic stress states," *Computer Methods in Applied Mechanics and Engineering*, Volume 194, Issues 34-35, Pages 3689-3709.

Malla, R.B. and Nalluri, B.B. (1995). "Dynamic effects of member failure on response of truss type space structure," *Journal of Spacecrafts and Rockets*, Vol. 32, No. 3, 545-551.

Malvern, L.E. (1969). Introduction to the Mechanics of a Continuous Medium, Prentice-Hall.

Mandel, J. (1973), "Equations constitutives et directeurs dans les milieux plastiques et viscoplastiques," *International Journal of Solids and Structures*, Vol. 9, Issue 6, 725-740.

Marjanishvili, S., and Agnew, E. (2006). "Comparison of Various Procedures for Progressive Collapse Analysis," *Journal of Performance of Constructed Facilities*, Volume 20, Issue 4, 365-374.

Marsden, J.E., and Hughes, T.J.R. (1994). Mathematical Foundations of Elasticity, Dover Publications.

McClintock, F.A., (1968). "A criterion for ductile fracture by the growth of holes," *Journal of Applied Mechanics,* June 1968, 363-371.

McConnel, R.E. and Kelly, S.J. (1983). "Structural Aspects of progressive collapse of warehouse racking," *The Structural Engineer*, Vol. 61A, No.11, 343-347.

McGuire, W. (1975). "Prevention of progressive collapse," presented at the Jan., 1975, ASCE International Association for Bridge and Structural Engineering Regional Conference on Tall Buildings, Asian Institute of Technology, Bangkok, Thailand.

Mediavilla, J., Peerlings, R.H.J., and Geers, M.G.D. (2006). "A nonlocal triaxiality-dependent ductile damage model for finite strain plasticity," *Computer Methods in Applied Mechanics and Engineering*, Vol. 195(33-36), 4617-4634.

Menzel, A., Ekh, M., Runesson, K., and Steinmann, P. (2005). "A framework for multiplicative elastoplasticity with kinematic hardening coupled to anisotropic damage," *International Journal of Plasticity*, Vol. 21, No. 3, 397-434.

Menzel, A., and Steinmann, P. (2001). "A theoretical and computational framework for anisotropic continuum damage mechanics at large strains," *International Journal of Solids and Structures*, Vol. 38, No. 52, 9505-9523.

Menzel, A., and Steinmann, P. (2003). "Geometrically non-linear anisotropic inelasticity based on fictitious configurations: Application to the coupling of continuum damage and multiplicative elasto-plasticity," *International Journal for Numerical Methods in Engineering*, Vol. 56, No. 14, 2233-2266.

Mlakar P.F., Dusenberry, D.O., Harris, J.F., Haynes, G., Phan, L.T. and Sozen, M.A. (2003). "Findings and recommendations from pentagon crash", *Forensic Engineering : Proceedings of the Third Congress,* San Diego, California. Pp. 43-45.

Mote C. D. (1971). "Global-local finite element," *International Journal for Numerical Methods in Engineering*, Vol. 3, 565-574.

Nair R.S. (2004). "Progressive collapse basics," *Modern steel construction*, March 2004, 37-42.

Needleman, A. (1988). "Material rate dependence and mesh sensitivity in localization problems," *Computer Methods in Applied Mechanics and Engineering*, Vol. 67, Issue 1, 69-85.

Nemat-Nasser, S. (1999). "Averaging theorems in finite deformation plasticity," *Mechanics of Materials*, Vol. 31, 493-523.

Nemat-Nasser, S. (2004). Plasticity: A Treatise on Finite Deformation of Heterogeneous Inelastic Materials, Cambridge University Press.

Nemat-Nasser, S., and Hori, M. (1998). Micromechanics: Overall Properties of Heterogeneous Materials, North Holland, 2nd ed.

NFPA 5000 (2006): Building Construction and Safety Code, National Fire Protection Association, Quincy, MA.

Nair, R.S. (2006). "Preventing Disproportionate Collapse," *Journal of Performance of Constructed Facilities*, Volume 20, Issue 4, 309-314.

Norris, D.M., Jr., Reaugh, J.E., Moran, B. and Quinones, D.F. (1978). "A plastic-strain, mean-stress criterion for ductile fracture," *Journal of Engineering Materials and Technology*, Vol 100, 279-286.

Oden, J. T. (2006). Finite Elements of Nonlinear Continua, Dover Publications.

Oden, J.T. and Reddy, J.N. (1976), An Introduction to the Mathematical Theory of Finite Elements, Wiley, New York.

Ogden, R.W. (1997). Non-Linear Elastic Deformations, Dover Publications.

Ortiz, M. (1985). "A constitutive theory for the inelastic behavior of concrete," *Mechanics of Materials*, Vol. 4, 67-93.

Ottosen, N.S. and Ristinmaa, M. (2005). The Mechanics of Constitutive Modeling, Elsevier Science.

Panontin, T. L., and Sheppard, S. D. (1995). "The relationship between constraint and ductile fracture initiation as defined by micromechanical analyses," *Fracture Mechanics: 26th Volume*. ASTM STP 1256.

Popov, E. P., Zayas, V. A., and Mahin, S. A. (1979). "Cyclic inelastic buckling of thin tubular columns," *Journal of The Structural Divison*, ASCE, 105(11), 2261-2277.

Prendergast, J. (1995). "Oklahoma City aftermath", *Civil Engineering (New York)*, Vol. 65, No. 10, 42-45.

Pretlove, A.J., Ramsden, M., and Atkins, A.G. (1991). "Dynamic effects in progressive failure of structures," *International Journal of Impact Engineering*, Vol. 11, No. 4, 539-546.

Pretlove, A.J. (1986). "Dynamic effects in fail-safe structural design," In: *Proceedings, International Conference on Steel Structures: Recent Advances and their Application to Design*, Budva, Yugoslavia, 749-757.

Rakin M., Cvijovic Z., Grabulov V., Putic S., and Sedmak, A. (2004). "Prediction of ductile fracture initiation using micromechanical analysis," *Engineering Fracture Mechanics*, 71(4), 813-827.

Rapaport, D.C. (2004). The Art of Molecular Dynamics Simulation, Cambridge University Press, 2nd ed.

Rassati, G. A., Leon, R. T., and Noè, S. (2004). "Component modeling of partially restrained composite joints under cyclic and dynamic loading," *Journal of Structural Engineering*, ASCE, 130(2), 343-351.

Reusch, F., Svendsen, B., and Klingbeil, D. (2003). "Local and non-local Gurson-based ductile damage and failure modelling at large deformation," *European Journal of Mechanics and Solids*, 22(6), 779-792.

Rice, J.R., and Tracey, D.M. (1969). "On the ductile enlargements of voids in the triaxial stress fields," *Journal of Mechanics and Physics of Solids*, Vol. 17, 201-217.

Ricles, J.M., Mao, C., Lu, L.W., and Fisher, J.W. (April 2000). "Development and evaluation of improved details for ductile welded unreinforced flange connections," *SAC Report: SAC Task 7.05.*

Ristinmaa, M. (1997). "Void growth in cyclic loaded porous plastic solid," *Mechanics of Materials*, Volume 26, Issue 4, 227-245.

Ritchie, R.O., Server, W.L., and Wullaert, R.A. (1979). "Critical fracture stress and fracture strain models for the prediction of lower and upper shelf toughness in nuclear pressure vessel steels," *Metallurgical Transactions A*, Vol. 10A, No. 10, 1557-1570.

Rousselier, G. (1987). "Ductile fracture models and their potential in local approach of fracture," *Nuclear Engineering and Design*, Vol. 105, 97-111.

Rudd, R.E., and Broughton, J.Q. (1998). "Coarse-grained molecular dynamics and the atomic limit of finite elements," *Physics Review B*, Vol. 58, Issue 10, 5893-5896.

SBCCI (1999). Standard Building Code, International Code Council, Washington, D.C.

Shankar, R. (1994). Principles of Quantum Mechanics, Springer; 2nd ed.

Shih-Ho, C., Khandelwal, K., and El-Tawil, S. (2006). "Analytical Investigation of the web fracture failure in steel shear links," *Journal of Structural Engineering*, ASCE. Vol. 132, No. 8, 1192-1200.

Simo, J.C. (1988). "A framework for finite strain elastoplasticity based on maximum plastic dissipation and the multiplicative decomposition. Part II Computational aspects," *Computer Methods in Applied Mechanics and Engineering*, Vol. 68, No. 1, 1-31.

Simo, J.C. (1992). "Algorithms for static and dynamic multiplicative plasticity that preserve the classical return mapping schemes of the infinitesimal theory," *Computer Methods in Applied Mechanics and Engineering*, Vol. 99, Issue 1, 61-112.

Simo, J.C., and Hughes, T.J.R. (1998). Computational Inelasticity, Springer, 1st ed.

Simo, J.C., and Ju, J.W., (1987a). "Strain- and stress-based continuum damage models Part I: Formulation," *International Journal of Solids and Structures*, Vol. 23, Issue 7, 821-840.

Simo, J.C., and Ju, J.W., (1987b). "Strain- and stress-based continuum damage models Part II: Computational Aspects," *International Journal of Solids and Structures*, Vol. 23, Issue 7, 841-869.

Simo, J.C., and Ortiz, M. (1985). "Unified approach to finite deformation elastoplastic analysis based on the use of hyperelastic constitutive equations," *Computer Methods in Applied Mechanics and Engineering*, Vol. 49, No. 2, 221-245.

Singh, D.J., and Nordstrom, L. (2005). Planewaves, Pseudopotentials, and the LAPW Method, Springer; 2nd ed.

Smith, E.M. (1988). "Alternate path analysis of space trusses for progressive collapse," *Journal of Structural Engineering*, ASCE, Vol. 114, no. 9, 1978-1999.

Special Issue: Mitigating the Potential for Progressive Disproportionate Structural Collapse, *Journal of Performance of Constructed Facilities*, Volume 20, Issue 4, pp. 305-437 (November 2006).

Steinmann, P., and Carol, I. (1998). "A framework for geometrically nonlinear continuum damage mechanics," *International Journal of Engineering Science*, Vol. 36, No. 15, 1793-1814.

Steinmann, P., Miehe, C., and Stein, E., (1994). "Comparison of different finite deformation inelastic damage models within multiplicative plasticity for ductile materials," *Int. J. Comput. Mech.*, 13(6), 458–474.

Strang, G.W. and Fix, G.J. (1973). An Analysis of the Finite Element Method, Prentice Hall, Englewood Cliffs, New Jersey.

Szabo, A., and Ostlund, N.S. (1996). Modern Quantum Chemistry: Introduction to Advanced Electronic Structure Theory, Dover Publications.

Takano N., Zako M., Okuno Y. (2003). "Multi-scale finite element analysis of porous materials and components by asymptotic homogenization theory and enhanced mesh superposition method," *Modeling and Simulation in Materials Science and Engineering*, Vol. 11, No. 2, 137-156.

Tai, W.H. (1990). "Plastic damage and ductile fracture in mild steels," *Engineering Fracture Mechanics*, 37(4) 853-880.

Thomason, P.F. (1985). "Three-dimensional models for the plastic limit-load at incipient failure of the intervoid matrix in ductile porous solids," *Acta Metallurgica*, Vol. 33, 1079-1085.

Thomason, P.F. (1990). Ductile fracture of Metals, Pergamon Press, Oxford.

Thomason, P.F. (1998). "A view on ductile-fracture modeling," *Fatigue and Fracture of Engineering Materials and Structure,* Vol. 21(5), 1105-1122.

Toribio, J., and Ayaso, F.J. (2004). "Macro and microscopic approach to fracture of high strength steel notched bars," *Macro and Microscopic Approach to Fracture*, Ed. S.I. Nishida, WIT Press, Southampton, Boston, 201-242.

Truesdell, C.A., Noll, W. and Antman S.S. (2004). The Non-Linear Field Theories of Mechanics, Springer, 3rd ed.

Truesdell, C.A., and Toupin, R. (1960). The classical field theories. In Flügge's Handbuch der Physik, Vol. 3, Part 1, 226-793, Berlin, Springer-Verlag.

Tvergaard, V. (1981). "Influence of voids on shear band instabilities under plane strain conditions," *International Journal of Fracture*, 17(2), 389-407.

Tvergaard, V. and Needleman A. (1984). "Analysis of the cup-cone fracture in a round tensile bar," *Acta Metallurgica*, 32(1), 157-169.

UBC (1997). Uniform Building Code, International Code Council, Washington, D.C.

Unified Facilites Criteria (UFC 2005). Design of buildings to resist progressive collapse, Dept. of Defense, Washington, D.C.

U.S. General Service Administration (GSA 2003). Progressive collapse analysis and design guidelines for new federal office buildings and major modernization projects, Washington, D.C.

Van der G.E., and Kollmann, F.G. (1996). "On mathematical aspects of dual variables in continuum mechanics, Part 1: mathematical principles," *Z. Angew. Math. Mech,* ZAMM, 76(8), 447-462.

Van der G.E., and Kollmann, F.G. (1996). "On mathematical aspects of dual variables in continuum mechanics, Part 2: Application in nonlinear solid mechanics," *Z. Angew. Math. Mech*, ZAMM, 76(9), 497-504.

Wagner, G.J. and Liu, W.K. (2003). "Coupling of atomistic and continuum simulations using a bridging scale decomposition," *Journal of Computational Physics*, Vol. 190, Issue 1, 249-274.

Weber, G., and Anand, L. (1990). "Finite deformation constitutive equations and a time integration procedure for isotropic hyperelastic-viscoplastic solids," *Computer Methods in Applied Mechanics and Engineering*, Vol. 79, Issue 2, 173-202.

Wempner, G., and Talaslidis, D. (2002). Mechanics of Solids and Shells: Theories and Approximations, CRC Press, 1st ed.

Wilsdorf, H.G.F. (1983). "The ductile fracture of metals: a microstructural viewpoint," *Material Science and Engineering*, Vol. 59, No. 1, 1-39.

Wriggers, P. (2006). Computational Contact Mechanics, Springer, 2nd ed.

Xia, L. and Shih F.C. (1995). "Ductile crack growth - I. A numerical study using computational cells with microstructurally based length scales," *Journal of Mechanics and Physics of Solids*, 43(2), 233-259.

Zienkiewicz, O. C., Taylor, R. L., and Zhu, J.Z. (2005). The Finite Element Method: Its Basis and Fundamentals, Butterworth-Heinemann, 6th ed.